Understanding Electrocatalytic Nitrate Reduction Catalyst Performance in Ideal and Practical Conditions

by

Danielle Richards

A dissertation submitted in partial fulfillment
of the requirements for the degree of
Doctor of Philosophy
(Chemical Engineering)
in the University of Michigan
2022

Doctoral Committee:

Assistant Professor Nirala Singh, Chair
Assistant Professor Bryan Goldsmith
Professor Suljo Linic
Professor Charles McCrory

Danielle Richards

daricha@umich.edu

ORCID iD: 0000-0002-3476-4098

Dedication

For my mother.
My first role model. My number one fan. My favorite person.
We did it.

Acknowledgements

I would like to express my gratitude to my friends, family, and colleagues who have helped dissertation be possible.

I would like to thank Prof. Nirala Singh for welcoming me into your lab as one of its first students and for teaching me catalysis and electrochemistry. New graduate students usually have older students in their lab to ask the "dumb" questions… for me those questions went to you, and I hope they got better over time. Thank you for being a good advisor and mentor when I was stubborn or discouraged from a week of bad research results. I appreciate you creating a welcoming and focused environment in our lab group, which helped me grow as a researcher. I would also like to thank Prof. Bryan Goldsmith, Prof. Suljo Linic, and Prof. Charles McCrory for agreeing to be on my committee and posing such insightful and challenging questions. I would additionally like to thank Bryan for his great intuition and guidance on the collaborations between our labs.

I would like to thank the Singh Lab for their support and camaraderie during these past five years: Harsh Agarwal, Cailin Buchanan, Zixuan Wang, Ben Silcox, James Akinola, Claire Yin, Jared Arkfeld, Wendy Yu, Libo Yao, and Gyan Sharma. I am extremely grateful to have met you all. I was incredibly lucky to start a new lab alongside Harsh, who took the initiative on many new technologies in the lab and was always available for my questions. I am glad Zixuan joined our nitrate efforts because misery loves company and you really helped push forward our understanding of nitrate reduction. Meeting up with Cailin in Vancouver, Canada for my only in-person conference was very fun and it was also great that we got to defend at almost the same

time! I only had one office mate during graduate school and I am glad it was Claire, who so often was on the exact same wavelength as me.

I want to thank the friends I made in graduate school for their love and support: Rachel Elias, Sean McSherry, Patrick Kinnunen, Alex Hill, Connor McGlothin, Zixuan Wang, Jacques Esterhuizen, Emily Makowski, Jordyn Polito, Zach Berquist, Tobias Burger, and Katey Thomas. I cannot express how much I love all of you. Seeing you every day was the best part of living in Ann Arbor and I'm already planning out the next time I will see each of you. Additionally, I need to express my gratitude for 8 of these people letting me live with them at some point over the past 5 years. You're all too kind.

Finally, I would like to thank my family for their love and support. Specifically, I would like to thank my mother, Debra Richards, and my grandparents, Ed and Mary Richards. You all helped me achieve my dreams and I am forever grateful.

Table of Contents

List of Tables

List of Figures

List of Schemes

List of Appendices

Abstract

Anthropogenic activities which modify atmospheric nitrogen gas to more reactive forms of nitrogen such as ammonium are essential for sustaining the growing global population and maintaining modern aspects of life. Electrocatalytic nitrate reduction is identified as a promising technology for nitrate remediation of waste streams and water sources but needs further development. Here we aim to understand the various levels of activity for transition metal nitrate reduction catalysts and evaluate catalyst activity under conditions which would be closer to remediation conditions. Namely, chloride is present in nearly all nitrate polluted waste streams and so we investigate the effect of chloride. Additionally, to remediate large volumes of waste streams, continuous flow electrochemical reactors are necessary, so we investigate the electrocatalysts in flow reactors to compare to batch reactor configurations.

First, we use density functional theory (DFT) modeling and microkinetic modeling to identify key parameters (descriptors) influencing nitrate reduction activity on seven transition metals. The descriptors are N and O adsorption energies to the metal surface, because these adsorption energies control the strength of nitrate adsorption and correlate with hydrogen adsorption. The best performing catalysts adsorb nitrate strongly, but not so strongly as to poison the surface. The computed trends match the reported experimental activity measurements for these catalysts in the literature. We validated the adsorption energy trends by probing the adsorption of nitrate using cyclic voltammetry on Pt and Rh. We confirmed that Rh adsorbs nitrate more strongly than Pt, which explains the higher activity of Rh for nitrate reduction. With these descriptors we

predict alloys that will be active for nitrate reduction based on their computed N and O adsorption energies, including PtRu.

Second, we investigate the effects of chloride during nitrate reduction. We show that for active catalysts like Rh the nitrate reduction activity is more severely decreased compared to a less active catalyst like Pt when chloride is present. The decrease in activity is due to competitive adsorption between nitrate and chloride. The more severe chloride poisoning for Rh was unexpected because nitrate binds more strongly on Rh than on Pt. However, we show that chloride also binds so much more strongly on Rh than on Pt that chloride outcompetes nitrate for active sites. Using DFT we show a relation between nitrate and chloride adsorption energies on transition metals such that metals that adsorb nitrate strongly will adsorb chloride even more strongly, and thus be poisoned by chloride. To address this, we explore Rh_xS_y as a chloride-resistant electrocatalyst. We show that Rh_xS_y is active for nitrate reduction, but is poisoned by chloride to a similar extent as Pt. We use DFT and microkinetic modeling to show that possible active sites for nitrate reduction on Rh_xS_y are sulfur vacancy sites that adsorb nitrate strongly, explaining the high activity, but also adsorb chloride strongly, explaining the moderate chloride poison resistance.

Third, we compare the activity of Pt/C, PtRu/C, and Rh/C when used in a batch cell on a rotating disk electrode to a flow cell on a carbon felt. We show that the activity measured in the batch cell does not match that in the flow cell, but the trends are the same in both systems (Pt < PtRu < Rh). The activity trends match those expected from the O and N adsorption energies from our earlier work.

Chapter 1
Introduction

Part of this chapter was adapted from Z. Wang, D. Richards, and N. Singh. "Recent discoveries in the reaction mechanism of heterogeneous electrocatalytic nitrate reduction." *Catalysis Science & Technology* 11 (2021): 705-725.

1.1 Motivation

This section provides an overview of the motivations for removing nitrate from water resources. **Section 1.1.1** will provide background for the distribution of nitrogen species within the environment, with focus on natural pathways for nitrate production and consumption. **Section 1.1.2** will show the change in nitrate levels in ground and surface water as a result of necessary human-led processes. **Section 1.1.3** will present human and environmental hazards associated with increased nitrate levels and increased general interest in remediation of nitrate from water sources.

1.1.1 The nitrogen cycle and natural sources of nitrate.

Nitrogen (N) is one of the most abundant elements on Earth and is essential for animals and plants. Nitrogen is 78% of our atmosphere as nitrogen gas (N_2), found in the Earth's crust and mantle, and present in the ocean and fresh water sources as nitrate (NO_3^-) and ammonium (NH_4^+).[1] Nitrogen is also the fourth most abundant element in the human body,[2] and is an essential component of amino acids which are necessary for plant growth.[3] Though N_2 is the most accessible form of nitrogen, N_2 itself is inert and cannot be used directly by most organisms.[4] Instead,

ammonia/ammonium (NH_3/NH_4^+) and nitrate are the forms of nitrogen used by most organisms for constructing building blocks molecules like amino acids, nucleic acids, and vitamins.[2,4]

Transformations from N_2 to more reactive forms of nitrogen (more oxidized or more reduced) are especially important as they allow nitrogen to be used by organisms to produce essential compounds. Large-scale inorganic nitrogen transformation is tracked though the nitrogen cycle (**Figure 1.1**). The nitrogen cycle consists of nitrogen species being more oxidized or reduced through natural reactions: nitrogen fixation, denitrification, and nitrification.[2] Nitrate is the most oxidized form of nitrogen and the least oxidized (most reduced) form is ammonia/ammonium (NH_3/NH_4^+).

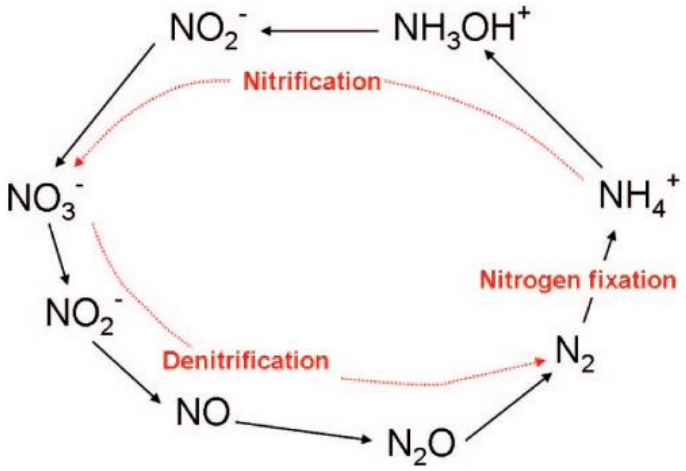

Figure 1.1. Transformations between reduced and oxidized forms of reactive nitrogen can be tracked through the nitrogen cycle. For simplicity, only the nitrogen containing species are shown here. Figure adapted from ref. [2].

In nature, the nitrogen cycle is kept in balance by enzyme-catalyzed reactions and natural phenomena. Nitrogen species are reduced or oxidized primarily through enzyme reactions called denitrifications or nitrifications, respectively. Several types of bacteria contain these nitrogen-focused enzymes and these bacteria have complex interactions with plants in which the plants strategically use the bacteria to obtain more useful (reactive) forms of nitrogen (i.e., NH_4^+) which then they will use to create amino acids, etc and grow.[5] Aside from enzyme reactions, nitrogen is

also oxidized through lightning (~ 5 Tg N per year).[6] Historically, there has been a balance of oxidation and reduction rates that prevent a buildup of oxidized or reduced forms of nitrogen; because of the importance of nitrogen for humans, animals, and plants, this balance is imperative.

1.1.2 Effects of anthropogenic activities on historic nitrate levels.

Human industrial and agricultural activities also contribute to the oxidation and reduction of nitrogen species, which have added additional reaction pathways and are causing an imbalance in the nitrogen cycle. The largest contributors to this are the Haber-Bosch process (nitrogen fixation), fossil fuel combustion (formation of NO_x gases), and agriculture-related biological nitrogen fixation.[1,6,7] Fertilizer for food production through the Haber-Bosch process results in 10^8 metric tonnes of nitrogen being fixed per year.[8] An additional 2.5×10^7 metric tonnes of nitrogen are produced from combustion of fossil fuels and 3.3×10^7 metric tonnes from cultivation of crops that fix nitrogen through biological pathways.[9] The rate of anthropogenic nitrogen fixed (203 Tg N per year) is estimated to be equal to the rate of natural nitrogen fixation (210 Tg N), effectively doubling the total amount of reactive nitrogen.[1,6] Even though bacterial species naturally convert fixed nitrogen back to N_2, the continuously increasing nitrogen fixation rates to support the world's growing population are much higher.

Although ammonia is the most produced reactive nitrogen species from industrial processes, it is nitrate pollution that is becoming a growing concern. 90% of nitrogen used for fertilizer is in the form of NH_4^+ and modern agricultural practices oversaturate crops to promote growth.[1] Nearly half of the applied fertilizer is unused by crops and drains into surface water sources where it is then oxidized via biologic nitrification to nitrate.[10] Thus, even though Haber-Bosch serves to fix N_2 and produce NH_3, the result is an increase in the amount of oxidized nitrogen

(NO_3^-) in the environment. Nitrate is very soluble in water and much of this nitrate accumulates in water sources.

Nitrate has been accumulating in all parts of the globe.[11,12] The trends in synthetic nitrogen fertilizer production using Haber-Bosch from 1900 to 2017 are shown in **Figure 1.2**.[13] The global population over the same time range is also shown in **Figure 1.2**.[14] The increase in N-fertilizer production enables greater food production which allows for this population growth. Global ammonia production is expected to increase 4% over the next 4 years,[15] which roughly matches the expected increase in world population over that time.[16] Additionally, since the population is expected to grow by 1% per year through 2050,[16] there will be an increasing need for fixed nitrogen for fertilizers to provide food. Although nitrogen utilization and fertilization technologies may become more efficient, anthropogenic nitrate will still be an issue. Many agricultural crops are inherently not efficient at up taking ammonia and nearly 50% of applied fertilizer is unused by the plant and lost to the environment.[17] Additionally, industrial processes (such as mining and metals refining) which produce nitrate waste must occur to maintain modern ways of life.[18]

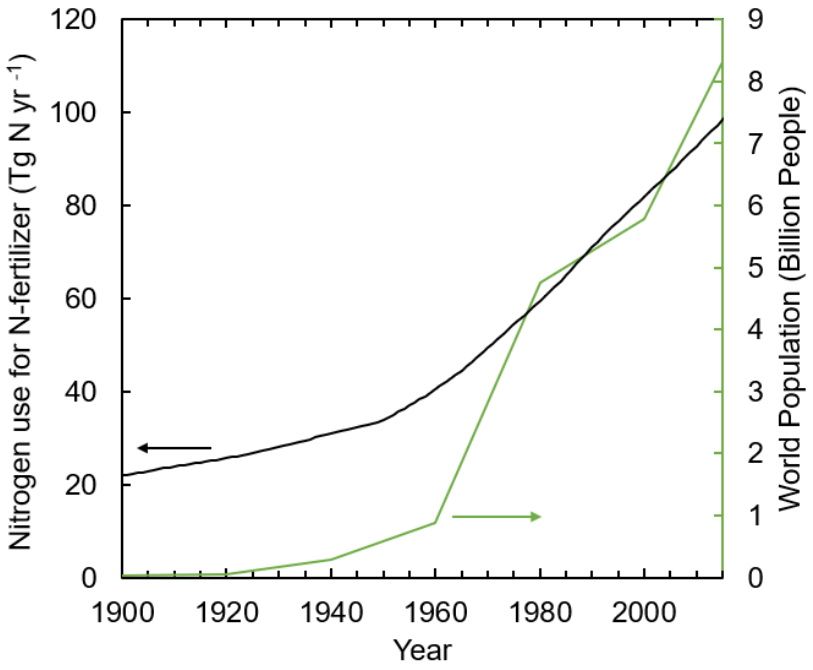

Figure 1.2. Teragrams per year of synthetic N-fertilizer produced globally since 1900. Global population vs. time plotted on secondary axis. Figure adapted from ref. [13].

1.1.3 Consequences of high nitrate levels on human health and the environment and agency regulations.

Balancing the nitrogen cycle is crucial for maintaining the environmental health of the Earth.[19] As of 2020, the National Academy of Engineering identifies the management of the nitrogen cycle, through improved fertilization technologies and by capturing and recycling waste, as a grand challenge.[20] The nitrogen cycle imbalance that may pose an even more immediate threat or exacerbate challenges with the carbon cycle.[21] An elevated concentration of nitrate in ground and surface water can have detrimental effects on aqueous ecosystems and human health. Leaching nitrate in water sources leads to negative environmental consequences, which include eutrophication, global acidification, climate change, and ozone loss in the stratosphere.[22] Consumption of nitrate contaminated water also has detrimental health impacts, such as methemoglobinemia and cancer.[10,22]

As a result of the harmful effects of nitrate, the United States Environmental Protection Agency (EPA) set a limit of 10 mg/L nitrate and 1 mg/L nitrite in drinking water to mitigate health hazards.[23] Similarly, the World Health Organization recommends no more than 50 mg/L nitrate and 3 mg/L nitrite in drinking water.[24] The increasing amount of nitrate species present and the strong evidence that it has a negative impact indicate we need technologies to remove or treat nitrate contaminated water.

1.2 Removing Nitrate from Contaminated Waste Sources

This section will provide an overview of target nitrate-laden waste streams and state of the art technologies for nitrate remediation. **Section 1.2.1** will present examples of nitrate streams and estimates of their compositions. **Section 1.2.2** will introduce technologies used to remove nitrate (separation) or chemically convert nitrate to other nitrogen species.

1.2.1 Candidate streams for nitrate remediation.

Common nitrate streams include fertilizer runoff, industrial wastewater, and low-level nuclear wastewater. Low-level nuclear waste consists of the highest concentrations of nitrate (>1 M).[25–29] Industrial nitrate streams typically are 1-50 mM nitrate.[30–32] Polluted groundwater will typically only have ~1 mM nitrate,[33–37] which is above the EPA limit (10 mg/L nitrate is about 0.16 mM nitrate). Real nitrate waste streams consist not only of nitrate but may also contain nitrite, chloride, calcium, magnesium, fluoride, sulfate, sulfide, and carbonate ions, as well as heavy metals.[29,31,32,38,39]

Industrial nitrate streams are most commonly treated by biological denitrification with the goal of converting nitrate to N_2.[18,40,41] Biological denitrification is advantageous for use in industrial streams with moderate to low nitrate concentration that can have trace amounts of other

contaminants.[18] Ion-exchange has been applied successfully to remove nitrate from drinking water but is difficult to implement for many industrial waste streams which can have high concentrations of co-contaminant anions and can require pre-processing.[18,42] We discuss the feasibility of treating different nitrate wastewater streams using electrocatalytic nitrate reduction (the method studied in this dissertation) in **Section 1.3.3**.

1.2.2 Proposed technologies for nitrate removal.

Physical nitrate removal

Nitrate separations methods include ion exchange, electrodialysis, and reverse osmosis.[39,43,44] In ion exchange, the nitrate is passed through a resin that takes up the nitrate, leaving a treated clean water stream. When the resin is recovered, the resulting waste stream will contain high concentrations of nitrate, as well as chlorides from the resin (NaCl is a popular anion exchange resin regeneration salt).[38,42] Electrodialysis treatment for nitrate water utilizes an electric field to separate ions. In the dialyzer, the nitrate wastewater is flowed between cation- and anion-selective membranes stacked between positively and negatively charged electrodes. The electric field drives the ions through the ion-selective membranes towards one of the electrodes, the charged species are effectively captured, and the outlet stream is cleaned water.[44] For removing nitrate using reverse osmosis, the nitrate stream is pressed at high pressure through a semipermeable membrane which only allows water to pass through resulting in a cleaned water stream.[45] Like ion exchange, electrodialysis and reverse osmosis will similarly produce clean water but also a concentrated nitrate stream. The nitrate concentrations in these streams following separation are typically 5 g/L (~0.08 M) nitrate.[38]

Biological nitrate reduction

Biological nitrate reduction consists of using bacteria with nitrate reductase enzymes to convert nitrate to other species, such as nitrogen.[46,47] To be successful in converting nitrate, these enzymes require specific electron donors for the reaction and the bacteria require inorganic carbon sources to survive.[44,47,48] Generally, biological nitrate reduction occurs within a batch reactor where the bacteria are fed a nitrate-rich stream with added electron donors and carbon sources. Biological denitrification has a disadvantage in that it creates biological sludge and potentially can create pathogenic bacteria,[41] and, therefore, it cannot be used for remediation for drinking water purposes.

Catalytic nitrate reduction

Catalytic nitrate reduction reduces nitrate to N_2 or NH_3 with a chemical reductant, such as hydrogen, over a catalyst surface.[41,49] Catalytic nitrate reduction is currently being investigated by thermo-, electro-, and photo-catalytic techniques. Using thermocatalytic nitrate reduction as an example, hydrogen is flowed over a palladium catalyst in a nitrate solution.[50] Catalytic nitrate reduction has disadvantages of requiring an external chemical, such as hydrogen, which would need to be stored for use, may require high temperatures to proceed, and there could be additional separations cost for non-gaseous reduction products (e.g., NH_4^+).

1.3 Electrocatalytic Nitrate Reduction

In this section we discuss an alternative method to remove nitrate that is the focus of this thesis. Electrocatalytic nitrate reduction reduces nitrate by supplying electrons through an electrode to reduce nitrate and protons or water to different species. Common electrocatalytic nitrate reduction reactions in acid are given in **Table 1.1**. In this thesis, we focus on the reduction of nitrate (NO_3^-) to ammonia (NH_3).

Table 1.1. Standard redox potentials for different electrocatalytic nitrate reduction reactions in acidic conditions.

Nitrate Reduction Reaction	Standard Redox Potential (V)
$NO_3^-{}_{(aq)} + 2\ H^+ + 2\ e^- \rightleftharpoons NO_2^-{}_{(aq)} + H_2O_{(l)}$	$E^0 = 0.85$ V
$NO_3^-{}_{(aq)} + 2\ H^+ + 2\ e^- \rightleftharpoons NO_2^-{}_{(aq)} + H_2O_{(l)}$	$E^0 = 0.89$ V
$NO_3^-{}_{(aq)} + 4\ H^+ + 3\ e^- \rightleftharpoons NO_{(g)} + 2\ H_2O_{(l)}$	$E^0 = 0.96$ V
$NO_3^-{}_{(aq)} + 7\ H^+ + 6\ e^- \rightleftharpoons NH_2OH_{(aq)} + 2\ H_2O_{(l)}$	$E^0 = 0.67$ V
$NO_3^-{}_{(aq)} + 9\ H^+ + 8\ e^- \rightleftharpoons NH_{3(aq)} + 3\ H_2O_{(l)}$	$E^0 = 0.82$ V
$2NO_3^-{}_{(aq)} + 10\ H^+ + 8\ e^- \rightleftharpoons N_2O_{(g)} + 5\ H_2O_{(l)}$	$E^0 = 1.12$ V
$2NO_3^-{}_{(aq)} + 12\ H^+ + 10\ e^- \rightleftharpoons N_{2(g)} + 6\ H_2O_{(l)}$	$E^0 = 1.25$ V

Electrocatalytic nitrate remediation is especially appealing as there is no waste stream produced, reduction is facilitated by already present protons in solution, and there is the potential to run solely off renewable resources, such as solar or wind generated electricity.[41,51] Unlike catalytic, there is no need for an external chemical such as hydrogen, which makes electrocatalytic nitrate reduction more amenable to distributed or point-source systems. Electrocatalytic processes also are desired due to the push for electrification of chemical industries and as the cost of renewable electricity decreases with the production of cheaper solar panels or wind turbines.[52]

Section 1.3.1 will review the mechanism of electrocatalytic nitrate reduction. **Section 1.3.2** will cover the electrocatalysts studied for nitrate reduction. **Section 1.3.3** will evaluate the current state of electrocatalytic nitrate reduction technology, identify science and engineering challenges, and discuss whether electrocatalytic nitrate reduction could be economically viable for treating different nitrate wastewater streams.

1.3.1 Mechanism

In this section we review the mechanism of electrocatalytic nitrate reduction on electrode surfaces. Common pathways are shown in **Figure 1.3**. The first step is nitrate adsorbing to the electrode surface. We define adsorbed nitrate as NO_3* where * represents a catalyst site. Then, adsorbed nitrate (NO_3*) is reduced to adsorbed nitrite (NO_2*). The adsorption and reduction of nitrate to nitrite are typically the rate-determining step of the reaction.[41] Nitrite is then reduced to

NO*, which can then be reduced to many different products. The reduction of NO* is typically referred to as the selectivity-determining step.

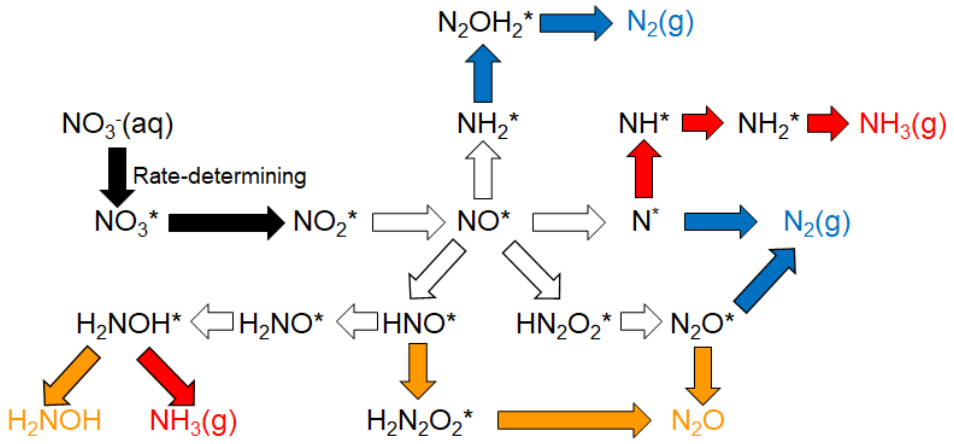

Figure 1.3. Electrocatalytic nitrate reduction reaction mechanism using reported mechanisms from ref. [53] and ref. [54]. Pathways to different products are labeled according to whether they form ammonia/ammonium (red), nitrogen (blue), or nitrogen oxides (orange). White colored arrows correspond to pathways that lead to different products, while black arrows are those steps commonly associated with the rate-determining step. Species adsorbed onto the catalyst surface are noted by *, representing a catalyst surface site. Only the nitrogen species are included. Figure adapted from ref. [55].

Nitrate to nitrite as the rate-determining step for electrocatalytic nitrate reduction

As discussed above, the first step in electrocatalytic nitrate reduction is nitrate adsorption (**Equation 1.1**), and thus nitrate's adsorption energy and mode are expected to play a significant role in the overall reaction pathway. Here we write nitrate adsorption as involving charge transfer as the electron is completely donated to the electrocatalyst surface. However, unlike protons or other anions such as chloride, there is not clear evidence about the valency of the adsorbed nitrate (i.e., whether it is NO_3* or NO_3^-*). In **Chapter 3.2.2**, we discuss indirect evidence of a charge transfer during NO_3^-, and so depict it in this way here. The thermodynamics of nitrate adsorption depend on the applied potential and the adsorption free energy of NO_3. Note that nitrate typically adsorbs onto two catalyst atoms, but we have written it adsorbing onto a single site here for simplicity. We note also that at very negative potentials, some proposed mechanisms involve the formation of nitrate radicals as an initial step.[56]

$$NO_{3\,(aq)}^{-} + * \rightleftharpoons NO_3^* + e^- \quad (1.1)$$

There are multiple possible elementary steps for adsorbed nitrate (NO_3*) to convert to NO_2* and water. The rate of the nitrate to nitrite step will depend on the rates of these individual elementary steps. We discuss several of the mechanisms in **Chapter 4**. Although the elementary steps may differ depending on reaction conditions and electrocatalyst, for Pt in acids, a proposed mechanism is shown in **Equations 1.2–1.6**. First, hydrogen is adsorbed onto the surface from reduction of protons along with nitrate. Then, hydrogen and nitrate react to form NO_2* and OH* in a surface reaction. The OH* is further hydrogenated to form water, while NO_2* is further reduced to form other products.

$$NO_3^* + * \rightleftharpoons NO_2^* + O^* \quad (1.2)$$

$$H_{(aq)}^+ + e^- + * \rightleftarrows H^* \quad (1.3)$$

$$O^* + H^* \rightarrow OH^* + * \quad (1.4)$$

$$OH^* + H^* \rightarrow H_2O_{(l)} + 2* \quad (1.5)$$

$$NO_2^* \rightarrow other\ species \quad (1.6)$$

The conversion of nitrate to nitrite is believed to be the rate-determining step (RDS) for electrocatalytic nitrate reduction on transition metals, but it is not always clear which specific elementary step of the nitrate to nitrite process is rate-determining.[57–60] The reaction order in nitrate is 0.51 and 0.34 for Pt and Rh from 0.001 to 0.1 M, respectively, indicating that the RDS occurs after nitrate adsorption and that nitrate adsorption (**Equation 1.1**) is quasi-equilibrated.[57] On Pt,[61] the reaction order is positive at low nitrate concentrations (< 0.1 M) but becomes negative at high concentrations (> 0.1 M). Because of the observation of a negative reaction order in nitrate, other species (e.g., H*, O*, OH*) must also compete for surface sites under those reaction conditions in addition to nitrate. If the hydrogenation (removal of the cleaved oxygen, **Equations 1.4** and **1.5**)

were sufficiently fast, the rate would be solely determined by the coverage of nitrate on the surface and the rate constant of deoxygenation. Thus, the coverage of nitrate is controlled by the adsorption energies of nitrate (**Equation 1.1**) and any other species that may adsorb and compete for sites on the catalyst surface (e.g., hydrogen, other anions). These considerations are discussed in **Chapter 4**.

Some electrocatalysts display a maximum in activity with potential rather than a monotonically increasing activity with more negative potential, most commonly seen for Pt (**Figure 1.4**).[41,53] This activity maximum can be explained by the competition between hydrogen and nitrogen species on the electrocatalyst surface.[62,63] Nitrate adsorption is more favorable at positive potentials while hydrogen adsorption is more favorable at negative potentials. Other possible elementary steps that would control the rate might be the hydrogenation of the adsorbed oxygen, but typically this step is assumed to be fast compared to nitrate deoxygenation such that it can be assumed to be at quasi-equilibrium. We probe the rate-determining steps in **Chapter 3**.

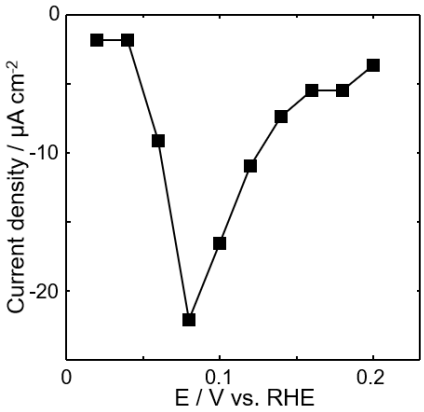

Figure 1.4. Steady-state nitrate reduction current densities on Pt in 0.5 M H_2SO_4 + 0.1 M $NaNO_3$. Figure adapted from ref. [57].

Reduction of adsorbed nitrite to products

Nitrate reduction to ammonia (E^0 = 0.82 V vs. RHE, **Table 1.1**) typically proceeds by sequential hydrogenation steps using 8 electrons. Following the formation of adsorbed nitrite,

further reduction leads to NO*. From the adsorbed NO, there are two major pathways to produce ammonia. One potential pathway is the conversion of NO* to hydroxylamine, then reduction of hydroxylamine to ammonia, as proposed by Kuwabata et al. (**Equations 1.7–1.10**).[64] The pathway to ammonia with hydroxylamine as an intermediate is supported by hydroxylamine detected as a byproduct of ammonia production on various Cu-based catalysts.[65,66]

$$NO^* + H^+_{(aq)} + e^- + * \rightleftarrows HNO^* \quad (1.7)$$

$$HNO^* + H^+_{(aq)} + e^- \rightarrow H_2NO^* \quad (1.8)$$

$$H_2NO^* + H^+_{(aq)} + e^- \rightarrow H_2NOH^* \quad (1.9)$$

$$H_2NOH^* + 2\,H^+_{(aq)} + 2\,e^- \rightarrow NH_{3\,(g)} + H_2O_{(l)} + * \quad (1.10)$$

Another ammonia pathway is NO* reacting with adsorbed hydrogen atoms in a strong reducing environment to produce NH_3 (**Equations 1.11–1.14**).

$$NO^* + 2\,H^* \rightarrow N^* + H_2O_{(l)} + 2* \quad (1.11)$$

$$N^* + H^* \rightarrow NH^* + * \quad (1.12)$$

$$NH^* + H^* \rightarrow NH_2^* + * \quad (1.13)$$

$$NH_2^* + H^* \rightarrow NH_{3\,(g)} + 2* \quad (1.14)$$

Electrocatalytic reduction of nitrate to N_2 (E^0 = 1.25 V vs. RHE) is comparable to biological denitrification, and thus is desired for 'closing' the nitrogen cycle.[41] Nitrogen production from nitrate is the most thermodynamically stable product of nitrate reduction and requires 5 electrons, but kinetic limitations control the selectivity.

There are three predominate mechanisms proposed for N_2 production from nitrate. NO*, formed from reduction of nitrite, can further be reduced to adsorbed atomic nitrogen (N*), as shown in **Equation 1.11**. Then, the adsorbed nitrogen can react with a second nitrogen atom to form N_2 (**Equation 1.15**).[67] However, this mechanism has not been experimentally confirmed.

$$NO^* + 2\,H^* \rightarrow N^* + H_2O_{(l)} + 2* \quad (1.11)$$

$$N^* + N^* \rightarrow N_{2\,(g)} + 2* \quad (1.15)$$

The Vooys-Koper and Duca-Feliu-Koper mechanisms are the two major proposed pathways experimentally confirmed for N_2 production. Using DEMS, Vooys et al. observed NO* reacting with aqueous NO to form HN_2O_2* in acidic solution (**Equation 1.16**) before further reducing into adsorbed N_2O* (**Equation 1.17**).[68] Chumanov and co-workers further confirmed that N_2O can be reduced to N_2O^- and N_2 via **Equations 1.18** and **1.19**.[69] Because N_2O readily desorbs during this reaction mechanism (**Equation 1.25**), it is important to identify N_2O via DEMS when targeting N_2 production from electrocatalytic nitrate reduction.[70]

$$NO^* + NO_{(aq)} + H^+_{(aq)} + e^- \rightarrow HN_2O_2^* \quad (1.16)$$

$$HN_2O_2^* + H^+_{(aq)} + e^- \rightarrow N_2O^* + H_2O_{(l)} \quad (1.17)$$

$$N_2O_{(g)} + e^- \rightarrow N_2O^-_{(aq)} \quad (1.18)$$

$$N_2O^-_{(aq)} + 2\,H^+_{(aq)} + e^- \rightarrow N_{2\,(g)} \quad (1.19)$$

In basic solution, the reaction most likely proceeds via the Duca-Feliu-Koper mechanism where NO* is protonated to from NH_2*. The NH_2* will react with NO* to form N_2OH_2* via a Langmuir-Hinshelwood reaction (**Equation 1.21**) before decomposing to N_2 and H_2O.[67]

$$NO^* + 3\,H_2O_{(l)} + 4\,e^- \rightleftarrows NH_2^* + 4\,OH^-_{(aq)} \quad (1.20)$$

$$NO^* + NH_2 \rightarrow N_2OH_2^* + * \quad (1.21)$$

$$N_2OH_2^* \rightarrow N_{2\,(g)} + H_2O_{(l)} \quad (1.22)$$

Aside from NH_3 and N_2, there are a variety of nitrogen oxides species produced from electrocatalytic nitrate reduction, which include N_2O (E^0 = 1.12 V vs. RHE) and hydroxylamine (E^0 = 0.67 V vs. RHE). NO and NO_2 can also be detected, but typically as intermediates using DEMS, rather than products that build up in solution.[71] There are two major mechanisms supported

in literature for producing N_2O from NO. This first is through the formation of nitroxyl (HNO) from NO* in acidic solution following the reaction mechanism in **Equation 1.7**. Katsounaros and Kyracou observed that adsorbed HNO* groups could dimerize into hyponitrous acid ($H_2N_2O_2$) via **Equation 1.23**.[67] Because this $H_2N_2O_2$ is unstable, it will decompose to N_2O (**Equation 1.24**).

$$NO^* + H^+_{(aq)} + e^- \rightleftarrows HNO^* \quad (1.7)$$

$$HNO^* + HNO^* \rightarrow H_2N_2O_{2\,(aq)} + 2\ * \quad (1.23)$$

$$H_2N_2O_{2\,(aq)} \rightarrow N_2O_{(g)} + H_2O_{(l)} \quad (1.24)$$

The second is the Vooys-Koper mechanism, shown in **Equations 1.16** and **1.17**, followed by N_2O* desorption (**Equation 1.25**).

$$NO^* + NO_{(aq)} + H^+_{(aq)} + e^- \rightarrow HN_2O^*_2 + * \quad (1.16)$$

$$HN_2O^*_2 + H^+_{(aq)} + e^- \rightarrow N_2O^* + H_2O_{(l)} \quad (1.17)$$

$$N_2O^* \rightarrow N_2O_{(g)} + * \quad (1.25)$$

1.3.2 Electrocatalysts.

The electrocatalyst material has a significant effect on electrocatalytic nitrate reduction rates and selectivities. This section summarizes classes of electrocatalyst materials recently studied, breaking them into groups of (1) single metals, (2) alloys, and (3) oxides, sulfides, oxysulfides, phosphides, and N-doped materials. Although the general nitrate reduction mechanism is believed to be the same for these different classes,[41] the way that these different classes control the reaction and their active sites may differ.

Single metal electrocatalysts

Although the platinum group metals and copper are the most studied single metal electrocatalysts, the range of other metals that have been studied has given a sense of how different electrocatalyst properties affect activity and selectivity. Cu is a commonly studied metal because it is highly active for nitrate reduction.[72,73] The order of platinum group metal activities (Rh > Ru > Ir > Pd ≈ Pt)[57] is hypothesized to be due to the differences in nitrate adsorption energies. We discuss the cause of this ordering in **Chapter 3**.

Typically, metals have a single type of active site that participates in the reaction. As nitrate reduction is a site dependent reaction, which site nitrate adsorbs onto (e.g., the metal facet) controls activity and selectivity.[74] For example, the product distribution is different on Cu(111) and Cu(100) sites where the formation of hydroxylamine is more prevalent on Cu(100) than Cu(111) in basic media.[75] Step sites are typically more active for single metals.[41]

To close the nitrogen cycle, metals that can produce N_2 from electrocatalytic nitrate reduction are of considerable environmental interest and are highlighted in **Figure 1.5**. Sn is highly active for nitrate reduction and displays 92% selectivity towards N_2 production in neutral electrolyte.[76] Bi is less activity than Sn but still reaches between 58% and 65% selectivity for N_2 under basic conditions.[77] Despite low nitrate reduction rates, Fe is a cheap metal that is highly selective towards N_2[54] because of its strong nitrate adsorption energy.[53] Fe in carbon microspheres were shown to have high N_2 selectivity and maintain high surface areas.[78] Al, In, Zn, and Pb also produce N_2 selectively with minor co-production of ammonia (<20% selectivity) and N_2O (>20% only for In and Zn).[79] In basic environments Pt has been reported to produce N_2 if sufficient nitrite ions are present.[80]

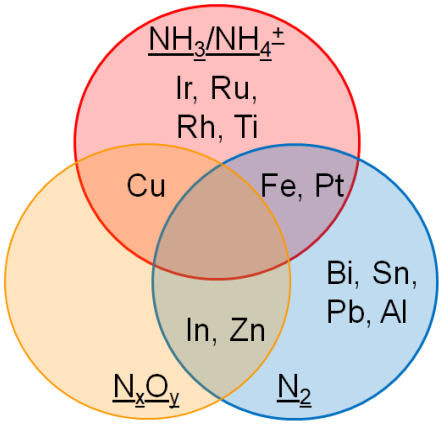

Figure 1.5. Distribution of dominant products (> 20% selectivity) formed for different pure metals in steady-state or cycling potential experiments. Red, blue, and orange circles represent selectivity towards NH_3/NH_4^+, N_2, and N_xO_y, respectively. Overlap regions indicate different product formations under various reaction conditions (e.g., acid vs. base) or a mixture of reaction products. Figure adapted from ref. [55].

Ammonia is produced on the platinum group metals at voltages positive of 0 V vs. RHE[57,81,82] and certain base metals at higher overpotentials (**Figure 1.5**). Even though the platinum group metals form ammonia at positive potentials, they typically are too active for hydrogen evolution to form nitrate reduction reaction products at high faradaic efficiency below 0 V vs. RHE. Ti produces ammonia with 82% faradaic efficiency in acidic pH at −1 V vs. RHE.[83] Cu, depending on reaction conditions, forms ammonia or nitrogen oxides such as hydroxylamine.[75] Fe operated at constant current density also forms ammonia and small concentrations of nitrite in neutral $NaNO_3/Na_2SO_4$ solutions.[84] There are no metals that solely make nitrogen oxides, as they tend to be side reactions or intermediates for ammonia and N_2 production.

Alloy electrocatalysts

A major advantage of alloys is the ability to enhance the activity and selectivity of pure metals. Additionally, alloys can be used to replace an expensive metal with cheaper transition metals, which can reduce the cost of the working electrode for industrial nitrate reduction. This section aims to summarize recent results on alloys for nitrate reduction and focus on the role that alloys play in improving the reaction rate and selectivity.

There are two major ways in which alloys function to improve the activity of nitrate reduction. One effect is tuning the adsorption energy of nitrate and other intermediate species on the surface. Examples of this include CuNi alloys[85–87], PtRh,[88] PtIr, [88] PtRu,[89] Cu/Ni/Zn alloys,[90] CuZn,[91] Cu-Pd,[92] Cu-Bi alloys,[93] and Au/Ag alloys,[94] where optimal alloy compositions were used to increase the nitrate reduction rate. Additionally, alloys could have a bifunctional effect, where two adjacent sites contribute to different steps of the mechanism. For example, synergistic effects between Pd and Cu create active sites for nitrate to reduce to nitrite and further conversion to nitrogen.[95]

Alloys can also be used to increase the selectivity towards a desired product or shift the selectivity towards other compounds. Bi[77] and Sn[76] have previous been studied to be selective towards N_2. By alloying these two metals, $Bi_{60}Sn_{40}$ improved the activity and displayed over 50% selectivity towards nitrogen.[96] Even though Pt tends to produce NH_3,[61] the addition of Sn shifts the selectivity of the alloy from NH_3 to hydroxylamine.[97]

Metal sulfide, oxides, and other electrocatalysts

Recently, oxides, sulfides, oxysulfides, and phosphides have been studied for nitrate reduction. The studies on sulfides and oxysulfides are motivated by nitrate reductase enzymes which include both metal (typically Fe and Mo) and sulfur/oxysulfur groups.[98] Oxides are cost-effective, and more chemically stable compared to metals. Lastly, there are a few reports for electrocatalytic nitrate reduction on both nitrogen or phosphorus doped materials and phosphides which are appealing as another possible way to enhance the activity of lower cost metals. The electrocatalytic nitrate reduction mechanism on these surfaces is less understood than on metals or alloys for two main reasons: (1) the role that O, S, N, and P (or their vacancies) play in the

mechanism is unclear, and (2) the complex structures and change in structure under reaction conditions make it more challenging to identify the active site of these materials.

Nitrate reductase enzymes are active and selective towards nitrite, ammonia, or N_2 at room temperature, and neutral pH,[99–101] unlike nitrate reduction on pure transition metals. Nitrate reductase enzymes utilize a central Mo coordinated by oxo and dithiolene sulfur ligands.[98] An early enzyme-inspired electrocatalytic NO_3RR study of $(n\text{-}Bu_4N)_3[Mo_2Fe_6S_8(SPh)_9]$ showed the production of NO_2^-, NH_3, and H_2 at −0.419 V vs. RHE at pH 10.[64] The activity was attributed to the ability of the reduced Mo-Fe complex to substitute terminal PhS^- ligands with nitrate.[64] Also, MoS_2 was found to have limited NO_3RR activity under neutral conditions and 0.1 M NO_3^-.[102,103]

Recently, oxo-MoS_x materials that more closely mimic the structures of nitrate reductase enzymes like those shown in **Figure 1.6a** and **1.6b** were successfully fabricated and found to be active for nitrate reduction in neutral conditions.[102] Oxo-MoS_x (**Figure 1.6c**) showed high selectivity towards NH_4^+ at 0 V vs. RHE in neutral electrolyte and 0.1 M NO_3^-.[102] Using operando electron paramagnetic resonance (EPR) spectroscopy, the signal associated with Mo^V=O on oxo-MoS_x was identified and diminished upon addition of nitrate (**Figure 1.6d**). When the oxo-MoS_x interacted with nitrate, the Mo^V=O was assumed to form an EPR silent Mo^{VI} species, which caused the Mo^V=O signal to decrease. The Mo^V−S EPR signal remained unchanged with addition of nitrate, indicating that it was not associated with nitrate reduction. Additionally, Raman spectroscopy showed similar phenomena for the Mo^V=O species with and without nitrate present (**Figure 1.6e**). The active site for nitrate reduction was then deduced to be the Mo^V=O center of the oxo-MoS_x electrocatalyst, which explains the activity of oxo-MoS_x despite MoS_2 not being active. Fe_3S_4 was also tested for nitrate reduction activity at pH 7 (the same conditions as the MoS_2

and oxo-MoS_x) but performed poorly.[103] Low nitrate reduction activity could be due to instability of the Fe_3S_4 catalyst at operating conditions where Fe^{2+} and iron oxides could form.

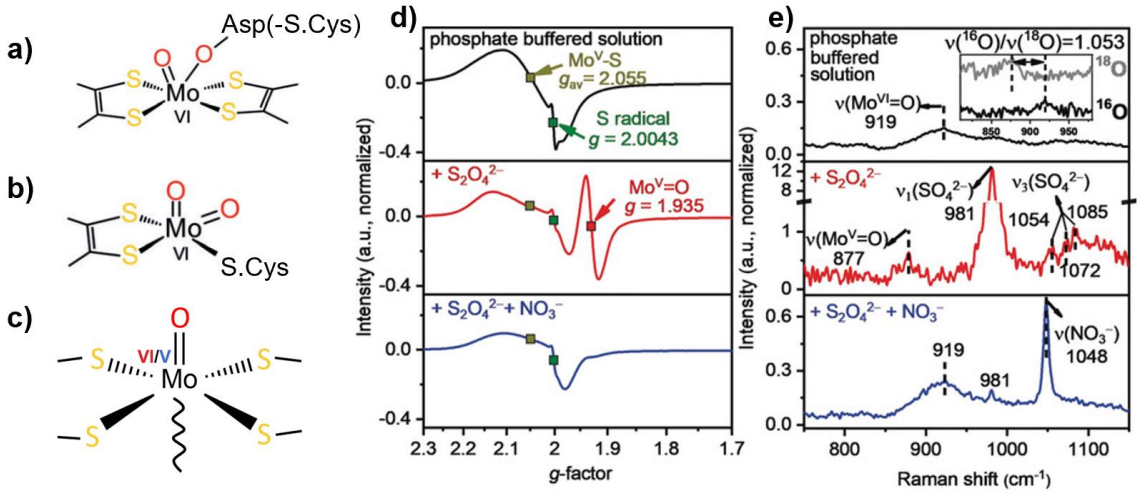

Figure 1.6. Active site structure of nitrate reductase enzymes a) *Desulfovibrio desulfuricans* and b) *Arabidopsis thaliana* which are used as analogs for the structure of the oxo-MoS_x. Adapted with permission from ref. [102]. c) The structure of oxo-MoS_x labeled with the $Mo^{VI/V}$ oxidation states adapted from ref. [104]. d) EPR and e) Raman spectroscopy of oxo-MoS_x in phosphate buffered solution, with 20 mM $S_2O_4^{2-}$ to simulate potential, and with 242 mM NO_3^- added to solution. Adapted from ref. [102].

Several metal oxides have been reported for nitrate reduction, but an important consideration for these catalysts is understanding the material structure under reaction conditions. For example, a Cu/Cu_2O catalyst for electrocatalytic nitrate reduction started as CuO at the beginning of the reaction.[105] While cycling between 0.05 to −0.85 V vs. RHE, *in situ* Raman spectroscopy showed characteristic CuO peaks gradually disappearing and Cu and Cu_2O peaks appeared instead. This further indicates that Cu and Cu_2O were the active surfaces for nitrate reduction. The formation of these new structures were also confirmed by X-ray photoelectron spectroscopy, Auger electron spectroscopy, and X-ray diffraction.[105] The Cu/Cu_2O catalyst had high selectivity towards NH_4^+ and follows a mechanism similar to Cu.

Another challenge for oxides is quantifying the contribution of vacancies compared to metals for the reaction. TiO_2 and TiO_{2-x} have been tested for nitrate reduction, and calculations attributed the enhancement in activity from oxygen vacancies to oxygen from nitrate filling the

vacancy and weakening the nitrate N-O bond.[106] However, it is unclear if the enhancement with oxygen vacancies is due to an increased surface area or an inherently more active catalyst as the current densities were normalized to geometric surface area, not electrochemically active surface area.[106] In another example, XPS measurements show the number of oxygen vacancies in a Co_3O_4/Ti nanosheet catalyst as a function of temperature. However, the effects of oxygen vacancies and temperature on the kinetics were not deconvoluted.[107]

Other oxides that have been studied for nitrate reduction include Co_3O_4-TiO_2/Ti[108], rod and sheet-like Co_3O_4/Ti, and Ni-Fe^0@Fe_3O_4.[109] Co_3O_4-TiO_2/Ti was tested in comparison to Co_3O_4/Ti and TiO_2/Ti.[108] XPS after the reaction indicated that the catalyst had changed from mostly Co^{2+} to a mixture of Co^{2+} and Co^{3+} and that leaching of cobalt was detected.[108] nitrate reduction activity on Co_3O_4-TiO_2/Ti was proposed to follow a direct mechanism where Co^{2+} donates an electron to NO_3^- or its reduction intermediates and Co^{3+} is formed. Co^{3+} then receives an electron from the electrode surface to form Co^{2+}, explaining the appearance of Co^{3+} after nitrate reduction. Co_3O_4 rod and sheet cathodes with enhanced Co^{2+}/Co^{3+} ratio and surface oxygen vacancies were compared to a nanoparticle Co_3O_4 catalyst.[110] The rod-like Co_3O_4/Ti had the highest internal resistance but also had the highest nitrate reduction at constant current of 50 mA.[110] The increased resistance results from loose arrangement structures from synthesis and the higher nitrate reduction rate was attributed to exposed (220) facets and higher Co^{2+} content/oxygen vacancies.[110] Ni-Fe^0@Fe_3O_4 are active at neutral pH for the production of N_2.[109] The enhanced N_2 selectivity can be attributed to Fe^{2+} at the surface which could create additional active sites by converting between Fe^0 and Fe_3O_4.[109]

Other materials have also been studied included phosphides[31,111] and N-doped materials.[112–114] P doping of a Co_3O_4 electrocatalyst enhanced NO_3RR performance, with $P_{2.1}$-

Co_3O_4 reporting the highest current efficiency and producing mostly ammonium at pH 7.[31] A Ni_2P/Ni foam formed ammonium at higher conversions and the nitrate reduction activity was reported to be higher with a greater number of exposed surface defects, indicating that the defect sites may be important for catalyzing the reaction.[111] N-doped carbon encapsulated Fe materials have also been reported for nitrate reduction, and for these materials N-doping of carbon was computationally shown to lower the work function of the carbon near Fe clusters and therefore make nitrate adsorption more favorable on the carbon surface, which enhanced nitrate reduction activity.[112–114] Though N-doped materials show moderate to high selectivity towards N_2, ^{15}N isotope labeling is necessary to definitively measure N_2 and clarify if the N_2 was sourced from NO_3^- reduction and not from the N-doped material.

1.3.3 Feasibility of electrocatalytic nitrate reduction.

State-of-the-art and challenges

Currently, electrocatalytic nitrate reduction is not used for nitrate remediation. Catalyst performance (nitrate reduction rate) is a limiting aspect of the technology. For the catalysts, the catalyst must (1) have high current densities with respect to the applied cell potential, (2) high current efficiencies to the desired products, (3) high stability in the electrolyte, and (4) low-cost. The best-performing electrocatalysts can achieve between -0.1 and -2.6 A/cm^2 (typically reported using geometric area) at potentials less than -0.6 V vs. Ag/AgCl with modest to high faradaic efficiency (FE) to ammonia (see **Figure 1.7**).[115] With the exception of Co nanoarrays (Co-NAs) at -1.3 V vs. Ag/AgCl,[116] the highest performing catalysts are still not active enough for consideration for nitrate reduction at an industrial level (~ -1 A/cm^2). The electrocatalysts that achieve high rates are typically operated at high overpotentials, and so it is unclear if the increased rate is worth the

higher expenditure of energy. For reference, 100 mV of overpotential at an electricity cost of \$0.07/kWh would increase the price of nitrate to N_2 by 1 cent per kilogram.[117]

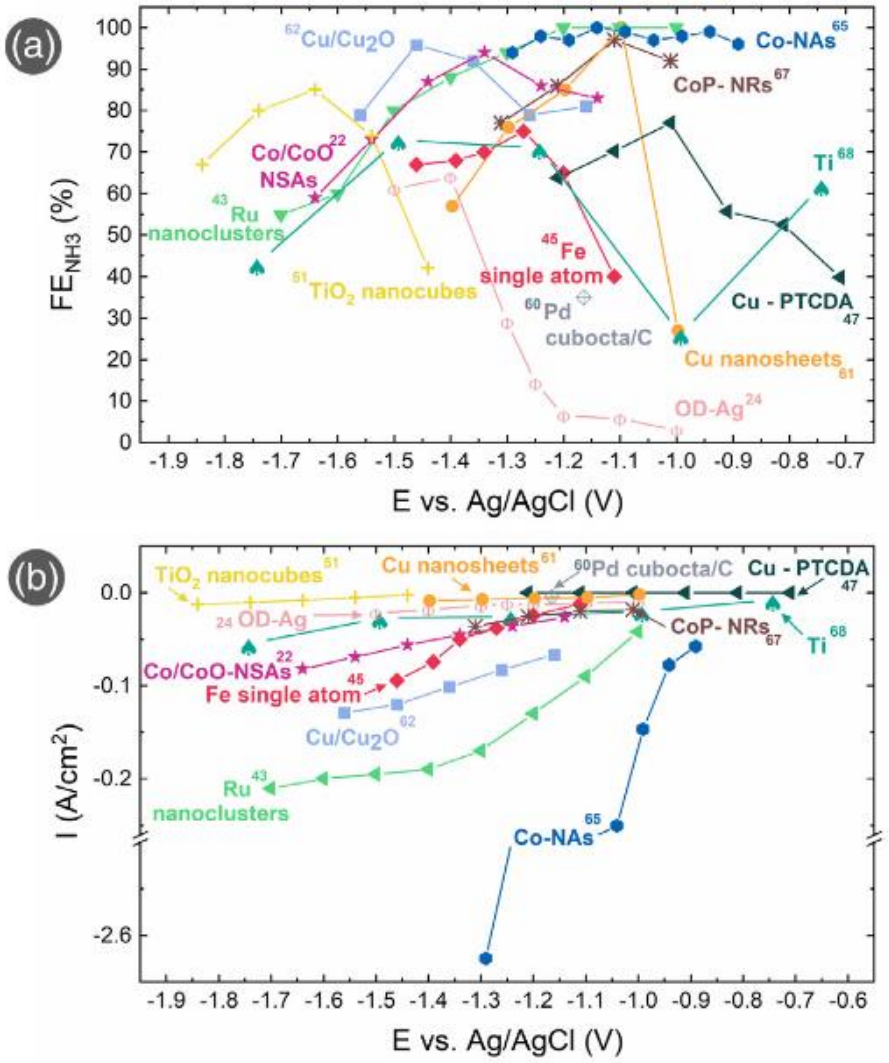

Figure 1.7. a) Faradaic efficiencies and b) current densities of catalysts reported for electrocatalytic nitrate reduction in the literature. Adapted from ref. [115]. See ref. [115] for catalyst name abbreviations.

Other factors that prevent electrocatalytic nitrate reduction from being deployed include (1) low concentrations of nitrate requiring upstream steps and (2) nitrate streams requiring removal of other ions prior to electrocatalytic reduction. For electrocatalytic nitrate reduction, the reaction is more efficient at high nitrate concentrations, so polluted groundwater (1 mM nitrate)[33–37] would need to be concentrated before using electrocatalysis to reduce nitrate. This concentration step

would add additional energy and capital costs. Other ions present in many nitrate waste streams (e.g., Cl^-, SO_4^{2-}) can lower the nitrate reduction activity, and so may need to be separated prior to reaction. These separation steps would also add energy and capital costs.

Conditions where electrocatalytic nitrate reduction may be commercially viable

Polluted groundwater is challenging to treat because of its very low concentration of nitrate[117] which would result in low nitrate reduction rates. Additionally, without concentrating the groundwater stream, to achieve practical current densities, the volumetric flow rate of low concentration nitrate streams would be unrealistically large.[49] Industrial wastewater streams are likely to be most amenable to treatment, as well as secondary nitrate streams from reverse osmosis or ion exchange. These streams would have predictable concentrations of nitrate and other ions present. For electrocatalytic nitrate reduction the higher concentrations of nitrate present in these streams (1-50 mM)[30–32] would be favorable for higher reduction rates.

Certain nitrate streams could be directly fed into an electrocatalytic nitrate reduction reactor, while others would require pre-processing. Groundwater streams may need to be pre-filtered to remove biological components, metals or metal ions, and other species that may severely decrease nitrate reduction rates. Certain streams like nitrate effluents following ion exchange could be directly treated if catalysts that are resistant to chloride poisoning are found. Post-processing of the nitrate streams may also be required to separate products like NH_3/NH_4^+. Alternatively, chloride can be recruited for an indirect reaction of ammonium to N_2 to modify the products after reaction.[119] The two major nitrate reduction products are N_2 and NH_3/NH_4^+, depending on whether a valuable product is desired or if rebalancing the nitrogen cycle and producing clean water is desired. N_2 is easier to separate from water streams and is benign. NH_3/NH_4^+ must be removed from water before it is suitable for drinking but is a valuable chemical if it can be collected.

Considerations beyond the catalyst

In addition to catalyst challenges, almost every part of the nitrate conversion process remains to be optimized. The best nitrate streams would need to be identified, purified, and the nitrate concentrated. The best operating parameters (such as method of catalyst loading onto the conductive support and ion-exchange membrane) for the electrochemical reactor would need to be explored. The post-processing and treatment of the product stream would also potentially require additional separations. In this dissertation we mainly focus on the electrocatalytic reaction, the effect of chloride poisoning, and translating to an electrochemical reactor.

1.4 Research Goals

The purpose of this thesis is to understand why certain catalysts are active for electrocatalytic nitrate reduction and then to identify whether these active catalysts retain their activity in practical conditions or environments for nitrate reduction. We identify that active catalysts have greater affinity for nitrate adsorption based on experimental measurements on a rotating disk electrode in ideal conditions (**Chapter 3**). We show that the active catalysts are poisoned by chlorides that are present in real waste streams (**Chapter 4**). Unexpectedly, metals such as Rh that have a high affinity for nitrate adsorption are poisoned by chloride more than metals that have a weaker affinity for nitrate adsorption, such as Pt. We show that this is because catalysts that adsorb nitrate more strongly also will adsorb chloride more strongly. We show that in a flow configuration, the active metals perform more poorly than in batch conditions on a rotating disk electrode, but the trend of more active catalysts having a greater affinity for nitrate adsorption remains (**Chapter 5**). Future work may consist of developing poison resistant catalysts through computational screening and additional methods to control adsorption of nitrate while minimizing chloride adsorption (**Chapter 6**). Future work on the flow configuration may consist

of improved mass transport and modifications of catalyst loading to achieve the performance seen in batch conditions.

Chapter 1: Introduction

This Chapter explores reasons for increasing nitrate levels and the need for nitrate removal. The Chapter reviews existing nitrate removal processes and their advantages and disadvantages. The Chapter discusses the electrocatalytic nitrate reduction mechanism, electrocatalysts, and feasibility of this technology for treating nitrate wastewater. This Chapter also outlines the goals of the thesis.

Chapter 2: Methods

This Chapter covers all experimental techniques used in this thesis. This includes methods to evaluate electrocatalytic performance, including electrochemical surface area measurements and product quantification, catalyst structural characterization, and flow cell reactor setup and operation. This Chapter is aimed at researchers interested in running experimental studies on electrocatalytic nitrate reduction or similar reactions.

Chapter 3: Activity and Selectivity Trends in Electrocatalytic Nitrate Reduction on Transition Metals

This Chapter helps to identify what properties of transition metals are responsible for high nitrate reduction activity. Density functional theory calculations coupled with a microkinetic model identify that the adsorption strengths of O and N atoms act as descriptors for overall activity. This is because those adsorption energies control the strength of nitrate adsorption. We experimentally show that Rh adsorbs nitrate more strongly than Pt, validating the calculations. We show through X-ray absorption spectroscopy that at potentials for nitrate reduction there is

competition on the surface between nitrate and hydrogen that controls the rate of reaction. The predictions here suggest alloy electrocatalysts that may be active for nitrate reduction.

Chapter 4: Electrocatalytic Nitrate Reduction on Rhodium Sulfide Compared to Pt and Rh in the Presence of Chloride

This Chapter helps explain why chloride can lower nitrate reduction on metal and metal sulfide catalysts. This Chapter studies the activity of Rh_xS_y for nitrate reduction and compared its activity to Pt and Rh in the presence of chloride. Rh_xS_y is 1.5 to 5.6 times more active than Rh and 10 to 24 times more active than Pt, depending on the potential. The activity is decreased in the presence of chloride for all catalysts in the order of Rh > Pt > Rh_xS_y. The decrease in nitrate reduction activity with chloride is due to competitive adsorption of chloride and nitrate on the surface. Density functional theory modeling predicts that chloride poisoning will consistently inhibit nitrate reduction activity on metals due to adsorbate scaling relations between nitrate and chloride. Density functional theory calculations and microkinetic modeling identify sulfur vacancy sites as the active site for Rh_xS_y and explain the high activity but moderate chloride poison resistance of Rh_xS_y for nitrate reduction.

Chapter 5: Comparison of Nitrate Reduction Activities of Rh/C, Pt/C, and PtRu/C as Measured in Batch and Flow Reactor Configurations

This Chapter explores measured activity for nitrate reduction between a batch reactor and a flow cell for the same catalysts (Pt/C, PtRu/C, and Rh/C). The Chapter shows that current densities measured in the batch cell do not quantitatively translate to the flow cell reactor. We hypothesize the current densities do not translate because the flow cell is unable to achieve the high mass transport conditions achievable in the rotating disk electrode in the batch cell. However, the catalyst activity trends are the same in both systems (Pt/C < PtRu/C < Rh/C). The catalyst

activity trends are related to their respective nitrate adsorption energies. In a flow cell, Rh/C has the greatest activity at 0.05 V vs. RHE with a flow rate of 2 mL/min with a nitrate reduction current density to ammonia of −0.32 mA/cm^2 normalized to the Rh surface area and −105 mA/cm^2 normalized to the geometric surface area (electrolyzer area).

Chapter 6: Conclusions and Outlooks

This Chapter summarizes the main findings of this dissertation and discusses caveats and uncertainties in the findings that further studies could address. This Chapter discusses the use of pulsed potential electrocatalysis and the possibility to use this to avoid linear adsorbate scaling limitations. This Chapter also discusses challenges of flow cell operation and discusses the need for long term operation of the flow cell (>24 hours) and testing of real waste streams. This Chapter also discusses the feasibility of electrocatalytic nitrate remediation beyond catalyst challenges.

1.5 References

1. Canfield, D. E., Glazer, A. N. & Falkowski, P. G. The Evolution and Future of Earth's Nitrogen Cycle. *Science (1979)* **330**, 192–196 (2010).
2. Rosca, V., Duca, M., de Groot, M. T. & Koper, M. T. M. Nitrogen Cycle Electrocatalysis. *Chem Rev* **109**, 2209–2244 (2009).
3. Kant, S., Bi, Y. M. & Rothstein, S. J. Understanding plant response to nitrogen limitation for the improvement of crop nitrogen use efficiency. *Journal of Experimental Botany* vol. 62 1499–1509 Preprint at https://doi.org/10.1093/jxb/erq297 (2011).
4. Lehnert, N., Dong, H. T., Harland, J. B., Hunt, A. P. & White, C. J. Reversing nitrogen fixation. *Nat Rev Chem* **2**, 278–289 (2018).
5. Bernhard, A. The nitrogen cycle: Processes, players, and human impact. *Nature Education Knowledge* **3**, (2010).
6. Fowler, D. *et al.* The global nitrogen cycle in the twenty-first century. *Philosophical Transactions of the Royal Society B: Biological Sciences* **368**, 20130164–20130164 (2013).
7. Galloway, J. N. & Cowling, E. B. Reactive Nitrogen and The World: 200 Years of Change. *AMBIO: A Journal of the Human Environment* **31**, 64–71 (2002).
8. Fields, S. Global Nitrogen: Cycling out of control. *Environ Health Perspect* **112**, 556–563 (2004).
9. Galloway, J. N. *et al.* The Nitrogen Cascade. *Bioscience* **53**, 341–356 (2003).
10. Ward, M. H. *et al.* Drinking Water Nitrate and Human Health: An Updated Review. *Int J Environ Res Public Health* **15**, 1557 (2018).

11. Zhang, W. L., Tian, Z. X., Zhang, N. & Li, X. Q. Nitrate pollution of groundwater in northern China. *Agric Ecosyst Environ* **59**, 223–231 (1996).
12. Fields, S. Global Nitrogen: Cycling out of control. *Environ Health Perspect* **112**, 556–563 (2004).
13. Battye, W., Aneja, V. P. & Schlesinger, W. H. Is nitrogen the next carbon? *Earths Future* **5**, 894–904 (2017).
14. Roser, M., Ritchie, H. & Ortiz-Ospina, E. World Population Growth. *OurWorldInData.org* (2013).
15. Geological Survey, U. *MINERAL COMMODITY SUMMARIES 2022*.
16. Population growth (annual %). *data.worldbank.org* (2022).
17. Adesemoye, A. O. & Kloepper, J. W. Plant-microbes interactions in enhanced fertilizer-use efficiency. *Applied Microbiology and Biotechnology* vol. 85 1–12 Preprint at https://doi.org/10.1007/s00253-009-2196-0 (2009).
18. Moloantoa, K. M., Khetsha, Z. P., van Heerden, E., Castillo, J. C. & Cason, E. D. Nitrate Water Contamination from Industrial Activities and Complete Denitrification as a Remediation Option. *Water (Switzerland)* vol. 14 Preprint at https://doi.org/10.3390/w14050799 (2022).
19. Lehnert, N., Dong, H. T., Harland, J. B., Hunt, A. P. & White, C. J. Reversing nitrogen fixation. *Nat Rev Chem* **2**, 278–289 (2018).
20. National Academy of Engineering. National Academy of Engineering Grand Challenges For Engineers. 19–22 (2017).
21. Gruber, N. & Galloway, J. N. An Earth-system perspective of the global nitrogen cycle. *Nature* **451**, 293–296 (2008).
22. Galloway, J. N. *et al.* The Nitrogen Cascade. *Bioscience* **53**, 341–356 (2003).
23. *Code of Federal Regulations (40 CFR 141)*. https://www.epa.gov/ground-water-and-drinking-water/national-primary-drinking-water-regulations (2022).
24. World Health Organization. *Nitrate and Nitrite in Drinking-water*. (2016).
25. Hobbs, D. T. *Summary technical report on the electrochemical treatment of alkaline nuclear wastes*. http://www.osti.gov/servlets/purl/10186407-XeDqa4/webviewable/ (1994) doi:10.2172/10186407.
26. Bockris, J. O. M. & Kim, J. Electrochemical treatment of low-level nuclear wastes. *J Appl Electrochem* **27**, 623–634 (1997).
27. Genders, J. D., Hartsough, D. & Hobbs, D. T. Electrochemical reduction of nitrates and nitrites in alkaline nuclear waste solutions. *J Appl Electrochem* **26**, 1–9 (1996).
28. Ondrejcin, R. S., Rideout, S. P. & Donovan, J. A. *Control of stress corrosion cracking in storage tanks containing radioactive waste*. (1978).
29. Katsounaros, I., Dortsiou, M. & Kyriacou, G. Electrochemical reduction of nitrate and nitrite in simulated liquid nuclear wastes. *J Hazard Mater* **171**, 323–327 (2009).
30. Chauhan, R. & Srivastava, V. C. Electrochemical denitrification of highly contaminated actual nitrate wastewater by Ti/RuO2 anode and iron cathode. *Chemical Engineering Journal* **386**, 122065 (2020).
31. Gao, J., Jiang, B., Ni, C., Qi, Y. & Bi, X. Enhanced reduction of nitrate by noble metal-free electrocatalysis on P doped three-dimensional Co3O4 cathode: Mechanism exploration from both experimental and DFT studies. *Chemical Engineering Journal* **382**, 123034 (2020).

32. Fernández-Nava, Y., Marañón, E., Soons, J. & Castrillón, L. Denitrification of wastewater containing high nitrate and calcium concentrations. *Bioresour Technol* **99**, 7976–7981 (2008).
33. Wick, K., Heumesser, C. & Schmid, E. Groundwater nitrate contamination: Factors and indicators. *J Environ Manage* **111**, 178–186 (2012).
34. Spalding, R. F. & Exner, M. E. Occurrence of Nitrate in Groundwater—A Review. *Journal of Environment Quality* **22**, 392 (1993).
35. Lacasa, E., Cañizares, P., Sáez, C., Fernández, F. J. & Rodrigo, M. A. Removal of nitrates from groundwater by electrocoagulation. *Chemical Engineering Journal* **171**, 1012–1017 (2011).
36. Sánchez Pérez, J. M., Antiguedad, I., Arrate, I., García-Linares, C. & Morell, I. The influence of nitrate leaching through unsaturated soil on groundwater pollution in an agricultural area of the Basque country: A case study. *Science of the Total Environment* **317**, 173–187 (2003).
37. Subramani, T., Elango, L. & Damodarasamy, S. R. Groundwater quality and its suitability for drinking and agricultural use in Chithar River Basin, Tamil Nadu, India. *Environmental Geology* **47**, 1099–1110 (2005).
38. Choe, J. K. *et al.* Performance and life cycle environmental benefits of recycling spent ion exchange brines by catalytic treatment of nitrate. *Water Res* **80**, 267–280 (2015).
39. Werth, C. J., Yan, C. & Troutman, J. P. Factors Impeding Replacement of Ion Exchange with (Electro)Catalytic Treatment for Nitrate Removal from Drinking Water. *ACS ES&T Engineering* **1**, 6–20 (2021).
40. Cyplik, P. *et al.* Biological denitrification of high nitrate processing wastewaters from explosives production plant. *Water Air Soil Pollut* **223**, 1791–1800 (2012).
41. Duca, M. & Koper, M. T. M. Powering denitrification: the perspectives of electrocatalytic nitrate reduction. *Energy Environ Sci* **5**, 9726–9742 (2012).
42. Bergquist, A. M., Choe, J. K., Strathmann, T. J. & Werth, C. J. Evaluation of a hybrid ion exchange-catalyst treatment technology for nitrate removal from drinking water. *Water Res* **96**, 177–187 (2016).
43. Bhatnagar, A. & Sillanpää, M. A review of emerging adsorbents for nitrate removal from water. *Chemical Engineering Journal* **168**, 493–504 (2011).
44. Choudhary, M., Muduli, M. & Ray, S. A comprehensive review on nitrate pollution and its remediation: conventional and recent approaches. *Sustain Water Resour Manag* **8**, 113 (2022).
45. Schoeman, J. J. & Steyn, A. Nitrate removal with reverse osmosis in a rural area in South Africa. *Desalination* **155**, 15–26 (2003).
46. Park, J. Y. & Yoo, Y. J. Biological nitrate removal in industrial wastewater treatment: Which electron donor we can choose. *Appl Microbiol Biotechnol* **82**, 415–429 (2009).
47. di Capua, F., Pirozzi, F., Lens, P. N. L. & Esposito, G. Electron donors for autotrophic denitrification. *Chemical Engineering Journal* vol. 362 922–937 Preprint at https://doi.org/10.1016/j.cej.2019.01.069 (2019).
48. di Capua, F., Pirozzi, F., Lens, P. N. L. & Esposito, G. Electron donors for autotrophic denitrification. *Chemical Engineering Journal* vol. 362 922–937 Preprint at https://doi.org/10.1016/j.cej.2019.01.069 (2019).
49. van Langevelde, P. H., Katsounaros, I. & Koper, M. T. M. Electrocatalytic Nitrate Reduction for Sustainable Ammonia Production. *Joule* **5**, 290–294 (2021).

50. Guo, S. *et al.* Insights into Nitrate Reduction over Indium-Decorated Palladium Nanoparticle Catalysts. 503–515 (2018) doi:10.1021/acscatal.7b01371.
51. Chaplin, B. P. The Prospect of Electrochemical Technologies Advancing Worldwide Water Treatment. *Acc Chem Res* **52**, 596–604 (2019).
52. Administration, U. S. E. I. *International Energy Outlook*. (2019).
53. Liu, J.-X., Richards, D., Singh, N. & Goldsmith, B. R. Activity and Selectivity Trends in Electrocatalytic Nitrate Reduction on Transition Metals. *ACS Catal* **9**, 7052–7064 (2019).
54. Martínez, J., Ortiz, A. & Ortiz, I. State-of-the-art and perspectives of the catalytic and electrocatalytic reduction of aqueous nitrates. *Appl Catal B* **207**, 42–59 (2017).
55. Wang, Z., Richards, D. & Singh, N. Recent discoveries in the reaction mechanism of heterogeneous electrocatalytic nitrate reduction. *Catal Sci Technol* **11**, 705–725 (2021).
56. Cook, A. R. *et al.* Reducing radicals in nitrate solutions. The NO32- system revisited. *Journal of Physical Chemistry A* **105**, 3658–3666 (2001).
57. Dima, G. E., de Vooys, A. C. A. & Koper, M. T. M. Electrocatalytic reduction of nitrate at low concentration on coinage and transition-metal electrodes in acid solutions. *Journal of Electroanalytical Chemistry* **554–555**, 15–23 (2003).
58. Gootzen, J. F. E., Lefferts, L. & Van Veen, J. A. R. Electrocatalytic nitrate reduction on palladium based catalysts activated with germanium. *Appl Catal A Gen* **188**, 127–136 (1999).
59. Shimazu, K. *et al.* Reduction of nitrate ions on tin-modified palladium thin film electrodes. *Journal of Electroanalytical Chemistry* **601**, 161–168 (2007).
60. Siriwatcharapiboon, W. *et al.* Promotion effects of Sn on the electrocatalytic reduction of nitrate at Rh nanoparticles. *ChemElectroChem* **1**, 172–179 (2014).
61. de Groot, M. T. & Koper, M. T. M. The influence of nitrate concentration and acidity on the electrocatalytic reduction of nitrate on platinum. *Journal of Electroanalytical Chemistry* **562**, 81–94 (2004).
62. Dima, G. E., Beltramo, G. L. & Koper, M. T. M. Nitrate reduction on single-crystal platinum electrodes. *Electrochim Acta* **50**, 4318–4326 (2005).
63. Gootzen, J. F. E., Lefferts, L. & Van Veen, J. A. R. Electrocatalytic nitrate reduction on palladium based catalysts activated with germanium. *Appl Catal A Gen* **188**, 127–136 (1999).
64. Kuwabata, S., Uezumi, S., Tanaka, K. & Tanaka, T. Assimilatory and Dissimilatory Reduction of NO3- and NO2- with an (n-Bu4N)3[Mo2Fe6S8(SPh)9] Modified Glassy-Carbon Electrode in Water. *Inorg Chem* **25**, 3018–3022 (1986).
65. Reyter, D., Bélanger, D. & Roué, L. Elaboration of Cu-Pd films by coelectrodeposition: Application to nitrate electroreduction. *Journal of Physical Chemistry C* **113**, 290–297 (2009).
66. Reyter, D., Bélanger, D. & Roué, L. Elaboration by high-energy ball milling of copper/palladium composite materials - characterization and electrocatalytic activity for the reduction of nitrate in alkaline medium. *Journal of Electroanalytical Chemistry* **622**, 64–72 (2008).
67. Katsounaros, I. & Kyriacou, G. Influence of nitrate concentration on its electrochemical reduction on tin cathode: Identification of reaction intermediates. *Electrochim Acta* **53**, 5477–5484 (2008).

68. De Vooys, A. C. A., Beltramo, G. L., Van Riet, B., Van Veen, J. A. R. & Koper, M. T. M. Mechanisms of electrochemical reduction and oxidation of nitric oxide. *Electrochim Acta* **49**, 1307–1314 (2004).
69. Zheng, J., Lu, T., Cotton, T. M. & Chumanov, G. Photoinduced Electrochemical Reduction of Nitrite at an Electrochemically Roughened Silver Surface. *Journal of Physical Chemistry B* **103**, 6567–6572 (1999).
70. Zheng, J., Lu, T., Cotton, T. M. & Chumanov, G. Photoinduced Electrochemical Reduction of Nitrite at an Electrochemically Roughened Silver Surface. *Journal of Physical Chemistry B* **103**, 6567–6572 (1999).
71. Estudillo-Wong, L. A., Alonso-Vante, N. & Manzo-Robledo, A. Electro-reduction of Nitrate and Nitrite Ions on Carbon-Supported Pt Nanoparticles. *ECS Trans* **15**, 385–393 (2008).
72. Butcher, D. P. & Gewirth, A. A. Nitrate reduction pathways on Cu single crystal surfaces: Effect of oxide and Cl−. *Nano Energy* **29**, 457–465 (2016).
73. Bae, S. E., Stewart, K. L. & Gewirth, A. A. Nitrate adsorption and reduction on Cu(100) in acidic solution. *J Am Chem Soc* **129**, 10171–10180 (2007).
74. Katsounaros, I., Figueiredo, M. C., Chen, X., Calle-Vallejo, F. & Koper, M. T. M. Interconversions of nitrogen-containing species on Pt(100) and Pt(111) electrodes in acidic solutions containing nitrate. *Electrochim Acta* **271**, 77–83 (2018).
75. Pérez-Gallent, E., Figueiredo, M. C., Katsounaros, I. & Koper, M. T. M. Electrocatalytic reduction of Nitrate on Copper single crystals in acidic and alkaline solutions. *Electrochim Acta* **227**, 77–84 (2017).
76. Katsounaros, I., Ipsakis, D., Polatides, C. & Kyriacou, G. Efficient electrochemical reduction of nitrate to nitrogen on tin cathode at very high cathodic potentials. *Electrochim Acta* **52**, 1329–1338 (2006).
77. Dortsiou, M. & Kyriacou, G. Electrochemical reduction of nitrate on bismuth cathodes. *Journal of Electroanalytical Chemistry* **630**, 69–74 (2009).
78. Su, L. *et al.* Tailoring the Assembly of Iron Nanoparticles in Carbon Microspheres toward High-Performance Electrocatalytic Denitrification. *Nano Lett* **19**, 5423–5430 (2019).
79. Dortsiou, M., Katsounaros, I., Polatides, C. & Kyriacou, G. Influence of the electrode and the pH on the rate and the product distribution of the electrochemical removal of nitrate. *Environmental Technology (United Kingdom)* **34**, 373–381 (2013).
80. Horányi, G. & Rizmayer, E. M. Electrocatalytic reduction of NO2- and NO3- ions at a platinized platinum electrode in alkaline medium. *Journal of Electroanalytical Chemistry* **189**, 265–272 (1985).
81. Zhu, J. Y. *et al.* Iridium Nanotubes as Bifunctional Electrocatalysts for Oxygen Evolution and Nitrate Reduction Reactions. *ACS Appl Mater Interfaces* **12**, 14064–14070 (2020).
82. Li, J. *et al.* Efficient Ammonia Electrosynthesis from Nitrate on Strained Ruthenium Nanoclusters. *J Am Chem Soc* **142**, 7036–7046 (2020).
83. Ma, X. *et al.* Development and reaction mechanism of efficient nano titanium electrode: Reconstructed nanostructure and enhanced nitrate removal efficiency. *Journal of Electroanalytical Chemistry* **782**, 270–277 (2016).
84. Li, M., Feng, C., Zhang, Z., Yang, S. & Sugiura, N. Treatment of nitrate contaminated water using an electrochemical method. *Bioresour Technol* **101**, 6553–6557 (2010).
85. Wang, Y. *et al.* Enhanced nitrate-to-ammonia activity on copper- nickel alloys via tuning of intermediate adsorption. *J Am Chem Soc* **142**, 5702–5708 (2020).

86. Mattarozzi, L. *et al.* Hydrogen evolution assisted electrodeposition of porous Cu-Ni alloy electrodes and their use for nitrate reduction in alkali. *Electrochim Acta* **140**, 337–344 (2014).
87. Reyter, D., Bélanger, D. & Roué, L. Optimization of the cathode material for nitrate removal by a paired electrolysis process. *J Hazard Mater* **192**, 507–513 (2011).
88. Duca, M., Sacré, N., Wang, A., Garbarino, S. & Guay, D. Enhanced electrocatalytic nitrate reduction by preferentially-oriented (100) PtRh and PtIr alloys: the hidden treasures of the 'miscibility gap'. *Appl Catal B* **221**, 86–96 (2018).
89. Wang, Z., Young, S. D., Goldsmith, B. R. & Singh, N. Increasing electrocatalytic nitrate reduction activity by controlling adsorption through PtRu alloying. *J Catal* **395**, 143–154 (2021).
90. Zhang, L. *et al.* Electrochemical behaviors and influence factors of copper and copper alloys cathode for electrocatalytic nitrate removal. *Water Environment Research* **91**, 1589–1599 (2019).
91. Mattarozzi, L. *et al.* Electrodeposition of Compact and Porous Cu-Zn Alloy Electrodes and Their Use in the Cathodic Reduction of Nitrate. *J Electrochem Soc* **162**, D236–D241 (2015).
92. Mattarozzi, L. *et al.* Electrodeposition of compact and porous Cu-Pd alloy layers and their application to nitrate reduction in alkali. *Electrochim Acta* **230**, 365–372 (2017).
93. Gao, W. *et al.* Removal of nitrate from water by the electrocatalytic denitrification on the Cu-Bi electrode. *Journal of Electroanalytical Chemistry* **817**, 202–209 (2018).
94. Calle-Vallejo, F., Huang, M., Henry, J. B., Koper, M. T. M. & Bandarenka, A. S. Theoretical design and experimental implementation of Ag/Au electrodes for the electrochemical reduction of nitrate. *Physical Chemistry Chemical Physics* **15**, 3196 (2013).
95. Zhang, Z. *et al.* Electrochemical-catalytic reduction of nitrate over Pd-Cu/γAl2O3 catalyst in cathode chamber: Enhanced removal efficiency and N2 selectivity. *Chemical Engineering Journal* **290**, 201–208 (2016).
96. Sanjuán, I., García-Cruz, L., Solla-Gullón, J., Expósito, E. & Montiel, V. Bi–Sn nanoparticles for electrochemical denitrification: activity and selectivity towards N2 formation. *Electrochim Acta* **340**, (2020).
97. Yang, J., Kwon, Y., Duca, M. & Koper, M. T. M. Combining voltammetry and ion chromatography: Application to the selective reduction of nitrate on Pt and PtSn electrodes. *Anal Chem* **85**, 7645–7649 (2013).
98. Stolz, J. F. & Basu, P. Evolution of nitrate reductase: Molecular and structural variations on a common function. *ChemBioChem* **3**, 198–206 (2002).
99. Oremland, R. S. *et al.* Isolation, growth, and metabolism of an obligately anaerobic, selenate- respiring bacterium, strain SES-3. *Appl Environ Microbiol* **60**, 3011–3019 (1994).
100. Cruz-García, C., Murray, A. E., Klappenbach, J. A., Stewart, V. & Tiedje, J. M. Respiratory nitrate ammonification by Shewanella oneidensis MR-1. *J Bacteriol* **189**, 656–662 (2007).
101. Sparacino-Watkins, C., Stolz, J. F. & Basu, P. Nitrate and periplasmic nitrate reductases. *Chem Soc Rev* **43**, 676–706 (2014).
102. Li, Y. *et al.* Enzyme Mimetic Active Intermediates for Nitrate Reduction in Neutral Aqueous Media. *Angewandte Chemie International Edition* **59**, 9744–9750 (2020).

103. Li, Y., Yamaguchi, A., Yamamoto, M., Takai, K. & Nakamura, R. Molybdenum Sulfide: A Bioinspired Electrocatalyst for Dissimilatory Ammonia Synthesis with Geoelectrical Current. *The Journal of Physical Chemistry C* **121**, 2154–2164 (2017).
104. He, D. *et al.* Selective Electrocatalytic Reduction of Nitrite to Dinitrogen Based on Decoupled Proton-Electron Transfer. *J Am Chem Soc* **140**, 2012–2015 (2018).
105. Wang, Y., Zhou, W., Jia, R., Yu, Y. & Zhang, B. Unveiling the Activity Origin of a Copper-based Electrocatalyst for Selective Nitrate Reduction to Ammonia. *Angewandte Chemie* **132**, 5388–5392 (2020).
106. Jia, R. *et al.* Boosting Selective Nitrate Electroreduction to Ammonium by Constructing Oxygen Vacancies in TiO 2. *ACS Catal* **10**, 3533–3540 (2020).
107. Li, C. *et al.* Electrochemical removal of nitrate using a nanosheet structured Co3O4/Ti cathode: Effects of temperature, current and pH adjusting. *Sep Purif Technol* **237**, 116485 (2020).
108. Gao, J. *et al.* Non-precious Co3O4-TiO2/Ti cathode based electrocatalytic nitrate reduction: Preparation, performance and mechanism. *Appl Catal B* **254**, 391–402 (2019).
109. Jonoush, Z. A., Rezaee, A. & Ghaffarinejad, A. Electrocatalytic nitrate reduction using Fe0/Fe3O4 nanoparticles immobilized on nickel foam: Selectivity and energy consumption studies. *J Clean Prod* **242**, 118569 (2020).
110. Li, K., Chen, C., Bian, X., Sun, T. & Jia, J. Electrolytic nitrate reduction using Co3O4 rod-like and sheet-like cathodes with the control of (220) facet exposure and Co2+/Co3+ ratio. *Electrochim Acta* **362**, 137121 (2020).
111. Huo, S. *et al.* Fabrication of Porous Configurated Ni2P/Ni Foam Catalyst and its Boosted Properties for pH-universal Hydrogen Evolution Reaction and Efficient Nitrate Reduction. *ChemCatChem* 1–12 (2020) doi:10.1002/cctc.202000426.
112. Duan, W. *et al.* Highly active and durable carbon electrocatalyst for nitrate reduction reaction. *Water Res* **161**, 126–135 (2019).
113. Wang, J., Ling, L., Deng, Z. & Zhang, W. xian. Nitrogen-doped iron for selective catalytic reduction of nitrate to dinitrogen. *Sci Bull (Beijing)* **65**, 926–933 (2020).
114. Teng, W., Fan, J. & Zhang, W. X. Iron-Catalyzed Selective Denitrification over N-Doped Mesoporous Carbon. *ACS Appl Mater Interfaces* **12**, 28091–28099 (2020).
115. Anastasiadou, D., Beek, Y., Hensen, E. J. M. & Costa Figueiredo, M. Ammonia electrocatalytic synthesis from nitrate. *Electrochemical Science Advances* 1–11 (2022) doi:10.1002/elsa.202100220.
116. Deng, X., Yang, Y., Wang, L., Fu, X. Z. & Luo, J. L. Metallic Co Nanoarray Catalyzes Selective NH3 Production from Electrochemical Nitrate Reduction at Current Densities Exceeding 2 A cm−2. *Advanced Science* **8**, (2021).
117. Singh, N. & Goldsmith, B. R. Role of Electrocatalysis in the Remediation of Water Pollutants. *ACS Catal* **10**, 3365–3371 (2020).
118. Garcia-Segura, S., Lanzarini-Lopes, M., Hristovski, K. & Westerhoff, P. Electrocatalytic reduction of nitrate: Fundamentals to full-scale water treatment applications. *Appl Catal B* **236**, 546–568 (2018).
119. Lan, Y., Chen, J., Zhang, H., Zhang, W. & Yang, J. Fe/Fe 3 C nanoparticle-decorated N-doped carbon nanofibers for improving the nitrogen selectivity of electrocatalytic nitrate reduction. *J Mater Chem A Mater* (2020) doi:10.1039/d0ta02317e.

Chapter 2
Methods

2.1 Introduction

This chapter provides a description of experimental techniques used in this dissertation. **Section 2.2** details catalyst preparation and deposition onto various supports used for nitrate reduction. **Section 2.3** covers the characterization techniques used ex situ and methods used to estimating the electrochemically active surface area. **Section 2.4** gives an overview of how catalysts were evaluated for determining activity and selectivity. **Sections 2.5** describes batch and flow cell operation for nitrate reduction. This chapter serves as a tool for researchers who wish to replicate the experimental work conducted in this dissertation.

2.2 Electrode Preparation Techniques

2.2.1 Electrode ink preparation.

Using a variety of commercial powdered catalysts, electrode inks were prepared to load the catalyst onto an electrode for electrochemical measurements. For deposition on a glassy carbon rotating disk electrode (RDE), the catalyst ink was prepared by adding 3 mg of the supported catalyst in 5 mL of Millipore water and isopropanol mixture (1:1 volume ratio). 17.5 μL of 5 wt% Nafion solution in isopropanol was added to the solution to act as a binder and the ink was ultrasonicated for at least two hours. A glassy carbon disk (5 mm diameter) was cleaned by polishing with 0.05 μm alumina suspension on a micropolishing cloth, then rinsed with Millipore water and sonicated at least 30 minutes in Millipore water. The prepared catalyst ink was sonicated

30 minutes prior to deposition on the clean glassy carbon surface. 8 μL of the sonicated ink solution was drop cast onto the surface of the cleaned glassy carbon electrode (assembled in Teflon rotating disk holder). The deposition was kept in closed containment as the ink dried (30 minutes). A second 8 μL of the ink was deposited onto the dried ink surface and again let dry. The total catalyst loading on the glassy carbon surface was 9.6 μg, including carbon.

For deposition of the commercial catalyst onto a carbon felt, the catalyst ink was prepared by combining either 5 or 10 mg of catalyst powder with a solution of 1 mL Millipore water, 1.5 mL isopropanol, and 8.8 μL of 5 wt% Nafion solution in isopropanol and then sonicated for at least 10 minutes. An approximately 2 cm x 2 cm section of carbon felt was prepared by alternating rinsing with Millipore water and acetone, repeating at least 3 times, and ending with a final Millipore water rinse. For carbon felts prepared for use in the flow cell, the carbon felts were cut to exactly 2.3 cm x 2.4 cm to fit the length and width of the flow field. The rinsed carbon felt was then let dry. The prepared carbon felt was then moved to a hot plate surface at 80 °C the freshly sonicated ink was deposited on the carbon felt using a dropper until the carbon felt was saturated (catalyst ink will be left over). The carbon felt with catalyst was then left to dry on the hot plate. After 30 minutes, the carbon felt was gently flipped over, and more of the ink was applied using a dropper until the carbon felt was saturated, and then the carbon felt was left to dry on the hot plate. This process was repeated until all the prepared catalyst ink was deposited on the carbon felt.

2.3 Characterization Techniques

The following characterization techniques were used in this dissertation to understand the electrode-electrolyte interface and are applied to normalize electrocatalyst performance to the active surface area (as opposed to normalizing by mass or geometric area). In each subsection, the background for each characterization technique is covered with essential information for

evaluating results obtained using the technique. Specific details for the equipment and conditions used in this work are included at the end of each technique.

2.3.1 X-ray diffraction.

X-ray diffraction (XRD) is a technique used to understand the structure of crystalline materials. In XRD, a beam of electrons is directed at a target which provides characteristic incident X-rays resulting from the displacement of core electrons replaced with outer shell electrons.[1] Cu is the most used electron beam target material and produces Cu-Kα (1.5418 Angstroms) X-rays.[1] The incident X-rays diffract off the crystalline structure of a sample and, at specific angles, the X-rays which constructively diffract off of repeating crystalline planes can be detected. Bragg's law (**Equation 2.1**) relates the angle of diffraction, or the Bragg angle (θ), and the lattice spacing (d) between adjacent identical crystal planes to the incident X-ray wavelength (λ) and the diffraction order (n) which indicates how many crystalline planes are interacting.[1] Using Bragg's law we can obtain information about the material's crystalline structure by identifying specific crystal planes using Miller indices.

$$2dsin(\theta) = n/\lambda \tag{2.1}$$

For metal nanoparticles, we can use the XRD spectra to estimate the particle size via the crystallite sizes using the Scherrer equation (**Equation 2.2**).[2] τ is the average size of the crystallite, K is the shape factor (0.9), λ is the wavelength of the X-ray, β is the full width of the peak at half the maximum as measured in radians, and θ is the Bragg angle of the peak in radians.

$$\tau = \frac{K\lambda}{\beta cos(\theta)} \tag{2.2}$$

In the work detailed in **Chapter 4** (with additional details in **Appendix A**), the XRD patterns were collected at the Michigan Center for Materials Characterization (MC)^2 facility using

a PANalytical Empyrean diffractometer operating at 45 kV and 40 mA ranging from 10° to 90° for Rh/C and Rh_xS_y/C and 30° to 90° for Pt/C with a 0.008° step size. For application of the Scherrer equation to find the average crystallite sizes, K = 0.9 and the X-ray wavelength was λ = 0.15405 nm (Cu K-α source).

2.3.2 Transmission electron microscopy.

Transmission electron microscopy (TEM) is a technique used to visualize a material at the nanometer level, which is helpful for further understanding a material's structure via particle size or even identifying atomic arrangement. TEM utilizes the small wavelength of electrons to achieve image resolution of nanometer lengths (typically observed in high-resolution TEM); the resolution of light microscopes is limited by the wavelength of light, and they can only resolve to about 300 nm.[3] In operation, a high energy beam of electrons is directed towards a thin sample in high vacuum conditions. The electrons can have elastic and inelastic interactions with the sample. In inelastic interactions, some of the energy from the electron is transferred into the sample which responds by emitting a secondary electron, emitting photons in the visible and X-ray wavelengths, or excitation and enhanced lattice vibrations of the sample which can lead to structural changes which ultimately damage the sample.[1]

In **Chapter 4**, TEM was used to confirm the average particle size of Rh_xS_y/C and Rh/C nanoparticles and compare with the crystallite sizes determined from XRD. TEM was performed on a JOEL 2010F electron microscope operating with 200 kV accelerating voltage. The image processing program ImageJ was used to analyze the nanoparticles' cross section length.

2.3.3 Double-layer capacitance surface areas.

For all interfaces between solids and liquids, liquid molecules come in contact with the solid surface and the distribution is dictated by the electrostatic field present. In electrochemical systems, the electrostatic field is manipulated by the application of a potential gradient between two electrodes which changes the distribution of molecules or ions on the solid material's surface. Like a capacitor, an electrode's surface is charged electrostatically with molecules and ions forming the double-layer. Current resulting from electrostatic surface charging is referred to as non-Faradaic current (on the other hand, Faradaic current is due to the transfer of electrons).

For materials which act close to ideal capacitors (where the capacitance is constant across applied potentials), the charge associated with the double-layer can be related to the electrochemical surface area. Using cyclic voltammetry, the electrode is cycled across the non-Faradaic region at different scan rates. The current at the midpoint potential is linearly related to the scan rates and the slope is the differential capacitance. Using the specific capacitance of the material the electrochemical surface area is obtained.[4] The charging of the double-layer during the experiment is assumed to match the conditions (e.g., electrolyte and potential) used to obtain the specific capacitance.

The electrochemical surface area is useful to use to normalize the measured current and identify intrinsic activity values for catalysts. Most catalysts do not act as ideal capacitors and, therefore, using the specific capacitance is a poor choice for estimating the electrochemical surface area. Other limitations estimating ECSA only from specific capacitance are that the non-faradaic and faradaic currents can be difficult to deconvolute, high surface area or porous structures can have non-linear relationships between surface-charging and scan rate, the capacitance contributions of the active metals of supported catalysts (e.g., 30 wt% Pt/C) are not easily separated from total capacitance, and the assumption that the distribution of species at the double-layer is

identical for each scan rate and within the potential range.[4,5] In the next sections, hydrogen underpotential deposition and copper underpotential deposition are discussed as more appropriate methods for estimating ECSA for Pt group metals and some transition metals.

An alternative ECSA estimation method combining information from electrochemical capacitance and crystallite size from XRD is used for nanoparticle catalysts supported on well-characterized carbon surfaces (i.e., Vulcan carbon) and is referred to as the "capacitance & XRD" method.[6] An example calculation using the capacitance & XRD method is shown below for Pt/C deposited onto a glassy carbon rotating disk:

$$\mathrm{ECSA_{cap\&XRD}\ (Pt)} = \mathrm{Capacitance} \times \frac{1\ \mathrm{cm^2}}{20\ \mu\mathrm{F}} \times \frac{1\ \mathrm{m^2}}{10^4\ \mathrm{cm^2}} \times \frac{1\ \mathrm{g_{cat}}}{250\ \mathrm{m^2}} \times \frac{0.3\ \mathrm{g_{Pt}}}{1\ \mathrm{g_{cat}}} \times \frac{1\ \mathrm{cm^3}}{21.45\ \mathrm{g_{Pt}}} \times \frac{10^{21}\ \mathrm{nm^3}}{1\ \mathrm{cm^3}} \times \frac{5(2.2\ \mathrm{nm})^2}{(2.2\ \mathrm{nm})^3} \quad (2.3)$$

where the capacitance is the total capacitance of the deposited catalyst and carbon support in μF. The specific capacitance of the Vulcan XC-72 carbon support is approximated as 20 μF cm^{-2},[7] the mass per area of Vulcan XC-72 carbon is 250 $m^2\ g^{-1}$, the metal loading is 30 wt% of Pt on Vulcan carbon, the density of Pt is 21.45 g cm^{-3}, and each nanoparticle is approximated as a cube with five faces showing and side lengths equal to the average size of the nanoparticle as determined by XRD using the Scherrer equation (for the commercial Pt/C, the average diameter was determined to be 2.2 nm). If for a particular deposition of a sample there is, for example, 10% more catalyst exposed to the electrolyte, the capacitance will be 10% higher, and will be normalized out by this method. By incorporating the crystallite/particle size of the active material the capacitance & XRD method attempts to separate capacitance contributions between the support and metal catalyst, but the capacitance & XRD method still shares many shortcomings for ECSA determination with the simple capacitance method described earlier. The capacitance & XRD method is used for normalizing the steady-state currents obtained on Rh_xS_y/C throughout **Chapter 4**.

2.3.4 Hydrogen underpotential deposition.

For platinum group metals (Pt, Ir, Pd, Rh, and Ru), the energy barrier for hydrogen adsorption on the surface is lower than for hydrogen evolution and hydrogen is adsorbed, forming just around a monolayer of hydrogen, on the metal surfaces.[8,9] The hydrogen adsorption/desorption reaction can be written as **Equation 2.4**, where hydrogen is present as a proton in solution (H^+), a surface site is represented as *, and hydrogen adsorbed to the surface is H*. The total charge of hydrogen desorbing from the surface (backwards reaction of **Equation 2.4**) and the average charge density are used to estimate the ECSA. For simplicity, hydrogen adsorption is shown to involve 1 electron per 1 hydrogen adsorbed on a surface site but, the total coverage was shown to be closer to 0.77 on a smooth Pt electrode[10] which results in a lower measured surface area than what is in contact with the solution.

$$H^+ + e^- + * \rightleftarrows H^* \tag{2.4}$$

The hydrogen underpotential deposition (H_{upd}) profiles for Pt and Rh are well characterized and shown in **Figure 2.1**. The polycrystalline Pt H_{upd} features two characteristic peaks which are associated with hydrogen adsorption/desorption on the (110) and (100) edge sites and a broad peak attributed to hydrogen adsorption/desorption on the (111) terrace sites.[11,12] Unlike Pt, the Rh H_{upd} profile does not have the distinct peaks associated with hydrogen adsorption/desorption on specific facets and instead is comprised of a single current peak. H_{upd} peaks have also been observed on Pd and several distinct current peaks can be attributed to hydrogen adsorption/desorption on different facets.[13] On Pd, Ir, and Ru, hydrogen is also known to absorb into the surface,[14–17] which makes H_{upd} less reliable as an ECSA determination technique for those metals.

A range of electrolytes were used as there is no "perfect" electrolyte to use across the platinum group metals in which the anions will not interact with the surface or hydrogen

adsorption. For Pt, perchloric acid ($HClO_4$) was preferred because the perchlorate anion interacts weakly with the surface.[18] For Rh, sulfuric acid (H_2SO_4) is better suited for H_{upd} because Rh facilitates the production of chloride ions when the perchlorate anion is present, and the bisulfate anion does not interact strongly with the Rh surface.[19,20]

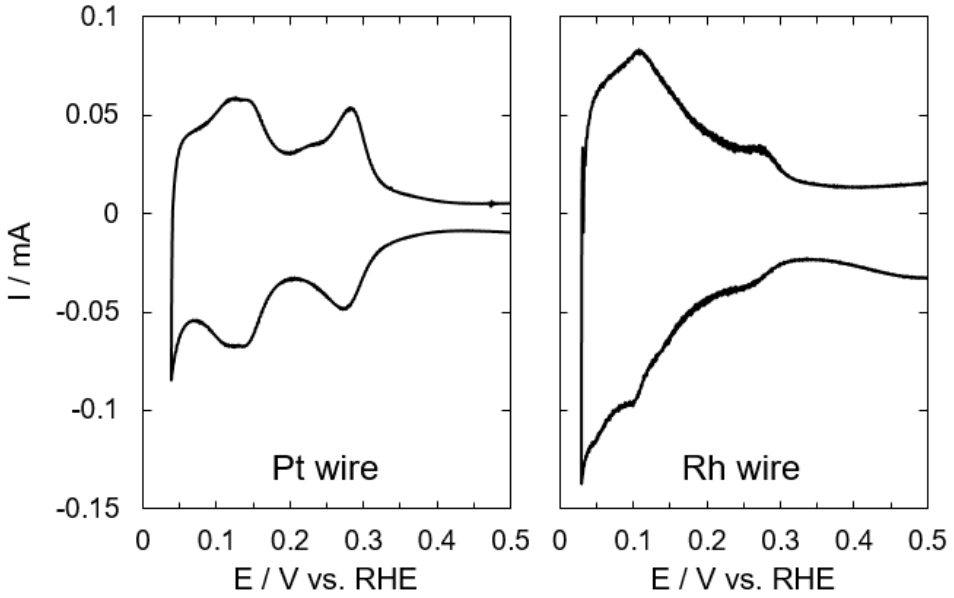

Figure 2.1. Hydrogen underpotential deposition curves for polycrystalline Pt and Rh wires at 100 mV/s in oxygen-deficient 0.1 M H_2SO_4.

For H_{upd} analysis in this thesis, measurements were typically taken in pH = 0 or 1 electrolyte. The scan rate range of 20–100 mV/s was used for the cyclic voltammograms, where changing the scan rate did not change the ECSA. The uncorrected H_{upd} charge (Q_1) was calculated by taking the charge from hydrogen desorption (oxidative half of a cyclic voltammogram) between the most negative potential of the scan and a potential where there is only non-Faradaic current (0.4 V vs. RHE). The charge of the double layer (Q_{dL}) was estimated as constant from the current obtained at 0.4 V and applied across the potential window used for H_{upd} current. The H_{upd} charge (Q_{Hupd}) used for estimating the ECSA was the uncorrected charge minus the double layer charge ($Q_{Hupd} = Q_1 - Q_{dL}$). The ECSA in cm^2 was obtained by using the charge density of the metal. The average charge densities are 210 $\mu C/cm^2$ (Pt and PtRu) and 221 $\mu C/cm^2$ (Rh).[9,10]

Hydrogen underpotential deposition was also used as a tool in this thesis (**Chapters 3** and **4**) to understand the competitive adsorption of anions (NO_3^- and Cl^-) and protons on Pt and Rh. The charge from the H_{upd} in only the supporting electrolyte (e.g., H_2SO_4 or $HClO_4$) was assumed to represent a complete coverage of hydrogen on the catalyst surface ($\theta_H = 1$). When an ion is added, if the ion (*i*) is blocking some of the surface sites and not allowing hydrogen to adsorb/desorb, the measured H_{upd} charge will be lower because the coverage of hydrogen on the surface will be less than 1 (i.e., the electron transfer in **Equation 2.4** will not occur as many times) and the coverage of the adsorbed ion will be non-zero ($\theta_i > 0$). The competitive adsorption for the species studied was modeled to follow a Langmuir isotherm which assumes the adsorption sites for hydrogen and the ion are uniform, only one ion can adsorb to a site at a time (forming a monolayer), there are no interactions between adjacent adsorbing species.[21] A Langmuir isotherm model was chosen based on simplicity and does not account for nitrate adsorption as a bridge over two sites,[22] site specific adsorption for different facets available on the polycrystalline surfaces, or electrostatic interactions that may change the observed H_{upd} charge but are not associated with specific adsorption. Additionally, this technique becomes more challenging to use if the ion is adsorbing/desorbing with an electron transfer in the H_{upd} region which can contribute to an increase in H_{upd} charge with increasing ion concentration (as explored on Pt for nitrate in **Chapter 3** and chloride in **Chapter 4**). Nevertheless, this concept was used for a wide range of nitrate and chloride concentrations on Pt and Rh to understand ion adsorption trends between the two metals.

2.3.5 Copper underpotential deposition.

Copper underpotential deposition (Cu_{upd}) is an electrochemical method used for determining the ECSA. Similar to H_{upd}, Cu_{upd} estimates the ECSA based on the charge from the stripping of a monolayer of Cu from the electrode surface and relating the charge to an area using

a known charge density. The copper adsorption/desorption reaction is shown as **Equation 2.5**. For Cu_{upd}, each copper atom is assumed to adsorb to one surface atom and transfer 2 electrons per site.[23] Cu_{upd} is considered more accurate than H_{upd} for ECSA measurements for metals which absorb hydrogen and form hydrides such as Ru or Pd.[24]

$$Cu^{2+} + 2\,e^- + * \rightleftarrows Cu^* \tag{2.5}$$

For a Cu_{upd} measurement, the potential where copper adsorbs as a monolayer is applied then a linear sweep from that potential to an oxidative potential is performed (stripping the copper monolayer from the surface). Copper deposition, where more than a monolayer of copper atoms is deposited, is observed at potentials more negative than Cu_{upd} but can influence the C_{upd} charge. Varying the amount of time the Cu_{upd} potential is applied will reveal if the charge is solely from Cu_{upd} or if bulk copper deposition is occurring; the Cu_{upd} charge should not change with time. Careful surveying of the potentials for Cu_{upd} must be performed to ensure the currents are only from copper as a monolayer.

In **Chapter 5**, Cu_{upd} was used to estimate the ECSA of commercial PtRu/C and normalize nitrate reduction currents. The initial cyclic voltammogram was taken at 100 mV/s in de-oxygenated 0.1 M H_2SO_4 and a slanted baseline was taken as half the double-layer current at 0.4 V vs. RHE. 2 mM $CuSO_4$ was then added to the solution. The electrode was held at 1.0 V vs. RHE for 2 minutes, the deposition potential of 0.42 V vs. RHE was applied for 3 minutes, and a linear voltammetric scan was taken at 100 mV/s from 0.42 V to 1.0 V vs. RHE. Deposition potentials between 0.3 and 0.5 V vs. RHE were surveyed from 2 to 10 minutes to determine the most appropriate potential for Cu_{upd}. The charge from copper stripping was corrected using the baseline charge prior to calculating the ECSA.

2.4 Performance Evaluation

The performance for nitrate reduction for catalysts used in this thesis was evaluated according to the intrinsic activity (non-mass transport limited current density) and faradaic efficiency. Determination of the total nitrate reduction product distribution (for catalyst selectivity) is challenging due to the number of possible products in both gas and liquid phases; thus, we focus on the faradaic efficiency towards aqueous products (NO_2^- and NH_4^+) and conversion of nitrate. Other performance metrics such as catalyst stability and catalyst cost per amount nitrate reduced are also valuable to consider for overall catalyst performance but are not addressed directly in this thesis.

2.4.1 Electrochemical kinetics.

Reaction kinetic measurements are essential for understanding catalyst activity though their reaction rates and mechanisms. An exchange of an electron between the electrode and an active species can be tracked through a current, and a current which results from an exchange of an electron is called a faradaic current. In electrocatalytic reactions, a faradaic current can be thought of as analogous to a reaction rate (i.e., current tracks the movement of electrons during the reaction).

In this dissertation, we aim to measure intrinsic reaction kinetics, meaning the rate of reaction is governed by the elementary steps of the catalytic reaction mechanism. However, experimental conditions can cause the observed reaction rate to differ from the intrinsic reaction rate if mass transport is slower than the intrinsic kinetics. A challenge for reactions occurring in liquid phase is the sluggishness of movement of reactants and products through the media. Transport of the reactants and products can influence the observed reaction rate if the transport is slow by changing the concentration of the reactants at the surface as they are depleted by the

reaction and misrepresenting the reaction rate under the desired conditions. To encourage movement of species within a solution and delivery to the electrode surface, reactions are often carried out with the help of stir bars, in flow devices where the electrolyte is pushed through a channel, or with a rotating disk electrode which can rotate at high speeds to draw the solution towards the electrode surface. All of these serve to increase mass transport and minimize concentration gradients. Only when there are no mass transport limitations, or when these mass transport limitations are accounted for, can the observed rate be compared to the elementary steps of the reaction mechanism. To identify if mass transport is limiting the rate of reaction, the reaction rate is measured at different mass transport conditions and the observed reaction rates are compared. When the observed rate is independent of influence from mass transport limitations, increasing the stir/rotation/flow rate will not affect the measured current. When a redox reaction has distinct regions of mass transport limited and kinetically limited current, a Koutecky-Levich analysis also can be used for separating observed current into its intrinsic kinetic and mass transport limiting currents,[25,26] but this method is not used in this thesis.

For nitrate reduction measurements in this dissertation, mass transport effects on the observed current were explored using various stir rates with a stir bar with the wire electrodes (**Chapter 3**), a range of rotation rates with the rotating disk electrode configuration (**Chapters 4** and **5**), and several flow rates with catalyst loaded on a carbon felt held in the flow cell (**Chapter 5**). High concentrations of nitrate (0.1 – 1 M NO_3^-) were used in this thesis, so mass transport limited currents were not anticipated to affect the observed current due to high diffusion rates of nitrate from the bulk. Interestingly, we did notice a difference in observed current from low to high mass transport environments, where the difference at low mass transport was attributed to a change

in local concentration of nitrate near the surface of the electrode which was different than the bulk and resulted in currents for reaction at lower nitrate concentrations.

2.4.2 Ultraviolet-visible spectroscopy.

Ultraviolet-Visible (UV-Vis) spectroscopy is a common technique used for determining the concentration of compounds present in liquid solutions. In application, a beam of light with a wavelength in the UV-Vis range (170–1200 nm) is directed onto a sample held in a cuvette and a detector collects the signal as to how much of the light passes through the sample. At specific wavelengths of light, the light will be absorbed by the sample. The difference between the signal with and without a UV-Vis active sample is the sample's absorbance. The absorbance is directly proportional to the concentration of a UV-Vis active species and scales linearly at low concentrations, following Beer's Law (**Equation 2.6**) where A is the absorbance, ε is the molar extinction coefficient, l is the pathlength of the sample (i.e., cuvette width), C is the concentration of the UV-Vis active species, I_0 is the incident light intensity, and I is the light intensity after passing through the sample.[27]

$$A = \varepsilon \mathrm{l} \mathrm{C} = \log\left(\frac{I_0}{I}\right) \tag{2.6}$$

An Evolution 300 Thermo Scientific double-slit UV-Vis spectrophotometer was used for absorbance measurement related to product quantification reported in **Chapters 4** and **5**. Plastic cuvettes were used for nitrite and ammonium absorbance measurements in the visible wavelengths. Only quartz cuvettes were used for nitrate absorbance in the UV wavelengths, as plastic distorts the absorbance at those wavelengths. All cuvettes had a 1 cm path length. The procedures for measuring the absorbance of nitrate, nitrite, and ammonium are detailed below. Nitrite and ammonium are not active species at the UV-Vis wavelengths, therefore colorimetric methods

(where a reagent reacts with the species and the product is observable in the visible range) were used for determining the concertation of those species.[28]

Nitrate (NO_3^-)

For NO_3^-, 10 µL from the aliquot at each time point was diluted to 3 mL with Millipore water then 1 mL of that solution was further diluted to 3 mL. The absorbance was detected at 220 nm and compared to samples of nitric acid at known concentrations that were prepared using the same procedure (**Figure 2.2**).

Nitrite (NO_2^-)

For NO_2^-, a color reagent was prepared by adding 100 mL of 85% H_3PO_4 (85%, ACROS Organics) and 10 g sulfanilamide (≥98%, Fisher Chemical) to 800 mL of distilled water. 1 g N-(1-naphthyl)-ethylenediamine dihydrochloride (≥98%, Sigma Aldrich) was added to the color reagent solution, mixed, and diluted to 1 L. 0.3 mL from aliquots at each time point were adjusted to a pH of 7 using 1 M NaOH and then diluted to 1 mL with Millipore water. 0.04 mL of the prepared color reagent was added to the aliquot dilution, mixed, and left covered for 30 minutes. The absorbance for nitrite was measured at 543 nm and compared to sodium nitrite standards in 0.1 M HNO_3 (**Figure 2.2**). The color reagent is colorless when initially prepared and over time will become pink, when it should be replaced.

Ammonium (NH_4^+)

For NH_4^+ quantification, a 0.25 mL aliquot from each time point was pH adjusted by adding 1 M NaOH solution until pH 12 was reached and diluted to 1 mL using Millipore water. 122 µL of 5 wt% sodium salicylate solution (99.5%, Sigma Life Science), 27.3 µL of 1 wt% sodium nitroprusside dihydrate (≥99%, Sigma-Aldrich), and 40 µL of sodium hypochlorite solution (4–

4.99%, Sigma-Aldrich) were added to the diluted aliquot sequentially, stirred, and left covered for 40 minutes. The NH_4^+ peak appeared around 650 nm and concentrations were determined using a calibration curve prepared from ammonium chloride calibration standards in 0.1 M HNO_3 (**Figure 2.2**).

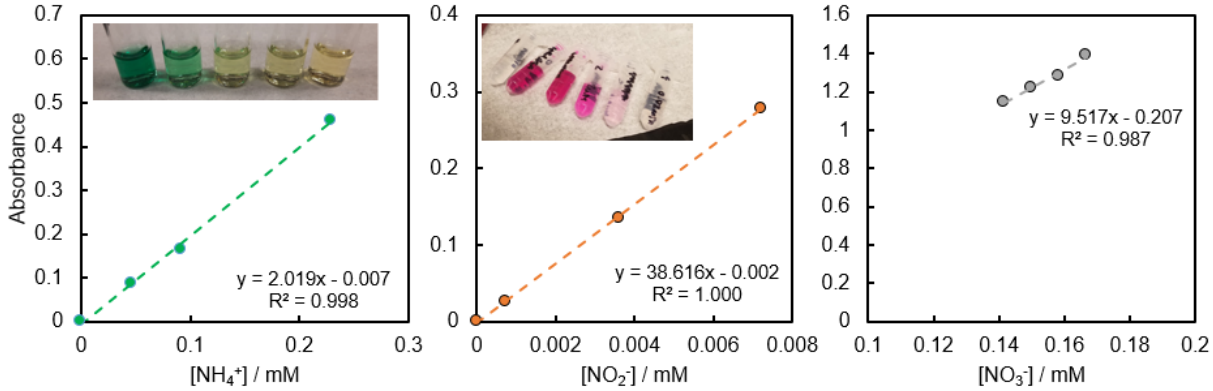

Figure 2.2. UV-Vis absorbance calibration curves prepared for quantifying ammonium, nitrite, and nitrate (left to right). Pictures of calibration samples for ammonium and nitrite after colorimetric reagents are added are shown. The nitrate calibration curve is for a set of standards prepared by diluting 0.1 M HNO_3. The nitrite calibration curve was prepared by diluting $NaNO_2$ (with a background of 0.1 M HNO_3). The ammonium calibration curve was prepared by diluting NH_4Cl (with a background of 0.1 M HNO_3). For NO_2^- and NH_4^+, a baseline measurement of only 0.1 M HNO_3 was subtracted from the absorbance measurements. Concentrations shown reflect the concentration in the cuvette during UV-Vis spectrophotometry.

The faradaic efficiency towards ammonia and nitrite was calculated by comparing the number of moles of product produced multiplied by moles of electrons per mole of product, multiplying by Faraday's constant (96,485 C/mol e^-), and dividing by the total charge passed during the measurement. For these calculations, 8 electrons per 1 ammonia molecule and 2 electrons per 1 nitrite molecule was assumed.

2.5 Reactor Basics and Operation for Electrocatalytic Reactions

For an electrocatalytic reaction, the electrochemical cell (batch/flow cell configuration) is comprised of a working electrode (WE), counter electrode (CE), reference electrode (RE), and a potentiostat. The working electrode contains the material of interest (the electrocatalyst) and performs the reaction of interest (nitrate reduction). The counter electrode is a stable material that

completes the electrochemical circuit, i.e., accepts electrons (e.g. water oxidation to oxygen). In this dissertation, we use Pt as a counter electrode, however, Pt can dissolve and redeposit on the working electrode and so should not be used for non-platinum group metal electrocatalysts. Instead, high surface area graphite can be used. The reference electrode is a stable redox couple that serves to reference the working electrode potential. The reference electrode does not have any current flow through it, to remain unpolarized. The potentiostat allows us to set the potential applied between the WE and the RE by controlling the potential between the WE and CE while measuring the potential between the WE and the RE. The potentiostat measures the current between the WE and CE. The potentiostat also can set the current between the WE and CE and measure the potential between the WE and RE.

2.5.1 Batch reactor.

A batch reactor is a simple environment in which to test an electrocatalyst and is the most common reactor configuration for taking kinetic measurements.[29] For the activity and faradaic efficiency measurements performed in this thesis in a batch cell configuration, a two-compartment electrochemical cell was used (**Figure 2.3**). The two-compartment cell is used to separate the reaction occurring at the WE and the CE. This is necessary for preventing re-oxidation of the nitrate reduction products. The two compartments are separated using a cation-conducting membrane (Nafion 117) to allow ion transfer between the electrodes while preventing product crossover.

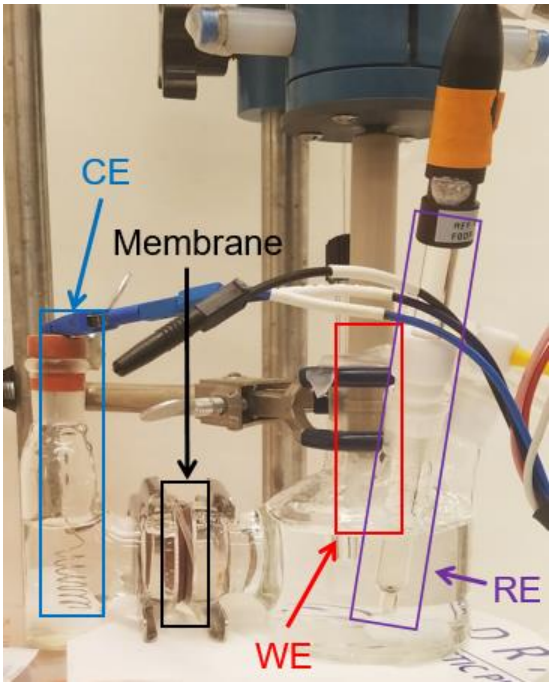

Figure 2.3. A glass two-compartment batch electrochemical cell with a rotating disk working electrode (WE, red) and Ag/AgCl reference electrode (RE, purple) separated by a cation-conducting membrane (black) from a Pt wire counter electrode (CE, blue). A gas sparging/blanket tool and stir bar are also included in the working electrode compartment but are not explicitly labeled.

For electrochemical measurements, the following procedure was generally used. The two compartments of the electrochemical cell were clamped together around a Nafion 117 membrane and two O-rings. The electrolytes for the working and counter electrode compartments were then added. On the WE side, the outlets were sealed with plastic stoppers, a stir bar was added, and a sparging frit was placed in the solution. N_2 was sparged with stirring to remove the dissolved O_2 in the solution. After sufficient N_2 sparging, the N_2 was switched to a blanket stream over the surface of the electrolyte solution and stir bar stirring was stopped. A N_2 blanket is held over the solution for the duration of the experiment to prevent O_2 from re-dissolving in the electrolyte. The prepared WE and RE are then added to the WE compartment, and the CE is added to the other compartment. Wire, rotating disk, and catalysts loaded on carbon felts were used in the batch electrochemical cell.

2.5.2 Flow reactor.

For conversion of more material, a flow reactor is used. For kinetic measurements, a RDE is an ideal system, where mass transport effects on current can be easily eliminated but restricts us to a relatively small electrode surface area and therefore we can only convert small amounts of reactants to our desired products. Practically speaking, in the lab this becomes an issue when the amount we convert is below our detection threshold. Additionally, for scaling up to larger chemical production demands, it is desirable to flow reactants/products to produce more. Previously, all kinetic measurements were taken in either a one- or two-compartment electrochemical cell operating as a batch reactor. In this section, a two-compartment flow cell is used, which we approximate as a plug flow reactor (PFR) or as a packed bed reactor (PBR) in continuous operation. The key differences between the batch system and a PFR/PBR are the concentration profiles with respect to time and the residence time distribution introduced by a flow rate.

The electrochemical flow reactor used has two compartments (working and counter/cathode and anode) and a connection for a RE (WE compartment) as show in **Figure 2.4** and is modified from a previous electrochemical flow cell.[30] The flow cell comprises of two end plates, two PEEK plates with O-rings, two current collectors, two Cu flags to establish connection to the potentiostat from the electrode each compartment, two gaskets with holes for fluid flow, two flow fields, and two gaskets without holes (listed from the outside of the flow cell to the center, the flow cell is symmetric). The compartments were designed for carbon felts as electrodes due to their high surface areas, conductivity, and similarities to a PBR design.[30] In both compartments, there are flow channels to help direct the electrolyte and encourage equal distribution across the compartment. As in the batch reactor, a membrane is necessary to prevent product crossover from

one compartment to another. In a flow reactor, the membrane also provides a physical separation between the WE and CE that prevents short circuiting.

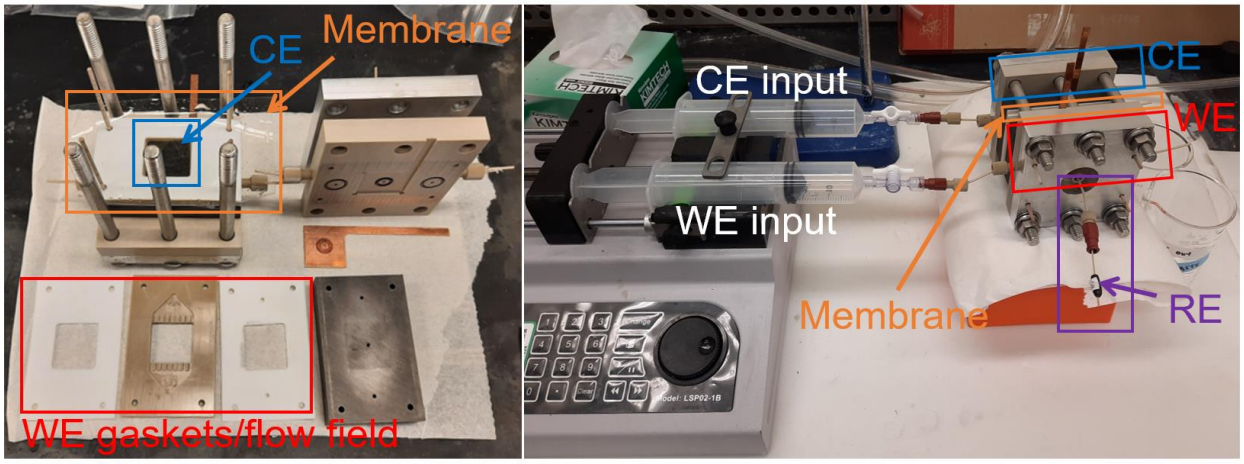

Figure 2.4. Top view (left image) of the partially assembled flow cell with the counter electrode (CE) compartment assembled showing the CE carbon felt (blue box) and the membrane (orange box) laying on top of the CE. The gaskets and flow field for the WE (in the red box) are spread out in the order they would be assembled (from left to right) until the current collector on the right. During operation of the flow cell (right image), the inlets are connected to two syringes (WE and CE input) in a syringe pump. The flow cell is assembled and only the reference electrode (purple) is visible from the outside of the WE compartment of the flow cell.

Major variables to consider for operation of the flow cell reactor in the lab are the electrolyte flow rate, the catalyst loading on the carbon felt, and the total cell voltage. The flow rate is important because if the flow rate is too slow there will be current limitations from mass transport effects but if the flow rate is too fast the reactants may not be able to interact with the catalyst surface before exiting the reactor. The catalyst loading is also important as it will determine the maximum amount of product/current that can be passed. The maximum cell voltage (potential between the WE and CE) that can be applied for a typical potential is ±10 V for potentiostat which requires maintaining a low cell resistance. The resistance of the contacts between the potentiostat and the cell can be lowered by ensuring direct contact of the potentiostat clips to the current collector, ensuring the potentiostat clips are not corroded. The mechanical connection between the working electrode or working electrode and current collector needs to be sufficient to maintain conductivity. The solution resistance and membrane resistance can be kept

low by minimizing the thickness (distance the ions need to travel) and maximizing the cross-sectional area.

The following procedure was used to assemble the flow cell. The working and counter electrodes were prepared as described in **Chapter 2.2.1**. In Millipore water, the WE felt was pressed using the flat edge of a scintillation vial to remove air and increase solution contact with the electrode. The CE felt was rinsed with Millipore water and acetone, alternating for rinsing with each at least three times, then rinsed once more with Millipore water and lastly pressed using a fresh scintillation vial in Millipore water to remove remaining air pockets. The flow cell was assembled as described in the assembly video.[31] A IrO_2 paper was also used as a CE alongside the unmodified carbon felt to lower the overpotential for oxygen evolution (and total cell potential). The carbon felt and IrO_2 paper CE was loaded into the counter electrode compartment and then covered with a Nafion 117 membrane which had been stored in Millipore water for at least 24 hours prior. The working electrode compartment was then constructed similarly using the prepared WE felt. Before tightening the screws on the flow cell, it is helpful to check that the gaskets and current collector on the working electrode side are aligned so the reference electrode can be placed.

For electrochemical measurements, the electrolyte was N_2 sparged, placed into a plastic 60 mL syringe, and degassed by repeatedly pulling a pressure deficit with the plunger and tapping the side of the syringe with a weighted object (the handle of a standard screwdriver was often used). The electrolyte was flowed though the flow cell for twice the residence time prior to electrochemical measurements. From open circuit voltage (~ 700 mV vs. RHE for Pt/C and Rh/C in 0.1 M H_2SO_4), for the first measurement the potentiostat has difficulty applying a potential or performing a cyclic voltammogram. This was attributed to the catalyst being oxidized after preparation (Pt oxide or Rh oxide) and applying a reducing potential resulted in a current which

was too large for the potentiostat controller. Instead, a constant current should be applied first to reduce the catalyst; -50 mA for approximately 3 minutes was applied. For best results for H_{upd} in the flow cell, a flow rate of 0.5 mL/min was used. A scintillation vial was used for collecting the samples at the outlet. Faradaic efficiency for these measurements was calculated based on the charge passed during one residence time interval before the sample was collected.

2.6 References

1. West, A. R. *Solid State Chemistry and Its Applications*. (John Wiley & Sons, Incorporated, 2014).
2. Cullity, B. D. & Stock. Stuart R. *Elements of X-ray Diffraction*. (Prentice Hall, 2001).
3. Williams, D. B. & Carter, C. B. *Transmission Electron Microscopy*. (Springer US, 1996). doi:10.1007/978-1-4757-2519-3.
4. S.Trasatti & Petrii, A. Real Surface Area Measurements in Electrochemistry. *Pure and Applied Chemistry* **63**, 711–734 (1991).
5. Wei, C. *et al.* Approaches for measuring the surface areas of metal oxide electrocatalysts for determining their intrinsic electrocatalytic activity. *Chemical Society Reviews* vol. 48 2518–2534 Preprint at https://doi.org/10.1039/c8cs00848e (2019).
6. Singh, N., Gordon, M., Metiu, H. & McFarland, E. Doped rhodium sulfide and thiospinels hydrogen evolution and oxidation electrocatalysts in strong acid electrolytes. *Journal of Applied Electrochemistry* **46**, 497–503 (2016).
7. Kim, H. & Popov, B. N. Characterization of Hydrous Ruthenium Oxide/Carbon Nanocomposite Supercapacitors Prepared by a Colloidal Method. *Journal of Power Sources* **104**, 52–61 (2002).
8. Jerkiewicz, G. Electrochemical Hydrogen Adsorption and Absorption. Part 1: Under-potential Deposition of Hydrogen. *Electrocatalysis* **1**, 179–199 (2010).
9. Lukaszewski, M., Soszko, M. & Czerwiński, A. Electrochemical methods of real surface area determination of noble metal electrodes - an overview. *International Journal of Electrochemical Science* **11**, 4442–4469 (2016).
10. Biegler, T., Rand, D. A. J. & Woods, R. Limiting oxygen coverage on platinized platinum; Relevance to determination of real platinum area by hydrogen adsorption. *Journal of Electroanalytical Chemistry and Interfacial Electrochemistry* **29**, 269–277 (1971).
11. Gómez, R., Orts, J. M., Álvarez-Ruiz, B. & Feliu, J. M. Effect of temperature on hydrogen adsorption on Pt(111), Pt(110), and Pt(100) electrodes in 0.1 M HClO4. *Journal of Physical Chemistry B* **108**, 228–238 (2004).
12. Climent, V. & Feliu, J. M. Thirty years of platinum single crystal electrochemistry. *Journal of Solid State Electrochemistry* vol. 15 1297–1315 Preprint at https://doi.org/10.1007/s10008-011-1372-1 (2011).
13. Baldauf, M. & Kolb, D. M. A hydrogen adsorption and absorption study with ultrathin Pd overlayers on Au(111) and Au(100). *Electrochimica Acta* **38**, 2145–2153 (1993).

14. Woods, R. *HYDROGEN ADSORPTION ON PLATINUM, IRIDIUM AND RHODIUM ELECTRODES AT REDUCED TEMPERATURES AND THE DETERMI-NATION OF REAL SURFACE AREA. Electroanal ytical Chemistry and liTter facial Electrochemistry* vol. 49 (1974).
15. Baldauf, M. & Kolb, D. M. *A HYDROGEN ADSORPTION AND ABSORPTION STUDY WITH ULTRATHIN Pd OVERLAYERS ON Au(111) AND Au(100)*. vol. 38 (1993).
16. Hubkowska, K., Koss, U., Łukaszewski, M. & Czerwiński, A. Hydrogen electrosorption into Pd-rich Pd-Ru alloys. *Journal of Electroanalytical Chemistry* **704**, 10–18 (2013).
17. Martin, M. H. & Lasia, A. Study of the hydrogen absorption in Pd in alkaline solution. *Electrochimica Acta* **53**, 6317–6322 (2008).
18. Dima, G. E., de Vooys, A. C. A. & Koper, M. T. M. Electrocatalytic reduction of nitrate at low concentration on coinage and transition-metal electrodes in acid solutions. *Journal of Electroanalytical Chemistry* **554–555**, 15–23 (2003).
19. Rhee, C. K., Wasberg, M., Zelenay, P. & Wieckowski, A. Reduction of perchlorate on rhodium and its specificity to surface crystallographic orientation. *Catalysis Letters* **10**, 149–164 (1991).
20. Ahmadi, A., Evans, R. W. & Attard, G. Anion—surface interactions. *Journal of Electroanalytical Chemistry* **350**, 279–295 (1993).
21. Foo, K. Y. & Hammer, B. Insights into the modeling of adsorption isotherm systems. *Chemical Engineering Journal* **156**, 2–10 (2010).
22. Nakata, K. *et al.* Surface-Enhanced Infrared Absorption Spectroscopic Studies of Adsorbed Nitrate, Nitric Oxide, and Related Compounds 2: Nitrate Ion Adsorption at a Platinum Electrode. *Langmuir* **24**, 4358–4363 (2008).
23. Green, C. L. & Kucernak, A. Determination of the platinum and ruthenium surface areas in platinum-ruthenium alloy electrocatalysts by underpotential deposition of Copper. I. Unsupported catalysts. *Journal of Physical Chemistry B* **106**, 1036–1047 (2002).
24. Wang, Z., Young, S. D., Goldsmith, B. R. & Singh, N. Increasing electrocatalytic nitrate reduction activity by controlling adsorption through PtRu alloying. *Journal of Catalysis* **395**, 143–154 (2021).
25. Bard, A. J. & Faulkner, L. R. *Electrochemical methods : fundamentals and applications*.
26. Koutecky-Levich analysis: the principles. *BioLogic Sciences Instruments* (2020).
27. Perkampus, H.-H. *UV-VIS Spectroscopy and Its Applications*. *UV-VIS Spectroscopy and Its Applications* (Springer Berlin Heidelberg, 1992). doi:10.1007/978-3-642-77477-5.
28. Eaton, A., Clesceri, L. & Greenberg, A. (Eds.). *Standard Methods for the Examination of Water and Wastewater*. (APHA, 1995).
29. Moniri, S., van Cleve, T. & Linic, S. Pitfalls and best practices in measurements of the electrochemical surface area of platinum-based nanostructured electro-catalysts. *Journal of Catalysis* **345**, 1–10 (2017).
30. Egbert, J. D. *et al.* Development and Scale-up of Continuous Electrocatalytic Hydrogenation of Functionalized Nitro Arenes, Nitriles, and Unsaturated Aldehydes. *Organic Process Research and Development* **23**, 1803–1812 (2019).
31. Flow Cell Assembly. https://youtube.com/playlist?list=PLhiH6AFhCFtDsiHHcFwmdJ6DK6sqMKyEb (2022).

Chapter 3

Activity and Selectivity Trends in Electrocatalytic Nitrate Reduction on Transition Metals

This chapter was adapted from Liu, J.-X., Richards, D., Singh, N., and Goldsmith, B.R. "Activity and selectivity trends in electrocatalytic nitrate reduction on transition metals." *ACS Catalysis* 9 (2019): 7052-7064. Computational modeling was performed by Dr. Jin-Xun Liu. Experimental measurements for validation of computational results was performed by Danielle Richards (steady-state currents and nitrate adsorption measurements) and Prof. Nirala Singh (X-ray absorption near-edge structure and extended X-ray absorption fine structure).

3.1 Introduction

Nitrate (NO_3^-) pollution of aquatic ecosystems and drinking water disrupts the global nitrogen cycle and poses a threat to human health and the environment.[1–3] Managing the nitrogen cycle has been recognized as a grand challenge by the National Academy of Engineering, and part of reducing the human impact on the nitrogen cycle will require nitrate remediation.[4] To help balance the nitrogen cycle, various physical, biological, and chemical treatments of nitrate have long been studied.[5–7] Compared with these traditional approaches, electrocatalytic nitrate reduction (NO_3RR) is a promising way to remove nitrate using renewable electricity without producing a secondary waste stream.[8] Unlike thermocatalytic nitrate reduction, NO_3RR does not require a supply of H_2 or other reducing agents and instead uses electricity to reduce protons in the aqueous phase to convert nitrate to products such as N_2, NH_3, NO, N_2O, and NH_2OH.[9,10] Among these products, N_2 is considered as the most desirable product because of its benign nature and ease of separation.

The widespread use of NO_3RR is hindered because no sufficiently active, selective, and stable electrocatalyst is known. As a rough estimate, we adopt the target metrics of a commercial proton-exchange membrane electrolyzer to propose that a practical nitrate reduction electrocatalyst must have a turnover frequency (TOF) of >1 s^{-1} at > −0.1 V vs. reversible hydrogen electrode (RHE) over a three-year lifetime (typical proton-exchange membrane lifetime) while selectively producing desired products in alkaline or acidic media. For reference, NO_3RR on Pt and Rh has a measured TOF ≈ 0.1−1 s^{-1} (100 mM $NaNO_3$ in sulfuric acid at 0.1 V vs RHE),[11] without high selectivity toward a desired product.

Multiple experimental studies have probed the mechanism, activity, and selectivity of transition metal electrocatalysts for NO_3RR.[8,11–14] Prior studies indicate that nitrate reduction to nitrite (NO_2^-) is the rate-determining step (RDS) on many transition metal surfaces under acidic conditions.[11,15–17] Platinum group metals (PGMs) were measured to have NO_3RR activities of Rh > Ru > Ir > Pd ≈ Pt in acidic conditions at potentials ranging from 0 to 0.4 V vs RHE.[11] The higher activity of Rh compared with Pt and Pd has been hypothesized to arise from stronger nitrate adsorption on Rh surfaces.[18] Coinage metals are typically less active than PGMs for NO_3RR, with the exception of Cu, and have relative activities of Cu > Ag > Au in the same acidic media and potential range as those reported for PGMs.[11] Some pure transition metals can achieve appreciable activity (e.g., Rh and Cu) but do not simultaneously show high stability, activity, and selectivity for N_2 or NH_3 in acidic or alkaline media, necessitating the synthesis of multicomponent electrocatalysts.[19–24]

Alloying of an active metal catalyst with a second metal is a common approach to tune catalytic performance, whether through ligand,[25–27] ensemble,[28–30] or strain effects.[31] Bimetallics composed of PGMs and promoter metals show superior thermal and electrocatalytic nitrate

reduction activity or selectivity toward N_2 than their pure metal counterparts.[17,32–42] For example, Sn-modified Rh nanoparticles on carbon increased NO_3RR activity by roughly 2-fold relative to Rh/C at ~0.1 V vs RHE.[17] PdCu, PtSn, PtCu, and PtRh show improved performance for NO_3RR over the corresponding pure metals as well.[37,40–42] Non-PGM alloys have also shown enhanced performance relative to their pure metal counterparts, for example, a stable FeCu electrocatalyst had higher activity than Fe and Cu catalysts for NO_3RR.[43]

Bimetallic catalyst design for NO_3RR remains challenging in practice due to the complexity of the nitrate reduction reaction. Multiple questions remain unanswered regarding (i) nitrate reduction electrocatalyst activity and selectivity trends across metals and bimetallics, (ii) the nature and abundance of the surface intermediates, and (iii) whether the RDS changes as a function of applied potential. Mechanistic insight into the activity and selectivity trends of NO_3RR is needed to engender a framework for electrocatalyst design with higher selectivity toward N_2 or NH_3 while maintaining appreciable activity. From a modeling perspective, the existence of linear scaling relations between (i) the adsorption strength of intermediates (adsorbate scaling relations) and (ii) reaction energies and activation energies (Brønsted−Evans−Polanyi (BEP) relations) provides an efficient way to use thermodynamic descriptors to describe the activity of catalysts.[44–46] In particular, DFT modeling is a powerful approach to identify and exploit adsorbate and BEP linear scaling relations to predict the activity and selectivity of electrocatalysts.[47–49] Nevertheless, adsorbate linear scaling and BEP relations for NO_3RR have not yet been identified.

To address these three open questions surrounding NO_3RR, we use DFT modeling to explore trends in electrocatalyst activity and selectivity for nitrate reduction to N_2, NO, N_2O, and NH_3 products over eight transition metal surfaces under acidic conditions, namely, Co, Cu, Rh, Pd, Pt, Ag, Au, and Fe. These eight metals were chosen because of the previous studies of their

activity toward NO_3RR and their large variation in d-band center, which we hypothesized would result in different adsorption strengths of intermediates. We identify adsorbate linear scaling and BEP relations for these transition metals and use this knowledge to conduct DFT-based microkinetic simulations to predict NO_3RR activity and selectivity as a function of applied potential. The coverages and rates predicted from our microkinetic simulations are consistent with our in situ experimental X-ray absorption near-edge structure (XANES) and extended X-ray absorption fine structure (EXAFS) spectroscopy under operating conditions and steady-state NO_3RR activity measurements on Pt and Rh, as well as literature reports of kinetics and vibrational spectroscopy on both pure metals and bimetallics. As a result of the microkinetic simulations, we explain how changes in surface coverage of intermediates with potential impact the overall reaction kinetics and cause a maximum in the NO_3RR activity. We also identify that the activity and selectivity trends across metals can be described by the adsorption strengths of atomic oxygen (O) and nitrogen (N). Using the framework enabled by our adsorbate linear scaling and BEP relations, we predict the activity and selectivity of four additional metals (Ru, Ir, Ni, and Zn) and 30 Fe-, Pt-, Pd-, and Rh-based alloys toward NO_3RR. In particular, Fe_3Ru, Fe_3Ni, Fe_3Cu, and Pt_3Ru are predicted to be promising electrocatalysts for nitrate reduction to N_2 or NH_3 in the potential range of 0−0.2 V.

3.2 Results and Discussion

3.2.1 Direct electrocatalytic nitrate reduction mechanism.

Nitrate reduction can follow two different mechanisms, namely, (i) “direct” or (ii) “indirect” nitrate reduction.[12] Direct nitrate reduction is the dominant mechanism at moderate nitrate concentrations (<1 M) and involves nitrate dissociation and the reaction of adsorbed hydrogen with adsorbed nitrate reduction intermediates. Indirect nitrate reduction only occurs at

high nitrate concentrations (>1 M) in the presence of nitrite, and nitrate itself is not involved in the actual electron transfer.[12,50] Because we are considering nitrate concentrations (1 M) without excess nitrite in the solution in both our experiments and computational modeling, there should be minimal contribution from the indirect mechanism; thus, we focus on the direct nitrate reduction mechanism.

The direct NO_3RR mechanism we consider is outlined in **Scheme 3.1**, based on a proposed mechanism.[24] A variety of products are considered to form via electroreduction of nitrate, namely, N_2, N_2O, NO, and NH_3, based on experimental reports for identified products.[51] NH_2OH formation was omitted to facilitate computational tractability. The first steps in direct nitrate reduction involve adsorption of NO_3^- and hydrogen (from H^+ reduction) from the aqueous phase. N_2 can be produced through dissociation of adsorbed nitrate (NO_3*) to nitrite (NO_2*) and then NO*, followed by association of N* (**Scheme 3.1a**). Alternatively, N_2O* that is generated via NO* disproportionation can dissociate to form N_2. The NO* and N_2O* intermediates may desorb from the surface to produce NO and N_2O byproducts. Also, NH_3 can be formed by sequential hydrogenation of N*. Details about the computed elementary reaction steps, including geometric and energetic information on the intermediates and transition states, are in **Appendix B**. We report all applied potentials with respect to RHE below, unless noted otherwise.

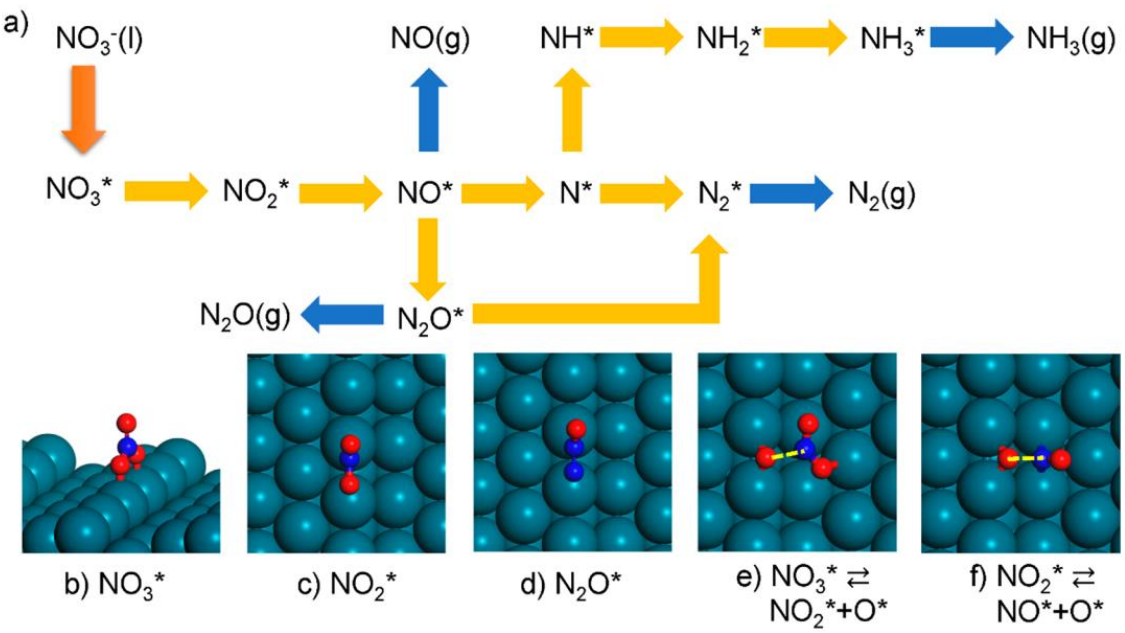

Scheme 3.1. (a) Direct electrocatalytic nitrate reduction mechanism to yield N_2, N_2O, NO, and NH_3 products on transition metals used for our microkinetic model. Protons (H^+) and adsorbed hydrogen are not shown to highlight the N species, but H* serves to form the NH_x* species and convert surface-bound oxygen (O*, also not shown) to water. Hydrogen is assumed to react only at the surface and not through proton-coupled electron transfer. (b–d) Representative configurations (top or side views) of adsorbates NO_3*, NO_2*, and N_2O* on a stepped transition metal surface. (e–f) Representative transition-state configurations for NO_3* and NO_2* dissociation. The dashed yellow line is drawn to signify the bond breaking. * indicates an open active site. The orange, yellow, and blue arrows in (a) denote nitrate adsorption from the aqueous phase, dissociation/formation of intermediates, and desorption of products, respectively. Atom color legend: transition metal = cyan; nitrogen = blue; oxygen = red.

3.2.2 Adsorbate scaling relationships.

Identification of adsorbate linear scaling relationships, coupled with the Sabatier principle,[45,52] provides a simple and fast way to evaluate catalytic activity.[53] Our calculations show that the electronic (ΔE_j) and Gibbs free energies (ΔG_i) of adsorption for NO_3RR intermediates on different metal surfaces linearly scale with the adsorption energy of either an oxygen (ΔE_O) or nitrogen (ΔE_N) atom (**Figure 3.1**). The similar adsorption strength trends of N and O on these metals can be understood by the d-band model, where a higher d-band center with respect to the Fermi level will typically result in stronger adsorption for different adsorbates.[54] Our analysis indicates that the adsorption strength of NO_3RR intermediates scales more accurately (higher coefficient of determination, R^2) with ΔE_O or ΔE_N depending on whether the intermediate adsorbs

to the metal surface through an O or N atom, respectively. This dependence on the adsorbing atom has previously been seen for NH_x, CH_x, and CH_xO_y.[53,55] Specifically, we find that the adsorption strengths of nitrate, nitrite, OH, and H_2O linearly scale with ΔE_O on the stepped surfaces and adsorb through an oxygen atom, whereas H, N_2, N_2O, NO, NH, NH_2, and NH_3 linearly scale with ΔE_N and adsorb through nitrogen. Generally, the atom (N or O) that an intermediate adsorbs through does not change with the metal, despite the large variation (>3 eV) in O or N adsorption strength from Fe to Ag or Au. The adsorbate linear scaling relations all have positive slopes; thus, stronger adsorption of O or N atoms (i.e., more negative ΔE_O or ΔE_N) is accompanied by stronger adsorption of intermediates involved in NO_3RR.

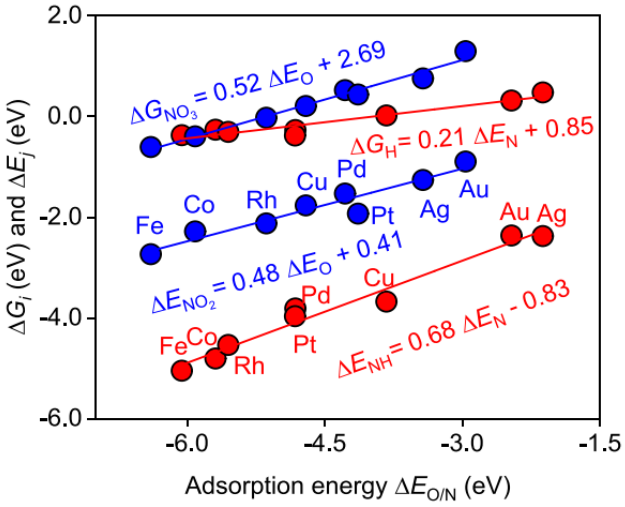

Figure 3.1. Linear adsorbate scaling relationships between the Gibbs free energy of adsorption (ΔG_i , i = NO_3 or H) or electronic adsorption energies (ΔE_j , j = NO_2 or NH) of key intermediates and adsorption energies of either nitrogen (ΔE_N) or oxygen (ΔE_O) atoms. Gibbs free energies of adsorption for ionic reactants (NO_3^- and H^+) are computed at 300 K and 1 M NO_3^- at 0 V vs RHE using a thermodynamic cycle, whereas electronic adsorption energies are computed for the neutral adsorbed intermediates. Color legend: Blue circles show scaling through ΔE_O, and red circles show scaling through ΔE_N.

For the potential-dependent adsorption of NO_3^- and hydrogen from solution, the Gibbs free energy of adsorption of NO_3^- (ΔG_{NO3}) becomes more negative (exothermic) as the potential becomes more positive, whereas hydrogen adsorption (from reduction of H^+) becomes more positive (see **Appendix B**). We find that ΔG_{NO3} linearly correlates with ΔE_O due to NO_3^- preferring

to adsorb through two oxygen atoms to the surface in a chelating O,O-bidentate configuration (**Scheme 3.1b**). This predicted nitrate adsorption mode is corroborated by infrared experiments on polycrystalline Pt.[56] Also, the present DFT calculations predict stronger adsorption of nitrate on Rh than Pt and Pd surfaces at 0 V. Our experimental measurements by cyclic voltammetry in the hydrogen underpotential deposition (H_{upd}) region on polycrystalline Rh and Pt shown in **Figure 3.2** corroborate the stronger binding of nitrate to Rh than Pt, as evidenced by the greater inhibition (site blocking) of hydrogen adsorption on Rh than on Pt at the same nitrate concentrations, indicating higher equilibrium nitrate coverage and stronger nitrate adsorption. These findings are consistent with the previous hypothesis that Rh binds nitrate more strongly than Pt and Pd.[18]

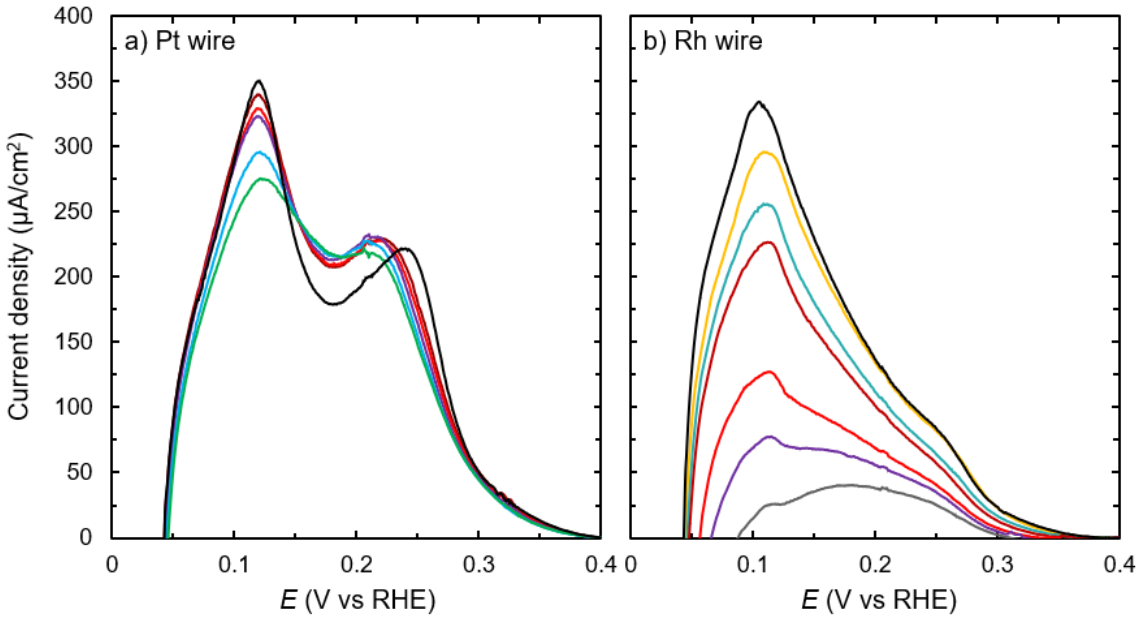

Figure 3.2. Cyclic voltammograms of a) Pt and b) Rh wire in the hydrogen underpotential region at increasing nitrate concentrations in 1 M H_2SO_4. Scan rate was 250 mVs^{-1}. Color legend for $NaNO_3$ concentrations: 0 M (black), 0.001 M (yellow), 0.005 M (teal), 0.01 M (dark red), 0.05 M (light red), 0.1 M (purple), 0.15 M (gray), 0.2 M (light blue), and 0.3 M (green). Measurements with 0.001 M and 0.005 M $NaNO_3$ in 0.1 M H_2SO_4 were taken on the Pt wire but are not included in this figure.

Generally, hydrogen adsorbs stronger than NO_3^- on metals at 0 V, except for Fe and Co. The trends for hydrogen adsorption (ΔG_H) on different transition metal stepped surfaces are in line with previous reported trends on (111) facets.[57] We compute that ΔG_H linearly scales with ΔE_N,

where both N and H atoms usually bind to three metal atoms at the edge of the step site. The adsorption geometries and strengths for the other intermediates are consistent with previous reports.[58–61]

3.2.3 Brønsted-Evans-Polanyi relations for NO_3RR.

We present evidence for the first time that BEP relations between the calculated activation energy (E_a) and reaction energy (ΔE_{rxn}) exist for all the elementary steps involved in direct NO_3RR. BEP relations for NO_3* dissociation, N_2* formation, and NH* formation at 0 V vs RHE are shown in **Figure 3.3**. The BEP relations for all the elementary steps at 0 V vs RHE are given in **Appendix B**. Cu, Ag, and Au do not follow the same BEP relationship for N_2O* dissociation due to the weak physisorption of N_2O on those metals. We observe from the BEP relations that the reaction step with the lowest activation barrier is dependent on the metal. Fe and Co have the lowest barriers for NO_3*, NO_2*, NO*, and N_2O* dissociation steps, whereas Ag or Au have the lowest barrier for N_2* formation via N* atom recombination and hydrogenation of N*, NH*, NH_2*, O*, and OH*. Generally, the barriers on Cu and the platinum group metals (i.e., the more active metals for NO_3RR) lie in between the two extremes.

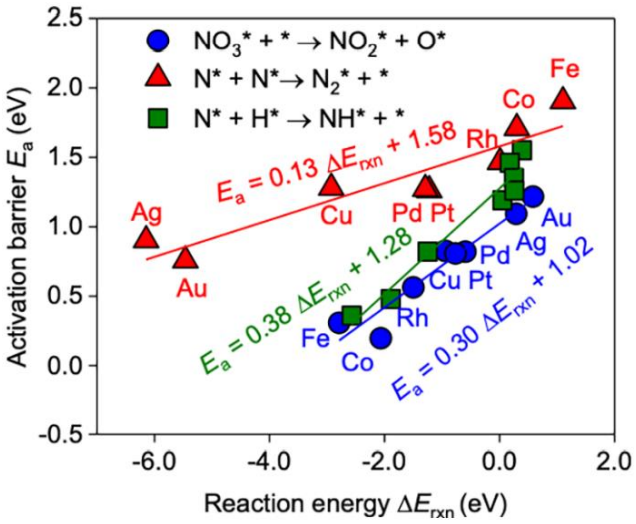

Figure 3.3. Computed Brønsted−Evans−Polanyi relationships for NO_3* dissociation, N_2* formation, and N* hydrogenation at 0 V vs RHE.

For the NO_x* (x = 1, 2, and 3) dissociation steps, E_a generally increases with decreasing x on a specific metal, implying that the final dissociation step has the highest activation energy; nonetheless, as we show below, the first dissociation step of nitrate to nitrite is typically rate-controlling due to the low coverage of nitrate on the surface as a result of both weak binding strength and competitive adsorption with hydrogen. Compared with NO_x* dissociation and N* association, the hydrogenation activation barriers are less sensitive to metal type because the hydrogen adsorption energies at 0 V vs RHE (ΔG_H = −0.38 to 0.48 eV) change less compared to the adsorption energies of atomic oxygen and nitrogen. The metals with stronger adsorption of H* have a lower activation energy for hydrogenation reactions. The forward and backward hydrogenation activation barriers increase or decrease linearly with increasing potential, respectively.

3.2.4 NO_3RR activity over transition metal catalysts.

Combining the adsorbate scaling relations with the BEP relations allows the activation energies for the elementary steps to be rapidly calculated as a function of ΔE_N or ΔE_O. Thus, ΔE_N

and ΔE_O can be used to estimate all activation energies for NO_3RR (given in **Appendix B**), serving as descriptors for NO_3RR performance on metals. To predict the activity of nitrate reduction electrocatalysts at different applied potentials, we computed theoretical volcano plots as a function of ΔE_N or ΔE_O by DFT-based mean-field microkinetic modeling (**Figure 3.4**). The first-principles based mean-field microkinetic modeling approach we apply here uses all computed elementary steps of the reaction pathway and requires no fitting parameters. This approach has been widely used for electrocatalysis studies, for example, CO_2 electrochemical reduction by Nørskov and co-workers[49,62] and Janik and co-workers.[63,64] Importantly, we consider the impact of applied potential on both the thermodynamics and kinetics of each elementary step involving proton and electron transfer.[65,66] This framework enables the construction of potential-dependent volcano plots, thereby allowing us to elucidate the impact of applied (over)potential on NO_3RR activity and selectivity trends. Although mean-field microkinetic modeling using a surface science approach requires calculations of activation energies and reaction energies for all elementary steps, as well as judicious approximations for how to treat the applied potential on the thermodynamics and kinetics, these studies have successfully reproduced experimental findings in electrocatalysis. Similarly, our NO_3RR results presented here qualitatively match previous experimental findings from earlier work and our own experimental work. Using the free energies of transition states (i.e., the energy difference from the abundant surface species to the transition state with the highest free energy) instead of activation energies (i.e., the energy difference between the transition state and a reactive intermediate) is also a powerful approach for facile microkinetic modeling using quasi-equilibrium known from chemical kinetics in experiment,[67,68] but our microkinetic model does not require the quasi-equilibrium assumption to be made for any given elementary step.

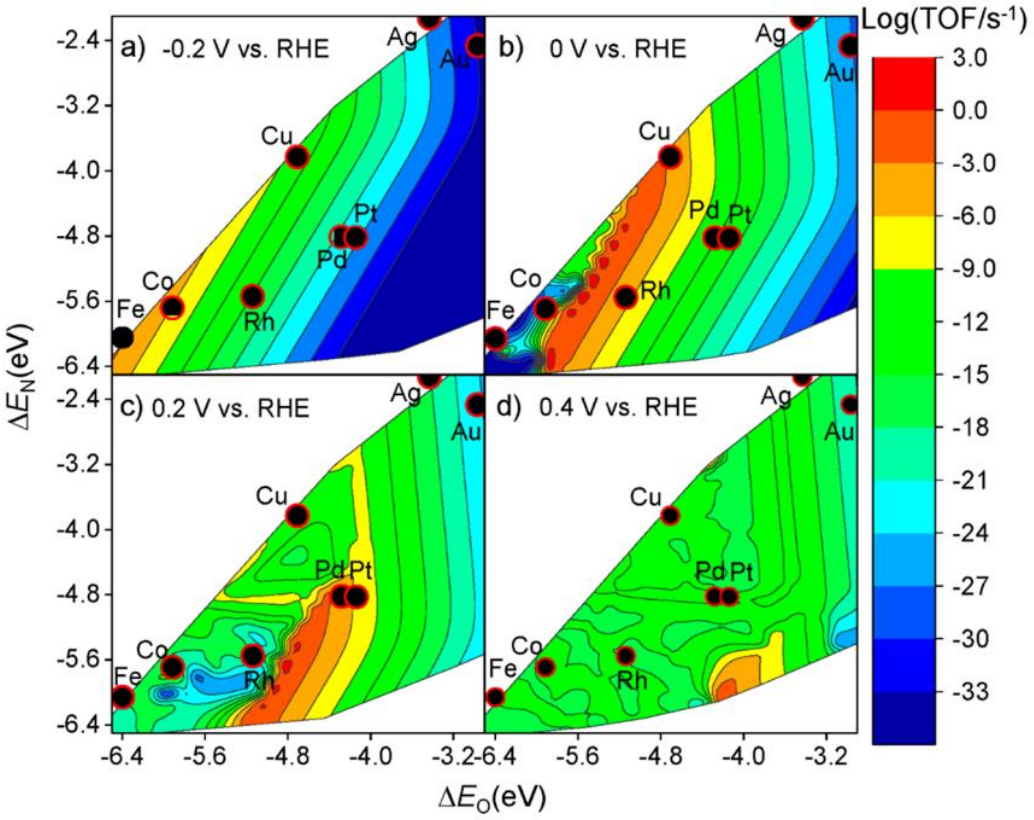

Figure 3.4. Theoretical volcano plots of the TOF as a function of atomic oxygen (ΔE_O) and nitrogen (ΔE_N) adsorption energies for electrocatalytic nitrate reduction on transition metal surfaces based on DFT-based microkinetic simulations at (a) −0.2 V, (b) 0 V, (c) 0.2 V, and (d) 0.4 V vs RHE. Reaction conditions are T = 300 K with a H^+/NO_3^- molar ratio of 1:1. White indicates unphysical regions where the activation energies of some elementary steps are negative. Ag falls within the white region due to errors associated with using linear scaling relationships.

The volcano plots illustrate the dependencies of NO_3RR rate on N and O adsorption strengths at four different potentials, specifically, −0.2, 0, 0.2, and 0.4 V. For our microkinetic simulations, we chose a range of potentials (−0.2 to 0.4 V) to identify the activity and selectivity trends for NO_3RR. The chosen potentials are lower than the standard equilibrium potentials for NO_3RR to gaseous N_2, NO_2, NH_4^+, and NO (ranging from 0.74 to 0.96 V at 25 °C).[6] The calculated turnover frequencies for the eight transition metals are given in **Appendix B**. At 0 V, Cu and Co exhibit the highest NO_3RR rates, followed by Rh, Pd, Ag, and Pt. In contrast, Au has the lowest activity for NO_3RR at 0 V. Importantly, because of the dependence of adsorption of nitrate and hydrogen on potential, the maximum activity for a given catalyst is potential-dependent. The

potential dependence of the rate highlights the deficiencies in directly comparing different catalysts at the same applied potential (experimentally or computationally), without knowledge about how their activity changes with potential. Our potential-dependent volcano plots can be used to more effectively compare relative TOFs between catalysts and identify active catalysts at each potential.

Generally, we find that the activity of a specific catalyst is determined by the adsorption strength of intermediates and the applied potential, which both control the surface coverages of intermediates and reactants. For a given metal, the reaction rate of NO_3RR generally increases to a maximum and decreases rapidly with increasingly positive potential (**Figure 3.4**). The electrocatalyst activity correlates with ΔE_O or ΔE_N at a given potential, but the adsorption energies corresponding to the maximum activity in the volcano plot are different at each potential. At −0.2 V, metals with strong adsorption of N and O have the highest nitrate reduction rate, which originates from the need for stronger adsorption of nitrate, which is competing for sites with adsorbed hydrogen. Although metallic Fe is predicted to have the highest activity for NO_3RR at −0.2 V, Fe will be oxidized under experimental conditions and will be much less active in practice.[69–71] At 0 V, the peak of the volcano moves toward metal surfaces that adsorb both O and N more weakly, and Cu has the highest NO_3RR activity ($\sim$10−3 s^{-1}), followed by Rh (**Figure 3.4b**). At more positive potentials, namely, 0.2 (**Figure 3.4c**) and 0.4 V (**Figure 3.4d**), the maximum TOF shifts to catalysts with weaker O adsorption and stronger N adsorption, and Pt and Pd metals have the highest NO_3RR rate, followed by Rh, Co, Fe, Ag, and Au. Comparing the maximum activities for each metal, Rh has the highest activity for NO_3RR (at 0.1 V), followed by Cu (at 0 V), Pd/Pt, Ag, and Au. This activity ordering is consistent with experimental observations in acidic solution.[11] Generally, the region (i.e., a range of ΔE_O and ΔE_N) containing TOFs greater

than 10−3 s^{-1} increases in size with applied potential from −0.2 to 0 V and then decreases from 0 to 0.4 V. Above 0.4 V, the TOF decreases to ∼10−9 s^{-1} for all eight transition metals considered. To more deeply understand the reason for the potential dependence on NO_3RR activity shown in **Figure 3.4**, we take Pt as an example to compare the DFT calculations with experimental measurements and spectroscopy.

The maximum rates with applied potential on Pt qualitatively agree between the volcano plots and our experimental measurements (**Figure 3.5a**). As the potential is made more negative on Pt, the measured current density increases, reaches a maximum at ∼0.12 V, and then decreases again at , qualitatively consistent with previous experimental reports, although the exact location of the maximum is dependent on nitrate concentration and the supporting acid.[11] The cause of this maximum is hypothesized to be due to changes in the intermediate coverages with potential,[72,73] namely, hydrogen displacing nitrate or its intermediates at more negative potentials.

To probe this phenomenon, we measure in situ XANES and EXAFS of Pt/C under reaction conditions as a function of potential and electrolyte environment. Our in situ XANES measurements of nanoparticulate Pt/C under operating conditions at 0.05 and 0.2 V are shown in parts b and c of **Figure 3.5**, respectively. The XANES shoulder at ∼11565− 11575 eV relative to the bulk Pt foil is due to adsorbed hydrogen.[74–76] The magnitude of this shoulder is qualitatively proportional to the coverage of H on the Pt surface (i.e., when the potential is set to values where H desorbs from the surface, this shoulder decreases). At 0.2 V (**Figure 3.5c**), nitrate addition into the solution decreases the XANES shoulder corresponding to adsorbed hydrogen and increases the white line intensity, which is attributed to oxidized Pt (possibly from adsorbed O or N species).[77] At 0.05 V, however, the addition of nitrate does not impact the XANES. This finding implies that, at more positive potentials (e.g., 0.2 V), nitrate competes with hydrogen for adsorption, whereas

at more negative potentials (e.g., 0.05 V), the surface is covered with hydrogen, even in the presence of nitrate in the bulk solution. The potential dependence of the in situ XANES and EXAFS signals supports the hypothesis that a high coverage of hydrogen suppresses nitrate reduction at potentials more negative than 0.1 V on Pt because adsorbed hydrogen blocks the sites for adsorption of nitrate and reduction intermediates. This phenomenon is corroborated qualitatively by our microkinetic simulations, in which the Pt surface is fully covered by hydrogen at a low potential of −0.2 V, while hydrogen coverage becomes much lower at 0.2 V in the presence of nitrate (**Figure 3.6**). We hypothesize that this observation for Pt can be extended to explain the potential-dependent behavior of all the transition metals studied in this work and reported in the literature, that is, the maximum in activity with potential.

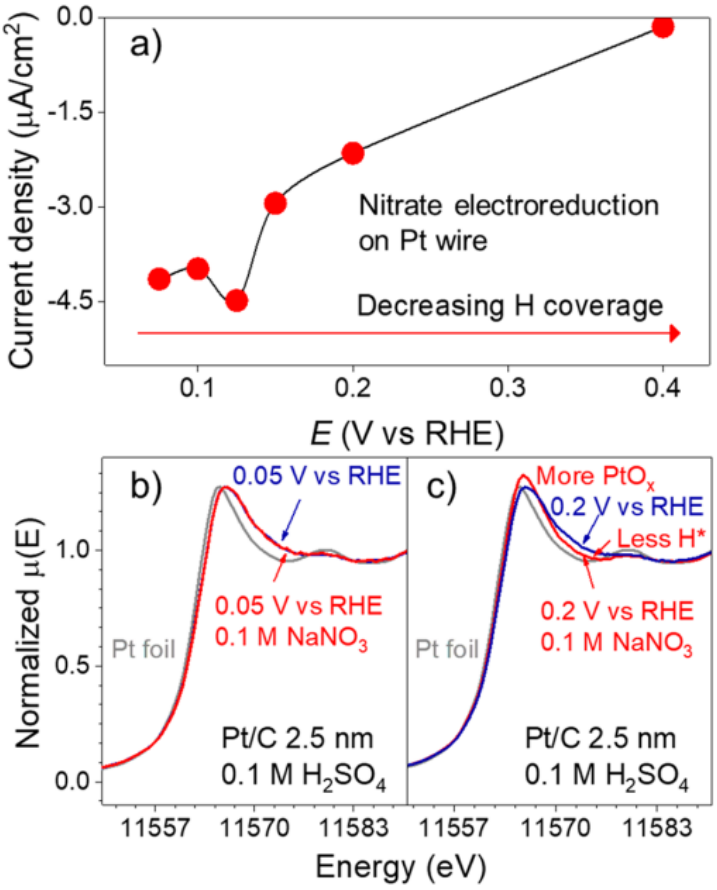

Figure 3.5. (a) Steady-state current density in 1 M H_2SO_4 + 1 M $NaNO_3$ as a function of potential on a Pt wire. Steady-state measurement values are calculated by averaging the current during a constant voltage measurement. Current densities are calculated by normalizing to the Pt surface area determined by H_{upd} in 1 M H_2SO_4 before addition of nitrate. Currents at potentials <0.05 V vs RHE are dominated by the hydrogen evolution reaction and are omitted. In the potential region shown, current densities in the absences of nitrate were negligible. Solution resistance compensation resulted in <1 mV correction. Normalized in situ XANES spectra of Pt L_3 edge of 2.5 nm Pt/C with and without 0.1 M $NaNO_3$, with Pt foil for reference at (b) 0.05 V and (c) 0.2 V vs RHE. The supporting electrolyte for the XANES measurements is 0.1 M H_2SO_4.

To clarify the origin for the activity and selectivity differences of the transition metal catalysts at varying potentials, we analyze the predicted nitrate, hydrogen, and reduction intermediates coverages and degree of rate control (DRC). The coverage distribution for the key intermediates NO_2*, O*, and H* for NO_3RR is shown in **Figure 3.6** at the highest and lowest potential studied. The complete surface coverages are included in the **Appendix B**. The relative activity of metals can be understood by the different coverages of all the intermediates at applied potentials. At −0.2 V, Fe, Co, Rh, Pd, Pt, and Cu surfaces are mostly covered by hydrogen, due to

the stronger driving force for adsorption of hydrogen than nitrate at these potentials. On these metals, both hydrogen evolution and nitrate dissociation control the NO_3RR activity, which is attributed to the high surface coverage of hydrogen and lack of empty sites for nitrate adsorption. Fe is the most active among these metals because it adsorbs nitrate the strongest, although the nitrate coverage is still low. In contrast, at −0.2 V, Ag and Au surfaces have mostly empty sites because of the weak adsorption of all the intermediates in NO_3RR, including hydrogen.

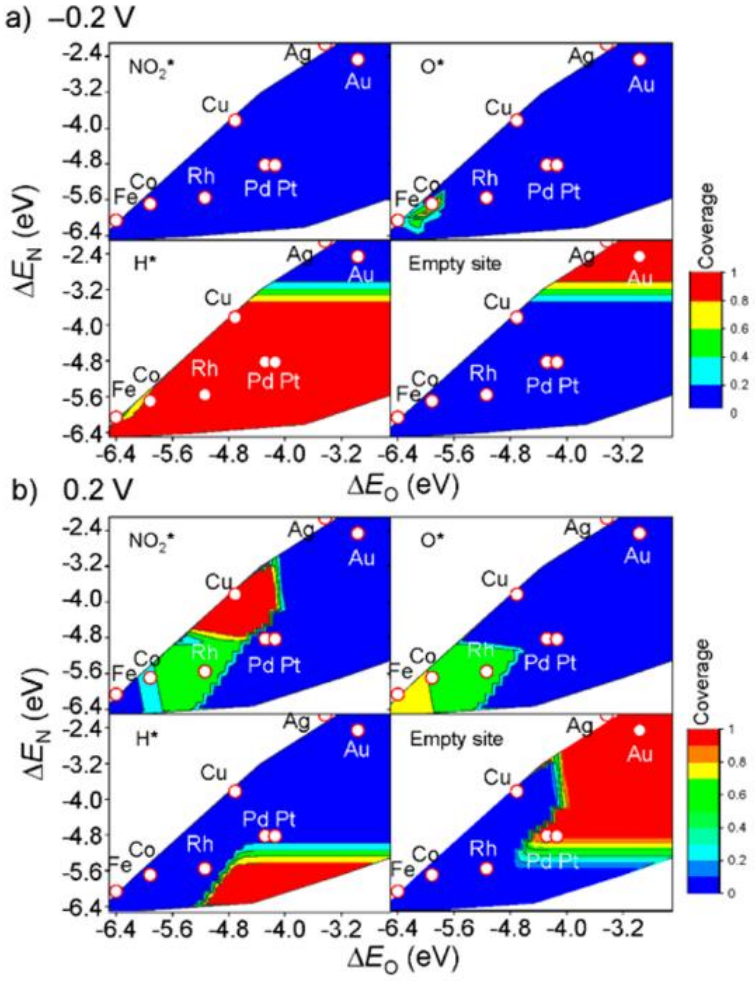

Figure 3.6. Predicted coverage distribution of key intermediates (NO_2*, O*, and H*) for NO_3RR by microkinetic simulations at (a) −0.2 V and (b) 0.2 V vs RHE as a function of nitrogen and oxygen adsorption energy. Blue indicates low coverage, and red indicates high coverage.

As the potential increases from −0.2 to 0.2 V, the region of ΔE_O and ΔE_N for high hydrogen coverage decreases in size, while the region with high NO_2*, NH_x*, and O* coverages increases

in size (**Figure 3.6**). Correspondingly, the region in which nitrate dissociation and hydrogen evolution are rate-controlling decreases with more positive potential, while the region of ΔE_O and ΔE_N where water formation, NO_2* dissociation, NO* adsorption, and N_2* formation are rate-controlling increases. Our microkinetic simulations show that NO_3* dissociation is rate-controlling at low potentials (−0.2 to 0 V) on Pt and Pd, which is corroborated by experiments on Pt that show a nitrate reaction order of indicating that nitrate adsorption precedes the RDS.[51] However, NO* desorption becomes rate-controlling on Pt and Pd at more positive potentials (0.4 V), although the overall rate is much lower at these potentials. The DRC distribution for elementary steps on Rh is similar to that for Pt and Pd except that N_2* formation, rather than NO* desorption, becomes rate-controlling above 0.2 V. The change in RDS with potential on these metals mirrors the change in maximum in activity with potential. Additional details on the DRC analysis are given in **Appendix B**.

The rate-determining step on Fe and Co changes from NO3* dissociation to N_2 formation when the potential increases from −0.2 to 0 V and higher. When the potential increases to 0.2 V on Cu, the RDS switches from NO_3* dissociation to NO_2* dissociation because of the high coverage of NO_2*. NO_3* dissociation is the RDS for Ag and Au regardless of potential due to the weak adsorption and low coverage of nitrate.

3.2.5 NO_3RR selectivity over transition metal catalysts.

The microkinetic simulations involved possible NO_3RR products of NO, N_2O, N_2, and NH_3.[11] Catalyst selectivity toward a specific product is sensitive to the applied potential and the adsorption strengths of O and N atoms. Consequently, quantitative predictions of the product distributions are beyond the accuracy of our first-principles microkinetic model because small changes in the energetics of NO^3RR will result in a dramatic variation of catalytic selectivity.

However, the qualitative trends seen in this work are nevertheless informative. Although quantitatively the predicted selectivities do not match experimental reports, many of the qualitative trends observed in the experiments are explained below.

The applied potential and the adsorption strengths of oxygen and nitrogen have a large impact on catalyst selectivity (**Figure 3.7**). N_2 formation requires strong adsorption of O and N at all potentials (e.g., Fe and Co), whereas selectivity toward NH_3 or NO is obtained by catalysts with moderate adsorption of O and N, such as Rh. Generally, more negative potentials promote NH_3 production, whereas more positive potentials promote N_2 production. Our prediction differs from experimental reports that NH_2OH and NH_3 are formed on Rh,[11] as we neglect NH_2OH formation in the present work. NO is the preferred product on metals that adsorb N weakly (Ag, Au, Pt, and Pd), enabling its rapid desorption. N_2O generation is favorable on Cu due to the lower N_2O* formation barrier compared with the NO* dissociation step.

Among the considered pure metals, Fe is predicted to have the highest selectivity toward N_2 rather than NO because it strongly adsorbs NO* and promotes NO* dissociation to form N* and O*, where the N* atoms can recombine with each other to form N_2*. The maximum NO_3RR activity ($\sim 10{-}3\ s^{-1}$) while simultaneously producing N_2 with high selectivity can be obtained on Fe at −0.2 V. The predicted selectivity of Fe toward N_2 is in line with an experimental report where an Fe catalyst was shown to reach nearly 100% N_2 selectivity but with a prohibitively low NO_3RR rate.[24]

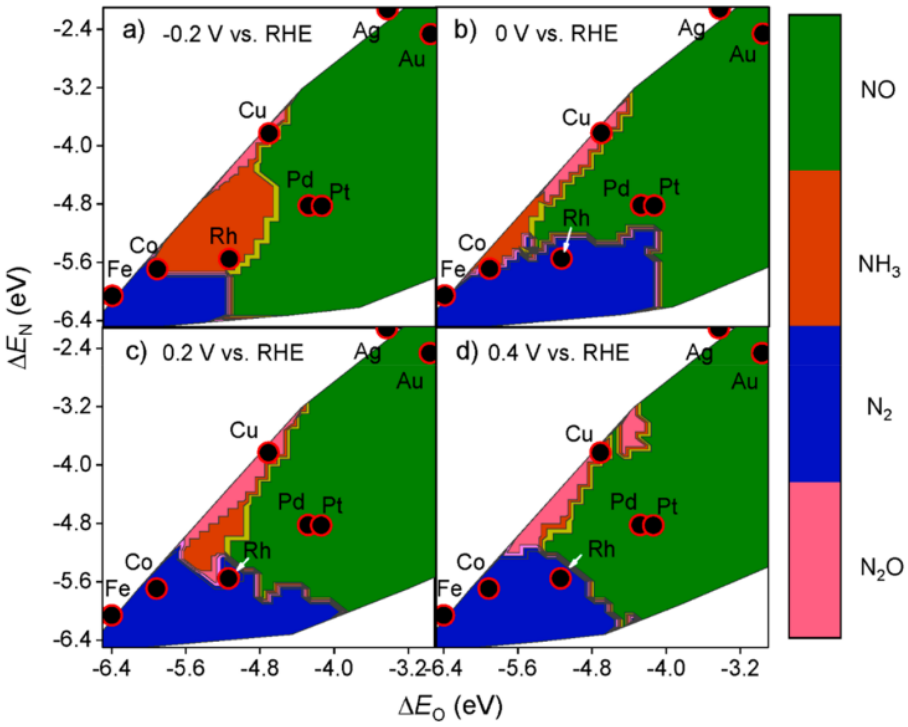

Figure 3.7. Theoretical selectivity maps to NO, N_2O, N_2, or NH_3 products from electrocatalytic nitrate reduction as a function of oxygen and nitrogen adsorption energy at (a) −0.2 V, (b) 0 V, (c) 0.2 V, and (d) 0.4 V vs RHE. Reaction conditions are identical with those of Figure 4. The color bar indicates the major product. Color legend: NO = green; NH_3 = red; N_2 = blue; N_2O = pink.

With increasing potential from −0.2 to 0.4 V, the range of adsorption strengths where N_2 production is favorable increases with a corresponding decrease in the range where NH_3 formation is favorable (**Figure 3.7**). This can be attributed to the decreasing hydrogen adsorption when making the applied potential more positive, leading to low hydrogen coverages and slow NH_x* hydrogenation rates. The moderate activation energies for N* hydrogenation steps and NH_3* adsorption strength give rise to relatively high selectivity for NH_3 synthesis on Co and Rh at negative potential, but with low NO_3RR activity.

Although both Pt and Pd exhibit the highest activity among the platinum group metals for NO formation at 0.2 V, the overall TOF for NO_3RR is still low (<10 s^{-1}). Rh displays the highest activity (TOF = 1−10 s^{-1}) among the eight considered metals at 0.1 V for N_2 formation. Cu produces mainly N_2O regardless of the applied potential. However, N_2O formation is not observed

in the experiment on bulk Cu, which is likely due to the oxidation of Cu in an acidic nitrate solution.[11] Improvements in stabilizing Cu nanoparticles by alloying or adding surface capping ligands[78] could enhance nitrate conversion and N_2O selectivity. Likewise, if metallic Fe can be stabilized under acidic conditions using Fe-based alloys, it may be a promising catalyst for NO_3RR to generate N_2 at slightly negative potentials.

3.2.6 Predicting metal and bimetallic alloy catalysts.

Here we exploit our identified BEP and adsorbate scaling relations in combination with microkinetic modeling to study the NO_3RR activity and selectivity of four additional transition metals (Ru, Ir, Ni, and Zn) and 30 Fe_3M, Pt_3M, Pd_3M, and Rh_3M alloys. These alloys are selected here because the host metals (Fe, Pt, Pd, and Rh) are widely used and often exhibit relatively high selectivity toward N_2 in NO_3RR. The configurations for N and O adsorption on select alloys and their adsorption energies are given in **Appendix B**.

As mentioned, N_2 formation requires strong adsorption of both oxygen and nitrogen. Because Fe binds N and O the strongest of the studied transition metals, we hypothesized that Fe-based alloys, which can be more stable than Fe, can shift the selectivity toward N_2 production in NO_3RR at negative potentials. Among the Fe_3M catalysts, Fe_3Ru has the highest predicted selectivity to N_2 at −0.2 V (**Figure 3.8**). However, the predicted TOFs for Fe_3Ru, Fe_3Ni, and Fe_3Cu are still as low as $\sim 10^{-3}$ s^{-1} at −0.2 V. Likewise, the other Fe_3M alloys are selective for N_2 or NH_3 formation but still have low activity. The NO_3RR rate on Fe_3M alloys can be further maximized for N_2 formation by controlling the potential between −0.2 and 0 V. Compared with pure Pd, alloying Pd by a metal with a higher d-band center will enhance the adsorption strengths of nitrogen and oxygen. As a result, the Pd_3Co, Pd_3Ni, Pd_3Pt, and Pd_3Rh electrocatalysts may exhibit higher activity than Pd for NO formation between 0 and 0.2 V. In contrast, Pd_3Ru is predicted to

have relatively high selectivity for N_2 formation regardless of potential but with low NO_3RR activity.

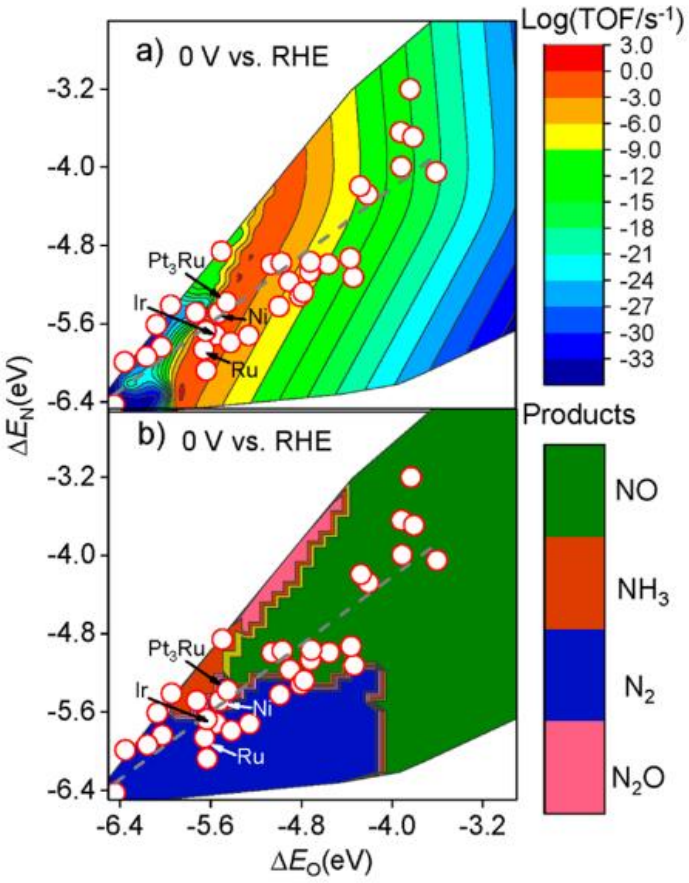

Figure 3.8. Theoretical (a) TOF and (b) selectivity plots of metal and bimetallic alloys catalysts for NO_3RR at 300 K with a H^+/NO_3^- molar ratio of 1:1 at 0 V vs RHE. The solid white circles show the activity and selectivity of the stepped surface of Fe_3M, Pt_3M, Pd_3M, and Rh_3M (M = Ag, Co, Cu, Ni, Pt, Rh, Ru, and Sn) alloys and Ru, Ir, Ni, and Zn metals predicted using adsorbate and BEP linear scaling relations. Only select points are labeled for clarity. The dashed gray line shows the fitted linear relationship between the adsorption energies of N and O with $\Delta E_O = 0.86\Delta E_N - 0.77$.

We predict that Pt_3Ru will have high NO_3RR activity (TOF > 1 s^{-1}) due to the suitable and moderate N and O adsorption, with moderate selectivity toward NH_3/N_2 production. Recently, synthesized Pt_xRu_y (x = 48-100%) alloys confirmed this prediction; $Pt_{78}Ru_{22}$ showed enhanced NO_3RR compared to Pt and other PtRu alloys.[79,80] Pt_3Ni and Rh_3Sn yield NO with higher activity compared with the other Pt_3M and Rh_3M transition metal stepped surfaces at 0.2 V. Also, our computational results for Rh_3Sn corroborate the experimental measurement that a Sn/Rh alloy has

higher nitrate reduction activity than Rh with the products containing NO.[17] Because the adsorption strength of oxygen is correlated with the adsorption strength of nitrogen, the overall catalyst performance on metals and alloys is constrained. This is seen in **Figure 3.8**, where all the alloys roughly fall on a single line in the volcano plots. For single-site catalysts, the adsorbate linear scaling relationships limit the maximum possible activity (i.e., the maximum in the theoretical volcano plot at a given potential often cannot be reached due to the coupled O and N adsorption strengths). One possibility to break these scaling relations and reach the optimum point in the volcano plots is to develop catalysts that have two different active sites, for example, by using single-atom alloys[81–83] with spillover for oxygen and nitrogen adsorption.

3.3 Conclusions

The work herein gives insight into activity and selectivity trends of transition metals for electrocatalytic nitrate reduction to benign or useful chemicals such as N_2 or NH_3. We computationally identified thermodynamic descriptors that correlate with electrocatalyst performance toward nitrate reduction to N_2 or NH_3, namely, the adsorption strengths of nitrogen and oxygen atoms. The rate-determining step and rates for nitrate reduction on transition metals were predicted to be potential-dependent due to large changes in surface coverages of adsorbed species, particularly the influence of adsorbed hydrogen and nitrate. In situ XANES and EXAFS were used to directly probe changes in adsorption with potential on Pt/C in the presence of nitrate and explain the observed reactivity dependence, consistent with previous hypotheses and our microkinetic model predictions. The highest predicted electrocatalytic activities for single metals are on Rh, followed by Cu, Pt, and Pd at positive potentials (0−0.4 V) because of their moderate nitrate and hydrogen adsorption energies. Although Fe is predicted to be the most selective for N_2 production at negative potentials, it is unstable in acids unless cathodically protected. Theoretical

volcano plots and selected maps predict that Fe_3Ru, Fe_3Ni, Fe_3Cu, and Pt_3Ru are potential catalysts for N_2 formation at ≤0 V, which may be stable in acids.

3.4 Computational and Experimental Methods

3.4.1 DFT modeling.

All DFT calculations were performed using projector augmented wave (PAW)[84] potentials and the Perdew−Burke−Ernzerhof (PBE) functional[85] as implemented in the Vienna Ab initio Simulation Package (VASP).[86,87] Magnetic systems (i.e., those containing Fe, Co, and Ni) were treated using spin-polarized DFT. The cutoff energy for the plane wave basis was 400 eV. We used the (211) surface to model the step site for all considered face-centered cubic (FCC) transition metals and the Pt- and Rh-based alloys. Because Fe has a body-centered cubic structure (BCC), the (310) surface was chosen instead to model the step site on Fe and Fe-based alloys. The model structures of FCC(211) and BCC(310) surfaces are shown in **Appendix B**. We chose to model stepped surfaces because step sites are typically more active than flat terraces for NO_3RR[88] due to the presence of coordinatively unsaturated surface atoms and B_5-type step sites, where the adsorbate is surrounded by five surface atoms.[13,89–92] All the DFT calculations were performed on a p(2 × 2) slab model, which is small enough to be computationally tractable, with the surface coverage of all intermediates at 1/4 monolayer as an approximation. The nitrate electroreduction reaction is potential-dependent such that the adsorption free energies of ionic intermediates vary with the potential (within the computational hydrogen electrode model). During our mean-field microkinetic simulations to predict the overall surface coverage and the nitrate electroreduction reaction rate as a function of applied potential, the lateral interactions between the adsorbates were neglected as an approximation by using the calculated energetics (i.e., adsorption energetics, reaction energetics, and activation energies) at 1/4 monolayer coverage of each intermediate. The

surfaces were modeled by a 12-layers thick metal slab. Periodic slab images in the *z*-direction were separated by a vacuum layer of 15 Å to avoid spurious interactions between them. All adsorbates and the six topmost slab layers were relaxed by geometry optimization, with forces converged to <0.02 eV/Å. Monkhorst-Pack k-points sampling[93] of $2 \times 4 \times 1$ were used for all calculations.[38] To search for transition states, the improved force reversed method[92] with a force tolerance of 0.05 eV/Å was used. Some transition states were verified using the climbing-image nudged elastic band method.[95,96] Select transition states were also confirmed by vibrational frequency analysis. The zero-point energy correction for adsorbates was not included.

The impact of applied potential on thermodynamics was treated using the well-known computational hydrogen electrode model.[97,98] The potential dependence on activation energies was incorporated by finding transition states for analogous nonelectrochemical surface reactions and linearly extrapolating to the potential-dependent system (described below).[64] Here, we examined nitrate reduction at 1 M NO_3^- to N_2, N_2O, NO, and NH_3 products via 19 elementary steps over eight stepped metal surfaces.

The surrounding electrolyte was not considered in our modeling studies of reaction intermediates. Because we studied a 19 elementary step mechanism on eight different transition metals, it was prohibitively computationally expensive to consider explicit solvent effects via techniques like ab initio molecular dynamics[99] or using a water bilayer.[100,101] However, we calculated the Gibbs free energy changes for nitrate and hydrogen adsorption in the aqueous phase using thermodynamic cycles because these species are involved in rate-controlling steps and their adsorption is strongly dependent on the applied potential. Details on the thermodynamic cycles used for nitrate and hydrogen adsorption free energies is provided in **Appendix B**. This approximation appears to be reasonable for reproducing trends in our systems, given our

qualitative agreement with activity trends on pure metals from experiment. The usual adsorbate scaling relations found in the gas phase are often applicable at the solid−liquid interface because the adsorption energies are all shifted by a constant value due to solvation of the adsorbates.[102]

3.4.2 Microkinetic simulations.

DFT-based microkinetic modeling of NO_3RR was performed using the identified adsorbate and BEP scaling relations and the MKMCXX software suite,[103–105] allowing us to predict the catalyst TOF, the surface coverage of intermediates, the DRC, and the product selectivity as a function of potential. We used the Gibbs free energies and electronic energies of adsorption to describe the reactants' (NO_3^- and H^+) and products' (NO, N_2, N_2O, and NH_3) adsorption strengths, respectively. The hydrogen evolution reaction (HER) was included in our microkinetic simulations model to clarify the competitive adsorption of H^+ and NO_3^-. The activation energies for each elementary step along the computed reaction pathway were used to obtain the forward and backward rate constants for each elementary step of direct NO_3RR.

In our simulations, the molar ratio of NO_3^- and H^+ in the solution was 1:1 at a reaction temperature of 300 K, which is close to typical experimental reaction conditions. For our microkinetic simulations, we chose a wide range of potentials (−0.2 to 0.4 V) to identify the activity and selectivity trends for NO_3RR. Because of uncertainties in DFT calculations, the applied potentials at which maxima in activity are predicted may be shifted from experiment; thus, examining a wide range of potentials is informative. By solving the coupled differential equations for each elementary reaction step, steady-state coverages were computed by integrating the ordinary differential equations in time until changes in the surface coverages were small ($<10^{-12}$). Rates of the individual elementary steps were obtained based on the computed steady-state surface coverages. The elementary steps that control the rate of the overall reaction were determined using

DRC analysis.[106–108] Further details on the microkinetic modeling procedure are provided in **Appendix B**.

3.4.3 Energetics of potential-dependent reactions.

For reactions involving proton and electron transfer,

$$\mathrm{A} + \mathrm{H}^+ + \mathrm{e}^- \rightarrow \mathrm{AH} \tag{3.1}$$

the reaction free energies were estimated through the computational hydrogen electrode model.[97,98] Specifically, the free energy dependence of the proton−electron pair on the electrode potential was determined using the linear free energy dependence of the electron energy at this potential, which shifts the electron energy by $-eU$,

$$(\mathrm{H}^+) + \mu(\mathrm{e}^-) = \frac{1}{2}\mu(\mathrm{H}_2) - eU \tag{3.2}$$

where e is the elementary positive charge ($1.602176634 \times 10^{-19}$ C) and U is the electrode potential on the RHE scale. The free energy change for a specific electrochemical hydrogenation reaction i as a function of potential, $\Delta G_i(U)$, was computed as

$$\Delta G_i(U) = \Delta G_i + eU \tag{3.3}$$

where ΔG_i is the reaction free energy at 0 V vs RHE and U is the potential. For example, the Gibbs free energy of hydrogen adsorption is

$$\Delta G_{\mathrm{H}}(U) = \Delta G_{\mathrm{H}} + eU = \Delta E_{\mathrm{H}} + 0.24\ \mathrm{eV} + eU \tag{3.4}$$

where ΔE_{H} is the DFT-computed electronic adsorption energy of hydrogen.

For nitrate adsorption from the aqueous phase,

$$\mathrm{NO_3^-}_{(l)} + \mathrm{H}^+ + * \rightarrow \mathrm{NO_3^*} + \mathrm{H}^+ + \mathrm{e}^- \tag{3.5}$$

The Gibbs free energy change is

$$\Delta G_{\mathrm{NO3}}(U) = \Delta G_{\mathrm{NO3}} - eU \tag{3.6}$$

where ΔG_{NO3} is the Gibbs free energy for nitrate adsorption from solution at 0 V vs RHE. From **Equations 3.3−3.6**, the Gibbs free energy of NO_3^- adsorption becomes more negative (i.e., more favorable) as the potential becomes more positive, whereas the Gibbs free energy of hydrogen adsorption becomes more positive (i.e., less favorable). We adjusted the Gibbs free energy of each reaction step containing proton−electron pairs by the applied potential when performing the microkinetic simulations.

For computing potential-dependent kinetics, we following the procedure of Akhade et al.[109] For nonelectrochemical surface hydrogenation,

$$A^* + H^* \rightleftharpoons AH^* + * \tag{3.7}$$

the activation energy (E_a) can be obtained by DFT calculations of the reactant's minimum-energy geometry and the corresponding hydrogenation transition state. For the corresponding electrochemical step, at equilibrium $H^+ + e^- + * \rightleftharpoons H^*$ conditions, the activation energy $E_a(U^0)$ for $A^* + H^+ + e^- \rightleftarrows AH^*$ equals E_a. U^0 is the equilibrium potential at which the analogous nonelectrochemical state, $\mu(H^*)$, is in equilibrium with its equivalent electrochemical state, $\mu(H^+_{(aq)} + e^-)$.[107] Here, U^0 equals the hydrogen adsorption free energy (ΔG_H) for a given surface at 0 V vs RHE. The free energy change for the electrochemical surface hydrogenation can then be computed by $U^0 = [G(AH^*) - G(A^*) - 1/2G(H_2)]/e$. We assume that the forward activation energy at an electrode potential U follows the Butler−Volmer formalism,[110]

$$E_a(U) = E_a(U^0) + \alpha ne(U - U^0) \tag{3.8}$$

where n is the number of electrons transferred. The activation energies for the backward reactions were calculated in a similar way, leading to

$$E_b(U) = E_b(U^0) - \beta ne(U - U^0) \tag{3.9}$$

In the current work, α and β were set to 0.5 for all elementary steps, which has been shown to often be a reasonable approximation.[64,110]

3.4.4 Experimental methods.

The experimental setup used for cyclic voltammograms and steady-state current measurements was a single-compartment, three-electrode glass electrochemical cell and SP-150 potentiostat (Bio-Logic Science Inst.), with measurements taken at room temperature. For all measurements, a coiled Pt wire (99.99%, Pine Research Inst., Inc.) and a single junction Ag/AgCl electrode (4 M KCl, Pine Research Inst., Inc.) were used for the counter electrode and reference electrodes, respectively. All electrode potentials are referenced to RHE; −0.21 V vs Ag/AgCl (4 M KCl), based on calibrating the Ag/AgCl reference electrode against a Pt wire with 1 bar H_2 in the electrolyte. All sulfuric acid electrolyte was prepared by adding concentrated H_2SO_4 (99.999%, Sigma-Aldrich) into deionized water (18.2 MΩ, Millipore Milli-Q system). Before every experiment, ultrapure nitrogen (99.999%, Cryogenic Gases) was bubbled through the electrolyte for 1 h to remove oxygen from the solution. Nitrogen blanketed the solution during the experiments.

Electrocatalyst Preparation

Both the Pt wire (99.997%, Alfa Aesar) and the Rh wire (99.8%, Alfa Aesar) were flame-annealed, soaked in 1 M H_2SO_4 solution, and thoroughly rinsed with deionized water prior to use. The metal electrodes were cycled from metal oxidation to hydrogen evolution 50 times at 100 mV/s before use (Rh: −0.19 to 1.07 V; Pt: −0.19 to 1.27 V).

Hydrogen Underpotential Deposition (H_{upd})

H_{upd} in the hydrogen desorption region was used to estimate the electrochemically active surface area for the Pt and Rh wires.[111] The average charge densities used to calculate areas for polycrystalline Pt and Rh were 210 and 221 $\mu C/cm^2$, respectively. For both metals, a baseline double-layer charging current was measured at 0.4 V and subtracted to determine the H_{upd} charge.

Steady-state Nitrate Reduction Measurements

The electrocatalytic activity of Pt and Rh toward NO_3^- reduction in 1 M H_2SO_4 + 1 M $NaNO_3$ was studied using a Pt wire and a Rh wire. Prior to chronoamperometric measurements, the electrochemically active surface area (ECSA) was estimated from the hydrogen desorption charge using H_{upd} in 1 M H_2SO_4 at 100 mV/s. Twenty mL of 1 M H_2SO_4 electrolyte was removed from the electrochemical cell and supplemented with 20 mL of appropriate concentration $NaNO_3$ in 1 M H_2SO_4. The electrolyte solution was then stirred and sparged with N_2 for at least 30 min. To eliminate mass-transfer effects during reduction, the solution was mixed at 600 rpm (stir bar). The steady-state current at the desired potential was measured for 30 min, and the average of the last 5 min was reported. Electrochemical impedance spectroscopy was performed to correct the applied potential for solution resistance, but measured resistances and currents were very low, so the corrections were <1 mV. All current densities reported are normalized to the ECSA of the Pt or Rh wires determined by H_{upd} in the absence of nitrate. H_2SO_4 was used despite the interference from (bi)sulfate, to avoid potential chloride formation from perchlorate.[112,113]

X-ray Absorption Spectroscopy Measurements

The in situ X-ray absorption spectroscopy measurements were conducted as outlined in a previous study.[114] Briefly, a Pt/C catalyst (5 wt %, Sigma-Aldrich) was loaded onto a carbon felt (Alfa Aesar, 6.35 mm thick) and assembled into a poly(methyl methacrylate) (PMMA) 3D-printed

electrochemical cell as the working electrode with a Ag/AgCl reference electrode (Warner Instruments) and graphite rod counter electrode. XANES and EXAFS measurements were taken under electrolyte flow conditions with the potential controlled using a Gamry potentiostat. The Pt L_3 edge spectra were taken at the Sector 20 bending-magnet beamline of the Advanced Photon Source at Argonne National Laboratory. Prior to measurements, the Pt/C was prereduced electrochemically in sulfuric acid.

3.5 References

1. Gruber, N. & Galloway, J. N. An Earth-system perspective of the global nitrogen cycle. *Nature* **451**, 293–296 (2008).
2. Burow, K. R., Nolan, B. T., Rupert, M. G. & Dubrovsky, N. M. Nitrate in groundwater of the United States, 1991-2003. *Environ Sci Technol* **44**, 4988–4997 (2010).
3. Pennino, M. J., Compton, J. E. & Leibowitz, S. G. Trends in Drinking Water Nitrate Violations Across the United States. *Environ Sci Technol* **51**, 13450–13460 (2017).
4. National Academy of Engineering. *National Academy of Engineering Grand Challenges for Engineers*. (2017).
5. Bockris, J. O. M. & Kim, J. Electrochemical treatment of low-level nuclear wastes. *J Appl Electrochem* **27**, 623–634 (1997).
6. Rosca, V., Duca, M., de Groot, M. T. & Koper, M. T. M. Nitrogen Cycle Electrocatalysis. *Chem Rev* **109**, 2209–2244 (2009).
7. Yang, J., Sebastian, P., Duca, M., Hoogenboom, T. & Koper, M. T. M. pH dependence of the electroreduction of nitrate on Rh and Pt polycrystalline electrodes. *Chem. Commun.* **50**, 2148–2151 (2014).
8. Barrabés, N. & Sá, J. Catalytic nitrate removal from water, past, present and future perspectives. *Appl Catal B* **104**, 1–5 (2011).
9. Xu, D. *et al.* Electrochemical removal of nitrate in industrial wastewater. *Front Environ Sci Eng* **12**, 1–14 (2018).
10. Vorlop, K.-D. & Tacke, T. Erste Schritte auf dem Weg zur edelmetallkatalysierten Nitrat- und Nitrit-Entfernung aus Trinkwasser. *Chemie Ingenieur Technik* **61**, 836–837 (1989).
11. Dima, G. E., de Vooys, A. C. A. & Koper, M. T. M. Electrocatalytic reduction of nitrate at low concentration on coinage and transition-metal electrodes in acid solutions. *Journal of Electroanalytical Chemistry* **554–555**, 15–23 (2003).
12. de Groot, M. T. & Koper, M. T. M. The influence of nitrate concentration and acidity on the electrocatalytic reduction of nitrate on platinum. *Journal of Electroanalytical Chemistry* **562**, 81–94 (2004).
13. Calle-Vallejo, F., Huang, M., Henry, J. B., Koper, M. T. M. & Bandarenka, A. S. Theoretical design and experimental implementation of Ag/Au electrodes for the electrochemical reduction of nitrate. *Physical Chemistry Chemical Physics* **15**, 3196 (2013).

14. G. Casella, I. & Contursi, M. Highly dispersed rhodium particles on multi-walled carbon nanotubes for the electrochemical reduction of nitrate and nitrite ions in acid medium. *Electrochim Acta* **138**, 447–453 (2014).
15. Gootzen, J. F. E., van Hardeveld, R. M., Visscher, W., van Santen, R. A. & van Veen, J. A. R. *The study of NO adsorbate layers on platinized platinum in the liquid phase with cyclic voltammetry, DEMS and FTIRS. Trav. Chim. Pays-Bas* vol. 115 (1996).
16. Shimazu, K. *et al.* Reduction of nitrate ions on tin-modified palladium thin film electrodes. *Journal of Electroanalytical Chemistry* **601**, 161–168 (2007).
17. Siriwatcharapiboon, W. *et al.* Promotion effects of Sn on the electrocatalytic reduction of nitrate at Rh nanoparticles. *ChemElectroChem* **1**, 172–179 (2014).
18. Petrii, O. A. & Safonova, T. Y. Electroreduction of nitrate and nitrite anions on platinum metals : a model process for elucidating the nature of the passivation by hydrogen adsorption *. *Journal of Electroanalytical Chemistry* **331**, 897–912 (1992).
19. Pintar, A., Markošetinc, M. M. & Levec, J. *Hardness and Salt Effects on Catalytic Hydrogenation of Aqueous Nitrate Solutions*. *JOURNAL OF CATALYSIS* vol. 174 (1998).
20. Palomares, A. E., Prato, J. G., Rey, F. & Corma, A. Using the 'memory effect' of hydrotalcites for improving the catalytic reduction of nitrates in water. *J Catal* **221**, 62–66 (2004).
21. D'Arino, M., Pinna, F. & Strukul, G. Nitrate and nitrite hydrogenation with Pd and Pt/SnO2 catalysts: The effect of the support porosity and the role of carbon dioxide in the control of selectivity. *Appl Catal B* **53**, 161–168 (2004).
22. Mikami, I., Yoshinaga, Y. & Okuhara, T. Rapid removal of nitrate in water by hydrogenation to ammonia with Zr-modified porous Ni catalysts. *Appl Catal B* **49**, 173–179 (2004).
23. Shukla, A., Pande, J. v., Bansiwal, A., Osiceanu, P. & Biniwale, R. B. Catalytic Hydrogenation of Aqueous Phase Nitrate over Fe/C Catalysts. *Catal Letters* **131**, 451–457 (2009).
24. Martínez, J., Ortiz, A. & Ortiz, I. State-of-the-art and perspectives of the catalytic and electrocatalytic reduction of aqueous nitrates. *Appl Catal B* **207**, 42–59 (2017).
25. Ponec, V. & Sachtllk, W. M. H. *The Reactions Between Cyclopentane and Deuterium on Nickel and Nickel-Copper Allpys*.
26. Sinfelt, J. H., Carter, J. L. & Yates, D. J. C. *Catalytic Hydrogenolysis and Dehydrogenation over Copper-Nickel Alloys*. *JOURNAL OF CATALYSIS* vol. 24 (1972).
27. Bligaard, T. & Nørskov, J. K. Ligand effects in heterogeneous catalysis and electrochemistry. *Electrochim Acta* **52**, 5512–5516 (2007).
28. Soma-Not0, Y. & Sachtler, W. M. H. *Infrared Spectra of Carbon Monoxide Adsorbed on Supported Palladium and Palladium-Silver Alloys*. *JOURNAL OF CATALYSIS* vol. 32 (1974).
29. Li, H., Shin, K. & Henkelman, G. Effects of ensembles, ligand, and strain on adsorbate binding to alloy surfaces. *Journal of Chemical Physics* **149**, (2018).
30. Sachtler, J. W. A. & Somoriai, G. A. *Influence of Ensemble Size on CO Chemisorption and Catalytic n-Hexane Conversion by Au-Pt(lll) Bimetallic Single-Crystal Surfaces*. *JOURNAL OF CATALYSIS* vol. 81 (1983).
31. Mavrikakis, M., Hammer, B. & Nørskov, J. K. Effect of Strain on the Reactivity of Metal Surfaces. *Phys Rev Lett* **81**, 2819–2822 (1998).

32. Barrabés, N. *et al.* Catalytic reduction of nitrate on Pt-Cu and Pd-Cu on active carbon using continuous reactor: The effect of copper nanoparticles. *Appl Catal B* **62**, 77–85 (2006).
33. Marchesini, F. A., Irusta, S., Querini, C. & Miró, E. Nitrate hydrogenation over Pt,In/Al2O3 and Pt,In/SiO2. Effect of aqueous media and catalyst surface properties upon the catalytic activity. *Catal Commun* **9**, 1021–1026 (2008).
34. Mikami, I., Kitayama, R. & Okuhara, T. Hydrogenations of nitrate and nitrite in water over Pt-promoted Ni catalysts. *Appl Catal A Gen* **297**, 24–30 (2006).
35. Neyertz, C., Marchesini, F. A., Boix, A., Miró, E. & Querini, C. A. Catalytic reduction of nitrate in water: Promoted palladium catalysts supported in resin. *Appl Catal A Gen* **372**, 40–47 (2010).
36. Pintar, A., Batista, J. & Muševič, I. Palladium-copper and palladium-tin catalysts in the liquid phase nitrate hydrogenation in a batch-recycle reactor. *Appl Catal B* **52**, 49–60 (2004).
37. Soares, O. S. G. P., Órfão, J. J. M. & Pereira, M. F. R. Bimetallic catalysts supported on activated carbon for the nitrate reduction in water: Optimization of catalysts composition. *Appl Catal B* **91**, 441–448 (2009).
38. Hamid, S., Kumar, M. A. & Lee, W. Highly reactive and selective Sn-Pd bimetallic catalyst supported by nanocrystalline ZSM-5 for aqueous nitrate reduction. *Appl Catal B* **187**, 37–46 (2016).
39. Restivo, J., Soares, O. S. G. P., Órfão, J. J. M. & Pereira, M. F. R. Bimetallic activated carbon supported catalysts for the hydrogen reduction of bromate in water. *Catal Today* **249**, 213–219 (2015).
40. Anastasopoulos, A., Hannah, L. & Hayden, B. E. High throughput optimisation of PdCu alloy electrocatalysts for the reduction of nitrate ions. *J Catal* **305**, 27–35 (2013).
41. Yang, J., Kwon, Y., Duca, M. & Koper, M. T. M. Combining voltammetry and ion chromatography: Application to the selective reduction of nitrate on Pt and PtSn electrodes. *Anal Chem* **85**, 7645–7649 (2013).
42. Duca, M., Sacré, N., Wang, A., Garbarino, S. & Guay, D. Enhanced electrocatalytic nitrate reduction by preferentially-oriented (100) PtRh and PtIr alloys: the hidden treasures of the 'miscibility gap'. *Appl Catal B* **221**, 86–96 (2018).
43. Zhang, Y. *et al.* Fe/Cu Composite Electrode Prepared by Electrodeposition and Its Excellent Behavior in Nitrate Electrochemical Removal. *J Electrochem Soc* **165**, E420–E428 (2018).
44. Dahl, S., Logadottir, A., Jacobsen, C. J. H. & Nørskov, J. K. *Electronic factors in catalysis: the volcano curve and the effect of promotion in catalytic ammonia synthesis*. *Applied Catalysis A: General* vol. 222 (2001).
45. Nørskov, J. K., Bligaard, T., Rossmeisl, J. & Christensen, C. H. Towards the computational design of solid catalysts. *Nature Chemistry* vol. 1 37–46 Preprint at https://doi.org/10.1038/nchem.121 (2009).
46. Yuan, H., Chen, J., Wang, H. & Hu, P. Activity Trend for Low-Concentration NO Oxidation at Room Temperature on Rutile-Type Metal Oxides. *ACS Catal* **8**, 10864–10870 (2018).
47. Wang, D., Jiang, J., Wang, H. F. & Hu, P. Revealing the Volcano-Shaped Activity Trend of Triiodide Reduction Reaction: A DFT Study Coupled with Microkinetic Analysis. *ACS Catal* **6**, 733–740 (2016).

48. Seh, Z. W. *et al.* Combining theory and experiment in electrocatalysis: Insights into materials design. *Science (1979)* **355**, (2017).
49. Liu, X. *et al.* Understanding trends in electrochemical carbon dioxide reduction rates. *Nat Commun* **8**, (2017).
50. Garcia-Segura, S., Lanzarini-Lopes, M., Hristovski, K. & Westerhoff, P. Electrocatalytic reduction of nitrate: Fundamentals to full-scale water treatment applications. *Appl Catal B* **236**, 546–568 (2018).
51. Duca, M. & Koper, M. T. M. Powering denitrification: the perspectives of electrocatalytic nitrate reduction. *Energy Environ Sci* **5**, 9726–9742 (2012).
52. Calle-Vallejo, F., Martínez, J. I., García-Lastra, J. M., Rossmeisl, J. & Koper, M. T. M. Physical and chemical nature of the scaling relations between adsorption energies of atoms on metal surfaces. *Phys Rev Lett* **108**, (2012).
53. Calle-Vallejo, F., Loffreda, D., Koper, M. T. M. & Sautet, P. Introducing structural sensitivity into adsorption-energy scaling relations by means of coordination numbers. *Nat Chem* **7**, 403–410 (2015).
54. Hammer, B. & Nørskov, J. K. Theoretical surface science and catalysis—calculations and concepts. *Advances in Catalysis* **45**, 71–129 (2000).
55. Abild-Pedersen, F. *et al.* Scaling properties of adsorption energies for hydrogen-containing molecules on transition-metal surfaces. *Phys Rev Lett* **99**, (2007).
56. Nakata, K. *et al.* Surface-Enhanced Infrared Absorption Spectroscopic Studies of Adsorbed Nitrate, Nitric Oxide, and Related Compounds 2: Nitrate Ion Adsorption at a Platinum Electrode. *Langmuir* **24**, 4358–4363 (2008).
57. Nørskov, J. K. *et al.* Trends in the Exchange Current for Hydrogen Evolution. *J Electrochem Soc* **152**, J23 (2005).
58. Lu, X., Xu, X., Wang, N. & Zhang, Q. Bonding of NO2 to the Au atom and Au(111) surface: A quantum chemical study. *Journal of Physical Chemistry A* **103**, 10969–10974 (1999).
59. Getman, R. B. & Schneider, W. F. DFT-based characterization of the multiple adsorption modes of nitrogen oxides on Pt(111). *Journal of Physical Chemistry C* **111**, 389–397 (2007).
60. Sebastiani, D. & Delle Site, L. Adsorption of water molecules on flat and stepped nickel surfaces from first principles. *J Chem Theory Comput* **1**, 78–82 (2005).
61. Kolb, M. J., Calle-Vallejo, F., Juurlink, L. B. F. & Koper, M. T. M. Density functional theory study of adsorption of H2O, H, O, and OH on stepped platinum surfaces. *Journal of Chemical Physics* **140**, (2014).
62. Hansen, H. A., Varley, J. B., Peterson, A. A. & Nørskov, J. K. Understanding trends in the electrocatalytic activity of metals and enzymes for CO2 reduction to CO. *Journal of Physical Chemistry Letters* **4**, 388–392 (2013).
63. Nie, X., Esopi, M. R., Janik, M. J. & Asthagiri, A. Selectivity of CO2 reduction on copper electrodes: The role of the kinetics of elementary steps. *Angewandte Chemie - International Edition* **52**, 2459–2462 (2013).
64. Nie, X., Luo, W., Janik, M. J. & Asthagiri, A. Reaction mechanisms of CO2 electrochemical reduction on Cu(1 1 1) determined with density functional theory. *J Catal* **312**, 108–122 (2014).

65. Exner, K. S. Is Thermodynamics a Good Descriptor for the Activity? Re-Investigation of Sabatier's Principle by the Free Energy Diagram in Electrocatalysis. *ACS Catal* 5320–5329 (2019) doi:10.1021/acscatal.9b00732.
66. Exner, K. S. Beyond the Traditional Volcano Concept: Overpotential-Dependent Volcano Plots Exemplified by the Chlorine Evolution Reaction over Transition-Metal Oxides. *Journal of Physical Chemistry C* **123**, 16921–16928 (2019).
67. Bockris, J. O. M. & Reddy, A. K. N. *Modern electrochemistry.* vol. 1 (Plenum Publishers, 2000).
68. Exner, K. S., Sohrabnejad-Eskan, I. & Over, H. A Universal Approach to Determine the Free Energy Diagram of an Electrocatalytic Reaction. *ACS Catal* **8**, 1864–1879 (2018).
69. Huang, C.-P., Wang, H.-W. & Chiu, P.-C. Nitrate reduction by metallic iron. *Water Res* **32**, 2257–2264 (1998).
70. Sohn, K., Kang, S. W., Ahn, S., Woo, M. & Yang, S. K. Fe(0) nanoparticles for nitrate reduction: Stability, reactivity, and transformation. *Environ Sci Technol* **40**, 5514–5519 (2006).
71. Suzuki, T., Moribe, M., Oyama, Y. & Niinae, M. Mechanism of nitrate reduction by zero-valent iron: Equilibrium and kinetics studies. *Chemical Engineering Journal* **183**, 271–277 (2012).
72. Gootzen, J. F. E. *et al.* The electrocatalytic reduction of NO-3 on Pt, Pd and Pt + Pd electrodes activated with Ge. *Journal of Electroanalytical Chemistry* **434**, 171–183 (1997).
73. Dima, G. E., Beltramo, G. L. & Koper, M. T. M. Nitrate reduction on single-crystal platinum electrodes. *Electrochim Acta* **50**, 4318–4326 (2005).
74. Teliska, M., O'Grady, W. E. & Ramaker, D. E. Determination of H adsorption sites on Pt/C electrodes in HClO4 from Pt L23 X-ray absorption spectroscopy. *Journal of Physical Chemistry B* **108**, 2333–2344 (2004).
75. Reifsnyder, S. N., Otten, M. M., Sayers, D. E. & Lamb, H. H. Hydrogen Chemisorption on Silica-Supported Pt Clusters: *In Situ* X-ray Absorption Spectroscopy. *J Phys Chem B* **101**, 4972–4977 (1997).
76. Sugino, R. *et al. Hydrogen Electrocatalysis by Carbon Supported Pt and Pt Alloys An In Situ X-Ray Absorption Study. 10. Y. Kobayashi and K. Sugii, ibid* vol. 143 (1996).
77. Teliska, M., O'Grady, W. E. & Ramaker, D. E. Determination of O and OH adsorption sites and coverage in situ on Pt electrodes from Pt L 23 X-ray absorption spectroscopy. *Journal of Physical Chemistry B* **109**, 8076–8084 (2005).
78. LEÓN, Y., BRITO, I., CÁRDENAS, G. & GODOY, O. SYNTHESIS AND CHARACTERIZATIONS OF Ag, Cu AND AgCu METALLIC NANOPARTICLES STABILIZED BY DIVALENT SULFUR LIGANDS. *Journal of the Chilean Chemical Society* **54**, (2009).
79. Wang, Z., Young, S. D., Goldsmith, B. R. & Singh, N. Increasing electrocatalytic nitrate reduction activity by controlling adsorption through PtRu alloying. *J Catal* **395**, 143–154 (2021).
80. Wang, Z., Ortiz, E. M., Goldsmith, B. R. & Singh, N. Comparing electrocatalytic and thermocatalytic conversion of nitrate on platinum–ruthenium alloys. *Catal Sci Technol* **11**, 7098–7109 (2021).
81. Marcinkowski, M. D. *et al.* Pt/Cu single-atom alloys as coke-resistant catalysts for efficient C-H activation. *Nat Chem* **10**, 325–332 (2018).

82. Greiner, M. T. *et al.* Free-atom-like d states in single-atom alloy catalysts. *Nat Chem* **10**, 1008–1015 (2018).
83. Darby, M. T., Stamatakis, M., Michaelides, A. & Sykes, E. C. H. Lonely Atoms with Special Gifts: Breaking Linear Scaling Relationships in Heterogeneous Catalysis with Single-Atom Alloys. *Journal of Physical Chemistry Letters* vol. 9 5636–5646 Preprint at https://doi.org/10.1021/acs.jpclett.8b01888 (2018).
84. Blöchl, P. E. Projector augmented-wave method. *Phys Rev B* **50**, 17953–17979 (1994).
85. Perdew, J. P., Burke, K. & Ernzerhof, M. Generalized Gradient Approximation Made Simple. *Phys Rev Lett* **77**, 3865–3868 (1996).
86. Kresse, G. & Hafner, J. *Ab initio* molecular dynamics for liquid metals. *Phys Rev B* **47**, 558–561 (1993).
87. Kresse, G. & Furthmüller, J. Efficient iterative schemes for *ab initio* total-energy calculations using a plane-wave basis set. *Phys Rev B* **54**, 11169–11186 (1996).
88. Taguchi, S. & Feliu, J. M. Electrochemical reduction of nitrate on Pt(S)[n(1 1 1) × (1 1 1)] electrodes in perchloric acid solution. *Electrochim Acta* **52**, 6023–6033 (2007).
89. Boudart, M. Catalysis by Supported Metals. *Advances in Catalysis* **20**, 153–166 (1969).
90. Hammer, B., Nielsen, O. H. & Nørskov, J. K. Structure sensitivity in adsorption: CO interaction with stepped and reconstructed Pt surfaces. *Catal Letters* **46**, 31–35 (1997).
91. Nørskov, J. K. *et al.* The nature of the active site in heterogeneous metal catalysis. *Chem Soc Rev* **37**, 2163–2171 (2008).
92. Somorjai, G. A. & Li, Y. Impact of surface chemistry. *Proc Natl Acad Sci U S A* **108**, 917–924 (2011).
93. Monkhorst, H. J. & Pack, J. D. Special points for Brillouin-zone integrations. *Phys Rev B* **13**, 5188–5192 (1976).
94. Sun, K., Zhao, Y., Su, H. Y. & Li, W. X. Force reversed method for locating transition states. *Theor Chem Acc* **131**, 1–10 (2012).
95. Henkelman, G. & Jónsson, H. Improved tangent estimate in the nudged elastic band method for finding minimum energy paths and saddle points. *Journal of Chemical Physics* **113**, 9978–9985 (2000).
96. Henkelman, G., Uberuaga, B. P. & Jónsson, H. Climbing image nudged elastic band method for finding saddle points and minimum energy paths. *Journal of Chemical Physics* **113**, 9901–9904 (2000).
97. Karlberg, G. S. *et al.* Cyclic voltammograms for H on Pt(111) and Pt(100) from first principles. *Phys Rev Lett* **99**, (2007).
98. Nørskov, J. K. *et al.* Origin of the overpotential for oxygen reduction at a fuel-cell cathode. *Journal of Physical Chemistry B* **108**, 17886–17892 (2004).
99. Herron, J. A., Morikawa, Y. & Mavrikakis, M. Ab initio molecular dynamics of solvation effects on reactivity at electrified interfaces. *Proceedings of the National Academy of Sciences* **113**, 4937–4945 (2016).
100. Hamada, I. & Morikawa, Y. Density-functional analysis of hydrogen on Pt(111): Electric field, solvent, and coverage effects. *Journal of Physical Chemistry C* **112**, 10889–10898 (2008).
101. Sha, Y., Yu, T. H., Liu, Y., Merinov, B. v. & Goddard, W. A. Theoretical study of solvent effects on the platinum-catalyzed oxygen reduction reaction. *Journal of Physical Chemistry Letters* **1**, 856–861 (2010).

102. Nørskov, J. K., Studt, F., Abild-Pedersen, F. & Bligaard, T. *Fundamental Concepts in Heterogeneous Catalysis*. (John Wiley & Sons, Inc., 2014).
103. Filot, I. A. W., van Santen, R. A. & Hensen, E. J. M. The Optimally Performing Fischer-Tropsch Catalyst. *Angewandte Chemie* **126**, 12960–12964 (2014).
104. Filot, I. A. W. *et al.* First-Principles-Based Microkinetics Simulations of Synthesis Gas Conversion on a Stepped Rhodium Surface. *ACS Catal* **5**, 5453–5467 (2015).
105. https://www.mkmcxx.nl/ . (2018).
106. Campbell, C. T. *Micro-and macro-kinetics: their relationship in heterogeneous catalysis*. *Topics in Catalysis I* (1994).
107. Campbell, C. T. Finding the rate-determining step in a mechanism: Comparing DeDonder relations with the 'Degree of Rate Control'. *Journal of Catalysis* vol. 204 520–524 Preprint at https://doi.org/10.1006/jcat.2001.3396 (2001).
108. Stegelmann, C., Andreasen, A. & Campbell, C. T. Degree of rate control: How much the energies of intermediates and transition states control rates. *J Am Chem Soc* **131**, 8077–8082 (2009).
109. Akhade, S. A., Bernstein, N. J., Esopi, M. R., Regula, M. J. & Janik, M. J. A simple method to approximate electrode potential-dependent activation energies using density functional theory. *Catal Today* **288**, 63–73 (2017).
110. Rostamikia, G., Mendoza, A. J., Hickner, M. A. & Janik, M. J. First-principles based microkinetic modeling of borohydride oxidation on a Au(1 1 1) electrode. *J Power Sources* **196**, 9228–9237 (2011).
111. Lukaszewski, M., Soszko, M. & Czerwiński, A. Electrochemical methods of real surface area determination of noble metal electrodes - an overview. *Int J Electrochem Sci* **11**, 4442–4469 (2016).
112. Ahmadi, A., Evans, R. W. & Attard, G. Anion—surface interactions. *Journal of Electroanalytical Chemistry* **350**, 279–295 (1993).
113. Rhee, C. K., Wasberg, M., Zelenay, P. & Wieckowski, A. Reduction of perchlorate on rhodium and its specificity to surface crystallographic orientation. *Catal Letters* **10**, 149–164 (1991).
114. Singh, N. *et al.* Carbon-supported Pt during aqueous phenol hydrogenation with and without applied electrical potential: X-ray absorption and theoretical studies of structure and adsorbates. *J Catal* **368**, 8–19 (2018).

Chapter 4

Electrocatalytic Nitrate Reduction on Rhodium Sulfide Compared to Pt and Rh in the Presence of Chloride

This chapter was adapted from Richards, D., Young, S. D., Goldsmith, B. R., and Singh, N. "Electrocatalytic nitrate reduction on rhodium sulfide compared to Pt and Rh in the presence of chloride." *Catalysis Science & Technology* 11 (2021): 7331-7346. Experimental measurements and microkinetic modeling were performed by Danielle Richards. Computational work was performed by Samuel D. Young.

4.1 Introduction

Nitrate (NO_3^-) contamination of lakes, rivers, and ground water from agricultural, livestock, and industrial activities is a major threat to human (e.g., congenital disease, cancer) and ecosystem health.[1–5] The electrocatalytic nitrate reduction reaction (NO_3RR) is a promising approach to remediate nitrate by converting nitrate to products such as N_2 or NH_3 with a corresponding oxidation reaction such as oxygen or chlorine evolution.[3,6–14] However, NO_3RR rates are hindered by the chloride present in many nitrate-laden waste streams. Streams containing both nitrate and chloride can arise from industrial effluent[15–17] and the brine that comes from using ion exchange to separate nitrate contaminated water into clean water and concentrated nitrate.[18,19] In addition to chloride inhibiting the rates, Cl_2/Cl_3^- produced at the anode can cross over and corrode the NO_3RR electrocatalyst,[20,21] which is particularly an issue for metal nanoparticle catalysts that are typically used to obtain high active surface areas.[22] Understanding the effect of chloride on NO_3RR and developing chloride-resistant nitrate reduction catalysts are both needed

to create an effective electrocatalytic process that can remediate waste streams containing both nitrate and chloride. In this work, we demonstrate that rhodium sulfide on carbon (Rh_xS_y/C) is more active for NO_3RR than Pt/C and Rh/C in both the presence and absence of chloride. We also explain the rate-determining step (RDS) of NO_3RR on Pt, Rh, and Rh_xS_y and the chloride poisoning mechanism.

Catalytic inhibition of NO_3RR by chloride has been reported for Pt, Rh, Fe, and Cu electrodes,[23–26] for which the reduction current is hypothesized to be suppressed by strong chloride adsorption on metals.[26–29] NO_3RR occurs at potentials where both nitrate and hydrogen can adsorb (**Scheme 4.1**); for Pt and Rh this potential is between 0–0.3 V vs. RHE.[3,30] Nitrate coverages are related to the free energy of nitrate adsorption (ΔG_{NO_3}) on a catalyst surface. Nitrate adsorption is favorable at potentials more positive than $\Delta G_{NO_3}(E = 0 \text{ V vs. SHE})/F$, where F is Faraday's constant. Hydrogen adsorption is favorable at potentials more negative than $\Delta G_H/F$, where ΔG_H is the hydrogen adsorption free energy at 0 V vs. RHE. Therefore, hydrogen covers the catalyst surface at negative potentials (**Scheme 4.1a**). Chloride adsorption is also potential-dependent, and chloride will adsorb at potentials more positive than $\Delta G_{Cl}(E = 0 \text{ V vs. SHE})/F$, where ΔG_{Cl} is the free energy of chloride adsorption. The potentials at which chloride adsorbs at high coverages may overlap with the potentials required for high NO_3RR activity.[31] At these potentials (**Scheme 4.1b–c**), adsorbed chloride may block active sites for hydrogen and nitrate adsorption. We hypothesize that NO_3RR requires high coverages of both nitrate and hydrogen, so a decrease in hydrogen and nitrate coverage from competitive adsorption of chloride will decrease the reaction rate. Therefore, an ideal chloride-resistant catalyst should adsorb nitrate and hydrogen more strongly than chloride.

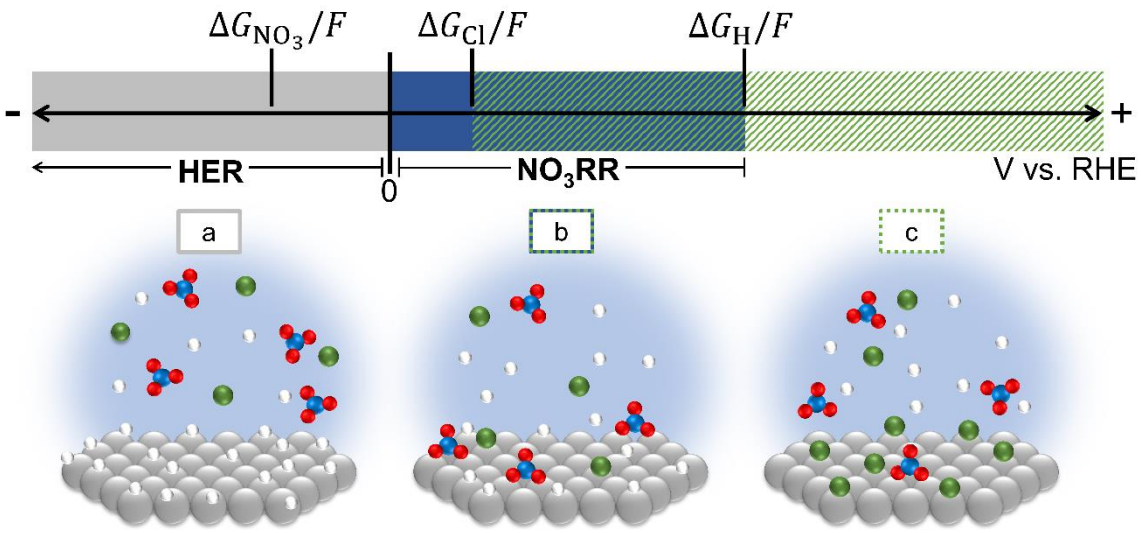

Scheme 4.1. Potentials and free energies associated with different adsorption and reaction events on electrode surfaces, including hydrogen evolution reaction (HER, gray potential window), nitrate adsorption ($\Delta G_{NO_3}, NO_3^- + * \rightleftarrows NO_3{}^* + e^-$), nitrate reduction reaction (NO_3RR, blue potential window), Cl– adsorption ($\Delta G_{Cl}, Cl^- + * \rightleftarrows Cl^* + e^-$, green-hatched potential window), and hydrogen adsorption (ΔG_H, $H^+ + * + e^- \rightleftarrows H^*$). The potential region where chloride, nitrate, and hydrogen are all present on the surface is the overlap of blue with green hatches. Representative electrode surface coverages are shown for a) HER, b) NO_3RR with Cl*, and c) adsorbed chloride regions. F is Faraday's constant, used to convert between potentials and free energies. ΔG_{NO_3}, ΔG_{Cl}, and ΔG_H labeled on the scheme are all the values at 0 V vs. SHE and pH = 0. Atom color legend: metal = gray; oxygen = red; nitrogen = blue; chlorine = green; hydrogen = white.

Herein, we study the performance of rhodium sulfide supported on carbon (Rh_xS_y/C) for NO_3RR as a potential chloride-resistant electrocatalyst and compare it to Pt/C and Rh/C to understand chloride poisoning and the NO_3RR mechanism. We choose Pt and Rh for study for several reasons: 1) they are two of the few metals that have previously been investigated and reported to be poisoned by chloride,[23,24] motivating this study into the cause; 2) Pt binds nitrate weakly and Rh binds nitrate strongly,[30] allowing a comparison between two different systems to investigate whether chloride poisoning is different; and 3) Pt and Rh are both active for nitrate reduction in the potential range where hydrogen evolution is not thermodynamically possible (>0 V vs. RHE), making it experimentally simpler to study nitrate reduction, as the reduction current comes solely from nitrate reduction, rather than a mixture of hydrogen evolution and nitrate reduction. We study Rh_xS_y because Rh is the most active platinum group metal for NO_3RR and

Rh_xS_y is known to be halide-resistant for electrocatalytic oxygen reduction and hydrogen evolution.[22,32–39] Our experiments show that Rh_xS_y/C is more active for NO_3RR than Rh/C when the activity is normalized to the number of surface sites. In the presence of 1 mM Cl^-, however, Rh_xS_y/C has only slightly better poison resistance than Rh/C and Pt/C (i.e., with 1 mM Cl^- the NO_3RR current decreases 33–42% for Rh_xS_y/C, 32–52% for Pt/C, and 56–63% for Rh/C between 0.05–0.2 V vs. RHE at pH 0 with 1 M $NaNO_3$). To rationalize the NO_3RR rate inhibition observed between Rh_xS_y/C, Pt/C, and Rh/C, we develop a microkinetic model based on our experimental results and perform density functional theory (DFT) calculations. Our experimental rate measurements on Pt/C are qualitatively explained by a rate law for NO_3RR where the RDS is the surface reaction between adsorbed H and adsorbed nitrate. Our rate measurements on Rh/C match the rate laws where the RDS is a surface reaction between adsorbed H and adsorbed nitrate or direct deoxygenation of nitrate to nitrite without the addition of H. Our DFT calculations do not find a feasible pathway on Rh for adsorbed H and adsorbed nitrate to react, whereas the direct deoxygenation of nitrate to nitrite without the addition of H is found. DFT-predicted linear scaling relations between the adsorption free energies of nitrate and chloride on transition metals show that a metal that adsorbs nitrate strongly will also adsorb chloride strongly. The competition for surface sites between chloride and nitrate, combined with their linear adsorbate scaling relations explains why Pt and Rh are poisoned similarly by chloride for NO_3RR, despite Rh binding nitrate more strongly. DFT calculations predict that pristine Rh_xS_y terraces adsorb nitrate too weakly to yield high NO_3RR activity. However, Rh_xS_y terraces with sulfur (S) vacancies adsorb nitrate strongly, and the S-defected Rh_3S_4 surface has a low enough activation barrier for direct nitrate dissociation to be responsible for the observed NO_3RR activity. Additionally, this S-defected Rh_3S_4 surface binds chloride strongly and follows adsorbate linear scaling similar to the transition

metal surfaces, thus explaining the weaker-than-expected chloride resistance for Rh_xS_y/C toward NO_3RR. The combined experimental and computational findings reported here clarify the role of chloride poisoning of NO_3RR catalysts and the importance of considering S vacancies for metal sulfide electrocatalysts.

4.2 Methods

4.2.1 Electrocatalyst preparation.

A Pt rotating disk (Pine Research Inst., Inc.), a Rh wire (99.8%, Alfa Aesar), 30 wt% Pt/C (Fuel Cell Store), 20 wt% Rh/C (Fuel Cell Store), and 30 wt% Rh_xS_y/C (details of catalyst available in refs.[22,34,40]) were used as catalysts. The Pt rotating disk electrode (RDE) was hand-polished using a 0.05 μm alumina suspension (Allied High Tech Products, Inc.) on a micropolishing cloth and ultrasonicated in deionized water (18.2 MΩ cm, Millipore Milli-Q system) for 30 minutes before assembling in the Teflon rotating disk holder. Subsequently, the assembled Pt RDE was electrochemically cleaned in the supporting electrolyte from –0.2 to 1.2 V vs. RHE at 100 mV s^{-1} for 50 cycles. The Rh wire was flame-annealed, then electrochemically cleaned in the supporting electrolyte from –0.2 V to 1.0 V vs. RHE at 100 mV s^{-1} for 50 cycles.

All catalysts supported on carbon were deposited in the form of a prepared ink on a glassy carbon disk. The catalyst inks were prepared by combining 3 mg of supported catalyst (Rh_xS_y/C, Rh/C, or Pt/C) with 5 mL of 50:50 deionized water and isopropanol mixture in a scintillation vial. 17.5 μL of 5 wt% Nafion solution (5 wt% Nafion, Sigma Aldrich) in isopropanol was added and the vial was ultrasonicated for two hours. 8 μL catalyst ink was deposited twice on a clean glassy carbon disk (Pine Research Inst., Inc), allowing the disk to air-dry between depositions. Prior to measurements, the catalysts deposited on glassy carbon were electrochemically cleaned (–0.2 to

1.2 V vs. RHE at 100 mV s^{-1} for 50 cycles for Pt/C, –0.2 to 0.75 V vs. RHE at 50 mV s^{-1} for 50 cycles for Rh/C, and –0.2 to 0.75 V vs. RHE at 50 mV s^{-1} for 50 cycles for Rh_xS_y/C).

4.2.2 Electrochemically active surface area and hydrogen underpotential deposition.

Hydrogen underpotential deposition (H_{upd}) was used to determine the electrochemically active surface area (ECSA) for Pt and Rh (RDE, wire, and supported catalysts). The Pt and Rh electrodes were cycled at 100 mV s^{-1} from 0.05 to 1.2 V vs. RHE and 0.05 to 1.0 V vs. RHE, respectively. A three-electrode electrochemical setup was used with a Pt wire (99.99%, Pine Research Inst., Inc.) counter electrode and a double junction Ag/AgCl (10% KNO_3 outer solution/4 M KCl inner solution, Pine Research Inst., Inc.) reference electrode. A two-compartment cell was used in which the compartment with the working electrode and reference electrode was separated from the counter electrode compartment using a Nafion 117 membrane. The supporting electrolyte was 1 M H_2SO_4 prepared from concentrated H_2SO_4 (99.999%, Sigma Aldrich) for Rh and 1 M $HClO_4$ prepared from 61% $HClO_4$ (Fisher Chemical) for Pt. For Rh, H_2SO_4 was selected instead of $HClO_4$ because perchlorate poisons the Rh surface via reduction to chloride[41,42] whereas bisulfate and sulfate anions are not known to interact strongly with Rh. $HClO_4$ was selected as the supporting electrolyte for Pt measurements because the perchlorate anion adsorbs less strongly than bisulfate and sulfate anions on Pt, which interfere with H_{upd}.[23,43] Electrolytes were sparged with N_2 (99.999%, Cryogenic Gases) for 60 min before use. All electrochemical measurements were collected using a VSP potentiostat (Bio-Logic Science Inst.). For Pt and Rh, a baseline double-layer charging current was measured at 0.4 V vs. RHE and subtracted to determine only the H_{upd} charge from the hydrogen desorption process as shown in **Chapter 2.3.4**. This H_{upd} desorption charge was used to calculate the ECSAs for Pt and Rh using average charge densities of 210 and 221 μC cm^{-2}, respectively.[44]

For Rh_xS_y/C, the ECSA was approximated by first using cyclic voltammetry in the non-faradaic region (0.45 to 0.75 V vs. RHE) as a function of the scan rate (100 to 20 mV s^{-1}) to determine the total capacitance associated with the electrochemical double layer (for both carbon and Rh_xS_y). The total capacitance, Rh_xS_y particle sizes, weight loading, specific capacitance, and specific area of carbon were used to approximate the ECSA of Rh_xS_y (approximating the Rh_xS_y particles as cubes; see **Chapter 2.3.3**).[45,46] All particle sizes were determined using X-ray powder diffraction (XRD) and crystallite sizes were estimated using the Scherrer equation. Particle size distributions were measured using transmission electron microscopy with the mean particle size of Rh_xS_y/C slightly lower than that observed by XRD. Effects of the differences between XRD and TEM particle sizes and size distribution on the ECSA estimates are discussed in **Appendix A**. This capacitance & XRD method estimates ECSA within 53% of H_{upd} values compared to Pt/C and Rh/C, giving confidence in the ability for it to accurately estimate ECSA for Rh_xS_y/C. The Rh_xS_y crystallites used were 12 nm in diameter. For Pt/C and Rh/C, the crystallite sizes were 2.2 nm and 2.3 nm, respectively. The Rh_xS_y surfaces are not metallic Rh under reaction conditions based on a lack of observable H_{upd} charge and the absence of metallic Rh using XRD as shown in **Appendix A**.

4.2.3 Steady-state electrocatalytic nitrate reduction measurements.

The same three-electrode, two-compartment electrochemical cell setup used to determine the ECSA was used for steady-state current measurements. The working electrolyte was purged with N_2 for 60 minutes prior to measurements. NO_3RR activity was measured under steady-state conditions by performing constant potential electrolysis for 2 hours, where the reported current is the steady-state current that was reached. Steady-state measurements were taken at room temperature (23 °C). All measurements were taken at a RDE rotation rate of 2500 rpm to minimize

the concentration gradient between the electrode surface and the bulk solution. The effect of rotation rate and a comparison of the results in 1 M HNO_3 to those with 1 M $NaNO_3$ are discussed in **Appendix A**. Loss of catalyst due to poor adhesion to the glassy carbon disk was less than 11% of the ECSA, based on the capacitance before and after steady-state measurements. Electrochemical impedance spectroscopy was used to measure the series resistance, but because the currents were low, the ohmic resistance corrections to the voltage were less than 1 mV. The steady-state current with and without chloride for each potential was taken via individual experiments. The concentration of chloride was chosen as 1 mM to probe the effect of poisoning, which is in the lower range of chloride concentrations in wastewater and ion exchange brine streams (0.14 mM to 2.8 M Cl^-).[15–19,47] We also explored 10 and 100 mM Cl^- to test how higher chloride concentration affected poisoning. For supported Rh_xS_y/C, Pt/C, and Rh/C, the measurements were repeated three times, but each time a new catalyst was used to prevent any loss of material because of adhesion issues. Pt/C and Rh/C currents were normalized to the ECSA obtained by H_{upd} and Rh_xS_y/C currents were normalized to the approximated ECSA from the capacitance & XRD method. Each current measurement was normalized to the ECSA to account for differences in catalyst weight loading (30 wt% Pt/C, 20 wt% Rh/C, and 30 wt% Rh_xS_y/C) and variation in individual ink depositions. This method of normalizing resulted in the same current densities reported even for different amounts of a given catalyst deposited onto the electrode.

4.2.4 Product quantification.

For measurements of the faradaic efficiency, the commercial Rh_xS_y/C and Rh/C powders were loaded onto carbon felts (6.35 mm thick, 99.0%, Alfa Aesar) instead of the glassy carbon disk to increase the amount of catalyst loading to enable sufficient product formation detectable in a reasonable amount of time. The carbon felts were pretreated thermally at 400 °C with H_2 at 60

psi for four hours. A catalyst ink was prepared by combining 10 mg of supported catalyst (Rh_xS_y/C or Rh/C) with 1.5 mL isopropanol and 1 mL deionized water in a scintillation vial and sonicating for 10 minutes. The catalyst ink was deposited onto the thermally treated carbon felt (1 cm × 3 cm) and allowed to dry. The carbon felt with catalyst was then attached to a graphite rod (6.15 mm diameter, 99.9995%, Alfa Aesar). Prior to nitrate conversion, the catalyst on carbon felt was electrochemically cleaned in 1 M H_2SO_4 (N_2-sparged) by cycling the potential as described above. The electrochemical cleaning was completed in a single-compartment electrochemical cell with a graphite rod counter electrode and double-junction Ag/AgCl reference electrode. After cleaning, the catalyst on carbon felt was then transferred to a two-compartment electrochemical cell for the product quantification measurements (with the same electrochemical set up used for steady-state current measurements). The working electrolyte was 0.1 M HNO_3 (N_2-sparged). Because of the higher currents enabled by the larger catalyst surface area, 85% of the voltage drop due to solution resistance was compensated for during the measurement. The remaining 15% amounted to less than 15 mV on average. For measuring the faradaic efficiency, 0.1 V vs. RHE was chosen because this was the potential with the highest nitrate reduction current without background currents observed from the supporting electrolyte. The faradaic efficiency for Pt/C at these conditions (0.1 V vs. RHE, 0.1 M HNO_3) has been reported as almost 100% towards ammonium.[10]

The products formed were determined by extracting 0.5 mL aliquots of the solution in the electrochemical cell every hour during operation and storing them at room temperature until all measurements were taken. A portion of each aliquot was used for NO_3^-, NO_2^-, and NH_4^+ quantification separately. NO_3^- and NO_2^- were detected using standard spectrophotometric methods[48] and NH_4^+ was detected using the indophenol blue test[49,50] (described in **Chapter 2.4.2**). After appropriate dilution, the sample was transferred into a quartz cuvette with a 1 cm pathlength,

and the UV-Vis spectra was taken using a UV-Vis spectrophotometer (Evolution 350, Thermo Scientific). Concentrations were determined using the absorbances against prepared standard calibration curves.

4.2.5 Cyclic voltammetry studies of chloride adsorption.

Adsorption of chloride and hydrogen on the Pt rotating disk and Rh wire was studied via the H_{upd} charge in $HClO_4$ and H_2SO_4 with NaCl (≥ 99.5%, Sigma Aldrich) concentrations of 0, 0.001, 0.01, 0.1, and 0.15 M Cl^-. The setup and operation were the same as for H_{upd} to measure the ECSA, other than the addition of chloride. The chloride concentration was adjusted by adding small volumes (less than 0.5 mL) of concentrated chloride solution to the electrochemical cell at room temperature. After addition, the solution was stirred and sparged with N_2 for 10 minutes. Polycrystalline surfaces (RDE and wire) were used for cyclic voltammograms because they have more well-defined H_{upd} peaks than the carbon-supported nanoparticle catalysts.

4.2.6 Langmuir adsorption model and Langmuir-Hinshelwood reaction model.

For an aqueous system with nitrate and chloride present, NO_3^-, Cl^-, and H^+ can occupy active catalyst sites (denoted as $*$). The equilibrium coverage of hydrogen, nitrate, and chloride is modeled assuming Langmuir competitive adsorption between the species (**Equations 4.1**-**4.3**).

$$H^+_{(aq)} + * + e^- \rightleftharpoons H^* \quad (4.1)$$

$$NO^-_{3\,(aq)} + * \rightleftharpoons NO^*_3 + e^- \quad (4.2)$$

$$Cl^-_{(aq)} + * \rightleftharpoons Cl^* + e^- \quad (4.3)$$

We assume that one electron is transferred per adsorbed chloride,[27] hydrogen, and nitrate based on previous measurements (see **Chapter 3** and discussion in **Appendix A**)[30] and our work shown below. Because of this electron transfer, the coverage of each species is a function of the

electrode potential. Equations relating the equilibrium adsorption constants and the potential-dependent coverages using a competitive Langmuir adsorption isotherm for hydrogen, nitrate, and chloride are given in **Appendix B**.

Nitrate dissociation is typically considered the RDS for NO_3RR, as experimentally observed for Pt and Rh under acidic conditions[43,51] and predicted for metals.[30] Direct nitrate reduction to selected products was modelled in our previous work, based on a microkinetic model of 19 elementary reactions.[30] Degree of rate control analysis showed that nitrate dissociation to nitrite and oxygen was rate controlling on Pt and Rh, which was modeled with **Equation 4.4** as the RDS. Assuming the adsorption steps (**Equations 4.1-4.3**) are quasi-equilibrated and the further reactions of adsorbed nitrite and oxygen (**Equations 4.5-4.7**) are infinitely fast, the rate law for direct nitrate dissociation as the RDS is **Equation 4.8**.

$$NO_3^* + * \rightleftarrows NO_2^* + O^* \tag{4.4}$$

$$O^* + H^* \rightleftarrows HO^* + * \tag{4.5}$$

$$HO^* \rightarrow \text{products} \tag{4.6}$$

$$NO_2^* \rightarrow \text{products} \tag{4.7}$$

$$\text{rate} = \frac{k_4 K_{NO_3} [NO_3^-]_0}{\left(1 + K_H [H^+]_0 + K_{NO_3} [NO_3^-]_0 + K_{Cl} [Cl^-]_0\right)^2} \tag{4.8}$$

K_H, K_{NO_3}, and K_{Cl} are the potential-dependent equilibrium adsorption constants of **Equations 4.1-4.3** and $[NO_3^-]_0$, $[H^+]_0$, and $[Cl^-]_0$ are the bulk concentration of each species in the solution. The rate constant k_4 is the rate constant for the forward reaction in **Equation 4.4**. However, the rate law in **Equation 4.8** that assumes direct nitrate dissociation is the RDS disagrees with experimental results shown in this work for Pt/C. Instead, a microkinetic model using the H-assisted nitrate dissociation to nitrite via a surface reaction of adsorbed nitrate and adsorbed

hydrogen (**Equation 4.9**) as the RDS resulted in a rate law that more closely matches our experimental observations for Pt/C.

$$H^* + NO_3^* \rightleftarrows NO_2^* + HO^* \quad (4.9)$$

$$HO^* \rightarrow \text{products} \quad (4.6)$$

$$NO_2^* \rightarrow \text{products} \quad (4.7)$$

Previous work has proposed an H-assisted nitrate dissociation mechanism via adsorbed HNO_3 on metal and oxide surfaces.[52,53] For subsequent analysis, we assume the H-assisted nitrate dissociation shown in **Equation 4.9** is the RDS and thus approximate the adsorption steps (**Equations 4.1-4.3**) of nitrate, chloride, and protons to be quasi-equilibrated. We assume that the formed hydroxide and nitrite on the surface (**Equations 4.6 and 4.7**) instantaneously react to form other products or leave the surface. Although the reaction in **Equation 4.9** may not correspond to an actual elementary step (if HNO_3 is a stable surface intermediate), we assume that it follows an elementary rate law in this work. Thus, the rate equation for NO_3RR is:

$$\text{rate} = k_9 \theta_{NO_3} \theta_H \quad (4.10)$$

where θ_i is the surface coverage of species i, k_9 is the reaction rate constant for the forward reaction in **Equation 4.9**, and the site balance is $1 = \theta_H + \theta_{NO_3} + \theta_{Cl} + \theta_*$. The coverages of the different species can be determined by assuming that the reactions in **Equations 4.1-4.3** are quasi-equilibrated. This would result in a rate law shown in **Equation 4.11**. Although the full microkinetic model is more complex, we show that this Langmuir-Hinshelwood model qualitatively predicts the observed inhibition of nitrate reduction in the presence of chloride.

$$\text{rate} = \frac{k_9 K_{NO_3} [NO_3^-]_0 K_H [H^+]_0}{\left(1 + K_H [H^+]_0 + K_{NO_3} [NO_3^-]_0 + K_{Cl} [Cl^-]_0\right)^2} \quad (4.11)$$

Two additional microkinetic models were explored, one using direct nitrate reduction by protons as the RDS and the other considering nitrate dissociation and hydroxide formation with a pseudo-steady state hypothesis for the coverage of oxygen. Their corresponding rate laws did not qualitatively match the experimental kinetic measurements and the rate law in **Equation 4.11**, so they are not used for analysis. Details for all microkinetic models considered are provided in **Appendix B**.

4.3 Results and Discussion

To better understand the NO_3RR activity and mechanism on Pt, Rh, and Rh_xS_y in the presence of chloride, in the following sections we: (i) compare Rh_xS_y activity for nitrate reduction against that of Pt and Rh, (ii) examine the competition between chloride and nitrate adsorption on Pt and Rh, (iii) provide a kinetic model that rationalizes chloride poisoning of NO_3RR on Pt and Rh, (iv) explain chloride-poisoning trends via adsorbate scaling relationships between chloride and nitrate adsorption energies, and (v) propose a plausible active site of Rh_xS_y based on experimental and computational observations.

4.3.1 Rh_xS_y performance for nitrate reduction compared to Pt and Rh.

The steady-state reduction current densities as a function of potential in **Figure 4.1a** show Rh_xS_y/C has higher NO_3RR activity than Rh/C and Pt/C with and without chloride. Pt/C has much lower activity than either Rh_xS_y/C or Rh/C, attributed to its weaker nitrate adsorption.[43] Without nitrate, no current is detected for Rh_xS_y/C other than the onset of hydrogen evolution at 0 V vs. RHE. The reported activities are normalized to the ECSA, however the difference in particle size of Pt/C and Rh/C (2.2 and 2.3 nm, respectively) compared to Rh_xS_y/C (12 nm) may lead to differences in nitrate reduction activity due to differences in the fraction of step sites at the surface.

On metals, stepped sites are reported to be more active than terraces.[54,55] Thus, smaller particles sizes (with a higher fraction of step sites sites) would be expected to be more active on a per-surface-area basis. Although the Rh_xS_y/C has higher area-normalized activity than Rh/C, the former has lower ammonia faradaic efficiency. The faradaic efficiency for Rh_xS_y/C in 0.1 M HNO_3 is 67% to NH_4^+ at 0.1 V vs. RHE (**Figure 4.1d**). The NO_3RR products of Rh/C under the same conditions are mainly NH_4^+ (92% faradaic efficiency). In 0.1 M $NaNO_3$ + 0.5 M H_2SO_4, nitrate reduction products on Rh have been posed to be either NO_2^- or NH_4^+,[43] of which we confirm the formation of NH_4^+ on Rh in this study. Rh has also been reported to have high selectivity towards NH_3/NH_4^+ between pH of 3.7–7.2 and moderate NH_4^+ production in more basic conditions (pH of 13 or 14).[56,57] Nitrite was not detected under these conditions for either catalyst. The remaining 33% of the faradaic efficiency for Rh_xS_y/C could be due to the formation of species such as NH_2OH, N_2, N_2O, or NO.

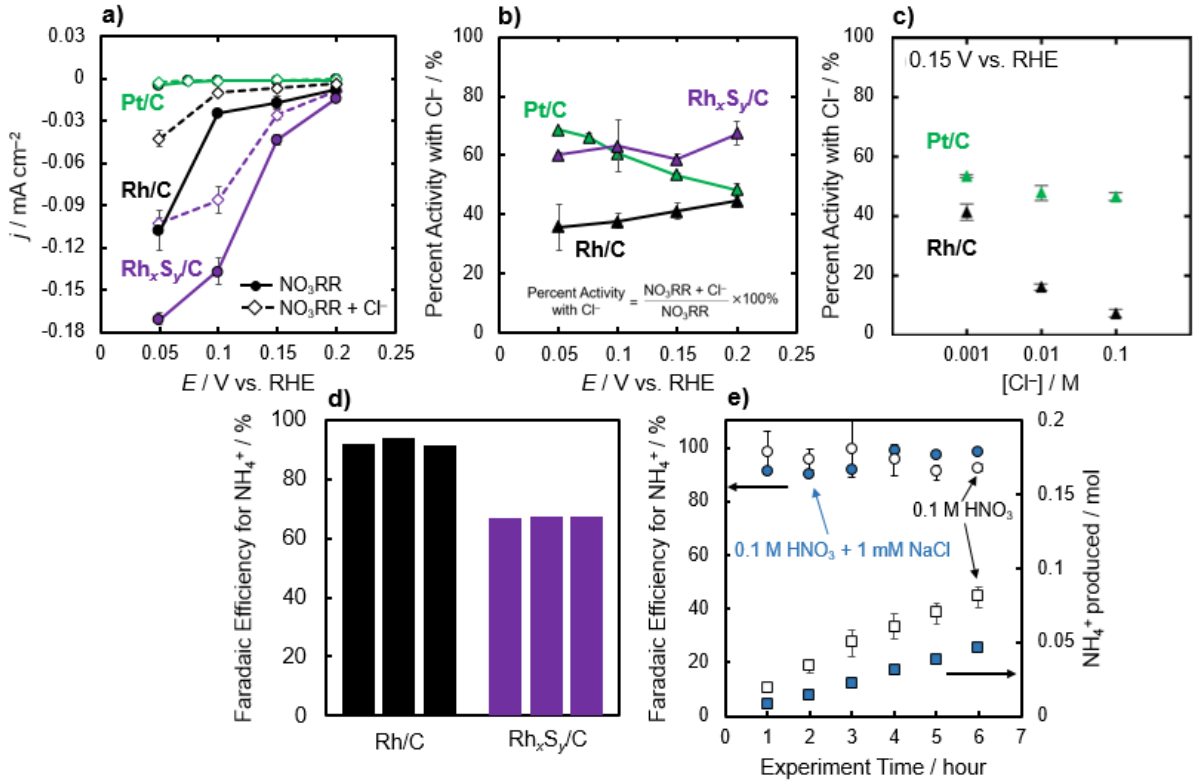

Figure 4.1. a) Steady-state nitrate reduction current density (j) on Pt/C (1 M $HClO_4$ + 1 M $NaNO_3$) and Rh/C and Rh_xS_y/C (1 M H_2SO_4 + 1 M $NaNO_3$) deposited on a glassy carbon rotating disk electrode at 2500 rpm rotation rate both without (filled circles) and with 1 mM Cl^- (open diamonds). b) The percent nitrate reduction current (filled triangles) from the reduction currents with and without 1 mM Cl^- is shown for Rh/C, Pt/C, and Rh_xS_y/C for the potentials 0.05–0.2 V. c) The percent nitrate reduction current from the reduction currents in 1 M $HClO_4$ + 1 M $NaNO_3$ on Pt/C (green) or 1 M H_2SO_4 + 1 M $NaNO_3$ on Rh/C (black) with and without Cl^- at 0.15 V for 0.001 to 0.1 M Cl^-. d) Faradaic efficiency towards ammonium for Rh/C and Rh_xS_y/C at 0.1 V vs. RHE. The results from three experiments for each catalyst are shown. Electrolysis time was 6 hours for each experiment. e) Faradaic efficiency towards ammonium and total ammonium produced for Rh/C at 0.1 V vs. RHE in 0.1 M HNO_3 (white) and 0.1 M HNO_3 + 1 mM NaCl (blue). For Rh/C without chloride, the error bars for the measurements without chloride are the standard deviation from the average of the three separate experiments shown in panel e. Conversion measurements with chloride were performed once.

The steady-state current density measurements for all catalysts in **Figure 4.1** show a decrease in NO_3RR activity in the presence of 1 mM Cl^-. The lower reaction rates on Pt/C and Rh/C due to chloride poisoning are similar to previous reports as discussed in **Appendix A**. The faradaic efficiency towards NH_4^+ for Rh/C is not significantly changed with the addition of 1 mM Cl^- (**Figure 4.1e**). Thus, the decrease in conversion rate of nitrate was decreased proportionally to the decrease in current density when chloride is present. The NO_3RR activity in the presence of Cl^- relative to the NO_3RR activity in the absence of chloride for Rh_xS_y/C, Rh/C, and Pt/C is shown

as a function of potential in **Figure 4.1b**; the decrease in activity is more severe on Rh/C than Pt/C or Rh_xS_y/C. The NO_3RR activity when chloride is present decreases for Pt/C with increasing potential but increases or stays constant with increasing potential for Rh/C and Rh_xS_y/C. Chloride concentrations above 1 mM cause more severe inhibition on both Pt/C and Rh/C (**Figure 4.1c**). Increasing the chloride concentration would increase the chloride coverage so greater NO_3RR inhibition is expected.

4.3.2 Competitive adsorption of Cl^- with H^+ on Pt and Rh.

To explain the inhibition of NO_3RR on Pt and Rh when chloride is present, we probe the adsorption of chloride on these surfaces. The competitive adsorption of Cl^- with H^+ on polycrystalline Pt and Rh is studied using cyclic voltammetry as a function of chloride concentration (1 mM–0.1 M Cl^-) between 0.05–0.4 V vs. RHE (**Figure 4.2a**–**b**). Because Rh_xS_y does not show hydrogen underpotential deposition (H_{upd}), the same study cannot be done on it. Without chloride, the measured anodic currents are due to electron transfer associated with underpotentially deposited hydrogen (H*) desorbing from the surface (**Equation 4.1**). The total anodic charge in the absence of chloride, Q_0, taken by integrating the current with respect to the time of the anodic sweep, is proportional to the change in surface coverage of adsorbed hydrogen when changing the potential from 0.05 to 0.4 V vs. RHE. For Pt and Rh without chloride, Q_0 corresponds to approximately one monolayer of adsorbed hydrogen. We denote the charge in the presence of chloride as Q and plot the ratio of Q to Q_0 for Rh and Pt in **Figure 4.2c**. One effect of chloride on Q is that chloride prevents hydrogen from adsorbing, so there is less than one monolayer of adsorbed hydrogen to desorb, decreasing the observed charge ($Q/Q_0 < 1$). **Figure 4.2a** reveals that on Rh the current decreases with increasing chloride concentration. The decrease in current is attributed to the presence of chloride on the surface at these potentials, in

which the adsorbed chloride blocks available sites for hydrogen to adsorb, reducing the total anodic charge observed (**Figure 4.2c**). We hypothesize that chloride has adsorbed at potentials more negative than 0.05 V vs. RHE on Rh, and the chloride coverage from 0.05 to 0.4 V vs. RHE is constant. Thus, there is no additional charge from chloride adsorption at these potentials and on Rh the only anodic current observed in **Figure 4.2a** comes from the desorption of H*, which is less in the presence of chloride.

The current from the anodic scan and charge for Pt with increasing chloride concentration are shown in **Figure 4.2b**–**c**, respectively. In the absence of chloride, the Pt current has characteristic H_{upd} peaks that correspond to step and terrace sites that adsorb hydrogen at different potentials instead of a single broad peak for all adsorption sites like on Rh.[58,59] The surface sites corresponding to the different H_{upd} peaks have been identified using a combination of single crystal studies and DFT modeling studies.[60–64] When the chloride concentration is increased, the H_{upd} peaks shift toward lower potentials, making it challenging to deconvolute the different surface sites. The behavior on Pt is different from that of Rh, most notably that on Pt the anodic charge increases with the addition of small concentrations of chloride ions ($Q/Q_0 > 1$), and the charge only decreases at the highest tested chloride concentrations (**Figure 4.2c**). This increase in anodic charge may seem counterintuitive, as it implies that the hydrogen coverage is higher in the presence of chloride. However, as the potential is increased on Pt chloride is also adsorbing on the surface,[65,66] which contributes additional anodic charge due to the electron transfer from the negatively charged chloride ion. Thus, the chloride coverage is increasing on Pt from 0.05 to 0.4 V vs. RHE. The observation from the experimental cyclic voltammograms that chloride is adsorbed at more negative potentials on Rh (<0.05 V vs. RHE as discussed above) than on Pt

(0.05–0.4 V vs. RHE), indicates that Rh binds chloride more strongly than Pt based on the Nernst equation.

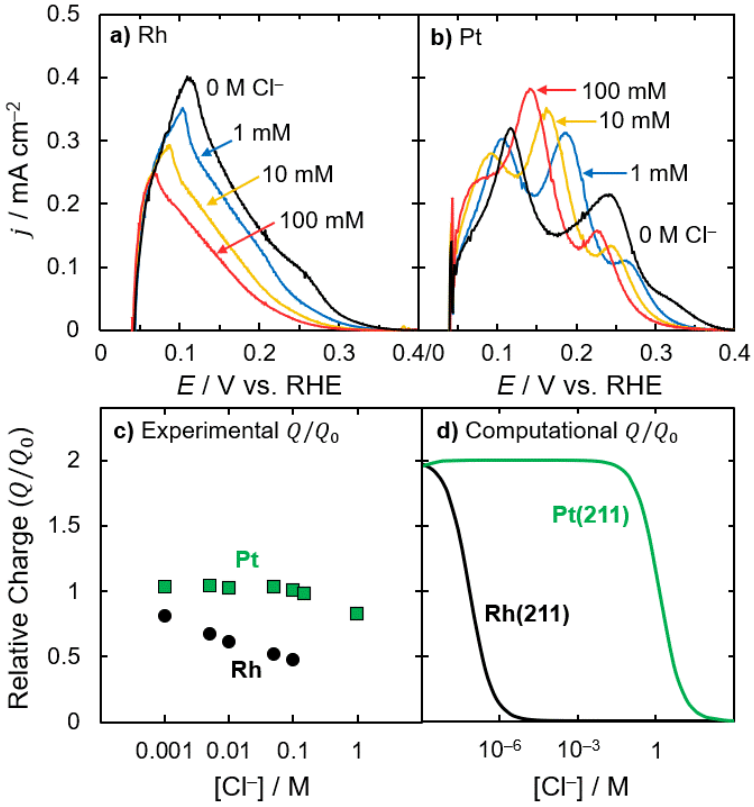

Figure 4.2. The anodic current during an oxidative scan as a function of potential for different concentrations of Cl^- on a) Rh wire in 1 M H_2SO_4 and b) Pt RDE in 1 M $HClO_4$ at 100 mV s^{-1}. c) Relative charge (Q/Q_0) of H_{upd} (0 to 0.4 V vs. RHE) on Rh wire and Pt RDE from a) and b), respectively. d) Computational Q/Q_0 on Rh(211) and Pt(211) were constructed by modeling the surface coverages of hydrogen and chloride from 0 to 0.4 V vs. RHE based on DFT modeling and assuming a scan rate of 100 mV s^{-1}. Rh and Pt are represented by black circles and green squares, respectively.

To better interpret the experimental cyclic voltammograms, we use DFT modeling to calculate the ΔG_{Cl} and ΔG_H on Rh and Pt and construct adsorption isotherms and computational cyclic voltammograms. Computational details for DFT modeled surfaces and adsorption energy calculations can be found in **Appendix B**. The competitive Langmuir adsorption isotherm is used to predict equilibrium coverages as a function of applied potential. We model (211) stepped sites because they bind nitrate more strongly than terraces and are hypothesized to be active sites for NO_3RR.[30,60,67] For Rh(211) and Pt(211) the ΔG_{Cl} at 0 V vs. SHE are –56.2 kJ mol^{-1} and –20.2 kJ

mol^{-1}, respectively, qualitatively matching the cyclic voltammogram observations that chloride binds more strongly to polycrystalline Rh than to Pt. The ΔG_{H} on Rh(211) and Pt(211) are –17.4 and –23.5 kJ mol^{-1}, respectively at 0 V vs. RHE. The coverages of chloride and hydrogen on Rh(211) and Pt(211) are predicted as a function of potential using a single site adsorption model. We computationally predict cyclic voltammograms for Pt(211) and Rh(211) with and without chloride, assuming for each potential the surface reaches equilibrium, and show the predicted charge in **Figure 4.2d**. The computational cyclic voltammograms and coverage plots are provided in **Appendix B**. We focus on qualitative trends between the two metals and with increasing chloride concentrations because the absolute values of the DFT-predicted adsorption energies are not quantitative because of challenges with predicting anion adsorption at solvated interfaces.[68] Additionally, as the experimental measurements are on polycrystalline Pt and Rh, the comparison between the experimental and computational results is qualitative.

The trends in charge from the computational cyclic voltammogram on Rh(211) and Pt(211) (**Figure 4.2d**) qualitatively agree with the experimental trends on Rh and Pt (**Figure 4.2c**). Chloride adsorbs strongly to the surface and competes with hydrogen to occupy sites. The decrease in the amount of adsorbed hydrogen is shown by the decrease in hydrogen adsorption charge on Rh(211) (**Figure 4.2d**). For Pt(211), the total charge is higher at low chloride concentrations and decreases at high chloride concentrations. From both the experimental and computational studies of hydrogen and chloride adsorption on Rh and Pt, we demonstrate that chloride interacts strongly with these metal surfaces by competitively occupying sites in the H_{upd} region, with chloride adsorbing more strongly on Rh than on Pt.

Based on the competitive Langmuir adsorption model, if we include nitrate adsorption then we expect that chloride and nitrate would compete to adsorb on the (211) sites. Due to this

competition, the presence of chloride would cause a decrease in the nitrate coverage, and thus reduction rate. Because chloride adsorption is potential-dependent, this inhibition would also be potential-dependent.

4.3.3 Computational model of chloride poisoning of NO_3RR on Pt and Rh.

We expand the adsorption model assuming competitive adsorption among H*, NO_3*, and Cl* and model the equilibrium coverages of these three species as a function of potential. The predicted equilibrium coverages are shown in **Figure 4.3a–b** for Rh(211) and Pt(211) at pH 0 with 1 M NO_3^- and 0 to 10^{-3} M Cl^-. For Rh(211) and Pt(211), the DFT-predicted ΔG_{NO_3} are –1.44 kJ mol^{-1} and 47.6 kJ mol^{-1} at 0 V vs. SHE respectively. The weaker adsorption of nitrate to Pt(211) than Rh(211) is consistent with previous reports.[30] For Rh(211), small concentrations of chloride greatly change the coverages of adsorbed species on the surface. Although Rh binds nitrate relatively strongly, chloride is bound even more strongly, and the equilibrium coverage is dominated by Cl*. On Pt(211), nitrate has low coverage in this potential range, therefore the hydrogen coverage with and without 1 M NO_3^- is almost identical and the nitrate coverage approaches zero when chloride is present.

If we assume the RDS of NO_3RR is the surface reaction between nitrate and hydrogen (**Equation 4.9**), the rate should be proportional to the coverage of nitrate times the coverage of hydrogen ($\theta_H \theta_{NO_3}$) as written in **Equation 4.10**. The product of these two coverages on Rh(211) and Pt(211) is shown in **Figure 4.3c–d** both with and without chloride. The maximum in reaction rate for 0 M Cl^- is qualitatively similar to what has been observed experimentally for NO_3RR on these two surfaces.[43] Particularly, the maximum rate is at a more positive potential on Pt than on Rh due to the weaker adsorption of nitrate on Pt. As expected, chloride decreases $\theta_H \theta_{NO_3}$, supporting the hypothesis that the decrease in NO_3RR activity from chloride is from competitive

adsorption of chloride. If we instead plot $\theta_* \theta_{NO_3}$, proportional to the rate law if the RDS is direct nitrate dissociation (**Equation 4.4**) the same trend is seen for Rh(211), but the behavior on Pt(211) does not match our experimental data, indicating Pt follows a H-assisted mechanism, whereas for Rh it is unclear which of the two mechanisms is occurring. Nitrate adsorbs stronger on Rh compared to Pt, nevertheless the Rh surface is poisoned more than that of Pt because of the stronger adsorption of chloride on Rh. This is evident by comparing the value of $\theta_H \theta_{NO_3}$ with and without chloride on Rh(211) and Pt(211) in **Figure 4.3c–d**, where the relative decrease is higher for Rh(211) at the same chloride concentration.

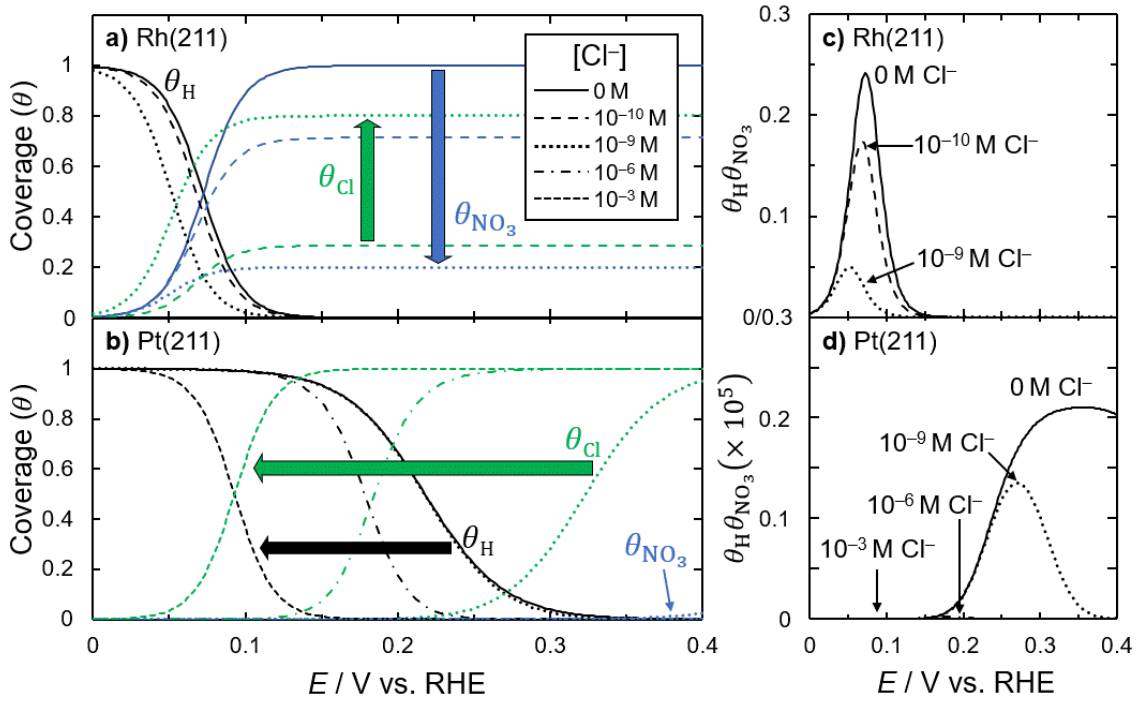

Figure 4.3. Predicted equilibrium coverage (θ) of hydrogen, chloride, and nitrate on a) Rh(211) and b) Pt(211) at pH 0 with nitrate (1 M NO_3^-) and chloride (Rh: 10^{-10} M, 10^{-9} M; Pt: 10^{-9} M, 10^{-6} M, 10^{-3} M Cl^-) assuming a single-site competitive adsorption model. Large arrows show direction of change in coverage as the chloride concentration is increased. The product of the equilibrium hydrogen and nitrate coverages is shown for c) Rh(211) and d) Pt(211) under the same conditions. Note that the data in d) is multiplied by 10^5 because of the low coverage of nitrate on Pt. Adsorbed species line color guide for a) and b): H* (black), NO_3* (blue), and Cl* (green).

The data in **Figure 4.3** shows that the decrease in $\theta_H \theta_{NO_3}$ in the presence of chloride is mainly from the decrease in the coverage of nitrate rather than a decrease in the hydrogen coverage.

This effect is clearly demonstrated on Rh; as the concentration of chloride is increased from 0 M to 10^{-9} M Cl^-, θ_H is only moderately decreased whereas θ_{NO_3} is considerably lowered (i.e., from 0 to 10^{-9} M Cl^- at 0.05 V vs. RHE, θ_H decreases from 0.8 to 0.5 and at 0.2 V vs. RHE, θ_{NO_3} decreases from almost full coverage to 0.2; see **Figure 4.3a**). A similar effect is observed with Pt at more positive potentials (where nitrate has a higher coverage). Therefore, although there is competition for sites between all three species, based on the adsorption energies the competition between the two adsorbing anions (Cl^- and NO_3^-) is most responsible for the decrease in the NO_3RR rate. The reason that Rh is still poisoned by Cl^- even though Rh(211) binds NO_3^- more strongly than Pt(211) (by 49 kJ mol^{-1}) is that Rh(211) also binds Cl^- more strongly than Pt(211) by a similar amount (39 kJ mol^{-1}). By showing that the NO_3RR poisoning is due to the competition of nitrate and chloride we rationalize our experimental studies in **Figure 4.1** for Pt and Rh. At more positive potentials the chloride coverage is higher for Pt (**Figure 4.2c,d** and **Figure 4.3b**), explaining the higher inhibition in **Figure 4.1b** at more positive potentials. For Rh, where the coverage of chloride is more constant with potential (**Figure 4.2c,d**), the inhibition of the NO_3RR rate is more constant as shown in **Figure 4.1b**.

4.3.4 Modeling chloride and nitrate adsorption and nitrate dissociation on metals and rhodium sulfide.

Nitrate reduction is inhibited when chloride adsorbs strongly to the catalyst surface and blocks sites, thus we explore whether certain metals and Rh_xS_y can adsorb Cl^- weakly while adsorbing NO_3^- strongly. The Gibbs energies of adsorption for both NO_3^- and Cl^- on metal (211) surfaces are computed using the same methods as described for Rh(211) and Pt(211). The computed nitrate and chloride adsorption free energies are shown in **Figure 4.4a** at 0 V vs. SHE for the (211) surfaces of Ag, Au, Cu, Pd, Pt, and Rh. We observe a linear adsorbate scaling between

the nitrate and chloride energies on these metals, indicated by the blue dotted line. The positive slope of the scaling relationship for metals implies that Cl^- adsorption energy increases concomitantly with the NO_3^- adsorption energy. Although Rh adsorbs NO_3^- more strongly than Pt, it also adsorbs Cl^- proportionally more strongly. Because of linear adsorbate scaling relationships and the fact that nitrate and chloride adsorption should shift similarly with potential, competitive adsorption of nitrate and chloride will be a persistent issue on many metals. This adsorbate scaling relation reveals that these metal surfaces would not be able to adsorb nitrate strongly (desired for NO_3RR activity) and adsorb chloride weakly (desired for resistance to chloride poisoning).

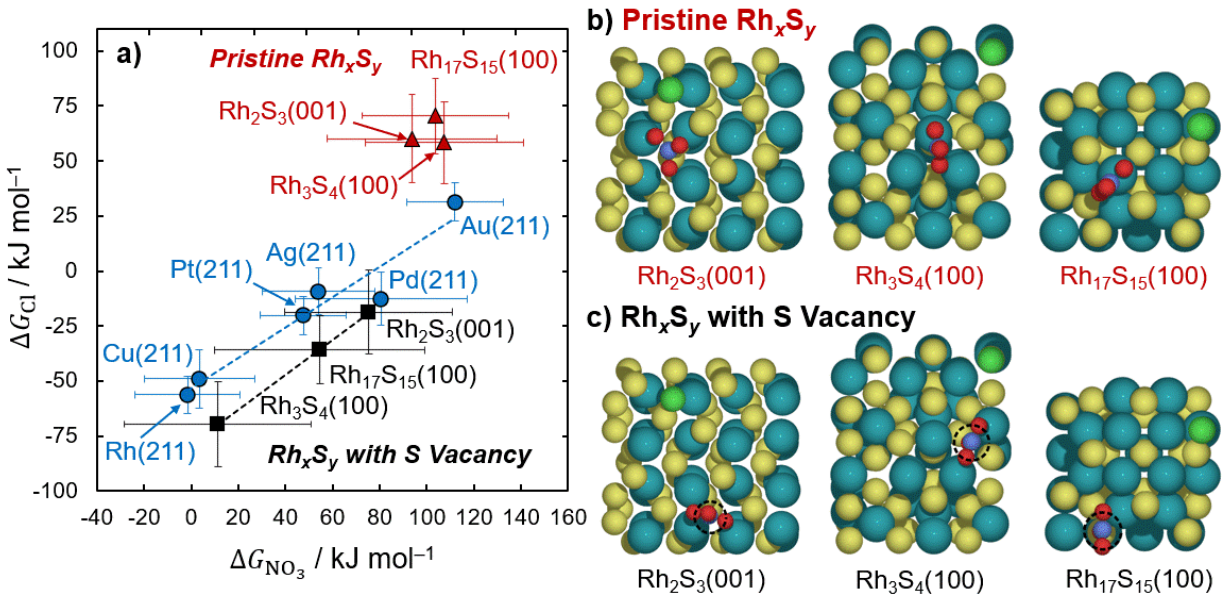

Figure 4.4. a) Computed Cl^- and NO_3^- adsorption Gibbs energies on metal (211) surfaces (blue circles), pristine Rh_xS_y surfaces (red triangles), and S-defected Rh_xS_y surfaces (black squares) at 0 V vs. SHE. The linear fit for metal (211) surfaces is $\Delta G_{Cl} = 0.69\Delta G_{NO_3} - 54$ kJ mol^{-1} with the coefficient of determination of the linear regression, $r^2 = 0.9338$. Linear fit for the Rh_xS_y surfaces with S vacancy is $\Delta G_{Cl} = 0.88\Delta G_{NO_3} - 75$ kJ mol^{-1} with $r^2 = 0.9997$. Error bars for uncertainties from the BEEF-vdW functional are shown. Top view of nitrate and chloride adsorption sites on b) pristine and c) S-defected Rh_xS_y surfaces. Teal = Rh, yellow = S, green = Cl, red = O, indigo = N, dashed circle = S vacancy.

Linear adsorbate scaling for one class of materials can be broken by moving to a different class of materials such as metal sulfides.[69] We predict that free energies of Cl^- and NO_3^- adsorption

on the surfaces of pristine Rh_2S_3(001), Rh_3S_4(100), and $Rh_{17}S_{15}$(100) are not constrained to the linear adsorbate scaling relationship established for metal (211) surfaces (**Figure 4.4a**). The Rh_xS_y surfaces shown in **Figure 4.4b** adsorb chloride more weakly relative to the metals. These Rh_xS_y surfaces (particularly Rh_3S_4) bind H^+ with ΔG_H near 0 (ideal for hydrogen evolution/oxidation) while binding Cl^- weakly, which is why Rh_xS_y is more active for hydrogen evolution in the presence of halides (e.g., Cl^-) than metals.[38] However, for Rh_xS_y/C, we report a 33–42% inhibition of NO_3RR rate with 1 mM Cl^- (**Figure 4.1**), similar to the inhibition on Pt/C (32–52%) and Rh/C (56–63%), which indicates that the active site for NO_3RR on Rh_xS_y may follow Cl^-/NO_3^- adsorbate scaling relations similar to those of pure metals. In addition, the Rh_xS_y surfaces shown in **Figure 4.4b** adsorb nitrate very weakly (ΔG_{NO_3} > 80 kJ mol^{-1}), thus it is unlikely the pristine Rh_xS_y surfaces are responsible for the NO_3RR activity seen in **Figure 4.1a**.

Oxygen vacancies catalyze nitrate reduction on TiO_2 and other metal oxide surfaces,[52] and active sites for metal sulfides are often S vacancies[70,71] or partially reduced surfaces,[33,70–74] so we investigate S vacancies in Rh_xS_y as possible active sites for NO_3RR. We study S vacancies present on each of the three Rh_xS_y surfaces (**Figure 4.4c**). Rh_xS_y is known to have partially exposed metal atoms because of sulfur leaching from extended X-ray absorption fine structure in strongly acidic conditions (6 M triflic acid).[33] Though the 1 M H_2SO_4 solution we use to investigate Rh_xS_y/C here is less harsh, we expect a small amount of sulfur leaching from Rh_xS_y to occur. As done for the pristine surfaces, Cl^-, H^+, and NO_3^- adsorption free energies are calculated on S-defected Rh_2S_3(001), Rh_3S_4(100), and $Rh_{17}S_{15}$(100). Gibbs adsorption energies of Cl^- and NO_3^- on the three defected surfaces are shown in **Figure 4.4a** also show linear scaling, indicated by the dotted black line (ΔG_H values are included in **Appendix B**). The adsorbate scaling for the S-defected Rh_xS_y is similar to the adsorbate scaling found on the transition metals. Nitrate adsorbs more strongly to S-

vacancy sites on Rh_xS_y compared to their pristine surface counterparts. However, the S-vacancy sites also adsorb Cl^- more strongly and would likely be poisoned by chloride. The similar experimental chloride poisoning on Rh_xS_y/C and Rh/C (**Figure 4.1**) implies that the S-vacancy may be an active site, as those sites follow the nitrate and chloride scaling relation. Because the S-defected $Rh_3S_4(100)$ is the surface that has the strongest calculated nitrate adsorption, most similar to Rh(211), we hypothesize it is the active site, as it would have the highest coverage of nitrate on the surface. However, the rate constant of the surface reaction will also strongly affect the rate and is dictated by the activation energy of the RDS, thus to predict the active site we need to include both of these factors.

We predict the transition state energies for the direct (**Equation 4.4**) and H-assisted nitrate dissociation (**Equation 4.9**) reactions on pristine and S-defected Rh_xS_y surfaces to estimate the activation energies and rate constants of nitrate reduction and clarify the active site and nitrate dissociation mechanism. The data in **Figure 4.5** shows the predicted transition state and intermediate energies of nitrate to nitrite on $Rh_2S_3(100)$, $Rh_3S_4(100)$, and $Rh_{17}S_{15}(100)$, both without (**Figures 4.5a,c**) and with (**Figures 4.5b,d**) S vacancies. For comparison, the energy profile for direct nitrate reduction to nitrite on Rh(211) is shown in **Figure 4.5a**. The geometries and corresponding activation barriers (E_a) are shown in **Appendix B**. For direct reduction, shown in **Figures 4.5a–b**, all barriers represent a single dissociation step ($NO_3^* \rightarrow NO_2^* + O^*$) and so E_a is just the difference in the energy of the transition state and the adsorbed nitrate. However, for H-assisted reduction in **Figures 4.5c–d**, a two-step mechanism is possible: hydrogenation of nitrate ($H^* + NO_3^* \rightarrow HNO_3^* + {}^*$) followed by dissociation of nitric acid ($HNO_3^* + {}^* \rightarrow NO_2^* + HO^*$). For the H-assisted nitrate dissociation, we take the highest barrier for any step on a specific surface as the E_a for the reaction on that surface. For S-defected $Rh_3S_4(100)$ and $Rh_{17}S_{15}(100)$, barrier

calculations did not converge when HNO_3^* was modeled as an intermediate, so the barrier was modeled as a single, combined hydrogenation-dissociation step ($H^* + NO_3^* \rightarrow NO_2^* + HO^*$) in **Figure 4.5d**. We were unable to obtain a converged barrier for H-assisted reduction on Rh(211) after several computational attempts, so only include the direct nitrate dissociation on Rh(211).

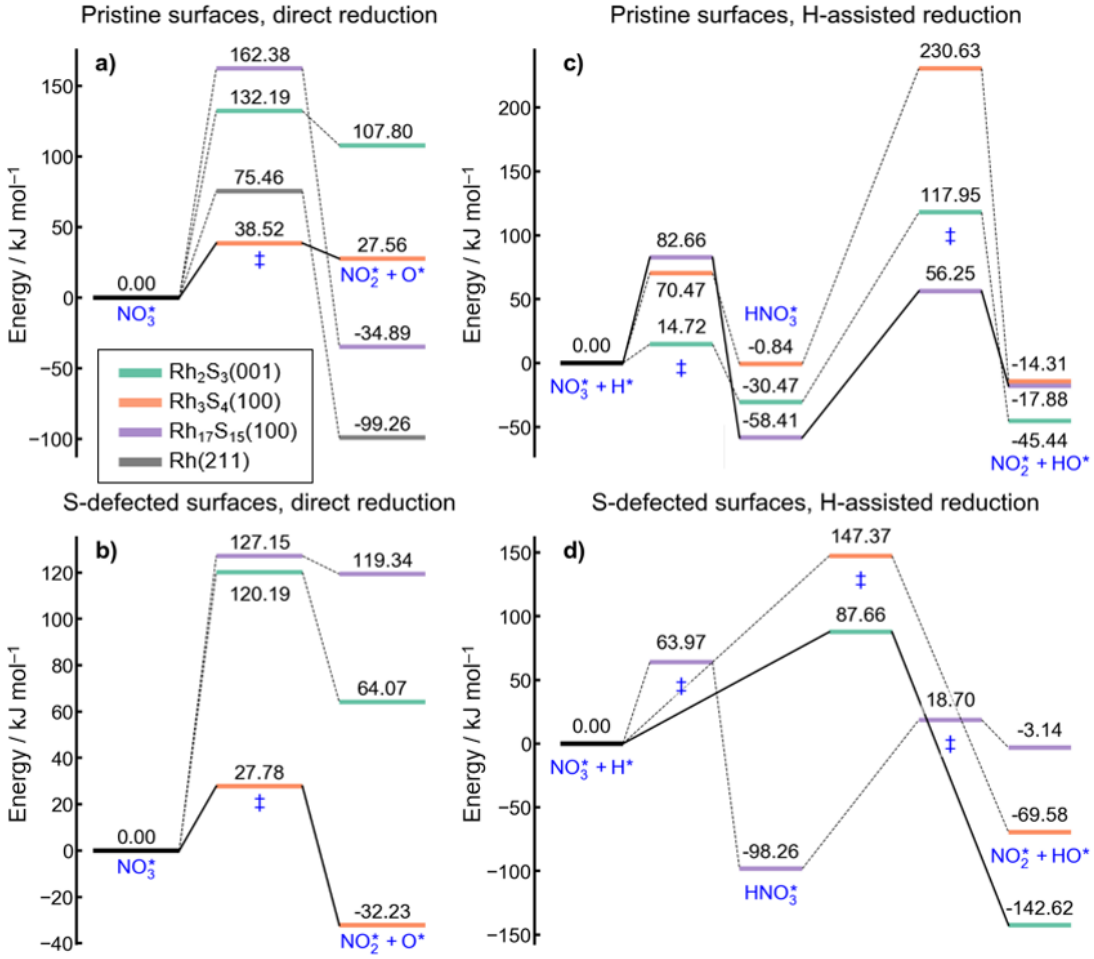

Figure 4.5. Reaction energy diagram for nitrate to nitrite dissociation on Rh_2S_3(001), Rh_3S_4(100), $Rh_{17}S_{15}$(100), and Rh(211) surfaces at 0 V vs. SHE. Diagrams are shown for (a, c) pristine versus (b, d) S-defected Rh_xS_y surfaces, and for (a, b) direct nitrate dissociation versus (c, d) H-assisted dissociation. Energies are referenced to the initial state in each diagram, and ‡ refers to a transition state. Color key shown in panel (a): teal = Rh_2S_3(001), orange = Rh_3S_4(100), purple = $Rh_{17}S_{15}$(100), gray = Rh(211).

With the adsorption energies of hydrogen and nitrate and activation barriers to convert NO_3* to NO_2* calculated on each surface, a theoretical turnover frequency (TOF) can be calculated for each facet and reaction mechanism. The adsorption energies are used to obtain the quasi-

equilibrated θ_{NO_3}, θ_*, and θ_H. The computed barriers are used to estimate the rate constants k_4 and k_9 in **Equation 4.8** and **Equation 4.10**, respectively, from an Arrhenius model, where 10^{12} s^{-1} is chosen as a representative pre-exponential factor for all reactions. The parameters input into the microkinetic model are shown in **Appendix B**. **Figure 4.6** shows the computed TOFs for each facet and the two possible mechanisms over the potential range E = 0 to 0.4 V vs. RHE.

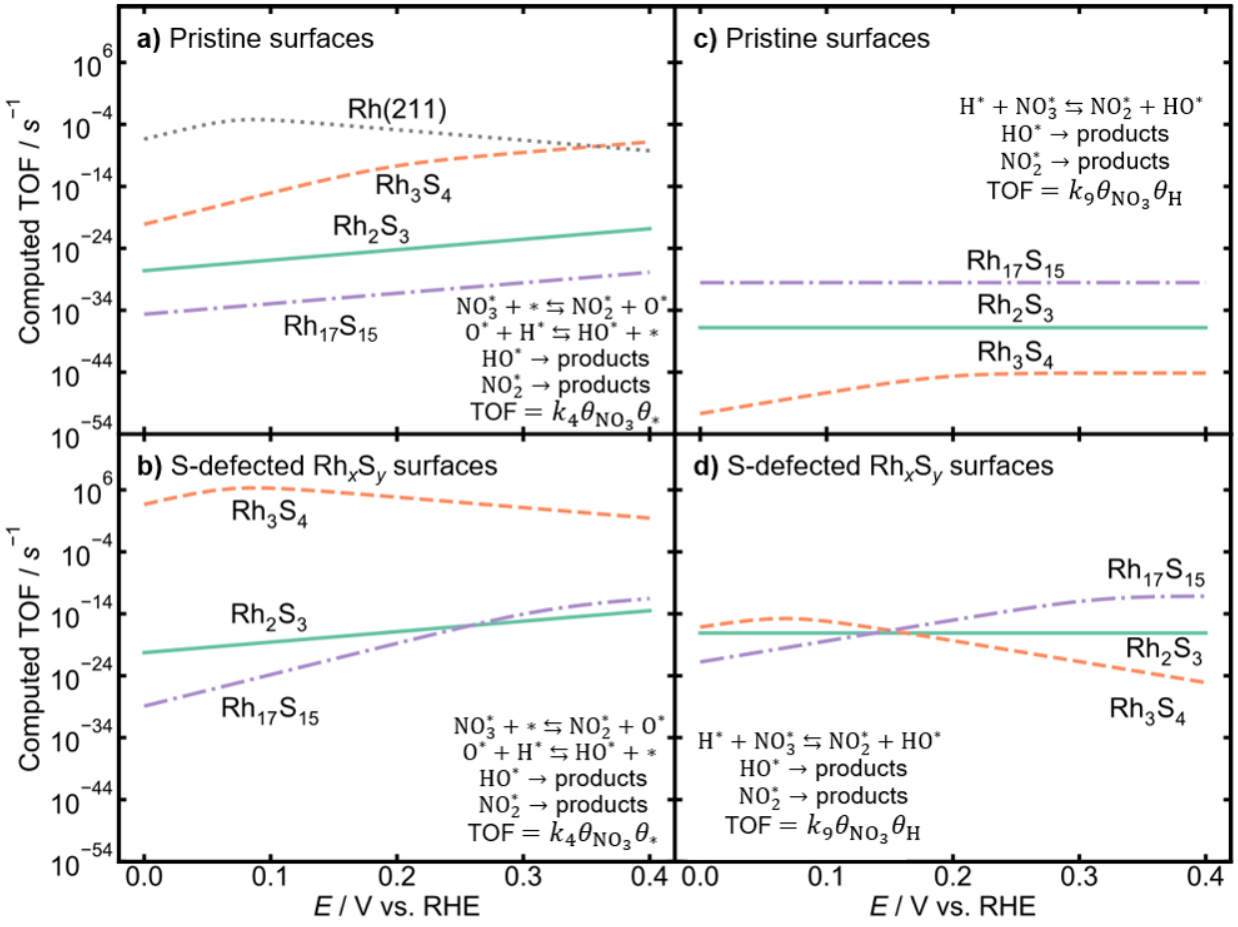

Figure 4.6. Computed TOFs for nitrate-to-nitrite dissociation as a function of applied potential on Rh_2S_3(001), Rh_3S_4(100), $Rh_{17}S_{15}$(100), and Rh(211), with initial solution concentrations of $[NO_3^-]_0$ = $[H^+]_0$ = 1 M and $[Cl^-]_0$ = 0 M. Diagrams are shown for (a, c) pristine versus (b, d) S-defected Rh_xS_y surfaces, and for (a, b) direct nitrate dissociation versus (c, d) H-assisted dissociation. Temperature is 298 K.

The computed TOF curves as a function of applied potential in **Figure 4.6** predict that S-defected Rh_3S_4(100) (**Figure 4.6b**) has the highest activity and follows the direct nitrate dissociation mechanism. The TOF is higher on the S-defected Rh_3S_4(100) facet than on any other

sulfide facet, as well as Rh(211). Although the S-defected Rh_3S_4(100) facet is predicted to have the highest activity by the H-assisted mechanism at potentials less than 0.15 V vs. RHE (**Figure 4.6d**), the absolute TOF through this mechanism is still lower than that of direct nitrate dissociation on the same surface. For applied potentials less than 0.35 V vs. RHE, no pristine surface is more active than Rh(211) (**Figure 4.6a**). The high activity of S-defected Rh_3S_4(100) is due to its strong nitrate adsorption energy, which enables high coverages of nitrate, and its relatively low activation barrier for nitrate dissociation (**Figure 4.5b**). S-defected Rh_3S_4(100) has a direct nitrate dissociation barrier lower than that of Rh(211), as well as comparable nitrate and chloride adsorption energies, rationalizing the high activity but moderate chloride poisoning resistance of Rh_xS_y/C observed experimentally. The experimental observation that Rh_xS_y/C has a higher nitrate reduction current density than Rh/C in 1 M H_2SO_4 + 1 M $NaNO_3$, but only by a factor of 1.6 to 5.6, is different than the several orders of magnitude shown in **Figure 4.6**. We attribute this qualitative agreement, but quantitative disagreement to 1) inaccuracies in our DFT modeling protocol, and 2) the fact that the predicted TOFs in **Figure 4.6** are for activity per site, and there may in fact be many fewer S-defects in the experimental system compared to non-defected sites, causing the measured TOF to be lower. However, as S-defected Rh_3S_4(100) is the most active defect site, and none of the pristine sites are predicted to have high nitrate reduction activity, we attribute the activity of Rh_xS_y/C for nitrate reduction to this site.

Future work to improve the performance of NO_3RR electrocatalysts in the presence of chloride will require verification of the active site and mechanism and preparation of materials with a higher fraction of these active sites. Selecting appropriate synthesis procedures and conditions will promote morphologies containing more such active sites at the surface.[75] Further testing of the hypothesis that the direct nitrate reduction mechanism is dominant on Rh_xS_y and H-

assisted mechanism is dominant on Pt may consist of isotopic labeling studies to identify kinetic isotopic effects. Spectroscopy to determine the active site of Rh_xS_y or to prove the H-assisted mechanism may include electron paramagnetic resonance to detect O- or H-containing radicals,[76] which may arise in the hydrogenation of nitrate and the dissociation of HNO_3. Ultimately, spectroscopy, such as Raman[40] or X-ray absorption spectroscopy,[33] under NO_3RR conditions is necessary to identify the catalyst structure. Additionally, the activity of the Rh_3S_4 phase can be tested by preparing Rh_xS_y with a higher fraction of Rh_3S_4 and determining whether the NO_3RR activity increases proportionally.[33,40] Higher catalyst utilization can be achieved by decreasing the particle size[77] or synthesizing Rh_xS_y catalysts as a shell over a less expensive and more earth-abundant core[78] to increase the fraction of active sites to total Rh atoms. Based on recent studies of the structure dependence of nitrate reduction,[54,55] Rh_xS_y/C may be even more active than Rh/C and Pt/C if compared at the same particle size. Future studies of the particle size dependence of nitrate reduction will be needed to confirm or deny this hypothesis. Exploration of site specific competitive adsorption of NO_3^- and Cl^- on Pt may be done using single crystals and deconvolution of the H_{upd} peaks.[61,62] To decrease the cost of the catalysts, new metal sulfides made of earth-abundant materials may be a useful target.[79]

4.4 Conclusions

In this work, we show Rh_xS_y/C is more active for electrocatalytic nitrate reduction than Rh and Pt and has 67% faradaic efficiency towards NH_4^+ at 0.1 V vs. RHE in 0.1 M HNO_3. When Cl^- is present, however, NO_3RR on Rh_xS_y/C is inhibited only slightly less than Pt/C and Rh/C, in contrast to the highly halide poison resistant behavior of Rh_xS_y/C for reactions such as oxygen reduction and hydrogen evolution. We develop microkinetic models considering direct nitrate dissociation and H-assisted nitrate dissociation to nitrite as the rate-determining step on Pt and Rh

and find that H-assisted nitrate dissociation best matches the experimentally observed NO_3RR activity and rate inhibition with chloride for Pt, whereas Rh matches either H-assisted or direct nitrate dissociation. Microkinetic modeling shows that competition between nitrate and chloride for surface coverage greatly influences the nitrate reduction rate. From DFT-calculated adsorption energies and microkinetic modeling, we show that metals that adsorb nitrate strongly and are active for NO_3RR will also adsorb chloride strongly and thus suffer inhibited NO_3RR activity. Rh_3S_4 terraces with S vacancies are predicted to adsorb nitrate strongly and have low activation barriers for direct nitrate dissociation compared to pristine surfaces, resulting in higher activity. S-defected $Rh_3S_4(100)$ is predicted to also adsorb chloride strongly and thus exhibit decreased NO_3RR rates, consistent with experimental measurements. Although Rh_xS_y/C is partially inhibited by chloride, it is more resistant to chloride poisoning and more active for NO_3RR than Pt/C or Rh/C. This makes Rh_xS_y/C a suitable catalyst for processes involving nitrate reduction with chloride present and motivates further studies of S vacancies in metal sulfides for NO_3RR.

4.5 References

1. Canfield, D. E., Glazer, A. N. & Falkowski, P. G. The Evolution and Future of Earth's Nitrogen Cycle. *Science* **330**, 192–196 (2010).
2. Lehnert, N., Dong, H. T., Harland, J. B., Hunt, A. P. & White, C. J. Reversing nitrogen fixation. *Nature Reviews Chemistry* **2**, 278–289 (2018).
3. Duca, M. & Koper, M. T. M. Powering Denitrification: The Perspectives of Electrocatalytic Nitrate Reduction. *Energy & Environmental Science* **5**, 9726–9742 (2012).
4. Ward, M. *et al.* Drinking Water Nitrate and Human Health: An Updated Review. *International Journal of Environmental Research and Public Health* **15**, 1557 (2018).
5. Council, N. R. *The Health Effects of Nitrate, Nitrite, and N-Nitroso Compounds*. *The Health Effects of Nitrate, Nitrite, and N-Nitroso Compounds: Part 1 of a 2-Part Study* (National Academies Press, 1981). doi:10.17226/19738.
6. Garcia-Segura, S., Lanzarini-Lopes, M., Hristovski, K. & Westerhoff, P. Electrocatalytic Reduction of Nitrate: Fundamentals to Full-Scale Water Treatment Applications. *Applied Catalysis B: Environmental* **236**, 546–568 (2018).
7. Singh, N. & Goldsmith, B. R. Role of Electrocatalysis in the Remediation of Water Pollutants. *ACS Catalysis* **10**, 3365–3371 (2020).

8. van Langevelde, P. H., Katsounaros, I. & Koper, M. T. M. Electrocatalytic Nitrate Reduction for Sustainable Ammonia Production. *Joule* **5**, 290–294 (2021).
9. Wang, Z., Richards, D. & Singh, N. Recent discoveries in the reaction mechanism of heterogeneous electrocatalytic nitrate reduction. *Catalysis Science & Technology* **11**, 705–725 (2021).
10. Wang, Z., Young, S. D., Goldsmith, B. R. & Singh, N. Increasing Electrocatalytic Nitrate Reduction Activity by Controlling Adsorption through PtRu Alloying. *Journal of Catalysis* **395**, 143–154 (2021).
11. Katsounaros, I. On the assessment of electrocatalysts for nitrate reduction. *Current Opinion in Electrochemistry* 100721 (2021) doi:10.1016/j.coelec.2021.100721.
12. Zhang, X. *et al.* Recent advances in non-noble metal electrocatalysts for nitrate reduction. *Chemical Engineering Journal* **403**, 126269 (2021).
13. Wang, Y., Wang, C., Li, M., Yu, Y. & Zhang, B. Nitrate electroreduction: mechanism insight, in situ characterization, performance evaluation, and challenges. *Chemical Society Reviews* **50**, 6720–6733 (2021).
14. Wang, Y., Yu, Y., Jia, R., Zhang, C. & Zhang, B. Electrochemical synthesis of nitric acid from air and ammonia through waste utilization. *National Science Review* **6**, 730–738 (2019).
15. Gao, J., Jiang, B., Ni, C., Qi, Y. & Bi, X. Enhanced reduction of nitrate by noble metal-free electrocatalysis on P doped three-dimensional Co3O4 cathode: Mechanism exploration from both experimental and DFT studies. *Chemical Engineering Journal* **382**, 123034 (2020).
16. Fernández-Nava, Y., Marañón, E., Soons, J. & Castrillón, L. Denitrification of wastewater containing high nitrate and calcium concentrations. *Bioresource Technology* **99**, 7976–7981 (2008).
17. Chauhan, R. & Srivastava, V. C. Electrochemical denitrification of highly contaminated actual nitrate wastewater by Ti/RuO2 anode and iron cathode. *Chemical Engineering Journal* **386**, 122065 (2020).
18. Bergquist, A. M., Choe, J. K., Strathmann, T. J. & Werth, C. J. Evaluation of a hybrid ion exchange-catalyst treatment technology for nitrate removal from drinking water. *Water Research* **96**, 177–187 (2016).
19. Choe, J. K. *et al.* Performance and Life Cycle Environmental Benefits of Recycling Spent Ion Exchange Brines by Catalytic Treatment of Nitrate. *Water Research* **80**, 267–280 (2015).
20. Reyter, D., Bélanger, D. & Roué, L. Optimization of the Cathode Material for Nitrate Removal by a Paired Electrolysis Process. *Journal of Hazardous Materials* **192**, 507–513 (2011).
21. Reyter, D., Bélanger, D. & Roué, L. Nitrate Removal by a Paired Electrolysis on Copper and Ti/irO2 Coupled Electrodes – Influence of the Anode/Cathode Surface Area Ratio. *Water Research* **44**, 1918–1926 (2010).
22. Singh, N. *et al.* Stable Electrocatalysts for Autonomous Photoelectrolysis of Hydrobromic Acid Using Single-Junction Solar Cells. *Energy Environ. Sci.* **7**, 978–981 (2014).
23. Horányi, G. & Rizmayer, E. M. Role of Adsorption Phenomena in the Electrocatalytic Reduction of Nitric Acid at a Platinized Platinum Electrode. *Journal of Electroanalytical Chemistry and Interfacial Electrochemistry* **140**, 347–366 (1982).
24. Wasberg, M. & Horányi, G. Electrocatalytic Reduction of Nitric Acid at Rhodized Electrodes and Its Inhibition by Chloride Ions. *Electrochimica Acta* **40**, 615–623 (1995).
25. Li, M., Feng, C., Zhang, Z. & Sugiura, N. Efficient Electrochemical Reduction of Nitrate to Nitrogen Using Ti/irO2-Pt Anode and Different Cathodes. *Electrochimica Acta* **54**, 4600–4606 (2009).

26. Pletcher, D. & Poorabedi, Z. The Reduction of Nitrate at a Copper Cathode in Aqueous Acid. *Electrochimica Acta* **24**, 1253–1256 (1979).
27. Li, N. & Lipkowski, J. Chronocoulometric Studies of Chloride Adsorption at the Pt(111) Electrode Surface. *Journal of Electroanalytical Chemistry* **491**, 95–102 (2000).
28. Horányi, G. & Wasberg, M. Comparative Radiotracer Study of the Adsorption of Cl−, HSO−4(SO2−4) and H2PO−4 Anions on Rhodized Electrodes. *Journal of Electroanalytical Chemistry* **404**, 291–298 (1996).
29. Horányi, G. & Wasberg, M. Polarization Behaviour of Nitric Acid at Rhodized Electrodes Partially Blocked by Chemisorbed Species. *Electrochimica Acta* **42**, 261–265 (1997).
30. Liu, J.-X., Richards, D., Singh, N. & Goldsmith, B. R. Activity and Selectivity Trends in Electrocatalytic Nitrate Reduction on Transition Metals. *ACS Catalysis* **9**, 7052–7064 (2019).
31. Gossenberger, F., Roman, T. & Groß, A. Equilibrium Coverage of Halides on Metal Electrodes. *Surface Science* **631**, 17–22 (2015).
32. Ziegelbauer, J. M., Gatewood, D., Gullá, A. F., Ramaker, D. E. & Mukerjee, S. X-Ray Absorption Spectroscopy Studies of Water Activation on an Rh_xS_y Electrocatalyst for Oxygen Reduction Reaction Applications. *Electrochemical and Solid-State Letters* **9**, A430 (2006).
33. Ziegelbauer, J. M. *et al.* Fundamental Investigation of Oxygen Reduction Reaction on Rhodium Sulfide-Based Chalcogenides. *The Journal of Physical Chemistry C* **113**, 6955–6968 (2009).
34. Singh, N. *et al.* Investigation of the Active Sites of Rhodium Sulfide for Hydrogen Evolution/Oxidation Using Carbon Monoxide as a Probe. *Langmuir* **30**, 5662–5668 (2014).
35. Ziegelbauer, J. M. *et al.* Chalcogenide Electrocatalysts for Oxygen-Depolarized Aqueous Hydrochloric Acid Electrolysis. *Electrochimica Acta* **52**, 6282–6294 (2007).
36. Ivanovskaya, A. *et al.* Transition Metal Sulfide Hydrogen Evolution Catalysts for Hydrobromic Acid Electrolysis. *Langmuir* **29**, 480–492 (2013).
37. Nguyen, T. V., Kreutzer, H., Yarlagadda, V., McFarland, E. & Singh, N. HER/HOR Catalysts for the H2-Br2 Fuel Cell System. *ECS Transactions* **53**, 75–81 (2013).
38. Masud, J. *et al.* Synthesis and Characterization of RhxSy/C Catalysts for HOR/HER in HBr. *ECS Transactions* **58**, 37–43 (2014).
39. Masud, J. *et al.* A Rh_xS_y/C Catalyst for the Hydrogen Oxidation and Hydrogen Evolution Reactions in HBr. *Journal of The Electrochemical Society* **162**, F455–F462 (2015).
40. Singh, N., Hiller, J., Metiu, H. & McFarland, E. Investigation of the Electrocatalytic Activity of Rhodium Sulfide for Hydrogen Evolution and Hydrogen Oxidation. *Electrochimica Acta* **145**, 224–230 (2014).
41. Rhee, C. K., Wasberg, M., Zelenay, P. & Wieckowski, A. Reduction of Perchlorate on Rhodium and Its Specificity to Surface Crystallographic Orientation. *Catalysis Letters* **10**, 149–164 (1991).
42. Ahmadi, A., Evans, R. W. & Attard, G. Anion—surface Interactions. *Journal of Electroanalytical Chemistry* **350**, 279–295 (1993).
43. Dima, G. E., de Vooys, A. C. A. & Koper, M. T. M. Electrocatalytic reduction of nitrate at low concentration on coinage and transition-metal electrodes in acid solutions. *Journal of Electroanalytical Chemistry* **554–555**, 15–23 (2003).
44. Lukaszewski, M., Soszko, M. & Czerwiński, A. Electrochemical Methods of Real Surface Area Determination of Noble Metal Electrodes - An Overview. *International Journal of Electrochemical Science* **11**, 4442–4469 (2016).

45. Connolly, J. F., Flannery, R. J. & Aronowitz, G. Electrochemical Measurement of the Available Surface Area of Carbon-Supported Platinum. *Journal of the Electrochemical Society* **113**, 577–580 (1966).
46. Singh, N., Gordon, M., Metiu, H. & McFarland, E. Doped Rhodium Sulfide and Thiospinels Hydrogen Evolution and Oxidation Electrocatalysts in Strong Acid Electrolytes. *Journal of Applied Electrochemistry* **46**, 497–503 (2016).
47. Katz, B. G., Griffin, D. W. & Davis, J. H. Groundwater quality impacts from the land application of treated municipal wastewater in a large karstic spring basin: Chemical and microbiological indicators. *Science of the Total Environment* **407**, 2872–2886 (2009).
48. Eaton, A. D., Clesceri, L. S. & Greenberg, A. E. (Eds.). *Standard Methods for the Examination of Water and Wastewater*. (APHA, 1995).
49. McEnaney, J. M. *et al.* Electrolyte Engineering for Efficient Electrochemical Nitrate Reduction to Ammonia on a Titanium Electrode. *ACS Sustainable Chemistry & Engineering* **8**, 2672–2681 (2020).
50. Chen, P. *et al.* Interfacial Engineering of Cobalt Sulfide/Graphene Hybrids for Highly Efficient Ammonia Electrosynthesis. *Proceedings of the National Academy of Sciences of the United States of America* **116**, 6635–6640 (2019).
51. Siriwatcharapiboon, W. *et al.* Promotion Effects of Sn on the Electrocatalytic Reduction of Nitrate at Rh Nanoparticles. *ChemElectroChem* **1**, 172–179 (2014).
52. Jia, R. *et al.* Boosting Selective Nitrate Electroreduction to Ammonium by Constructing Oxygen Vacancies in TiO_2. *ACS Catalysis* **10**, 3533–3540 (2020).
53. Liu, H. *et al.* Electrocatalytic Nitrate Reduction on Oxide-Derived Silver with Tunable Selectivity to Nitrite and Ammonia. *ACS Catalysis* **2**, 8431–8442 (2021).
54. Lim, J. *et al.* Structure Sensitivity of Pd Facets for Enhanced Electrochemical Nitrate Reduction to Ammonia. *ACS Catalysis* **11**, 7568–7577 (2021).
55. Han, Y. *et al.* Facet-controlled palladium nanocrystalline for enhanced nitrate reduction towards ammonia. *Journal of Colloid and Interface Science* **600**, 620–628 (2021).
56. Brylev, O., Sarrazin, M., Roué, L. & Bélanger, D. Nitrate and nitrite electrocatalytic reduction on Rh-modified pyrolytic graphite electrodes. *Electrochimica Acta* **52**, 6237–6247 (2007).
57. Guo, Y., Cai, X., Shen, S., Wang, G. & Zhang, J. Computational prediction and experimental evaluation of nitrate reduction to ammonia on rhodium. *Journal of Catalysis* **402**, 1–9 (2021).
58. Jerkiewicz, G. Electrochemical Hydrogen Adsorption and Absorption. Part 1: Under-Potential Deposition of Hydrogen. *Electrocatalysis* **1**, 179–199 (2010).
59. Łosiewicz, B., Jurczakowski, R. & Lasia, A. Kinetics of hydrogen underpotential deposition at polycrystalline rhodium in acidic solutions. *Electrochimica Acta* **56**, 5746–5753 (2011).
60. Taguchi, S. & Feliu, J. M. Electrochemical Reduction of Nitrate on Pt(S)[n(1 1 1) × (1 1 1)] Electrodes in Perchloric Acid Solution. *Electrochimica Acta* **52**, 6023–6033 (2007).
61. McCrum, I. T. & Janik, M. J. Deconvoluting Cyclic Voltammograms To Accurately Calculate Pt Electrochemically Active Surface Area. *The Journal of Physical Chemistry C* **121**, 6237–6245 (2017).
62. McCrum, I. T. & Janik, M. J. pH and Alkali Cation Effects on the Pt Cyclic Voltammogram Explained Using Density Functional Theory. *The Journal of Physical Chemistry C* **120**, 457–471 (2016).

63. Gómez, R., Orts, J. M., Álvarez-Ruiz, B. & Feliu, J. M. Effect of Temperature on Hydrogen Adsorption on Pt(111), Pt(110), and Pt(100) Electrodes in 0.1 M HClO 4. *The Journal of Physical Chemistry B* **108**, 228–238 (2004).
64. Ishikawa, Y., Mateo, J. J., Tryk, D. A. & Cabrera, C. R. Direct molecular dynamics and density-functional theoretical study of the electrochemical hydrogen oxidation reaction and underpotential deposition of H on Pt(111). *Journal of Electroanalytical Chemistry* **607**, 37–46 (2007).
65. Stamenkovic, V., M. Markovic, N. & Ross, P. N. Structure-Relationships in Electrocatalysis: Oxygen Reduction and Hydrogen Oxidation Reactions on Pt(111) and Pt(100) in Solutions Containing Chloride Ions. *Journal of Electroanalytical Chemistry* **500**, 44–51 (2001).
66. Markovic, N., Hanson, M., McDougall, G. & Yeager, E. The Effects of Anions on Hydrogen Electrosorption on Platinum Single-Crystal Electrodes. *Journal of Electroanalytical Chemistry and Interfacial Electrochemistry* **214**, 555–566 (1986).
67. Calle-Vallejo, F., Huang, M., Henry, J. B., Koper, M. T. M. & Bandarenka, A. S. Theoretical Design and Experimental Implementation of Ag/Au Electrodes for the Electrochemical Reduction of Nitrate. *Physical Chemistry Chemical Physics* **15**, 3196 (2013).
68. Mathew, K., Sundararaman, R., Letchworth-Weaver, K., Arias, T. A. & Hennig, R. G. Implicit Solvation Model for Density-Functional Study of Nanocrystal Surfaces and Reaction Pathways. *The Journal of Chemical Physics* **140**, 084106 (2014).
69. Zhao, Z.-J. *et al.* Theory-Guided Design of Catalytic Materials Using Scaling Relationships and Reactivity Descriptors. *Nature Reviews Materials* **4**, 792–804 (2019).
70. He, Z. *et al.* Indium Sulfide Nanotubes With Sulfur Vacancies as an Efficient Photocatalyst for Nitrogen Fixation. *RSC Advances* **9**, 21646–21652 (2019).
71. Hu, S., Chen, X., Li, Q., Zhao, Y. & Mao, W. Effect of Sulfur Vacancies on the Nitrogen Photofixation Performance of Ternary Metal Sulfide Photocatalysts. *Catalysis Science & Technology* **6**, 5884–5890 (2016).
72. Wang, L. *et al.* A Mechanism Investigation of How the Alloying Effect Improves the Photocatalytic Nitrate Reduction Activity of Bismuth Oxyhalide Nanosheets. *ChemPhotoChem* **4**, 110–119 (2020).
73. Hensen, E. J. M., Vissenberg, M. J., de Beer, V. H. J., van Veen, J. A. R. & van Santen, R. A. Kinetics and Mechanism of Thiophene Hydrodesulfurization Over Carbon-Supported Transition Metal Sulfides. *Journal of Catalysis* **163**, 429–435 (1996).
74. Brunet, R. C. & Garcia-Gil, L. J. Sulfide-Induced Dissimilatory Nitrate Reduction to Ammonia in Anaerobic Freshwater Sediments. *FEMS Microbiology Ecology* **21**, 131–138 (1996).
75. Ehsan, M. A. *et al.* Morphologically controlled rapid fabrication of rhodium sulfide (Rh 2 S 3) thin films for superior and robust hydrogen evolution reaction. *Sustainable Energy & Fuels* **5**, 459–468 (2021).
76. Senesi, N. & Senesi, G. S. Electron-Spin Resonance Spectroscopy. in *Encyclopedia of Soils in the Environment* 426–437 (Elsevier, 2005). doi:10.1016/B0-12-348530-4/00209-5.
77. Li, Y. & Nguyen, T. Van. High Hydrogen Evolution Reaction (HER) and Hydrogen Oxidation Reaction (HOR) Activity RhxSy Catalyst Synthesized with Na2S for Hydrogen-Bromine Fuel Cell. *Energies* **13**, 3971 (2020).

78. Li, Y. & Nguyen, T. Van. Core-shell rhodium sulfide catalyst for hydrogen evolution reaction / hydrogen oxidation reaction in hydrogen-bromine reversible fuel cell. *Journal of Power Sources* **382**, 152–159 (2018).
79. Fajardo, A. S., Westerhoff, P., Sanchez-Sanchez, C. M. & Garcia-Segura, S. Earth-abundant elements a sustainable solution for electrocatalytic reduction of nitrate. *Applied Catalysis B: Environmental* **281**, 119465 (2021).

Chapter 5

Comparison of Nitrate Reduction Activities of Rh/C, Pt/C, and PtRu/C as Measured in Batch and Flow Reactor Configurations

5.1 Introduction

Nitrate emissions from industry and agriculture practices have detrimental environment and health effects, therefore there is increased interest in methods for remediation of water sources and waste streams.[1–3] The United States Environmental Protection Agency has limited the maximum contaminant level of nitrate to 10 mg/L to reduce health risks associated with consuming high concentrations of nitrate in drinking water.[4–6] Methods explored for removing nitrate from water sources include ion exchange, biological denitrification, membrane separation, and catalytic nitrate reduction.[2,7] Electrocatalytic nitrate reduction is appealing over the other proposed methods from many standpoints. Unlike biological denitrification and thermal catalytic reduction, electrocatalytic nitrate reduction does not require additives such as carbon sources or hydrogen.[7] Additionally, electrocatalytic nitrate remediation could be powered entirely from renewable sources. The conversion of nitrate to value-added or benign products, such as NH_3/NH_4^+ or N_2, respectively, without producing a secondary waste stream is an exclusive advantage to this remediation method.

Exploration of catalysts and mechanism studies have allowed many low cost, active nitrate reduction reaction (NO_3RR) catalysts to be identified.[1,8,9] Rh is an active nitrate reduction electrocatalyst because it adsorbs nitrate strongly, but not so strongly that nitrate poisons the catalyst surface. On the other hand, Pt adsorbs nitrate weakly and has low activity for nitrate

reduction. In **Chapter 3**, we identified that the nitrate binding energy could be used to understand the activity of nitrate reduction electrocatalysts. One of the electrocatalysts that had a nitrate adsorption energy similar to that of Rh was Pt_3Ru.[10] The PtRu alloy was synthesized and tested for nitrate reduction activity and confirmed to have enhanced activity compared to Pt or Ru.[11] For understanding reaction kinetics, the Pt, PtRu, and Rh catalysts are tested in batch reactors with ideal nitrate reduction solutions.

Batch reactors are compatible for precise collection of kinetic information, with rotating disk electrode (RDE) assemblies often being used to eliminate mass transport effects but are not reflective of electrochemical reactors which are used industrially. Flow cell reactors can treat large volumes effluent. Until recently, there have been limited studies of electrocatalytic nitrate reduction in flow cells.[12–17] A study by Abdallah, et al. evaluated an electrodeposited Cu on Ni-modified graphite felt for nitrate reduction in a flow cell where they found a flow rate of 2 mL min^{-1} and pH of 7.2 (phosphate buffer) with 3 g L^{-1} nitrate resulted in the highest nitrate reduction current efficiency and highest selectivity towards ammonia when 1.24 A was applied.[18] Another study by Daiyan, et al. showed high yield of ammonium using a CuO electrode in a membrane electrode assembly integrated flow electrolyzer with 0.05 M KNO_3 and 0.05 M H_2SO_4 flowing at 10 mL min^{-1} at a total cell potential of 2.5 V.[19] Neither of these studies use a reference electrode during flow cell electrolysis, therefore fair comparison of activities obtained by catalysts in batch cells (e.g., using a wire or RDE) cannot be made. Currently there are no studies comparing nitrate reduction performance (activity and selectivity) of a single catalyst in both a batch and flow cell system. For other reactions such as oxygen evolution reaction or CO_2 reduction, there have been noted differences in catalyst performance between a batch and flow reactor configuration.[20–22]

Knowing how the activity of catalysts transfers between systems would be extremely useful in scaling up nitrate reduction.

In this chapter, we answer the following questions:

1. Can we use techniques to measure ECSA in the RDE for the flow cell?
2. Are the current densities in the RDE transferable to the current densities in the flow cell?
3. Is the mass transport different in the flow cell and RDE?
4. Are the catalyst activity trends the same in the flow cell as for the RDE? (Rh/C > PtRu/C > Pt/C)?
5. Are the potential dependences the same in the RDE and flow cell?
6. What is the maximum partial current density to ammonia achieved in a flow cell?

5.2 Methods

5.2.1 Electrocatalyst preparation.

Supported nanoparticle catalysts were prepared as inks and deposited on a glassy carbon rotating disk electrode (RDE, Pine Research Inst., Inc) or a carbon felt (6.35 mm thick, 99.0%, Alfa Aesar) as described in **Chapter 2.1.1.** 30 wt% Pt/C, 20 wt% Rh/C, and 30 wt% PtRu/C were used as catalysts (purchased from Fuel Cell Store). For all inks, a 5 wt% Nafion in alcohol solution (Sigma Aldrich) was used as the binder.

For RDE measurements, the glassy carbon disk was polished with 0.05 μm alumina suspension (Allied High Tech Products, Inc.) on a micropolishing cloth and ultrasonicated in ultrapure water (18.2 MΩ cm, Millipore Milli-Q system) for 30 minutes. Simultaneously, the catalyst ink was also sonicated for 30 minutes in a scintillation vial. The RDE disk was then rinsed gently with ultrapure water and assembled into the Teflon rotating disk holder. The catalyst was deposited on the surface via drop casting 8 μL of the ink twice, allowing the ink to air dry between

depositions. Prior to electrochemical measurements, the catalysts deposited on the RDE were electrochemically cleaned in 0.1 M H_2SO_4 (–0.2 to 1 V vs. RHE at 50 mV s^{-1} for 30 cycles for Pt/C, –0.2 to 0.75 V vs. RHE at 50 mV s^{-1} for 30 cycles for Rh/C, and –0.2 to 0.8 V vs. RHE at 50 mV s^{-1} for 30 cycles for PtRu/C).

For flow cell measurements, a 2.3 cm by 2.4 cm area of carbon felt was alternatingly rinsed with ultrapure water and acetone at least three times to remove the hydrophobic coating, with the last solvent as ultrapure water. The carbon felt was then dried on a hot plate at 80 °C. Meanwhile, the catalyst ink was prepared and sonicated in a scintillation vial for at least 30 minutes. Over the hot plate, the catalyst ink was drop cast on one side using a glass pipette until the side of the carbon felt was saturated (~ 1 mL of catalyst ink). The carbon felt was let dry over the hot plate for 30 minutes, flipped using tweezers, and more catalyst ink was applied to the second side (now top-facing). This procedure was repeated until all catalyst ink was drop cast onto the carbon felt and let dry over the hot plate at 80 °C. The dry carbon felt with catalyst was then placed in a beaker with ultrapure water and pressed gently using the flat bottom of a scintillation vial to remove the air pockets and increase contact with the electrolyte. Once placed into the flow cell, a negative current (-50 mA) was applied for 3-5 minutes with 0.1 M H_2SO_4 flowing at 0.5 mL/min to reduce the catalyst and pretreat before electrochemical measurements.

5.2.2 Electrochemically active surface area.

The electrochemically active surface area (ECSA) was measured using hydrogen underpotential deposition (H_{upd}) on Pt/C, Rh/C, and PtRu/C. Copper underpotential deposition (Cu_{upd}) was only measured on PtRu/C in the batch cell configuration. The average charge density for Pt/C and PtRu/C was 210 μC cm^{-2} and for Rh/C was 221 μC cm^{-2}.[23] The ECSA for normalizing

current was measured prior to each electrochemical measurement (each current density has an ECSA value).

In the batch electrochemical cell with the RDE, the H_{upd} measurements on all catalysts were taken at 50 mV/s in de-oxygenated 0.1 M H_2SO_4 without agitation and with 85% iR correction (<1 mV iR correction average). In the flow cell, the H_{upd} measurements were taken at 50 mV/s on Rh/C and PtRu/C carbon felts and at 5 mV/s for Pt/C (due to signal issues related to the high amount of Pt/C used) in 0.1 M H_2SO_4 flowing at 0.5 mL/min. The H_{upd} cyclic voltammograms from the flow cell were iR corrected after measurement. For both systems, the baseline current at 0.4 V vs. RHE was subtracted to correct for double-layer charging. The potential range used was 0.05 V to 0.8 V vs. RHE for Rh/C and 0.05 V to 1.0 V vs. RHE for Pt/C and PtRu/C.

Cu_{upd} was performed only in a batch electrochemical cell to avoid potential contamination issues that could arise from introducing Cu^{2+} into the flow cell. Cu_{upd} on PtRu/C was performed after H_{upd} but in a separate electrochemical cell with de-oxygenated 0.1 M H_2SO_4 + 2 mM $CuSO_4$. The electrode was held at 1.0 V vs. RHE to ensure no copper was adsorbed to the surface, 0.42 V vs. RHE was applied for 3 minutes to form a monolayer, and then a linear scan voltammogram at 100 mV/s from 0.42 V to 1.0 V vs. RHE was used to strip the copper monolayer from the surface. Other monolayer deposition potentials and times were investigated and 0.42 V vs. RHE was selected as the most appropriate (no bulk Cu deposition and maximum current). A slanted baseline charge from the H_{upd} current at 0.4 V vs. RHE was used to correct for charge contribution from double-layer charging.

5.2.3 Electrocatalytic nitrate reduction reaction measurements.

Nitrate reduction measurements were taken at a constant potential for 20 minutes on a VSP or SP 150 potentiostat using EC-Lab software (BioLogic, Inc.). In the both the batch and flow cell, the current density reported was from the average current during the last 5 minutes of the measurement. In the batch cell with the catalysts deposited on a RDE, 85% iR compensation was applied during the measurement and the correction was less than 1 mV. iR correction for the flow cell measurements was applied after measurement; the series resistance was ~0.05 Ω for all catalysts in 0.1 M H_2SO_4 and 0.1 M HNO_3. For the flow cell, a sample of the outlet solution was taken during the last 5 minutes of the measurement.

The electrolytes for the working and counter electrode compartments were held in 60 mL plastic syringes and flowed through the electrochemical cell using a syringe pump (LongerPump® model LSP02-1B). The electrolyte was sparged with N_2 for 1 hour prior to being drawn into the syringe. The electrolyte in the syringe was degassed by drawing a slight vacuum by pulling the plunger, tapping on the side of the syringe, and releasing the gases that accumulated at the opening of the syringe. Degassing was performed until the amount of gas at the opening of the syringe was negligible. The solution in the syringes was degassed to prevent formation of gas pockets (of O_2 or H_2) within the electrochemical cell or carbon felt during operation which could lower the available surface area for reaction or increase the cell potential.

5.2.4 Product quantification and faradaic efficiency towards ammonium.

The samples for constant potential measurements were collected in a scintillation vial at the outlet of the flow cell over the last 5 minutes of the measurement. With the electrochemical flow reactor, there is a time delay between the reaction/creation of product at the electrode and the collection point used for product analysis. Therefore, for constant potential measurements, the Faradaic efficiency cannot be calculated using the currents from the same time the sample was

collected. For Faradaic efficiency analysis, the currents from one residence time prior from the sample collection time were used.

Ultraviolet-visible (UV-Vis) spectroscopy was used for quantification of ammonium (NH_4^+) from the nitrate reduction measurements in the flow cell. Ammonium itself is not active in the UV-Vis range, therefore the salicylate colorimetric method was used.[24] Details on the colorimetric reagents and sample calibration curves are given in **Chapter 2.4.2**.

5.3 Results and Discussion

5.3.1 Determining the electrochemically active surface area of Pt/C, Rh/C, and PtRu/C as deposited with an ink on a rotating disk and carbon felt.

Measuring the electrochemical surface area is imperative to compare the catalyst performance in the batch RDE system and the carbon felt flow cell system. ECSAs were determined for catalysts in the batch RDE system and the flow cell system while loaded on a carbon felt. **Figure 5.1a-c** shows typical hydrogen underpotential deposition and **Figure 5.1d** shows a copper underpotential deposition measurement obtained when estimating the ECSAs of Rh/C, Pt/C, and PtRu/C catalysts. After normalization to the ECSA and adjusting for differences in scan rate, the current densities from H_{upd} are on the same order of magnitude between the two systems. For Rh/C and Pt/C, the characteristic hydrogen underpotential peaks are visible on both the carbon felt and RDE, even though the mass loading on the carbon felt is two to three orders of magnitude greater on the carbon felts compared to the RDEs. Though the currents are on of the same magnitude, the PtRu/C H_{upd} currents have an additional current peak in the H_{upd} region when measured in the flow cell.

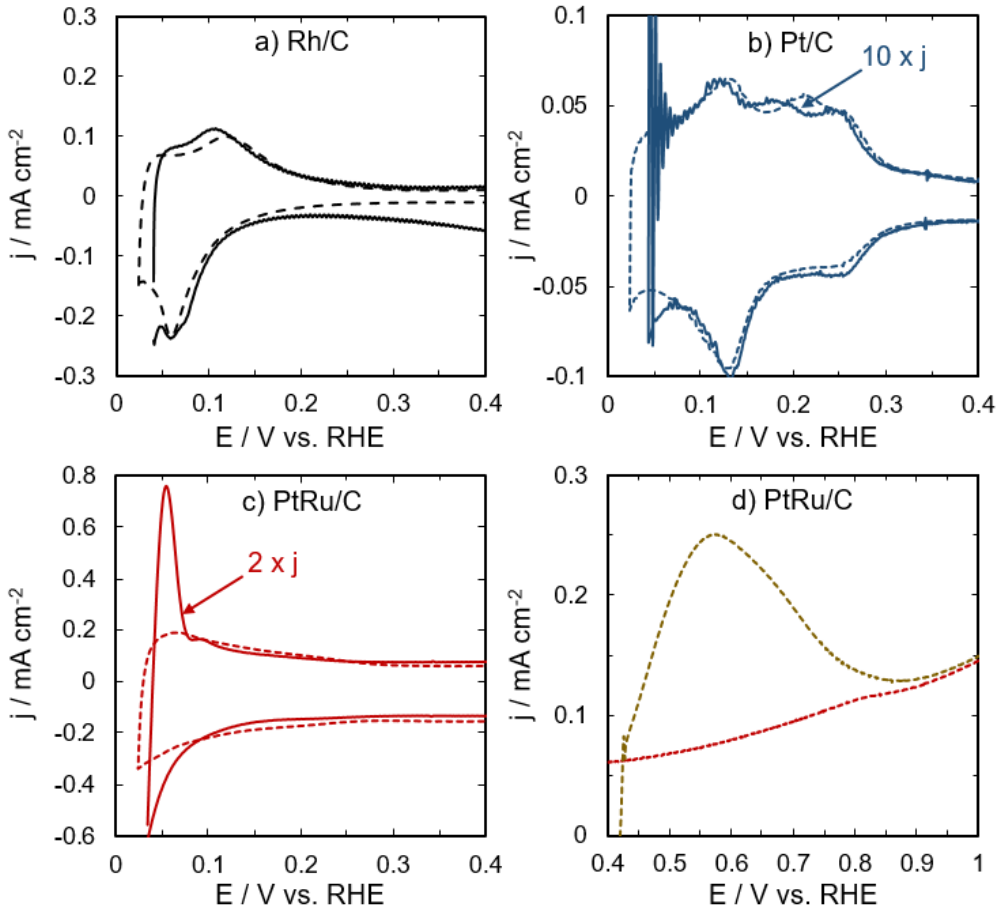

Figure 5.1. Hydrogen underpotential deposition (H_{upd}) and copper underpotential deposition (Cu_{upd}) were used to estimate the electrochemically active surface area of Rh/C, Pt/C, and PtRu/C deposited onto either a glassy carbon electrode (RDE, dashed lines) or a carbon felt (flow cell, solid lines). H_{upd} current densities for (a) Rh/C were taken at 50 mV/s. For (b) Pt/C, the H_{upd} was measured at 50 mV/s in the batch cell and at 5 mV/s in the flow cell. The flow cell currents for Pt/C are multiplied by 10 times to account for the difference in scan rate. The H_{upd} for (c) PtRu/C on was taken at 100 mV/s and 50 mV/s on the RDE and carbon felt in the flow cell, respectively. The currents for PtRu/C in the flow cell are multiplied by 2 to compare to the RDE H_{upd} currents. All H_{upd} measurements were taken in de-oxygenated 0.1 M H_2SO_4. (d) Cu_{upd} current density and the corresponding baseline current density (without $CuSO_4$) are given for PtRu/C deposited on a glassy carbon RDE in 0.1 M H_2SO_4 + 2 mM $CuSO_4$ at 100 mV/s.

The fraction of catalyst that is electrochemically active is higher on the RDE than on the carbon felt for all catalysts tested (**Table 5.1**). Reasons why the catalysts deposited onto the felt have lower ECSA per mass loaded when deposited are due to catalyst loss on the felts, parts of the catalyst may not be accessible to the electrolyte due to packing of the catalyst on the felt, and underestimation of ECSA using H_{upd} for catalyst in the felts. The felt loading is estimated by subtracting the mass of catalyst that does not adhere to the felt (collected after deposition) by the

total mass of catalyst attempted to be deposited onto the felt. Though an ionomer binder is used during catalyst deposition on to the carbon felts, the catalyst nanoparticles can be knocked loose from the felt during the reaction and have been observed in the outlet collection reservoir after the experiment. Catalyst loss on the felts would underestimate the ECSA per mass for the carbon felts with catalyst. Additionally, over-packing the electrocatalyst ink on the carbon felt could reduce the amount of active material that is available to the solution by creating layers of catalyst ink, where the bottom layer does not contact the solution. Lastly, for Pt group catalysts on high surface area supports, H_{upd} has limited accuracy for estimating the surface area. The support in these systems can contribute to the current in the H_{upd} and double-layer regions, affecting the H_{upd} analysis.

Table 5.1. Catalyst loading (metal only) onto RDE and felt, electrochemically active surface area from H_{upd} or Cu_{upd}, and ECSA per mass metal loaded. RDE geometric area is 0.196 cm^2 and felt geometric area is 5.52 cm^2.

Catalyst	RDE loading	ECSA from RDE	ECSA per mass	Felt loading	ECSA from felt	ECSA per mass
20 wt% Rh/C	2.9 µg	2.3 cm^2	78.1 m^2/g	2.0 mg	142 cm^2	34.6 m^2/g
30 wt% Pt/C	1.9 µg	2.0 cm^2	105.3 m^2/g	5.5 mg	1012 cm^2	60.6 m^2/g
30 wt% PtRu/C	1.9 µg	1.2 cm^2	63.7 m^2/g	3.3 mg	374 cm^2	37.8 m^2/g

5.3.2 Catalyst stability assessment using initial ECSA as a benchmark.

All three catalysts lose ECSA during nitrate reduction, but PtRu/C especially undergoes preferential Ru dissolution. **Figure 5.2** shows the H_{upd} currents observed on each catalysts before and after 20 minutes of chronoamperometry at 0.1 V vs. RHE in the batch RDE system. The Rh/C and Pt/C begin with ECSAs of 2.26 cm^2 and 2.00 cm^2 but decrease by 7-18% (to 1.84 cm^2 for Rh/C and 1.86 cm^2 for Pt/C) after 20 minutes of measurements. Using H_{upd} to estimate the ECSA, the PtRu/C begins with 0.76 cm^2 and increases to 0.95 cm^2 after nitrate reduction. In Figure 5.2c, the H_{upd} currents decrease at the adsorption potentials (0-0.3 V vs. RHE) and the overall increase

in ECSA is due to the decrease of charge in the double-layer (measured at 0.4 V vs. RHE) and changing of the electrode surface discussed below.

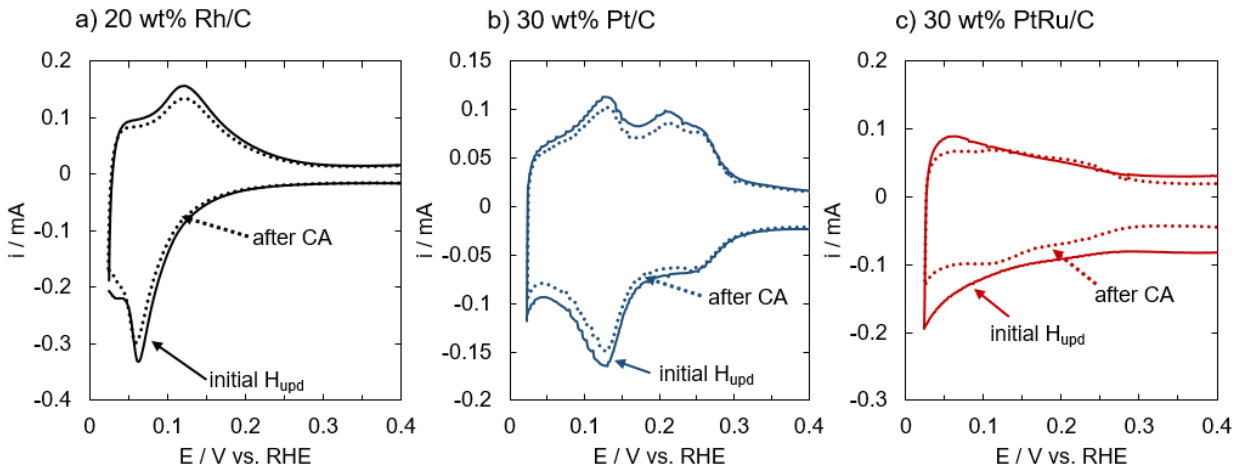

Figure 5.2. H_{upd} and Cu_{upd} currents at 50 mV/s in 0.1 M H_2SO_4 for a) Rh/C, b) Pt/C, and c) PtRu/C on RDE before and after the electrode was used for electrocatalytic nitrate reduction at 0.1 V vs. RHE in 0.1 M HNO_3. CA = chronoamperometry.

The cause of the ECSA loss may be related to poisoning of intermediates, surface restructuring, or mechanical loss. We have reported some catalyst loss from catalysts deposited as inks due to mechanical loss at high RDE rotation previously.[25] The PtRu is known to dissolve Ru preferentially at oxidative potentials.[26,27] To address the issue of varying ECSA for kinetic measurements, we measure the ECSA before and after kinetic measurements to account for the decrease in available surface area. Between prior to and between sequential nitrate reduction measurements, the electrodes are cycled between oxidative and reductive potentials to clean the electrode surface, which for PtRu/C would cause Ru dissolution during the cleaning procedure.

5.3.3 Comparison of nitrate reduction activity on Pt/C, Rh/C, and PtRu/C using a rotating disk electrode and flow cell assembly.

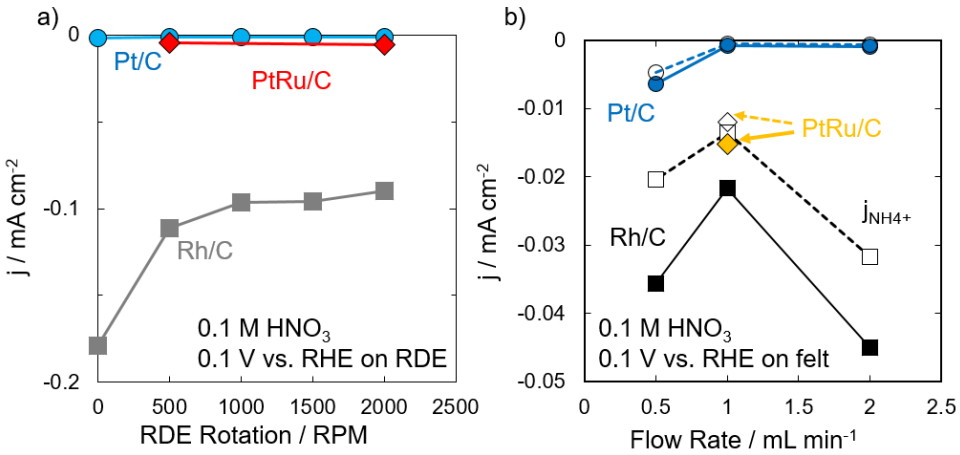

Figure 5.3. Steady-state nitrate reduction current density (j, solid lines) and partial current density to ammonia (dashed lines) at 0.1 V vs. RHE on Pt/C (circles), Rh/C (squares), and PtRu/C (diamonds) in 0.1 M HNO_3 at different a) rotation rates in the batch cell with catalyst on a rotating disk electrode and b) flow rates in the flow cell with catalyst supported on a carbon felt.

The magnitudes of the current densities at a given potential do not match for all catalysts between those in the RDE and those in the flow cell. Within the flow cell activity sets, there is large uncertainty in the value reported (e.g., Rh/C at 0.1 V vs. RHE at 2 mL/min is 4-5 times greater in **Figure 5.4c** compared to what is reported in **Figure 5.3b**) even though the data was collected and analyzed similarly. For RDE experiments, the currents densities for each catalyst measured at the same conditions are closer (less than 25% variations). This may be due to the uniformity of the RDE catalyst deposition compared to the poor uniformity when depositing on the carbon felt. At 0.1 V vs. RHE in 0.1 M HNO_3, the current density on Pt/C on the RDE in **Figure 5.3a** ranges from −0.002 to −0.001 mA cm^{-2}, with higher rates at lower rotation rates, while the current density in the flow cell ranges from −0.006 to −0.001 mA cm^{-2}, with higher rates at slower flow rates. Slower mass transport could result in a concentration gradient near the electrode surface, e.g., depletion of nitrate and protons. The local pH increase and nitrate concentration decrease may cause the differences in the reduction rate on the different catalysts. For Pt/C at 0.1 M $NaNO_3$ the nitrate reaction order is 0.51 for nitrate as measured in 0.5 M H_2SO_4.[28] For Pt with nitrate concentrations greater than 0.1 M, the nitrate reduction activity is expected to

increase with increasing nitrate concentration.[29] At higher pH values, the nitrate reduction rate of Pt is reported to decrease.[29] The reported pH and nitrate concentration effects suggest that a local pH increase and nitrate concentration decrease would not enhance the nitrate reduction activity on Pt. Alternatively other mechanisms, such as indirect nitrate reduction on Pt/C,[30] or non-uniformity in the fluid flow pattern within the flow cell at low flow rate could be considered but would need further exploration. The faradaic efficiency to ammonia on Pt/C in the flow cell is lower than what has been reported in batch systems.[11] We hypothesize this is due to higher ammonium crossover to the anode in the flow cell system due to the higher surface area of the membrane. For PtRu/C, on the RDE the current densities are approximately −0.005 mA cm^{-2}, while in the flow cell the current densities are approximately −0.015 mA cm^{-2}. We attribute this to the normalization of the activity, since the RDE measurements were normalized based on the H_{upd} ECSA, while the flow cell was normalized based on the dispersion. On Rh/C, the current densities in the RDE are higher than in the flow cell at 0.1 V vs. RHE. Similar to Pt/C, the higher current densities for Rh/C on the RDE may be due to mass transport at the electrode in the different cell configurations. Nitrate reduction on Rh in acidic conditions can proceed though both direct and H-assisted reduction pathways;[29] the concentration profiles provided by the different mass transport conditions may promote one or the other depending on the conditions. During a single pass, even at the highest current densities for Rh/C in the flow cell, the conversions are less than 1% (equivalent to 1 mM for 0.1 M $HNO_{3)}$, indicating depletion of nitrate is not a factor. The faradaic efficiency to ammonia for Rh/C in the flow cell are lower than previously measured in batch reactors.[25] Ultimately, the difference in magnitude between the RDE and the flow cell current densities could be attributed to the ECSA normalization for the measurements in the flow cell.

The activity trends on an RDE (Pt/C < PtRu/C < Rh/C) match those in the flow cell. In **Figure 5.3a**, under all rotation conditions Rh/C is the most active, followed by PtRu/C, then Pt/C. The same trends are seen in the flow cell in **Figure 5.3b**. Thus, although the exact values of the current densities imply inaccuracies in ECSA measurement, and possible mass transport artifacts, the trends in activity are captured in both reactors.

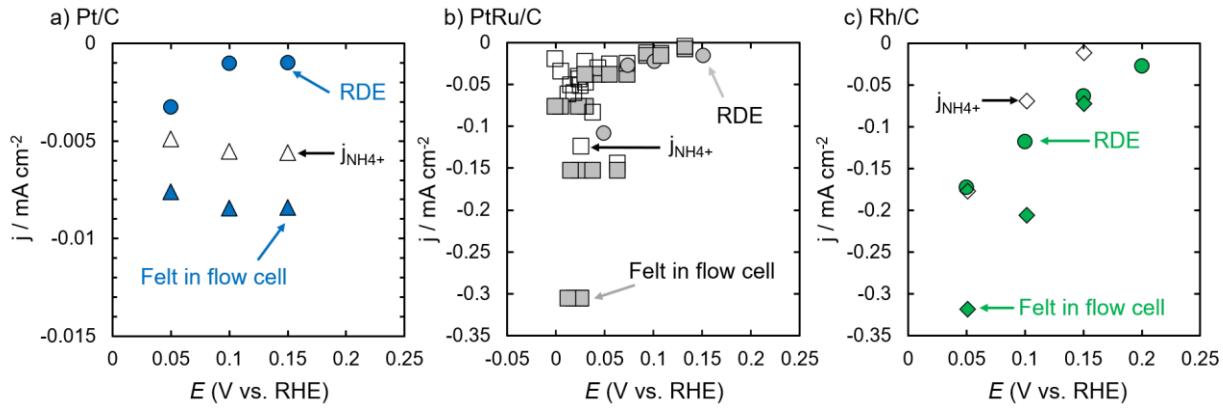

Figure 5.4. Steady-state nitrate reduction current density (j) and partial current density to ammonia (j_{NH4+}) at potentials between 0 and 0.2 V vs. RHE in the batch cell at 2000 rpm and the flow cell at 2 mL min^{-1} for a) Pt/C, b) PtRu/C, and c) Rh/C in 0.1 M HNO_3. Open symbols represent partial current densities.

The effect of potential is qualitatively similar in the RDE as in the flow cell on PtRu/C and Rh/C, but different on Pt/C. On Pt/C, with the RDE as the potential becomes more negative the activity increases, but in the flow cell as the potential becomes more negative the activity decreases slightly. The difference in the potential dependence on Pt/C implies that one or both of the observed activity measurements are not intrinsic kinetics (i.e., one or both are limited by mass transport). We hypothesize that the RDE measurements are at sufficiently high transport that they are not mass transfer limited. The flow cell may be transport limited due to the low flow rates achievable with the syringe pump. The effect of the applied potential is qualitatively similar in the RDE and the flow cell for PtRu/C and Rh/C, with an increase in nitrate reduction with more negative potentials. This implies that they may be not transport limited, however the flow rate dependence indicate that mass transport is still playing a role in the observed rates. More

measurements for catalysts in the flow cell would be useful for quantitatively comparing measured activities to those collected with a RDE.

The highest rate of ammonia production in the flow cell was with Rh/C at 0.05 V vs. RHE with a flow rate of 2 mL/min with a nitrate reduction current density to ammonia of −0.18 mA/cm^2 normalized to the Rh surface area and −105 mA/cm^2 normalized to the geometric surface area (electrolyzer area). It is unclear if further reducing conditions would continue increasing the partial current density to ammonia or if hydrogen evolution would dominate.

5.4 Conclusions

We show that H_{upd} currents can be used to estimate ECSA both in the RDE and in the flow cell, though in the flow cell the H_{upd} ECSA per mass catalyst used was smaller than the ECSA per mass catalyst in the RDE. The catalytic activity trends for nitrate reduction are qualitatively the same in the batch and flow reactor, Rh/C > PtRu/C > Pt/C, matching the ability to adsorb nitrate. However, the current densities in the RDE do not directly transfer to the measured current densities in the flow cell. Direct comparisons of current densities for catalysts between the two systems require additional flow cell measurements to provide better error estimates. Additionally, varying level of mass transport conditions within the reactors is suggested to contribute to the differences observed between the flow cell and RDE current densities on each catalyst. We show the maximum partial current density to ammonia is achieved in the flow cell with Rh/C at a potential of 0.05 V vs. RHE and 2 mL/min, where this is a tradeoff between nitrate reduction and hydrogen evolution.

5.5 References

1. van Langevelde, P. H., Katsounaros, I. & Koper, M. T. M. Electrocatalytic Nitrate Reduction for Sustainable Ammonia Production. *Joule* **5**, 290–294 (2021).
2. Martínez, J., Ortiz, A. & Ortiz, I. State-of-the-art and perspectives of the catalytic and electrocatalytic reduction of aqueous nitrates. *Appl Catal B* **207**, 42–59 (2017).

3. National Academy of Engineering. *National Academy of Engineering Grand Challenges for Engineers*. (2017).
4. *Code of Federal Regulations (40 CFR 141)*. https://www.epa.gov/ground-water-and-drinking-water/national-primary-drinking-water-regulations (2022).
5. Ward, M. H. *et al.* Drinking Water Nitrate and Human Health: An Updated Review. *Int J Environ Res Public Health* **15**, 1557 (2018).
6. Temkin, A., Evans, S., Manidis, T., Campbell, C. & Naidenko, O. v. Exposure-based assessment and economic valuation of adverse birth outcomes and cancer risk due to nitrate in United States drinking water. *Environ Res* **176**, 108442 (2019).
7. Duca, M. & Koper, M. T. M. Powering denitrification: the perspectives of electrocatalytic nitrate reduction. *Energy Environ Sci* **5**, 9726–9742 (2012).
8. Zhang, X. *et al.* Recent advances in non-noble metal electrocatalysts for nitrate reduction. *Chemical Engineering Journal* **403**, 126269 (2021).
9. Wang, Z., Richards, D. & Singh, N. Recent discoveries in the reaction mechanism of heterogeneous electrocatalytic nitrate reduction. *Catal Sci Technol* **11**, 705–725 (2021).
10. Liu, J.-X., Richards, D., Singh, N. & Goldsmith, B. R. Activity and Selectivity Trends in Electrocatalytic Nitrate Reduction on Transition Metals. *ACS Catal* **9**, 7052–7064 (2019).
11. Wang, Z., Young, S. D., Goldsmith, B. R. & Singh, N. Increasing electrocatalytic nitrate reduction activity by controlling adsorption through PtRu alloying. *J Catal* **395**, 143–154 (2021).
12. Li, S. *et al.* Reconstruction-induced NiCu-based catalysts towards paired electrochemical refining. *Energy Environ Sci* (2022) doi:10.1039/D2EE00461E.
13. Ma, J. *et al.* Electrochemical reduction of nitrate in a catalytic carbon membrane nano-reactor. *Water Res* **208**, 117862 (2022).
14. Ma, J. *et al.* Integrated electrocatalytic packed-bed membrane reactor for nitrate removal. *Sep Purif Technol* **292**, 121010 (2022).
15. Xu, H., Ma, Y., Chen, J., Zhang, W. & Yang, J. Electrocatalytic reduction of nitrate – a step towards a sustainable nitrogen cycle. *Chem Soc Rev* (2022) doi:10.1039/d1cs00857a.
16. Yuan, J., Xing, Z., Tang, Y. & Liu, C. Tuning the Oxidation State of Cu Electrodes for Selective Electrosynthesis of Ammonia from Nitrate. *ACS Appl Mater Interfaces* **13**, 52469–52478 (2021).
17. Wang, Y. *et al.* Enhanced Nitrate-to-Ammonia Activity on Copper-Nickel Alloys via Tuning of Intermediate Adsorption. *J Am Chem Soc* **142**, 5702–5708 (2020).
18. Abdallah, R. *et al.* Selective and quantitative nitrate electroreduction to ammonium using a porous copper electrode in an electrochemical flow cell. *Journal of Electroanalytical Chemistry* **727**, 148–153 (2014).
19. Daiyan, R. *et al.* Nitrate reduction to ammonium: From CuO defect engineering to waste NOx-to-NH3 economic feasibility. *Energy Environ Sci* **14**, 3588–3598 (2021).
20. Jung, E., Shin, H., Hooch Antink, W., Sung, Y. E. & Hyeon, T. Recent Advances in Electrochemical Oxygen Reduction to H2O2: Catalyst and Cell Design. *ACS Energy Letters* vol. 5 1881–1892 Preprint at https://doi.org/10.1021/acsenergylett.0c00812 (2020).
21. Weekes, D. M., Salvatore, D. A., Reyes, A., Huang, A. & Berlinguette, C. P. Electrolytic CO2 Reduction in a Flow Cell. *Acc Chem Res* **51**, 910–918 (2018).
22. Lazaridis, T., Stühmeier, B. M., Gasteiger, H. A. & El-Sayed, H. A. Capabilities and limitations of rotating disk electrodes versus membrane electrode assemblies in the investigation of electrocatalysts. *Nat Catal* **5**, 363–373 (2022).

23. Lukaszewski, M., Soszko, M. & Czerwiński, A. Electrochemical methods of real surface area determination of noble metal electrodes - an overview. *Int J Electrochem Sci* **11**, 4442–4469 (2016).
24. Eaton, A., Clesceri, L. & Greenberg, A. (Eds.). *Standard Methods for the Examination of Water and Wastewater*. (APHA, 1995).
25. Richards, D., Young, S. D., Goldsmith, B. R. & Singh, N. Electrocatalytic nitrate reduction on rhodium sulfide compared to Pt and Rh in the presence of chloride. *Catal Sci Technol* **11**, 7331–7346 (2021).
26. Sharma, R., Gyergyek, S., Morgen, P. & Andersen, S. M. On the Electrochemical Stability of PtRu Alloy Electrodes in Aqueous Acidic Baths: A Strategy for Recycling Pt and Ru. *J Electrochem Soc* **167**, 024521 (2020).
27. Antolini, E. The problem of Ru dissolution from Pt-Ru catalysts during fuel cell operation: Analysis and solutions. *Journal of Solid State Electrochemistry* vol. 15 455–472 Preprint at https://doi.org/10.1007/s10008-010-1124-7 (2011).
28. Dima, G. E., de Vooys, A. C. A. & Koper, M. T. M. Electrocatalytic reduction of nitrate at low concentration on coinage and transition-metal electrodes in acid solutions. *Journal of Electroanalytical Chemistry* **554–555**, 15–23 (2003).
29. Yang, J., Sebastian, P., Duca, M., Hoogenboom, T. & Koper, M. T. M. pH dependence of the electroreduction of nitrate on Rh and Pt polycrystalline electrodes. *Chem. Commun.* **50**, 2148–2151 (2014).
30. de Groot, M. T. & Koper, M. T. M. The influence of nitrate concentration and acidity on the electrocatalytic reduction of nitrate on platinum. *Journal of Electroanalytical Chemistry* **562**, 81–94 (2004).

Chapter 6
Conclusions and Outlooks

6.1 Summary and Overall Conclusions

The goal of the research described in this dissertation was to understand activity trends for transition metal catalysts for nitrate reduction in ideal environments and environments more applicable to performing electrocatalytic nitrate remediation. In **Chapter 3** using density functional theory, adsorption energies of O and N are identified as descriptors for understanding nitrate reduction activity trends on transition metals; active nitrate reduction catalysts adsorb nitrate strongly (nitrate adsorption is related to the O adsorption energy) but not too strongly that the surface will be poisoned. We experimentally show that Rh adsorbs nitrate more strongly than Pt, which explains the higher activity of Rh and validates the calculations. These descriptors were then applied to predict active nitrate reduction alloys based on how they adsorb nitrate. **Chapter 4** explains why chloride can lower nitrate reduction on metal and metal sulfide (Rh_xS_y) catalysts. Rh_xS_y is found to be more active than Rh or Pt for nitrate reduction. The nitrate reduction activity is decreased in the presence of chloride for all catalysts in the order of Rh > Pt > Rh_xS_y and is attributed to competitive adsorption of chloride and nitrate on the surface. Density functional theory modeling predicts that chloride poisoning will consistently inhibit nitrate reduction activity on metals and the predicted metal sulfide active sites due to adsorbate scaling relations between nitrate and chloride. **Chapter 5** compares measured activity for nitrate reduction between a batch reactor and a flow cell for the same catalysts (Pt/C, PtRu/C, and Rh/C). Current densities measured between the two systems do not quantitatively translate, though the activity trends are maintained

between the batch and flow reactors (Pt/C < PtRu/C < Rh/C). We hypothesize the current densities do not translate because the flow cell is unable to achieve the high mass transport conditions achievable in the rotating disk electrode in the batch cell. In the flow cell, Rh/C had the greatest activity at 0.05 V vs. RHE with a flow rate of 2 mL/min with a nitrate reduction current density to ammonia of -0.32 mA/cm^2 normalized to the electrochemically active surface area using hydrogen underpotential deposition.

6.2 Future Directions and Outlooks

Further steps or opportunities that could be explored as an extension of the work in this dissertation are oriented around (1) the related O and N adsorption energies (nitrate and hydrogen adsorption energies) dictating nitrate reduction activity for transition metals, (2) exploring effects of other waste stream contaminants beyond chloride on nitrate reduction activity and testing catalysts using real waste streams, and (3) optimization of flow cell use for nitrate reduction. Additionally, final thoughts for the feasibility for nitrate reduction as a remediation technology are mentioned.

6.2.1 Breaking adsorbate scaling relations for enhanced nitrate reduction activity.

In **Chapter 3** we establish that transition metals have linear adsorbate scaling between reactants and intermediates for the rate determining step of the reaction which limits the predicted maximum nitrate reduction activity. Breaking these scaling relations would allow for catalysts with improved nitrate reduction rates, addressing a significant challenge for electrocatalytic nitrate remediation. A well-explored method for breaking adsorbate scaling relations is through bimetallic catalysts and single-atom alloy catalysts to modify the adsorption thermodynamics.[1–3] An alternative route for circumventing the linear scaling relations is through an external modulation

of the applied potential (pulsing the potential).[4–6] By repeatedly switching the potential between a potential where nitrate covers the surface and a potential where nitrate reduction/hydrogen adsorption occurs, we may be able to decouple the adsorbate scaling (and competition for surface sites) between hydrogen and nitrate to achieve higher nitrate reduction rates on the same catalysts. Preliminary results for this technique for nitrate reduction are shown in **Figure 6.1** on a Pt/C electrode. The average current density produced during the entire measurement (high and low potentials) of a dynamic potential measurement is compared to the steady-state current produced by holding a constant potential. Though the maximum current observed in **Figure 6.1b** for the pulsed potential technique is larger than what is shown for steady-state measurement in **Figure 6.1a**, it is unclear if the current enhancement is due to breaking of the adsorbate scaling relations.

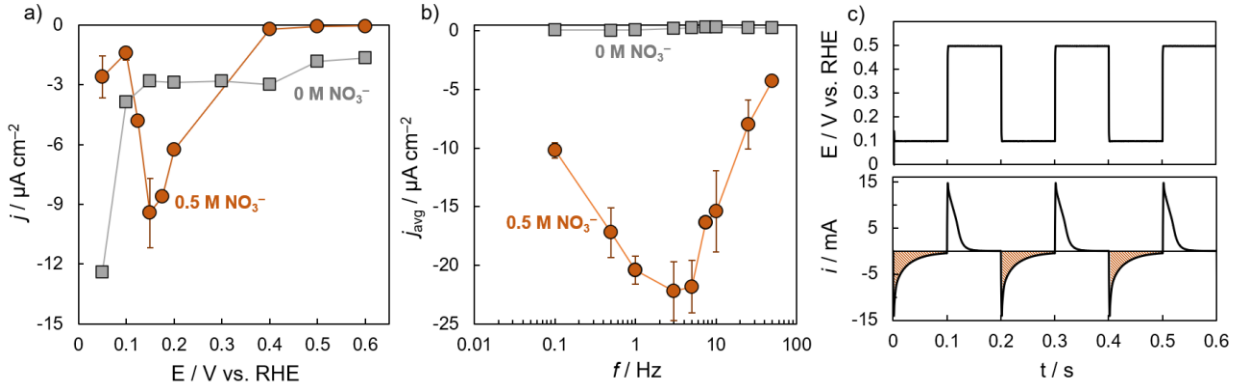

Figure 6.1. a) Steady-state current densities and b) average current densities from pulsing the potential at different frequencies on Pt/C deposited on a glassy carbon rotating disk measured at 2500 rpm in 0.1 M H_2SO_4 (labeled as 0 M NO_3^-, gray) and 0.1 M HNO_3 + 0.4 M $NaNO_3$ (labeled as 0.5 M NO_3^-, orange). c) The potential vs. time profile (top) for a 5 Hz measurement and a representative response (bottom) from the Pt/C electrode.

Recommendations for exploring pulse potentials for nitrate reduction are to validate the measurement technique using a breadboard circuit prior to measurements, to quantify products and nitrate conversion to understand allocation of charge, and to combine these electrochemical methods with vibrational spectroscopy, such as Raman spectroscopy. Knowledge of species on the surface of the electrode at the applied potentials would be useful for clarifying the cause of rate/conversion enhancement. Understanding how the rate orders change with respect to nitrate

and hydrogen should be explored by varying the nitrate concentration and pH. Because nitrate and hydrogen have potential dependent adsorption, the effects of concentration could also be explored by varying the potentials chosen for pulsing. Additionally, using cheaper catalysts that adsorb nitrate strongly such as copper and iron should be tested for nitrate reduction enhancement as those would be the conditions which would benefit most from breaking adsorbate scaling relations.

Currently there are two schools of thought on how pulsing the potential increases the average current density: creation of microenvironments which favor certain reactions[7–9] and harnessing resonance frequencies that match the rate of reaction to carefully deliver reactants to the surface and strip away the products.[6,10,11] For nitrate reduction, a lower nitrate concentration can be more favorable for nitrate reduction on some catalysts, so creation of a microenvironment with lower nitrate concentration could increase the nitrate reduction rate. Alternatively, if the rates are pulsed such that the surface of the electrode is cleaned constantly to allow more nitrate to adsorb, the surface poisoning intermediate NO would be removed from the surface and make more sites available for nitrate reduction, increasing the reduction rate. At this point, it remains unclear why there is enhancement in current from pulsing the potential on Pt and this is an exciting approach that should be explored for nitrate reduction.

6.2.2 Nitrate reduction in real waste streams.

Electrocatalytic nitrate reduction should be performed in real waste streams which can be variable in nitrate concentration, pH, and co-contaminants. Most nitrate waste streams, such a ground water, are pH neutral or slightly alkaline and have lower nitrate concentrations. For these lower nitrate concentrations, nitrate coverage on the surface will be low and this could potentially exacerbate competitive adsorption issues between nitrate and hydrogen. For pH neutral and alkaline conditions, the nitrate reduction mechanism is proposed to change from the H-assisted

nitrate reduction mechanism explored in this thesis and therefore it is less clear how the competition between adsorbed hydrogen and nitrate will affect the overall rate at these conditions.[12] Further work towards using real nitrate waste streams should explore pH effects and the potential-dependence at various pH for nitrate reduction at neutral and alkaline conditions.

As an extension of what was investigated in **Chapter 4**, the effects of other contaminants (in addition to chloride) of proposed nitrate sources on nitrate reduction rates should be investigated. As introduced in **Chapter 1.2.1**, common co-contaminants include a mix of anions (e.g., Cl^-, F^-, NO_2^-, HSO_2^-, SO^{2-}, CO_3^{2-}, and PO_4^{3-}), cations (e.g., Na^+, K^+, Mg^{2+}, Ca^{2+}, and NH_4^+) and heavy metals (e.g., Cr^{2+}).[13,14] Chloride was investigated due to its presence in almost all proposed nitrate remediation waste streams. Investigation of how other anions adsorb on surfaces relevant for nitrate reduction should be studied. Halides (e.g., Br^-) are well studied and are likely to have adsorption strengths that scale with nitrate adsorption, similar to what was found with Cl^-. It is unclear if other types of anions will also have adsorbate scaling with nitrate to the same degree; larger anions (e.g., HSO_2^-) also adsorb to metals but may adsorb with adsorption strengths similar to nitrate and inhibit the nitrate reduction reaction rate less than we showed for chloride (nitrate may be more competitive for active sites with larger anions than with chloride).

Cations such as sodium and potassium are also commonly found in polluted groundwater and other nitrate waste streams. Cation effects on the nitrate reduction reaction is poorly understood.[13,15] In laboratory studies for nitrate reduction kinetics, the cation is often not considered when reporting intrinsic kinetics though it may influence the measured rate. Recently for other electrocatalytic reduction reactions, such as CO_2 reduction, the effect of cations in the electrolyte is an increasing area of focus.[16] Just by changing the cation the measured CO_2 reduction rate can increase or decrease, which is non-intuitive since the cation is not expected to directly

participate in the reaction. Because cations are equivalently as abundant in the considered nitrate remediation waste streams as nitrate and other anions, there is a need to understand how these species can affect the nitrate reduction reaction rates.

Obtaining actual nitrate wastewater would be extremely helpful for both identifying relevant co-contaminants which can prevent nitrate reduction and for evaluating how appropriate a nitrate feed stream is for the electrocatalytic remediation process. Using nitrate wastewater could accelerate studies to understand effects of the most relevant co-contaminants, especially those which would require separation prior to electrocatalytic nitrate reduction. Physical separation methods discussed in **Chapter 1.2.2** can be employed to remove other ions and create more idealized nitrate waste streams. Evaluating separation technologies for separation efficiency, processing time, and power use will dictate which method is most appropriate for coupling with electrocatalytic nitrate reduction and removing co-contaminants from the inlet streams.

Exploration of poison-resistant nitrate reduction catalysts is needed. In this dissertation, rhodium sulfide was shown to have better performance for nitrate reduction with and without chloride compared to Rh and Pt, but nitrate was still less competitive than chloride for active sites on this material causing lower nitrate reduction activity. Computational methods could be used to screen for catalysts which deviate from the observed nitrate and chloride adsorption scaling and then can be synthesized and tested in the laboratory. Identifying a cheap, robust, and poison-resistant electrocatalyst which could eliminate waste stream purification steps prior to electrocatalytic remediation would decrease the cost of electrocatalytic nitrate remediation.

6.2.3 Flow cells to demonstrate capabilities of nitrate to ammonia.

Thorough investigation of catalyst activity and reactor optimization in a bench top flow cell would be an essential step towards scaling up the nitrate reduction process. In **Chapter 5**, we

established that there were more complexities involved in transferring catalysts from a rotating disk configuration (where we measure intrinsic kinetics) to a flow cell for high throughput conversion than simply loading the catalyst in the electrochemical cell. For flow cell optimization starting with the flow cell used in **Chapter 5** and its components, the following items warrant investigation as to how they contribute towards nitrate reduction in the flow cell: catalyst loading method on a carbon felt, using a carbon felt versus carbon cloth or carbon paper (flow through versus flow by), ionomer binder amount and type of ion conduction, counter electrode material, ion exchange membrane used to separate the two compartments, and degassed versus N_2 sparged solution at inlet.

Possible methods of improving uniformity of catalysts deposition might be to directly synthesize catalysts unto the carbon felt, spray deposition of catalysts similar to what is used for gas diffusion electrodes, or electrodeposition of the electrocatalysts directly onto a support. There is general interest in developing more durable methods for attaching catalyst to the support so to not waste precious metals and to test nitrate reduction with catalysts that are more uniform to reduce the deviation in values obtained for identical measurements. Specifically, a reliable method for deposition of catalyst on the carbon felt would allow use to quantitatively compare the currents between the rotating disk and flow cell reactors.

A significant shortcoming of **Chapter 5** was the limited flow range attained using a syringe pump, higher flowrates (greater than 2 mL per minute) should be investigated to determine if the currents measured are mass transport limited which would be apparent if the reduction rate changed with flow rate. Using a persistaltic pump with a beaker filled with electrolyte had the issue of difficulty in degassing the electrolyte and ‘stepping’ which caused electrolyte pulses. Degassing could potentially be done by assembling a system where the peristaltic pump uses a

larger reservoir with gas bubbles removed. Additionally, exploring different catalyst support geometries (carbon felt, carbon cloth, and carbon paper) for nitrate reduction could provide some insight on the flow cell transport properties. Carbon felt was selected in **Chapter 5** because it was most like a packed bed reactor with a flow through configuration but could have dead zones for electrolyte movement at different flowrates. Using carbon cloth or carbon paper with a flow by configuration would provide a good contrast to identify the existence of deadzones.

In **Chapter 5**, activity trends were attributed to nitrate and hydrogen concentration gradients introduced by slow mass transport conditions in the flow cell. Beside using a faster flow rate as discussed above, this concept should be explored by using different concentrations of nitrate and hydrogen to obtain reaction orders in the batch and flow reactors. By varying the concentrations, we can better evaluate the observed reaction rates for being intrinsic or influenced by mass transport artifacts.

6.2.1 Feasibility of electrocatalytic nitrate reduction.

Research on catalysts and activities for electrocatalytic nitrate continues to grow with the motivation of applying the technology towards remediation of waste streams but a holistic view of the entire nitrate reduction process is missing. Electrocatalytic nitrate reduction is not currently used for nitrate remediation which is attributed to the low activity of catalysts. Even the highest performing catalysts (-0.1 to -2.6 A/cm^2, where -2.6 A/cm^2 is an outlier)[17] are still not active enough for consideration for nitrate reduction at an industrial level (need to achieve about -1 A/cm^2).[18] Additionally, electrocatalysts that achieve highest reported rates are typically operated at high overpotentials (<-0.6 V vs Ag/AgCl) which can increase the cost of operation.[18] Catalysts which have nitrate reduction currents at industrial levels but also achieve these at low overpotentials need to be identified. Development of a cost analysis model between nitrate

reduction activity, faradaic efficiency, and applied overpotential would be beneficial for understanding the activity which would be required for electrocatalytic nitrate remediation at various overpotentials. Additionally, exploration of the manufacturing cost of microstructure catalysts identified as active for nitrate reduction would be useful to understand before attempting to scale up for nitrate remediation.

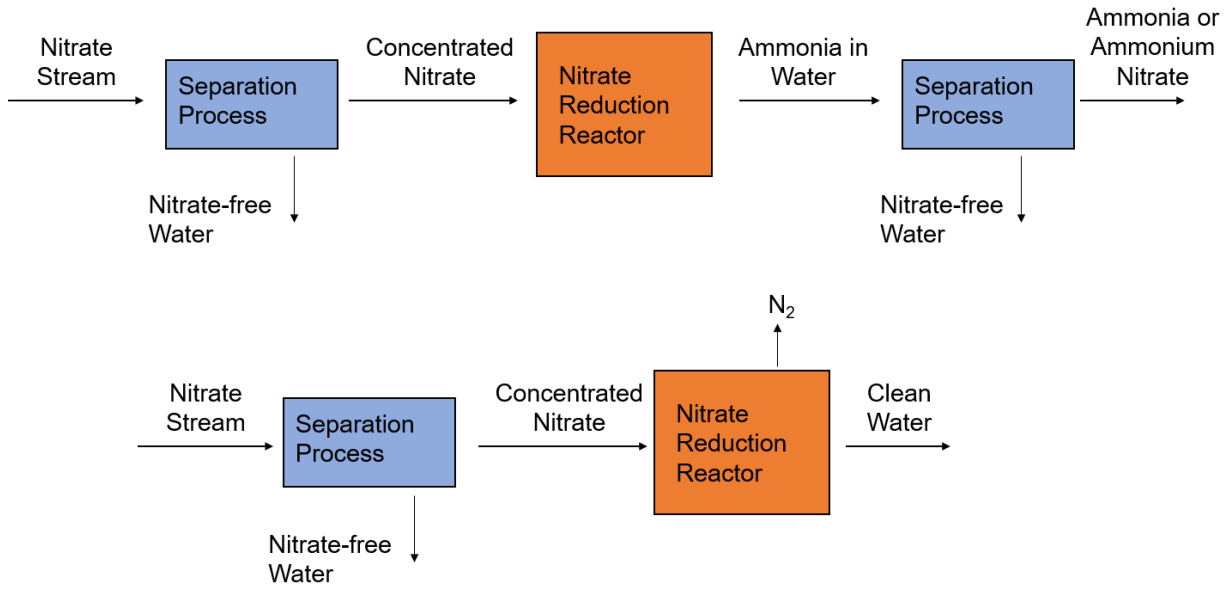

Figure 6.2. Proposed electrocatalytic nitrate reduction process including potential separation steps before and after the reaction depending on if the desired product is ammonia or ammonium nitrate (top) or nitrogen gas (bottom).

Beyond the electrocatalyst, the most appropriate nitrate streams still would need to be identified, purified, and the nitrate concentrated, the operating parameters for the electrochemical reactor would need to be explored and optimized, and costs of post-processing and treatment of the product stream would also need to be considered prior to establishing electrocatalytic nitrate reduction for wastewater remediation. Two simple scenarios are presented in **Figure 6.2** depending on the desired product. If the desired product is not easily separated from the electrolyte (e.g., ammonium or ammonia, which remain in aqueous phase) there is an additional separation step required to obtain the product. If nitrogen gas is the desired product, it will exit the stream in

the gas phase and requires no additional treatment. Many physical separation techniques (e.g., reverse-osmosis) have high performance but are energy intensive and costly. Incorporation of these additional processes and costs not directly associated with the nitrate reduction electrocatalyst should be considered for implementation of the technology.

6.3 References

1. Pérez-Ramírez, J. & López, N. Strategies to break linear scaling relationships. *Nat Catal* **2**, 971–976 (2019).
2. Darby, M. T., Stamatakis, M., Michaelides, A. & Sykes, E. C. H. Lonely Atoms with Special Gifts: Breaking Linear Scaling Relationships in Heterogeneous Catalysis with Single-Atom Alloys. *Journal of Physical Chemistry Letters* vol. 9 5636–5646 Preprint at https://doi.org/10.1021/acs.jpclett.8b01888 (2018).
3. Nwaokorie, C. F. & Montemore, M. M. Alloy Catalyst Design beyond the Volcano Plot by Breaking Scaling Relations. *The Journal of Physical Chemistry C* (2022) doi:10.1021/acs.jpcc.1c10484.
4. Ardagh, M. A., Abdelrahman, O. A. & Dauenhauer, P. J. Principles of Dynamic Heterogeneous Catalysis: Surface Resonance and Turnover Frequency Response. *ACS Catal* **9**, 6929–6937 (2019).
5. Dauenhauer, P. J. *et al.* Catalytic resonance theory: Parallel reaction pathway control. *Chem Sci* **11**, 3501–3510 (2020).
6. Shetty, M. *et al.* The Catalytic Mechanics of Dynamic Surfaces: Stimulating Methods for Promoting Catalytic Resonance. *ACS Catal* **10**, 12666–12695 (2020).
7. Kim, C., Weng, L. C. & Bell, A. T. Impact of Pulsed Electrochemical Reduction of CO2on the Formation of C2+Products over Cu. *ACS Catal* **10**, 12403–12413 (2020).
8. Bui, J. C., Kim, C., Weber, A. Z. & Bell, A. T. Dynamic Boundary Layer Simulation of Pulsed CO2Electrolysis on a Copper Catalyst. *ACS Energy Lett* **6**, 1181–1188 (2021).
9. Bui, J. C. *et al.* Engineering Catalyst-Electrolyte Microenvironments to Optimize the Activity and Selectivity for the Electrochemical Reduction of CO2on Cu and Ag. *Acc Chem Res* **55**, 484–494 (2022).
10. Gopeesingh, J. *et al.* Resonance-Promoted Formic Acid Oxidation via Dynamic Electrocatalytic Modulation. *ACS Catal* **10**, 9932–9942 (2020).
11. Gathmann, S. R., Ardagh, M. A. & Dauenhauer, P. J. Catalytic resonance theory: Negative dynamic surfaces for programmable catalysts. *Chem Catalysis* 1–24 (2022) doi:10.1016/j.checat.2021.12.006.
12. Wang, Z., Ortiz, E. M., Goldsmith, B. R. & Singh, N. Comparing electrocatalytic and thermocatalytic conversion of nitrate on platinum–ruthenium alloys. *Catal Sci Technol* **11**, 7098–7109 (2021).
13. van Langevelde, P. H., Katsounaros, I. & Koper, M. T. M. Electrocatalytic Nitrate Reduction for Sustainable Ammonia Production. *Joule* **5**, 290–294 (2021).
14. Wang, Z., Richards, D. & Singh, N. Recent discoveries in the reaction mechanism of heterogeneous electrocatalytic nitrate reduction. *Catal Sci Technol* **11**, 705–725 (2021).

15. Garcia-Segura, S., Lanzarini-Lopes, M., Hristovski, K. & Westerhoff, P. Electrocatalytic reduction of nitrate: Fundamentals to full-scale water treatment applications. *Appl Catal B* **236**, 546–568 (2018).
16. Resasco, J. *et al.* Promoter Effects of Alkali Metal Cations on the Electrochemical Reduction of Carbon Dioxide. *J Am Chem Soc* **139**, 11277–11287 (2017).
17. Anastasiadou, D., Beek, Y., Hensen, E. J. M. & Costa Figueiredo, M. Ammonia electrocatalytic synthesis from nitrate. *Electrochemical Science Advances* 1–11 (2022) doi:10.1002/elsa.202100220.
18. Singh, N. & Goldsmith, B. R. Role of Electrocatalysis in the Remediation of Water Pollutants. *ACS Catal* **10**, 3365–3371 (2020).

Appendix A

Catalyst Characterization and Evaluation

This appendix contains additional catalyst characterization results and analysis of chloride adsorption effects on Pt and Rh for the work presented in **Chapter 4**.

Comparison of Hupd and Capacitance-based ECSA Models

Though two prior studies showed limited charge in the H_{upd} region for rhodium sulfide (Rh_xS_y),[1,2] we did not detect H_{upd} peaks on Rh_xS_y/C (**Figure A.1**). Therefore, the H_{upd} charge cannot be used to compare the Rh_xS_y/C activity with the activity of Pt/C and Rh/C. Instead, we measure the double-layer capacitance in the non-faradaic region to determine the total surface area (catalyst plus carbon support) using a specific capacitance which is then used to estimate the surface area of the Rh_xS_y nanoparticles.[3] The nanoparticles are modeled as a cube with five exposed sides and one side in contact with the carbon support. X-ray diffraction (XRD) is used to measure the average crystallite size of the particles and this value is used as the cube side length (see **Chapter 2.3.1** for XRD analysis for these materials).[4] We refer to this method as the "capacitance & XRD" method (see **Chapter 2.3.3**). This method accounts for variations in the amount of catalyst deposited onto the glassy carbon disk from run to run and allows us to compare Rh_xS_y/C to Rh/C and Pt/C on an even basis.

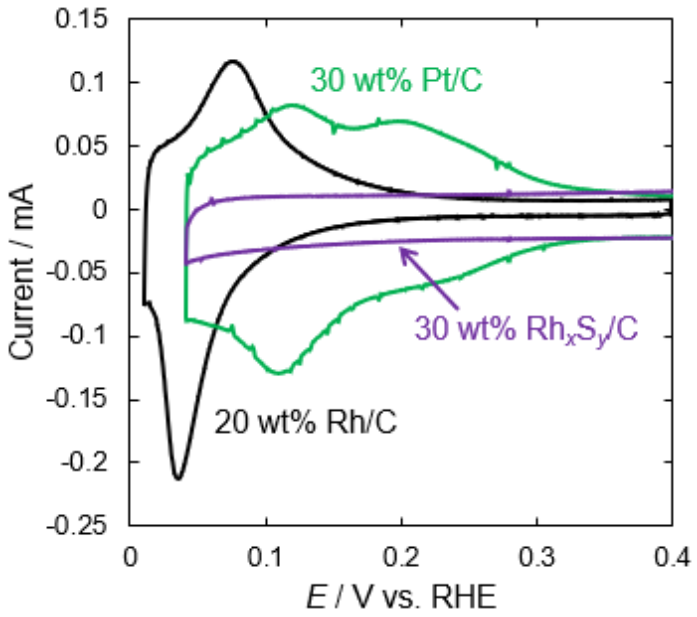

Figure A.1. Hydrogen underpotential deposition currents for 30 wt% Pt/C in 1 M $HClO_4$ and 20 wt% Rh/C and 30 wt% Rh_xS_y/C in 1 M H_2SO_4. All measurements taken in de-aerated solution under a N_2 blanket. The scan rate was 50 mV s^{-1} for each material. A Pt wire counter electrode and Ag/AgCl reference electrode were used.

The average ECSAs of Rh/C and Pt/C, and Rh_xS_y/C from the geometric area, H_{upd}, and capacitance & XRD method are shown in **Table A.1**. These averages are determined from the ECSA values from ink depositions used for steady-state NO_3RR current measurements in **Figure 4.1**. The ECSA values for Pt/C and Rh/C through the H_{upd} and capacitance & XRD method are similar, and both 5−9 times larger than the geometric area, highlighting both the importance of measuring ECSA and the relative accuracy of the capacitance & XRD technique. No observable H_{upd} charge for Rh_xS_y/C in **Figure A.1** suggests that the Rh_xS_y/C is not simply reduced to form metallic Rh/C. The ECSA of Rh_xS_y/C for the samples is comparable to that of Rh/C (**Table A.1**). Based on the similar ECSA, if Rh_xS_y/C was metallic Rh under reaction conditions, the H_{upd} current would be visible.

Table A.1. Geometric area, H_{upd} ECSA, crystallite size from the Scherrer equation analysis of XRD, and capacitance & XRD ECSA for Rh/C, Pt/C, and Rh_xS_y/C supported nanoparticles. The projected area of the glassy carbon rotating disk was used for the geometric area. The difference in ECSA methods is calculated

by subtracting the capacitance & XRD ECSA by the H_{upd} ECSA and normalizing to the H_{upd} ECSA for each ink deposition.

Catalyst	Geometric Area (cm^2)	H_{upd} ECSA (cm^2)	XRD Crystallite Size (nm)	Capacitance & XRD ECSA (cm^2)	(H_{upd} ECSA – Capacitance & XRD ECSA)/H_{upd} ECSA
Rh/C	0.196	1.02 ± 0.10	2.3 ± 0.4	1.56 ± 0.43	−0.53
Pt/C	0.196	1.47 ± 0.21	2.2 ± 0.1	1.74 ± 0.24	−0.18
Rh_xS_y/C	0.196	N/A	12	1.02 ± 0.11	N/A

X-ray Diffraction of Rh_xS_y/C, Pt/C, and Rh/C for Crystallite Sizes

X-ray powder diffraction was used to estimate the crystallite sizes of Rh/C, Pt/C, and Rh_xS_y/C. The diffraction patterns are shown in **Figure A.2**. The powder XRD patterns were collected using a PANalytical Empyrean diffractometer operating at 45 kV and 40 mA ranging from 10° to 90° for Rh/C and Rh_xS_y/C and 30° to 90° for Pt/C with a 0.008° step size. No metallic Rh is observed in the Rh_xS_y/C sample, in agreement with our cyclic voltammetry results. The Scherrer equation (**Equation 2.2**) was used to determine the mean crystallite size as discussed in **Chapter 2.3.1**.

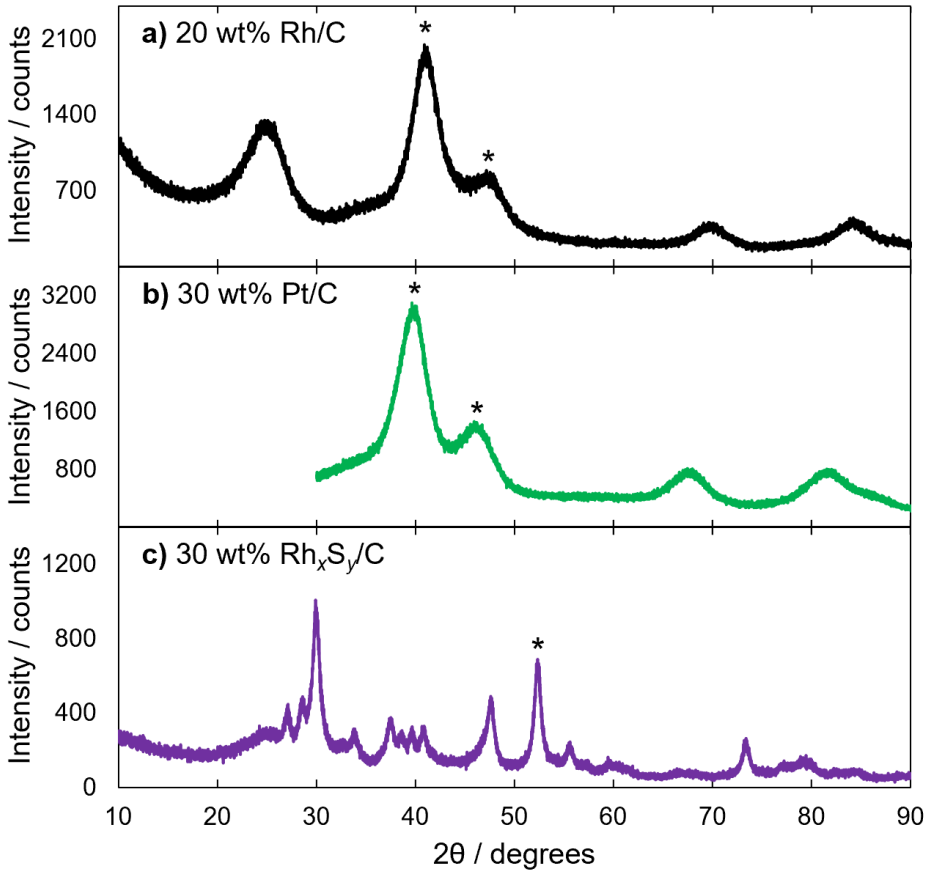

Figure A.2. XRD spectra of a) 20 wt% Rh/C, b) 30 wt% Pt/C, and c) 30 wt% Rh_xS_y/C. Peaks used for estimating the crystallite sizes are marked (*).

The average crystallite size from the two highest intensity diffraction peaks for Rh and Pt is taken as the catalyst's approximate particle size. The Rh/C particle size is 2.3 ± 0.4 nm approximated from the (111) peak at 41° and (200) peak at 47°. The Pt/C particle size is 2.2 ± 0.1 nm using the (111) peak at 40° and (200) peak at 46°. The standard deviation reported is from the particle sizes from the two peaks. The Rh_xS_y/C particle size is 12 nm approximated from the peak at 52°.

Transmission Electron Microscopy for Particle Size Distribution

Transmission electron microscopy (TEM) was used to find the particle size distribution for 30 wt% Rh_xS_y/C and 20 wt % Rh/C. TEM was performed on a JOEL 2010F electron microscope operating with 200 kV accelerating voltage. Samples were prepared

by dispersing a small amount of catalyst powder in Millipore water and dropping on a gold grid. TEM images for Rh_xS_y/C are shown in **Figure A.3**. TEM images for the 20 wt% Rh/C are included in ref. [5]. Since we normalize the Rh/C activity to the ECSA measured using H_{upd}, the accuracy of the particle size from the XRD crystallites does not affect the reported current density. For Rh_xS_y/C, we normalize the currents to the ECSA estimated using the XRD crystallite size, but could also use the particle sizes from TEM. If we use the average particle size from TEM micrographs (9.8 nm, **Figure A.3**) instead of from XRD (12 nm), the calculated ECSA would increase by < 20% and decrease the reported current density accordingly. Though the Rh_xS_y/C activity would decrease as a result of using this TEM particle size, Rh_xS_y/C would still be more active than Rh/C. However, when trying to estimate the total number of surface sites from a distribution of particle sizes, it is more accurate to weight each nanoparticle by the number of atoms present, rather than weighting a small and large nanoparticle equally.

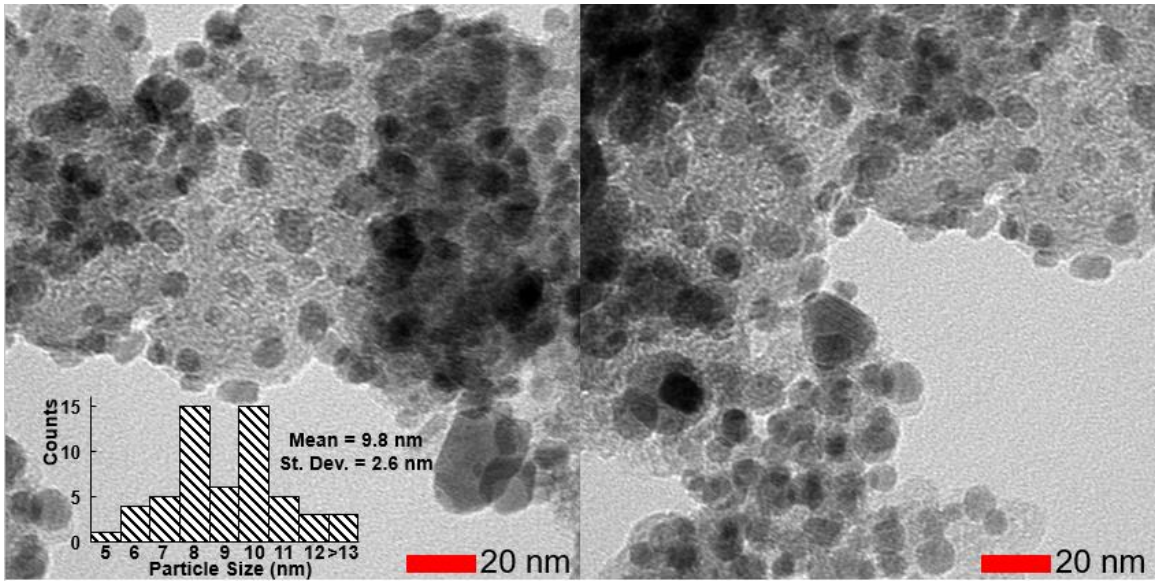

Figure A.3. Particle size distribution from TEM for 30 wt% Rh_xS_y/C from three micrographs (two shown here). The red scale bar indicates 20 nm in the micrograph. Histogram bins: [5,6], (6,7], (7,8], (8,9], (9,10], (10,11], (11,12], (12,13], >13.

Baseline Steady-state Currents (with and without $NaNO_3$) on Rh_xS_y/C, Rh/C, and Pt/C

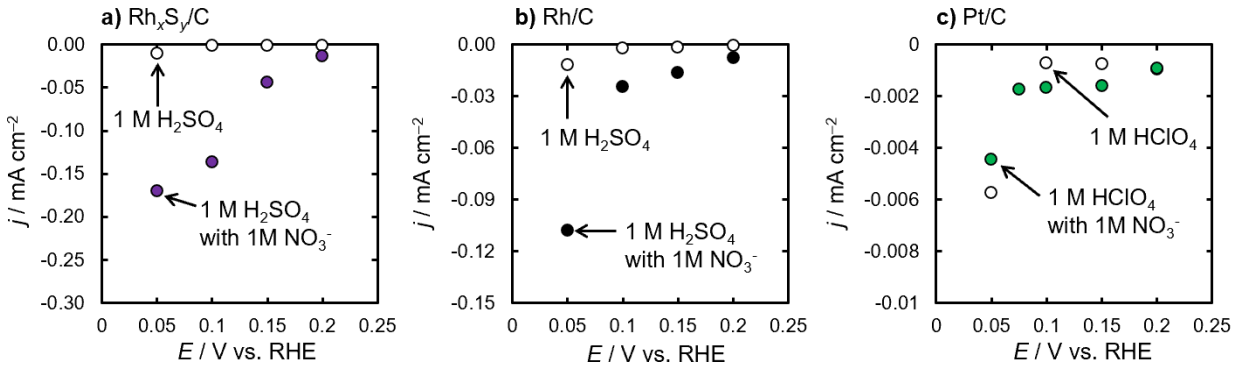

Figure A.4. Steady-state current densities for a) 30 wt% Rh_xS_y/C, b) 20 wt% Rh/C, and c) 30 wt% Pt/C in the supporting electrolyte (open circles) and with 1 M $NaNO_3$ (filled circles). Currents for Rh_xS_y/C are normalized to the capacitance & XRD estimated area. Currents for Rh/C and Pt/C are normalized to H_{upd} determined ECSA. Measurements were taken at 2500 rpm at each potential with 85% IR compensation.

Analysis of Electrolyte and Rotation Rate Effects for Nitrate Reduction on Rh/C and Rh_xS_y/C in 1 M HNO_3

In the **Chapter 4**, nitrate reduction measurements on Rh/C and Rh_xS_y/C were taken with sodium nitrate added to sulfuric acid (1 M H_2SO_4 + 1 M $NaNO_3$) to distinguish the background current (H_2SO_4 only) from the nitrate reduction current (**Figure 4.1** and **Figure A.4**) and to measure the ECSA in the supporting electrolyte more accurately. We also measure considerable reduction currents on Rh_xS_y/C and Rh/C in 1 M HNO_3 (**Figure A.5**), but because we are unable to measure a background current nor measure the ECSA in the supporting electrolyte of interest, we do not focus on pure nitric acid electrolyte in the main text. At 2500 rpm, the reduction currents on both Rh_xS_y/C and Rh/C are more negative in 1 M HNO_3 (**Figure A.5**) than in 1 M H_2SO_4 + 1 M $NaNO_3$ (**Figure 4.1**) which could be due to unwanted surface interactions (site blocking) of spectator ions (Na^+, HSO_4^-, SO_4^-), faster kinetics of nitrate reduction from nitric acid compared to the nitrate anion, issues with the inability to subtract the background current, or inaccuracies in the surface area measurements. In 1 M HNO_3, the ECSAs were measured in a separate electrolyte and then

the electrode was transferred to 1 M HNO_3 for kinetic measurements, rather than adding sodium nitrate without moving the electrode as explained in the main text.

When adding chloride to the nitric acid solution, the current density decreased (open diamonds in **Figure A.5**), similar to the effect observed in the sulfuric acid with sodium nitrate in **Figure 4.1**. Though the NO_3RR currents are greater for both Rh/C and Rh_xS_y/C in 1 M HNO_3 than in 1 M H_2SO_4 + 1 M $NaNO_3$, when 1 mM chloride is added the current densities become approximately the same in both electrolytes. This is rationalized by similar site blocking of chloride in both solutions. For NO_3RR in 1 M H_2SO_4 + 1 M $NaNO_3$ at 0.1 V vs. RHE, there may be site blocking by spectator anions and when chloride is added to the solution, the chloride will adsorb to the surface and block additional sites and displace the more weakly bound ions. In 1 M HNO_3, there are no spectator ions to occupy sites until chloride is added. On these surfaces it makes sense that once a strongly bound anion like chloride is added to solution there would be similar site blocking for this surface reaction.

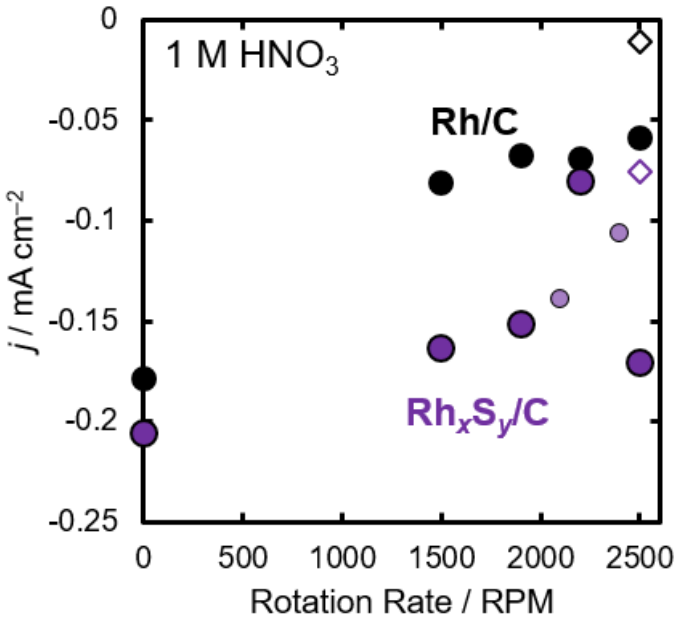

Figure A.5. NO_3RR on Rh/C (black circles) and Rh_xS_y/C (purple circles) in 1 M HNO_3 at 0.1 V vs. RHE at various rotation rates. Open diamonds represent the current density after 1 mM chloride was added. Smaller, light purple circles represent individual measurements on Rh_xS_y/C.

The rotation rate was observed to affect the current density of nitrate reduction at 0.1 V vs. RHE in 1 M HNO_3 (**Figure A.5**) and 1 M H_2SO_4 + 1 M $NaNO_3$ on Rh/C and Rh_xS_y/C. The rotation rate effects for NO_3RR on Pt/C were not distinguishable from overall measurement error. For both Rh/C and Rh_xS_y/C, the current densities at 0 rpm were more negative (higher rates) than at 2500 rpm. At low rotation rates the local surface concentration of nitrate will be lower than in the bulk due to the reaction at the electrode surface depleting nitrate, and higher rotation rates will minimize this concentration gradient. Although typically a lower concentration of the reactant at the surface reduces the reaction rate, we see the opposite effect here. We attribute this to a negative reaction order in nitrate at 1 M nitrate. At high concentrations of nitrate (>0.1 M), on Pt the reaction order is less than 0 for nitrate meaning that the reaction would be faster when nitrate concentrations are lower.[6] As Rh adsorbs nitrate more strongly than Pt, we believe this to be the case here as well. Thus, greater reduction current at low rotation rates could be due

to the decrease in the local concentration of nitrate near the electrode surface, causing an increase in the rate for Rh/C and Rh_xS_y/C. In the main text, we report current densities at 2500 rpm because, though it is not the rotation rate with the most negative NO_3RR current at 0.1 V, it is the rotation rate where the concentration of species at the surface most closely matches the bulk solution.

Comparison of Previous Reports of the Effect of Chloride on NO_3RR on Pt and Rh

The effect of chloride on NO_3RR current has been shown for Pt and Rh at pH 0. In **Figure A.6**, the percent nitrate reduction current remaining when Cl^- is added is shown for our measurements and from those reported in literature. Experimental conditions are given in **Table A.2** for the data in **Figure A.6**.

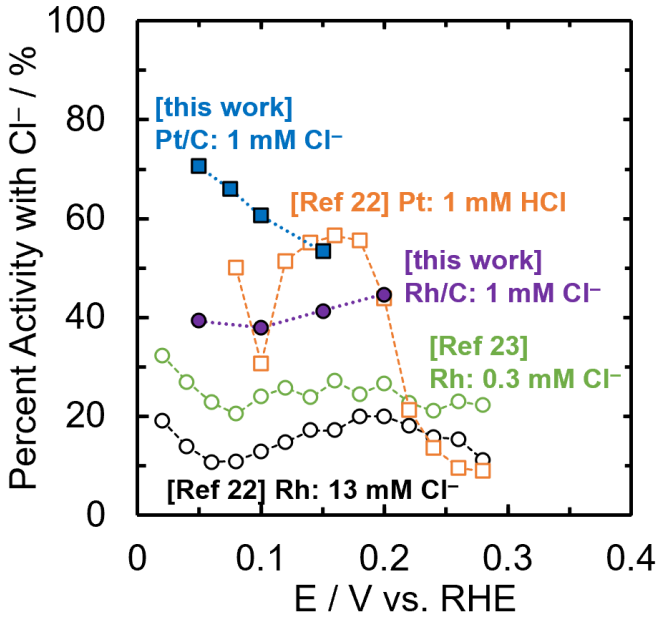

Figure A.6. Literature reports of the current density for NO_3RR activity on polycrystalline Pt and Rh from Horányi et al.[7] and Wasberg et al.[8], respectively, in different concentrations of chloride were extracted and normalized to the current density in the absence of chloride as a function of potential. Percent activity with Cl^- is also shown for Pt/C and Rh/C data from this work from **Figure 4.1a**. Other differences in experimental conditions between data series are summarized in **Table A.2**. Open data points represent cited works and closed data points are from this work. Circles and squares are used for Rh and Pt, respectively.

Table A.2. Experimental conditions for nitrate reduction measurements on Pt and Rh with chloride shown in **Figure A.6**

Electrode (Ref.)	$[NO_3^-]$ (M)	$[Cl^-]$ (M)	Supporting Electrolyte	Rotation/Stir Rate (rpm)
Pt (Horányi *et al.* [7])	0.015	10^{-3}	1 M H_2SO_4	N/A
Rh (Wasberg *et al.* [8])	0.114	3×10^{-4}, 1.3×10^{-2}	1 M H_2SO_4	N/A
Pt/C (this work)	1.0	10^{-3}	1 M $HClO_4$	2500 rpm
Rh/C (this work)	1.0	10^{-3}	1 M H_2SO_4	2500 rpm

The decrease in nitrate current in the presence of chloride is similar between the different studies for Pt and Rh. For Rh (Wasberg *et al.* [8] and this work), the percent change in current is similar across the studied potential range (0.05–0.2 V vs. RHE). Assuming nitrate reduction occurs as a Langmuir-Hinshelwood surface reaction between adsorbed nitrate and hydrogen, we attribute this decrease in activity to chloride adsorption beginning at negative potentials on Rh and limiting available surface sites in the potential range studied. The chloride is present on the surface and decreases the available surface sites for nitrate and hydrogen to adsorb and react. For Pt, the percent NO_3RR activity decreases for both ref. [7] and this work show that the NO_3RR rate is more affected by chloride at more positive potentials. We attribute this decrease in activity to the onset of chloride adsorption in the studied potential range, where at 0.05 V the surface has a negligible coverage of chloride and as the potential increases the chloride coverage increases and thus inhibits NO_3RR.

There are a few differences in experimental conditions to consider when comparing this work with the results from ref. [7] and ref. [8], namely that the nitrate concentrations are different and the results from literature may be in the mass transport limited regime. In our measurements on Rh/C and Pt/C, we use 2500 rpm to minimize mass transfer effects. The

results on Rh from ref. [7] are taken using a low stirring rate and are likely in the mass transfer limited regime, and therefore nitrate reduction inhibition by chloride could be lower than reported due to mass transport limitations. Ref. [8] does not indicate that stirring or rotation was used, so we can assume that there are mass transport limitations present.

Charge from Cyclic Voltammograms with Nitrate and Chloride on Pt and Rh

Like chloride, nitrate also adsorbs on the surface of Rh and Pt in what appears to be a charge transfer process (**Equation 4.2**). Using cyclic voltammograms in the H_{upd} region with different concentrations of nitrate,[9] the anodic charge on Pt and Rh changes with nitrate concentration (**Figure A.7a**). On Rh, the charge decreases with increasing nitrate concentration, mirroring the behavior with chloride concentration (**Figure A.7b**). On Pt, the charge increases at low concentrations of nitrate and decreases at concentrations greater than 0.1 M NO_3^-, also mirroring the behavior with Cl^- concentration on Pt. This additional anodic charge must come from an additional charge transfer reaction, indicating nitrate adsorption involves an electron transfer. For Pt and Rh, the potential region where chloride is adsorbed is the same in which nitrate adsorbs and nitrate reduction occurs.[6,10,11]

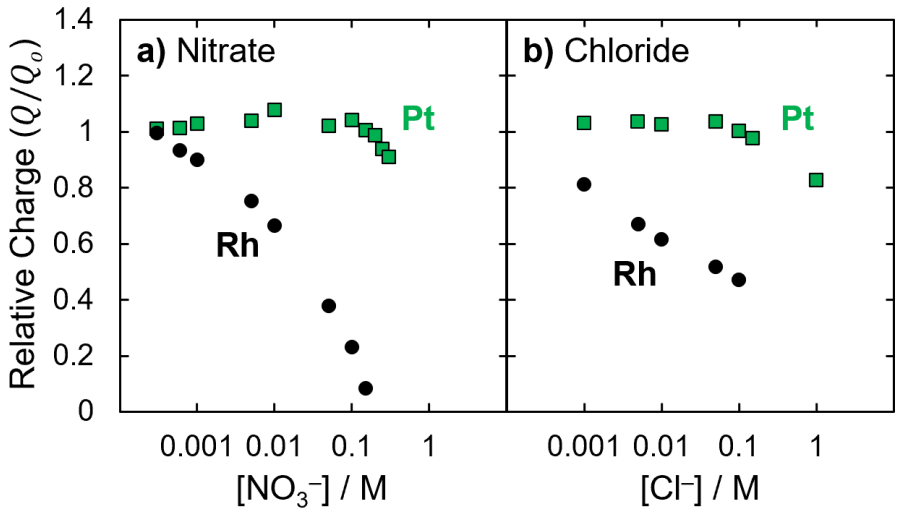

Figure A.7. The charge (Q) of the anodic scan from 0.05 to 0.4 V vs. RHE on a Pt RDE in 1 M $HClO_4$ and Rh wire in 1 M H_2SO_4 with a) 0.3 mM to 0.3 M NO_3^- (reproduced with permission from Ref. [9]) or b) 1 mM to 1 M Cl^- relative to the charge at the same potentials without nitrate or chloride (Q_0). Data in b) is reproduced from **Figure 4.2c**.

References

1. Ziegelbauer, J. M. *et al.* Fundamental Investigation of Oxygen Reduction Reaction on Rhodium Sulfide-Based Chalcogenides. *The Journal of Physical Chemistry C* **113**, 6955–6968 (2009).
2. Masud, J. *et al.* Synthesis and Characterization of RhxSy/C Catalysts for HOR/HER in HBr. *ECS Transactions* **58**, 37–43 (2014).
3. Singh, N., Gordon, M., Metiu, H. & McFarland, E. Doped Rhodium Sulfide and Thiospinels Hydrogen Evolution and Oxidation Electrocatalysts in Strong Acid Electrolytes. *Journal of Applied Electrochemistry* **46**, 497–503 (2016).
4. Connolly, J. F., Flannery, R. J. & Aronowitz, G. Electrochemical Measurement of the Available Surface Area of Carbon-Supported Platinum. *J Electrochem Soc* **113**, 577–580 (1966).
5. Wang, Z., Young, S. D., Goldsmith, B. R. & Singh, N. Increasing Electrocatalytic Nitrate Reduction Activity by Controlling Adsorption through PtRu Alloying. *Journal of Catalysis* **395**, 143–154 (2021).
6. De Groot, M. T. & Koper, M. T. M. The Influence of Nitrate Concentration and Acidity on the Electrocatalytic Reduction of Nitrate on Platinum. *Journal of Electroanalytical Chemistry* **562**, 81–94 (2004).
7. Horányi, G. & Rizmayer, E. M. Role of Adsorption Phenomena in the Electrocatalytic Reduction of Nitric Acid at a Platinized Platinum Electrode. *Journal of Electroanalytical Chemistry and Interfacial Electrochemistry* **140**, 347–366 (1982).
8. Wasberg, M. & Horányi, G. Electrocatalytic Reduction of Nitric Acid at Rhodized Electrodes and Its Inhibition by Chloride Ions. *Electrochimica Acta* **40**, 615–623 (1995).

9. Liu, J.-X., Richards, D., Singh, N. & Goldsmith, B. R. Activity and Selectivity Trends in Electrocatalytic Nitrate Reduction on Transition Metals. *ACS Catalysis* **9**, 7052–7064 (2019).
10. Dima, G. E., de Vooys, A. C. A. & Koper, M. T. M. Electrocatalytic reduction of nitrate at low concentration on coinage and transition-metal electrodes in acid solutions. *Journal of Electroanalytical Chemistry* **554–555**, 15–23 (2003).
11. Petrii, O. A. & Safonova, T. Y. Electroreduction of Nitrate and Nitrite Anions on Platinum Metals: A Model Process for Elucidating the Nature of the Passivation by Hydrogen Adsorption. *Journal of Electroanalytical Chemistry* **331**, 897–912 (1992).

Appendix B

Computational Modeling and Microkinetic Models for NO_3RR

This appendix contains the detailed methodology and additional results for the density functional theory (DFT) modeling work in **Chapters 3 and 4**. The computational work pertaining to **Chapter 3** is performed by Dr. Jin-Xun Liu. The DFT calculations for **Chapter 4** are performed by Samuel D. Young. Two sets of microkinetic models are proposed: (1) a detailed microkinetic model for **Chapter 3** to elucidate nitrate reduction activity and selectivity trends on transition metals and (2) four simplified microkinetic models (with and without the presence of chloride) to understand nitrate reduction features observed through measured current densities on Pt/C and Rh/C in **Chapter 4**.

Additional Computational Methods for Chapter 3

Microkinetic Simulation Methods

For surface reactions, the rate constants for the forward and backward elementary steps were determined by the Arrhenius equation:

$$k_i = Ae^{-\frac{E_a}{k_b T}} \tag{B.1}$$

where k_i is the rate constant in s^{-1} for elementary step i, A is the pre-exponential factor, E_a is the activation energy, T is the temperature, and k_b is Boltzmann's constant. A was approximated as 10^{13} s^{-1} for all the elementary surface reactions.[1] For non-activated molecular adsorption, the rate of adsorption was determined by the rate of surface

impingement of gas-phase molecules. Based on the Hertz-Knudsen equation,[2] the molecular adsorption rate constant of species *i* was computed as:

$$k_{ads} = \frac{pA'}{\sqrt{2\pi m k_b T}} S \tag{B.2}$$

where p is the partial pressure of the adsorbate in the gas phase, A' the surface area of the adsorption site, m the mass of the adsorbate, and S the sticking coefficient, which we assume takes a value of unity for all adsorbates.

For molecular desorption, we assumed there are three rotational degrees of freedom and two translational degrees of freedom in the transition state. Accordingly, the rate constant of desorption for adsorbate *i* was calculated as:

$$k_{des} = \frac{k_b T^3}{h^3} \frac{A'(2\pi k_b)}{\sigma \theta_{rot}} e^{-\frac{\mathrm{E_{des}}}{k_b T}} \tag{B.3}$$

where E_{des} is the desorption energy, h is Planck's constant, and σ and θ_{rot} are the symmetry number and the characteristic temperature for rotation, respectively.

The nitrate reduction rate was calculated by the MKMCXX microkinetic modeling software suite for heterogeneous catalysis.[3–5] In our simulations, the molar ratio of NO_3^- and H^+ in the solution was 1:1 at a reaction temperature of 300 K, which is close to typical experimental reaction conditions. For each of the M components in the kinetic network, a single differential equation for each elementary reaction step was written in the form of:

$$r_i = k_i \prod_{w=1}^{M} {c_w}^{v_w^i} \tag{B.4}$$

where k_i is the rate constant and c_w and v_w^i are the concentration and stoichiometric coefficient of species w in elementary reaction step i. Steady-state coverages were computed by integrating the ordinary differential equations in time until changes in the

surface coverages were small (< 10^{-12}). Rates of the individual elementary steps were obtained based on the computed steady-state surface coverages. The elementary steps that control the rate of the overall reaction were determined using degree of rate control (DRC) analysis.[6–8]

Calculating the Gibbs Free Energy of NO_3^- and Hydrogen Adsorption

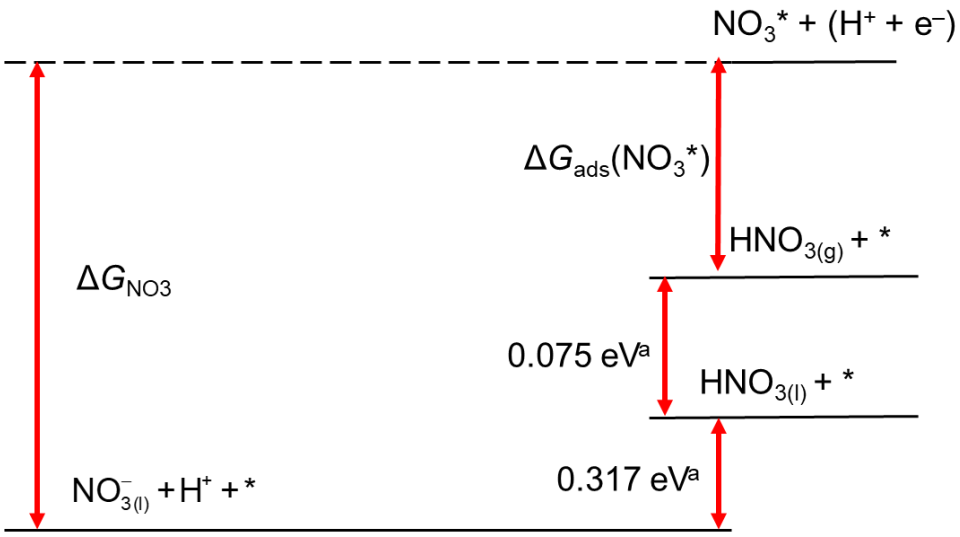

Scheme B.1. The thermodynamic cycle used to calculate the adsorption Gibbs free energy of NO_3^- in the aqueous phase. Schematic adapted from Ref. [9].[a] The thermodynamic values indicated are obtained from the CRC handbook of chemistry and physics. [10]

The Gibbs free energy change for nitrate in aqueous solution ($NO_{3(l)}^-$) to adsorb on an electrode surface (forming NO_3*) was calculated in three steps using the thermodynamic cycle shown in **Scheme B.1.** [9] At 0 V vs RHE, $H^+ + e^- \rightleftharpoons \frac{1}{2} H_2$ is in equilibrium [$\mu(H^+) + \mu(e^-) = \frac{1}{2} \mu(H_2)$] with p_{H2} = 1 atm. For nitrate adsorption on a surface with respect to gaseous HNO_3:

$$HNO_{3(g)} + * \rightarrow NO_3 * + \tfrac{1}{2} H_{2(g)} \qquad \text{(B.5)}$$

the adsorption Gibbs free energy of nitrate with respect to $HNO_{3(g)}$, $\Delta G_{ads}(NO_3*)$, was approximated as:

$$\Delta G_{\mathrm{ads}}(\mathrm{NO_3^*}) = G_{\mathrm{NO3*}} + \tfrac{1}{2} G_{\mathrm{H2}} - E_{\mathrm{sur}} - G_{\mathrm{gas}}(\mathrm{HNO_3}) \quad \text{(B.6)}$$

with

$$G_{\mathrm{NO3*}} = E_{\mathrm{NO3*}} \quad \text{(B.7)}$$

$$G_{\mathrm{H2}} = E_{\mathrm{H2}} + (\Delta H - T\Delta S)_{\mathrm{H2}} \quad \text{(B.8)}$$

$$G_{\mathrm{gas}}(\mathrm{HNO_3}) = E_{\mathrm{gas}}(\mathrm{HNO_3}) + (\Delta H - T\Delta S)_{\mathrm{H2}} \quad \text{(B.9)}$$

where $E_{\mathrm{NO3*}}$ and E_{sur} are the DFT-computed electronic energies of adsorbed nitrate and the bare surface, respectively. Here we neglected rotational, translational, and vibrational free energy contributions for adsorbed nitrate (i.e., $G_{\mathrm{NO3*}} = E_{\mathrm{NO3*}}$). G_{H2} and $G_{\mathrm{gas}}(\mathrm{HNO_3})$ are the corresponding Gibbs free energies of H_2 and HNO_3 molecules in the gas phase at 300 K and 1 atm. The entropic (ΔS) and enthalpic (ΔH) contributions to the free energy of the gaseous species were obtained from JANAF thermodynamic tables. [11] The change in Gibbs free energy of vaporization of $HNO_{3(l)}$ was calculated from the Gibbs free energy difference between the standard formation of HNO_3 in liquid and gas phases and has a value of 0.075 eV. The Gibbs free energy for $HNO_{3(l)}$ formation from NO_3^- in aqueous solution is 0.317 eV. These Gibbs free energies were all obtained from the CRC handbook of chemistry and physics. [10] Ultimately, at 0 V vs RHE, the overall Gibbs free energy for NO_3^- adsorption from the solution phase (ΔG_{NO3}) was calculated as:

$$\Delta G_{\mathrm{NO3}} = \Delta G_{\mathrm{ads}}(\mathrm{NO_3^*}) + 0.075 + 0.317 \quad \text{(B.10)}$$

$$= G_{\mathrm{NO3*}} + \tfrac{1}{2} G_{\mathrm{H2}} - E_{\mathrm{sur}} - G_{\mathrm{gas}}(\mathrm{HNO_3}) + 0.392\ \mathrm{eV}$$

$$= E_{\mathrm{NO3*}} + \tfrac{1}{2} E_{\mathrm{H2}} - E_{\mathrm{sur}} - E_{\mathrm{gas}}(\mathrm{HNO_3}) + 0.75\ \mathrm{eV}$$

The Gibbs free energy of hydrogen adsorption (ΔG_{H}) at 0 V vs RHE was calculated as:

$$\Delta G_H = E_{H*} - E_{\mathrm{sur}} - \tfrac{1}{2} G_{\mathrm{H2}} \quad \text{(B.11)}$$

which simplifies to:[12]

$$\Delta G_H = \Delta E_H + 0.24\ \text{eV} \quad \text{(B.12)}$$

Elementary Steps Involved in Electrocatalytic Nitrate Reduction (NO_3RR)

Nineteen elementary reactions involved in direct nitrate reduction were computed by DFT calculations and used as input for the microkinetic simulations. The 19 elementary steps are shown below:

$$NO_{3\,(l)}^- + * \rightleftarrows NO_3^* + e- \quad \text{(r1, B.13)}$$

$$H+ + e- + * \rightleftarrows H* \quad \text{(r2, B.14)}$$

$$2H^* \rightleftarrows H_{2\,(g)} + 2* \quad \text{(r3, B.15)}$$

$$NO_3^* + * \rightleftarrows NO_2^* + O^* \quad \text{(r4, B.16)}$$

$$NO_2^* + * \rightleftarrows NO^* + O^* \quad \text{(r5, B.17)}$$

$$NO^* + * \rightleftarrows N^* + O^* \quad \text{(r6, B.18)}$$

$$N^* + N^* \rightleftarrows N_2^* + * \quad \text{(r7, B.19)}$$

$$NO^* + NO^* \rightleftarrows N_2O^* + O^* \quad \text{(r8, B.20)}$$

$$N_2O^* + * \rightleftarrows N_2 + O^* \quad \text{(r9, B.21)}$$

$$O^* + H+ + e- \rightleftarrows OH^* \quad \text{(r10, B.22)}$$

$$OH^* + H+ + e- \rightleftarrows H_2O^* \quad \text{(r11, B.23)}$$

$$H_2O^* \rightleftarrows H_2O_g + * \quad \text{(r12, B.24)}$$

$$NO^* \rightleftarrows NO_g + * \quad \text{(r13, B.25)}$$

$$N_2^* \rightleftarrows N_{2\,(g)} + * \quad \text{(r14, B.26)}$$

$$N_2O^* \rightleftarrows N_2O_{\,(g)} + * \quad \text{(r15, B.27)}$$

$$N^* + H+ + e- \rightleftarrows NH^* \quad \text{(r16, B.28)}$$

$$NH^* + H+ + e- \rightleftarrows NH_2^* \quad \text{(r17, B.29)}$$

$$NH_2^* + H+ + e- \rightleftarrows NH_3^* \quad \text{(r18, B.30)}$$

$$NH_3^* \rightleftarrows NH_{3\,(g)} + * \quad \text{(r19, B.31)}$$

Adsorption Energy Calculations

Table B.1. Calculated adsorption energies (in eV) of the intermediates (O, OH, H_2O, NO_3, and NO_2) involved in NO_3RR with respect to the corresponding gaseous molecule or radical. All the intermediates bind through an O atom on the surface.

Metal	ΔE_O	ΔE_{OH}	ΔE_{H2O}	ΔE_{NO3}	ΔE_{NO2}
Ag	–3.43	–2.64	–0.21	–1.91	–1.26
Au	–2.97	–2.30	–0.17	–1.37	–0.89
Co	–5.91	–3.96	–0.58	–3.06	–2.28
Cu	–4.71	–3.33	–0.38	–2.46	–1.77
Fe	–6.40	–4.05	–0.52	–3.27	–2.73
Pd	–4.28	–2.93	–0.35	–2.14	–1.53
Pt	–4.14	–3.03	–0.36	–2.23	–1.93
Rh	–5.14	–3.44	–0.45	–2.69	–2.12

Table B.2. Calculated adsorption energies (in eV) of the intermediates (N, H, NO, N_2O, N_2, NH, NH_2, and NH_3) involved in NO_3RR with respect to the corresponding gaseous molecule or radical. All the intermediates bind through an N atom on the surface, except for hydrogen.

Metal	ΔE_N	ΔE_H	ΔE_{NO}	ΔE_{N2O}	ΔE_{N2}	ΔE_{NH}	ΔE_{NH2}	ΔE_{NH3}
Ag	–2.12	–2.02	–0.41	–0.05	–0.01	–2.38	–2.10	–0.38
Au	–2.47	–2.19	–0.56	–0.02	–0.02	–2.36	–2.13	–0.44
Co	–5.69	–2.76	–2.56	–0.75	–0.71	–4.81	–3.45	–0.85
Cu	–3.83	–2.48	–1.21	–0.17	–0.21	–3.68	–2.89	–0.63
Fe	–6.06	–2.87	–2.88	–0.98	–0.64	–5.05	–3.42	–0.72
Pd	–4.82	–2.77	–2.26	–0.21	–0.49	–3.81	–2.84	–0.79
Pt	–4.83	–2.88	–2.32	–0.28	–0.56	–3.97	–3.23	–1.04
Rh	–5.55	–2.81	–2.69	–0.47	–0.72	–4.54	–3.33	–0.92

Table B.3. Calculated Gibbs free energy change (ΔG_{NO3}) for nitrate adsorption in aqueous phase at 0 V vs RHE and T = 300 K.

Metal	ΔG_{NO3} (eV)
Ag	0.76
Au	1.30
Co	–0.39
Cu	0.21
Fe	–0.61
Pd	0.52
Pt	0.44
Rh	–0.02

Table B.4. Calculated Gibbs free energy change (ΔG_H) for hydrogen adsorption ($H^+ + e^- + * \rightarrow H^*$) at 0 V vs RHE and T = 300 K.

Metal	ΔG_H (eV)
Ag	0.48
Au	0.32
Co	–0.26
Cu	0.02
Fe	–0.37
Pd	–0.27
Pt	–0.38
Rh	–0.30

From the calculated adsorption energies in **Tables B.1 – B.4**, the adsorbate scaling relations for the intermediates relative to O or N adsorption were determined. The adsorbate scaling relation with the larger coefficient of determination, R^2, between O and N is reported in **Chapter 3**.

Activation Barrier Calculations

For the adsorption/desorption elementary reaction steps ($r_1 - r_3$ and $r_{12} - r_{14}$), the adsorption/desorption rate varies as a function of the adsorption energies of reactants/products. We show the calculated activation energies (i.e., activation barriers) and reaction energies for the elementary surface reactions below.

Table B.5. Calculated activation energies (Ea, in eV) and reaction energies (ΔE_{rxn}, in eV) for the elementary steps $r_4 - r_7$ involved in NO_3RR.

Metal	$NO_3^*+*\rightarrow NO_2^*+O^*$		$NO_2^*+*\rightarrow NO^*+O^*$		$NO^*+*\rightarrow N^*+O^*$		$N^*+N^*\rightarrow N_2^*+*$	
	E_a	ΔE_{rxn}	E_a	ΔE_{rxn}	E_a	ΔE_{rxn}	E_a	ΔE_{rxn}
Ag	1.09	0.29	2.15	1.61	2.90	2.15	0.90	–6.14
Au	1.22	0.58	1.62	1.56	2.90	2.42	0.76	–5.46
Co	0.20	–2.06	0.33	–1.99	0.15	–1.76	1.71	0.30
Cu	0.83	–0.94	1.02	0.04	1.20	–0.04	1.28	–2.93
Fe	0.31	–2.79	0.06	–2.35	0.06	–2.29	1.90	1.10
Pd	0.82	–0.59	0.71	–0.81	1.34	0.45	1.26	–1.22
Pt	0.81	–0.77	1.76	–0.34	1.84	0.65	1.27	–1.29
Rh	0.56	–1.50	0.98	–1.51	0.73	–0.72	1.47	0.01

Table B.6. Calculated activation energies (E_a, in eV) and reaction energies (ΔE_{rxn}, in eV) for the elementary steps $r_8 - r_{11}$ involved in NO_3RR.

Metal	NO*+NO*→N_2O*+O*		N_2O*+*→N_2*+O*		H*+O*→OH*+*		OH*+H*→H_2O*+*	
	E_a	ΔE_{rxn}	E_a	ΔE_{rxn}	E_a	ΔE_{rxn}	E_a	ΔE_{rxn}
Ag	0.00	–1.34	0.63	–0.51	0.32	–1.91	0.51	–1.07
Au	1.01	–0.56	1.28	–0.07	0.25	–1.86	1.21	0.76
Co	1.74	–0.24	0.00	–2.98	0.97	0.00	0.86	0.05
Cu	0.58	–1.14	0.00	–1.86	0.66	–0.86	1.38	1.02
Fe	2.31	–0.31	0.21	–3.17	1.48	0.50	0.87	–0.02
Pd	3.06	1.34	1.21	–1.67	0.65	–0.60	1.21	0.17
Pt	3.84	1.54	1.63	–1.54	0.51	–0.73	1.06	0.42
Rh	3.55	1.07	0.77	–2.50	0.70	–0.21	0.38	–0.92

Table B.7. Calculated activation energies (E_a, in eV) and reaction energies (ΔE_{rxn}, in eV) for the elementary reactions $r_{16} - r_{19}$ involved in NO_3RR.

Metal	N*+H*→NH*+*		NH*+H*→NH_2*+*		NH_2*+H*→NH_3*+*	
	E_a	ΔE_{rxn}	E_a	ΔE_{rxn}	E_a	ΔE_{rxn}
Ag	0.60	–2.09	0.67	–2.01	1.07	–1.14
Au	0.63	–1.58	0.84	–1.89	1.04	–1.00
Co	1.06	–0.21	1.07	–0.20	1.22	0.49
Cu	0.83	–1.23	0.99	–1.05	1.32	–0.13
Fe	1.36	0.02	1.37	0.19	1.61	0.69
Pd	1.32	–0.08	1.21	–0.57	1.14	–0.05
Pt	1.16	–0.13	1.36	–0.69	1.43	0.19
Rh	1.11	–0.04	1.19	–0.30	1.16	0.34

Table B.8. Calculated activation energies (E_a(0 V), in eV) and reaction energies (ΔE_{rxn}, in eV) for all the hydrogenation elementary reactions in NO_3RR involving electron transfer at 0 V vs RHE.

Metal	N*+H*→ NH*+*		NH*+H*→ NH_2*+*		NH_2*+H*→ NH_3*+*		O*+H*→ OH*+*		OH*+H*→ H_2O*+*	
	E_a	ΔE_{rxn}	E_a	ΔE_{rxn}	E_a	ΔE_{rxn}	E_a	ΔE_{rxn}	E_a	ΔE_{rxn}
Ag	0.36	–2.57	0.43	–2.49	0.83	–1.62	0.08	–2.39	0.14	–1.40
Au	0.48	–1.89	0.69	–2.21	0.88	–1.32	0.09	–2.18	0.36	–1.39
Co	1.19	0.05	1.20	0.07	1.35	0.75	1.10	0.26	1.34	1.03
Cu	0.82	–1.25	0.98	–1.07	1.31	–0.15	0.65	–0.88	0.85	0.03
Fe	1.55	0.39	1.56	0.56	1.79	1.06	1.67	0.87	1.56	1.39
Pd	1.46	0.18	1.35	–0.30	1.27	0.22	0.78	–0.33	1.00	0.25
Pt	1.35	0.25	1.54	–0.32	1.62	0.57	0.70	–0.35	1.39	0.55
Rh	1.26	0.26	1.34	0.01	1.31	0.64	0.85	0.09	1.22	0.72

BEP Relations

Table B.9. Linear relationships between the forward and backward activation energies (E_a(0 V) and E_b(0 V), respectively) and N and O atom adsorption energies (E_N and E_O) at 0 V vs RHE. All the energies are in eV and the coefficient of determination R^2 is given.

Elementary step	E_a(0 V)	R^2	E_b(0 V)	R^2
$NO_3^* + * \rightleftarrows NO_2^* + O^*$	$E_a = 0.234E_O + 0.054E_N + 2.047$	0.93	$E_b = -0.593E_O - 0.064E_N - 1.324$	0.94
$NO_2^* + * \rightleftarrows NO^* + O^*$	$E_a = 0.451E_O + 0.080E_N + 3.522$	0.69	$E_b = 0.036E_O - 0.628E_N - 1.056$	0.88
$NO^* + * \rightleftarrows N^* + O^*$	$E_a = 0.652E_O + 0.238E_N + 5.453$	0.96	$E_b = -0.561E_O + 0.043E_N - 1.119$	0.94
$N^* + N^* \rightleftarrows N_2^* + *$	$E_a = -0.250E_O - 0.063E_N - 0.117$	0.99	$E_b = -0.186E_O + 1.697E_N + 9.915$	1.00
$NO^* + NO^* \rightleftarrows N_2O^* + O^*$	$E_a = 1.725E_O - 1.887E_N + 1.640$	0.94	$E_b = 0.040E_O - 0.294E_N + 0.855$	0.63
$N_2O^* + * \rightleftarrows N_2^* + O^*$	$E_a = 1.049E_O - 0.742E_N + 2.188$	0.82	$E_b = 0.574E_O - 1.237E_N - 0.565$	0.35
$H^* + O^* \rightleftarrows OH^* + *$	$E_a = -0.273E_O - 0.131E_N - 1.104$	0.91	$E_b = -0.125E_O + 0.537E_N + 3.146$	0.98
$OH^* + H^* \rightleftarrows H_2O^* + *$	$E_a = 0.054E_O - 0.369E_N - 0.400$	0.91	$E_b = 0.223E_O + 0.205E_N + 2.772$	0.97
$N^* + H^* \rightleftarrows NH^* + *$	$E_a = 0.189E_O - 0.415E_N + 0.097$	0.89	$E_b = -0.405E_O + 0.750E_N + 3.078$	0.99
$NH^* + H^* \rightleftarrows NH_2^* + *$	$E_a = 0.211E_O - 0.397E_N + 0.356$	0.88	$E_b = 0.156E_O + 0.386E_N + 4.286$	0.99
$NH_2^* + H^* \rightleftarrows NH_3^* + *$	$E_a = -0.018E_O - 0.175E_N + 0.437$	0.63	$E_b = -0.082E_O + 0.528E_N + 3.234$	0.97

Table B.10. Predicted TOF (s^{-1}) for nitrate electroreduction by microkinetic simulations based on the calculated adsorption energies and activation energies over eight metals at 0 V vs RHE.

Metals	TOF (s^{-1}) for NO_3RR
Ag	1.2×10^{-18}
Au	1.0×10^{-29}
Co	3.0×10^{-5}
Cu	4.2×10^{-5}
Fe	1.7×10^{-11}
Pd	3.5×10^{-18}
Pt	4.9×10^{-20}
Rh	4.3×10^{-6}

Adsorption Energies on Bimetallic Alloys and Select Metal Surfaces

Table B.11. Calculated adsorption energies of oxygen and nitrogen atoms on the stepped surfaces of bimetallic alloys and pure Ir, Ni, Ru, and Zn metals

Catalyst	ΔE_O (eV)	ΔE_N (eV)
FCC Ir(211)	–5.55	–5.72
FCC Ni(211)	–5.52	–5.49
Stepped HCP Ru(0001)	–5.65	–5.86
Stepped HCP Zn(0001)	–3.60	–4.05
BCC Fe_3Ag(310)	–5.94	–5.41
BCC Fe_3Pt(310)	–5.72	–5.48
BCC Fe_3Rh(310)	–6.03	–5.84
BCC Fe_3Co(310)	–6.35	–5.99
BCC Fe_3Ni(310)	–6.16	–5.94
BCC Fe_3Cu(310)	–6.07	–5.61
BCC Fe_3Ru(310)	–6.44	–6.43

BCC Fe_3Sn(310)	–5.50	–4.86
FCC Pt_3Ag(211)	–3.91	–3.99
FCC Pt_3Co(211)	–5.06	–4.99
FCC Pt_3Cu(211)	–4.21	–4.28
FCC Pt_3Ni(211)	–4.55	–4.99
FCC Pt_3Rh(211)	–4.90	–5.17
FCC Pt_3Ru(211)	–5.45	–5.38
FCC Pt_3Sn(211)	–3.92	–3.64
FCC Rh_3Ag(211)	–4.72	–5.07
FCC Rh_3Co(211)	–5.42	–5.79
FCC Rh_3Cu(211)	–4.99	–5.42
FCC Rh_3Ni(211)	–5.26	–5.72
FCC Rh_3Pt(211)	–4.81	–5.32
FCC Rh_3Ru(211)	–5.63	–6.08
FCC Rh_3Sn(211)	–4.33	–5.12
FCC Pd_3Ag(211)	–3.81	–3.69
FCC Pd_3Co(211)	–4.97	–4.97
FCC Pd_3Cu(211)	–4.28	–4.19
FCC Pd_3Ni(211)	–4.71	–4.97
FCC Pd_3Pt(211)	–4.36	–4.93
FCC Pd_3Ru(211)	–5.64	–5.68
FCC Pd_3Sn(211)	–3.83	–3.20
FCC Pd_3Rh(211)	–4.78	–5.28

Adsorption Configurations Related to the Direct Electrocatalytic Nitrate Reduction Mechanism

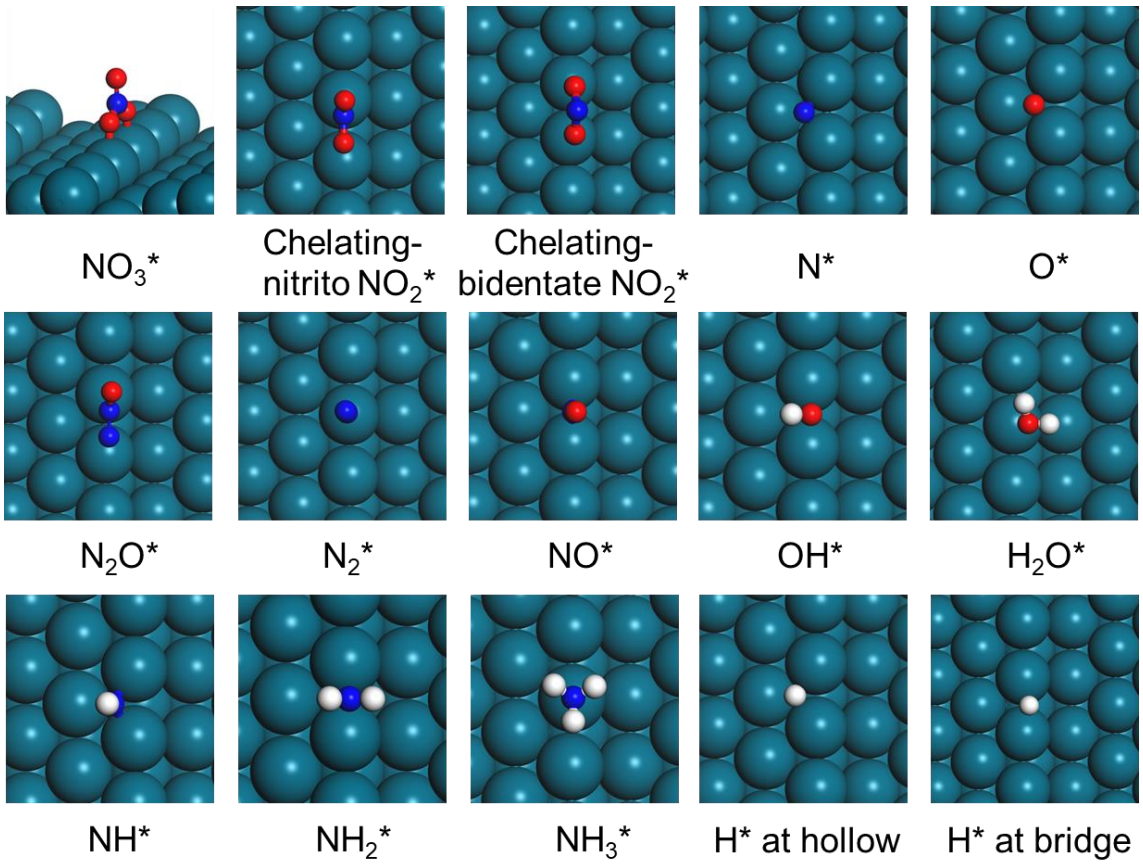

Figure B.1. Favorable adsorption configurations for the considered intermediates on the eight (Fe, Co, Cu, Rh, Pd, Pt, Ag, and Au) transition metal stepped surfaces. NO_2* prefers the chelating-nitrito configuration on Ag, Au, Cu, Co, and Fe and the chelating-bidentate configuration on Pd, Pt, and Rh. Hydrogen prefers to adsorb at a three-fold hollow site on all the metals at low coverage except for Pt, where instead adsorption on a bridge site is favored. N_2O physisorbs on the Ag, Au, and Cu step surfaces. Color legend: Blue = N; Red = O; White = H; Cyan = Transition metal.

Adsorbed nitrite (NO_2*) is a key intermediate in NO_3RR,[13] thus its adsorption geometry and adsorption strength can impact NO_3RR kinetics. The adsorption energy of nitrite generally scales linearly with ΔE_O because NO_2* prefers to adsorb at the step edge with two oxygen atoms binding on Ag, Au, Cu, Co, and Fe stepped surfaces, Figure 1c. On Pd, Pt, and Rh stepped surfaces, however, NO_2* prefers an N,O-nitrito configuration (Figure S1); nevertheless, nitrite adsorption on Pd, Pt and Rh still scales reasonably well with ΔE_O. Our predictions agree with previous DFT predictions that NO_2* adsorbs stronger

on Cu than on Ag or Au clusters via a O,O-chelating nitrito configuration[14] and that NO_2* on Pt(111) prefers the N,O-nitrito configuration. [15]

The geometry of other adsorption intermediates is consistent with previous work, e.g., OH and H_2O adsorb through oxygen at the bridge and top site of the stepped metal surfaces, respectively. [16,17] NO and N_2O prefer to adsorb at the bridge site through nitrogen. For NH_x* (x = 1−3), as x increases from one to three the preferred adsorption site switches from three-fold to the bridge site, then to the top site. Note that N_2O adsorption on Cu, Ag, and Au does not linearly scale with ΔE_N because N_2O weakly physisorbs to those metal surfaces.

Transition State Configurations Related to the Studied NO_3RR Mechanism

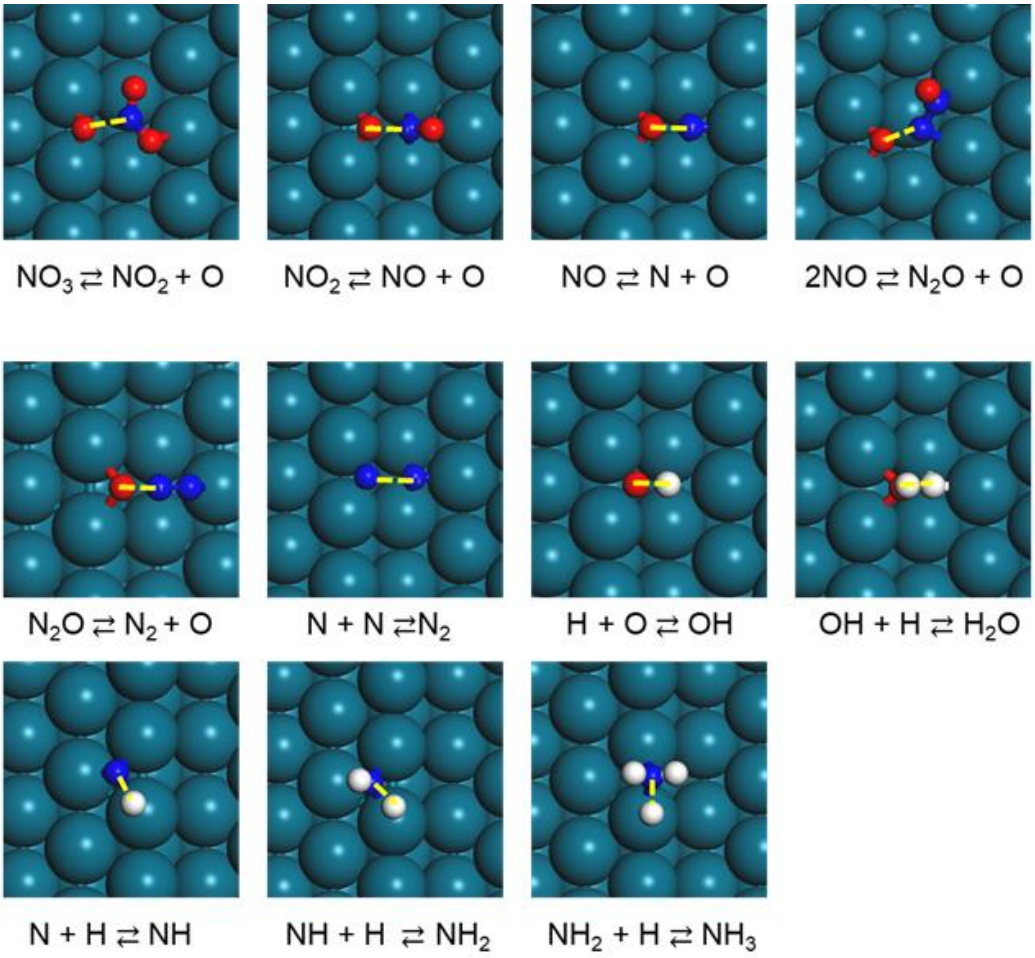

Figure B.2. Typical transition state configurations for NO_3RR on the considered metal stepped surfaces. Color legend: Blue = N; Red = O; White = H; Cyan = Transition metal. The dissociated or associated fragments in the transition state are connected by yellow dashed line.

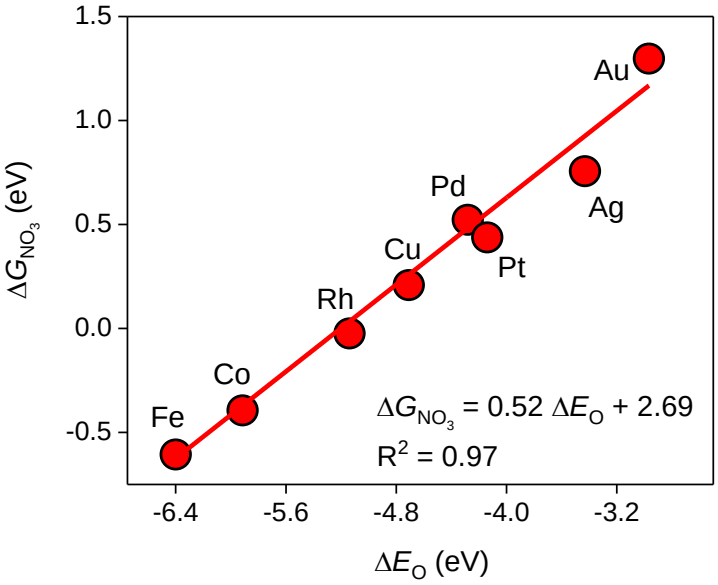

Figure B.3. The adsorbate linear scaling relationship between O atom adsorption energy (ΔE_O) and the Gibbs free energy of nitrate adsorption (ΔG_{NO3}) from the aqueous phase at 0 V vs RHE.

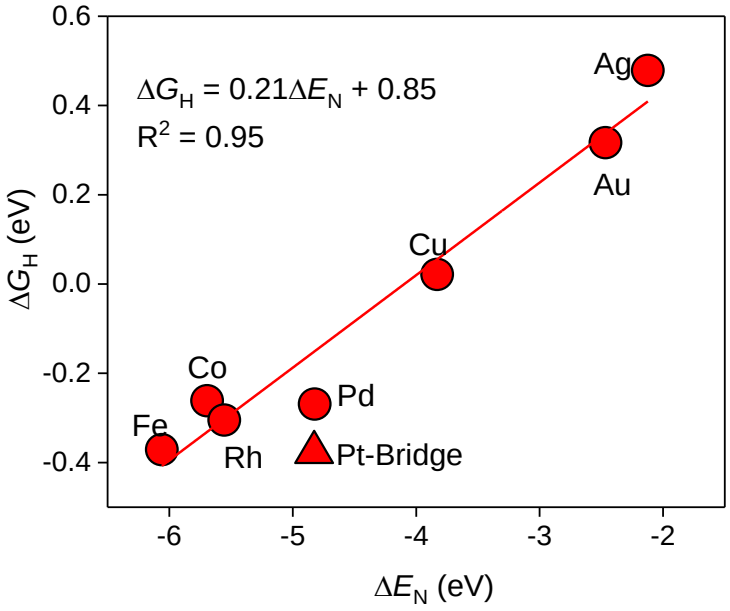

Figure B.4. The adsorbate linear scaling relationship between N atom adsorption energy (ΔE_N) and the Gibbs free energy of hydrogen adsorption (ΔG_H) at 0 V vs RHE. H* adsorbs to the three-fold site on the considered transition metals (circles), except for Pt where H* prefers to adsorb at the bridge site (triangle).

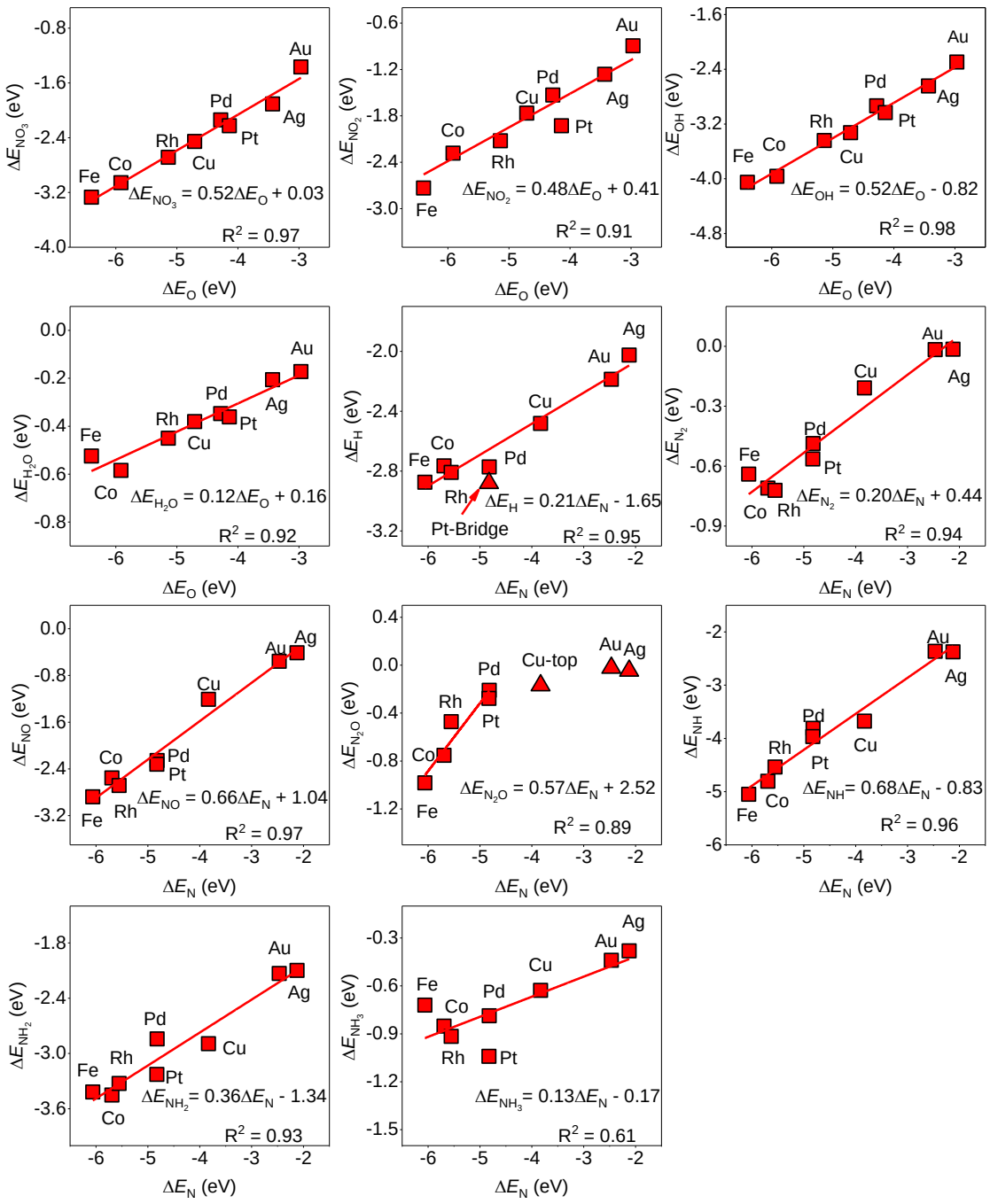

Figure B.5. The linear scaling relationships between the adsorption energy of intermediates involved in NO_3RR and atomic N and O adsorption energies. H* prefers to adsorb at the three-fold site on all the transition metal stepped surfaces, except for Pt where H* adsorbs at the bridge site. N_2O physisorbs weakly on Cu, Au and Ag metals, causing them to not follow the scaling relation.

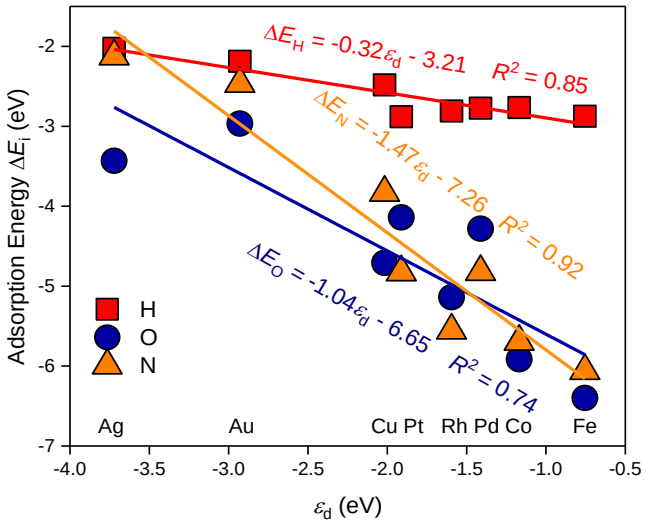

Figure B.6. Linear relationship between *d*-band center (ε_d) with respect to Fermi level and adsorption energies of atomic O, N, and H (ΔE_i, *i* = O, N, and H). The corresponding metals are labeled.

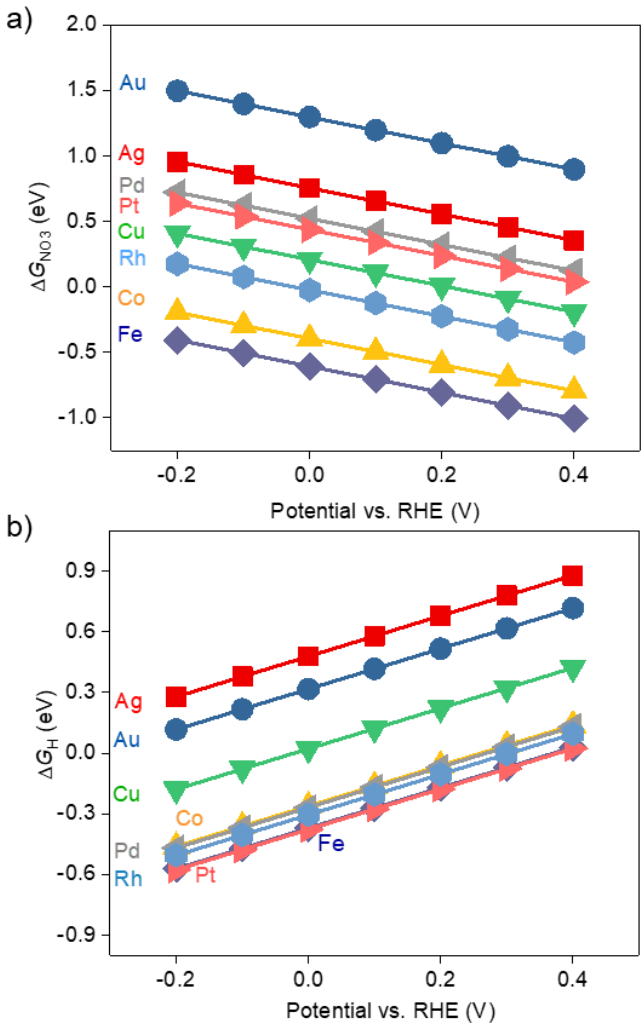

Figure B.7. The change in Gibbs free energies of a) NO_3^-(l) and b) hydrogen adsorption with potential based on the computational hydrogen electrode model.

BEP Relations

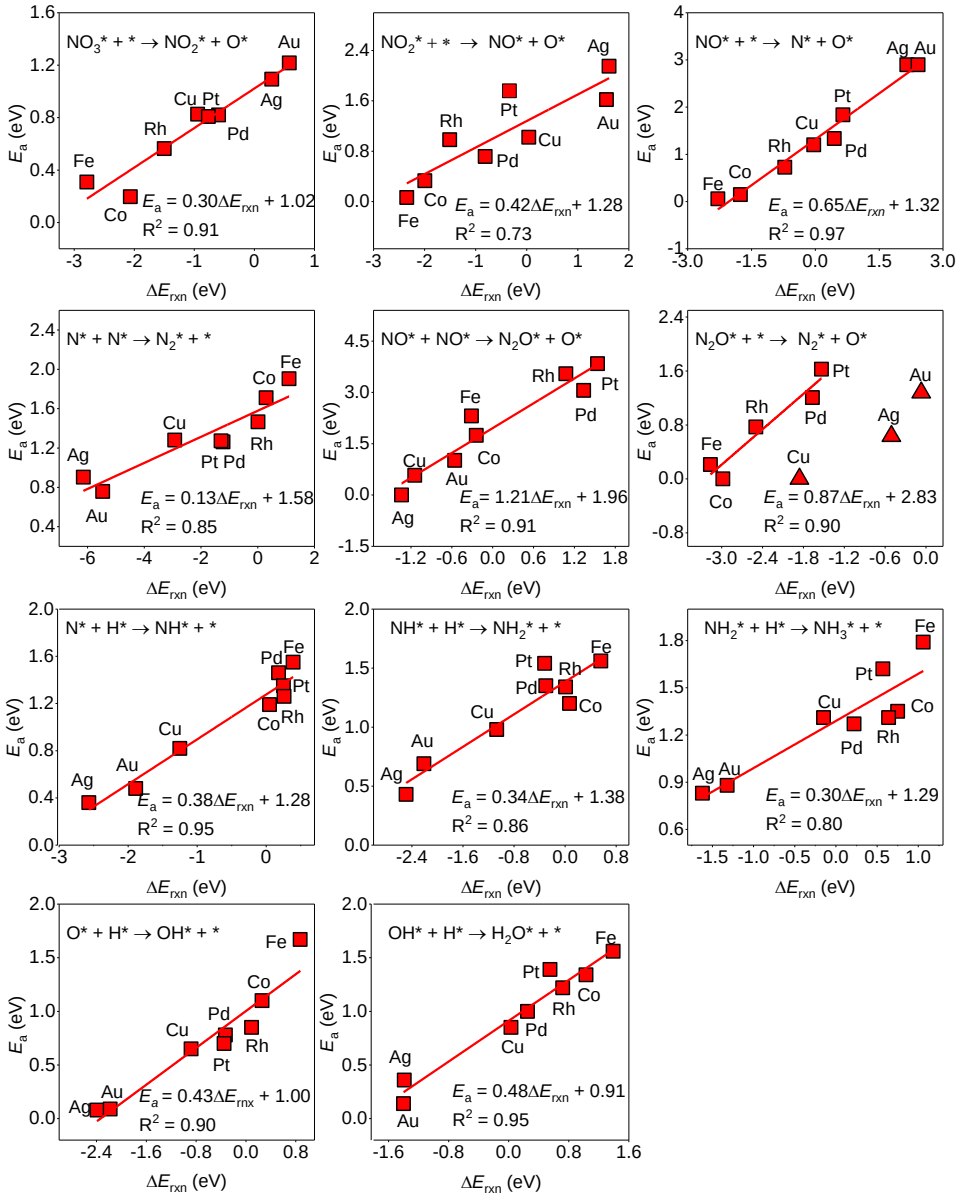

Figure B.8. BEP relationships between activation energies and reaction energies (ΔE_{rxn}) for all the considered elementary reactions involved in NO_3RR at 0 V vs RHE.

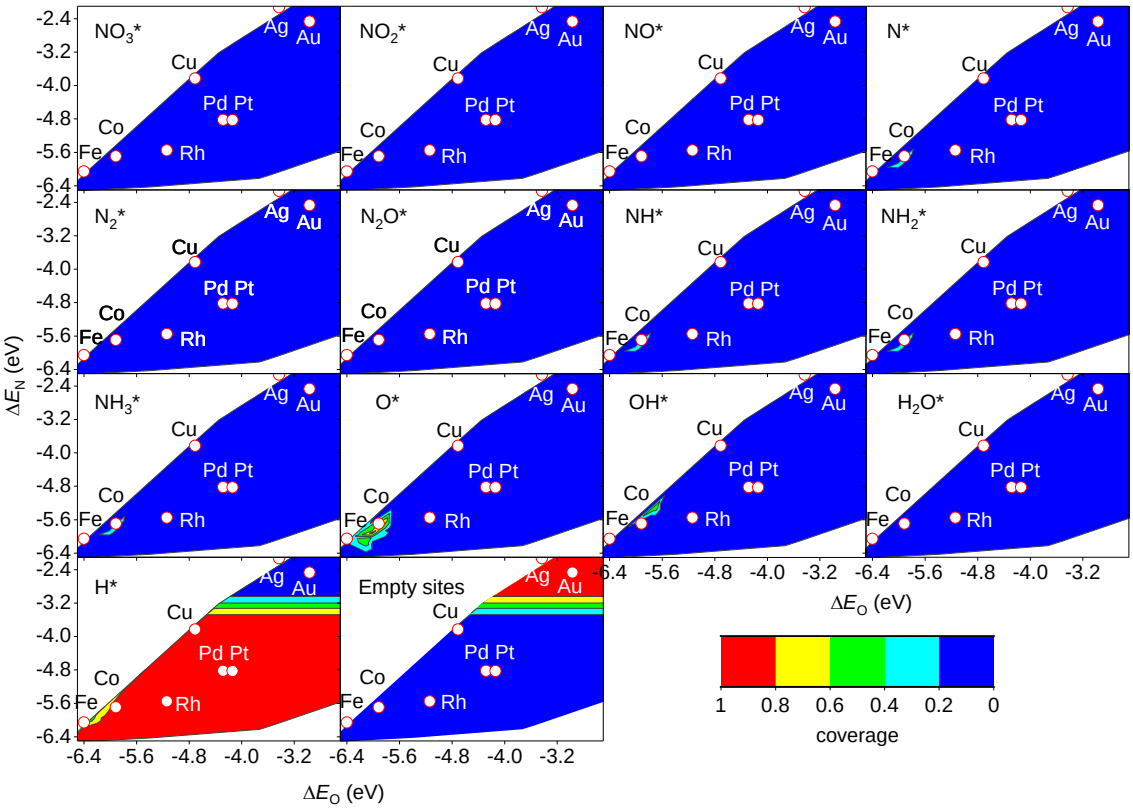

Figure B.9. The variation of coverage as a function of N and O adsorption energies for NO_3^- reduction by microkinetic simulations at 300 K and −0.2 V vs RHE. The color bar indicates the coverage value.

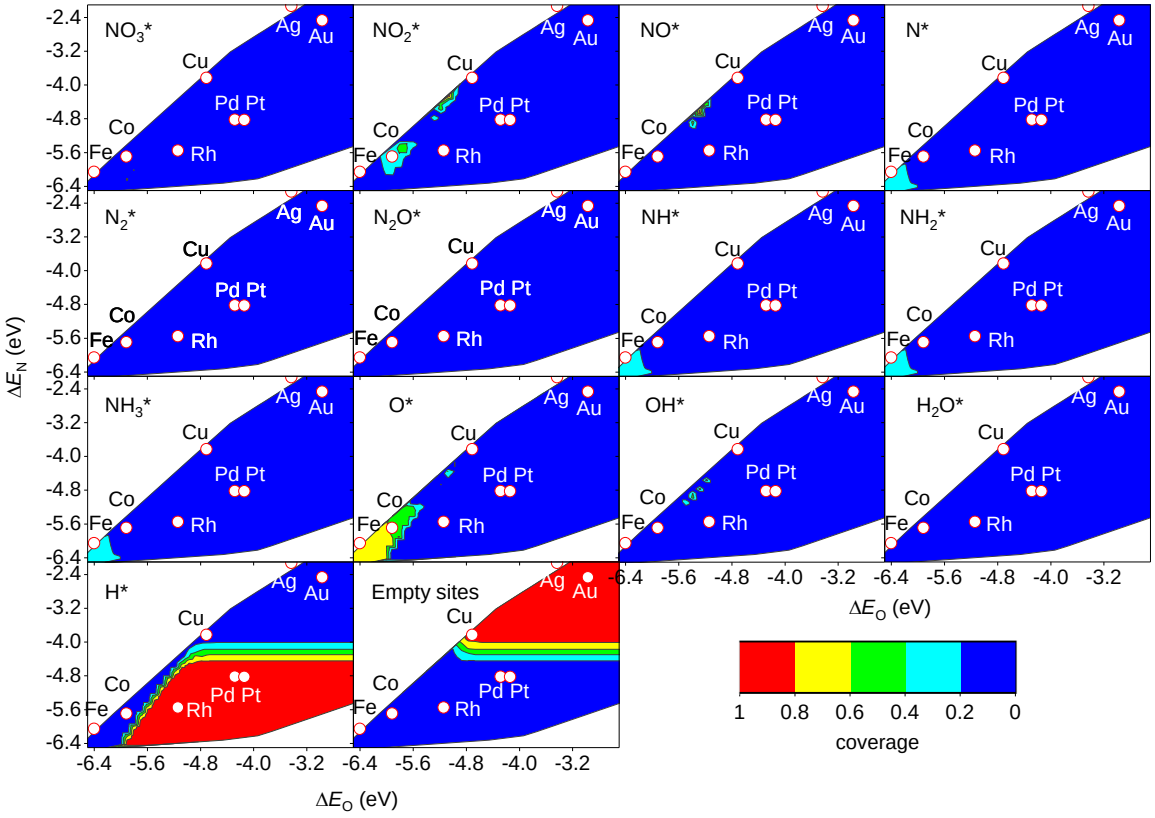

Figure B.10. The variation of coverage as a function of N and O adsorption energies for NO_3^- reduction by microkinetic simulations at 300 K and 0 V vs RHE.

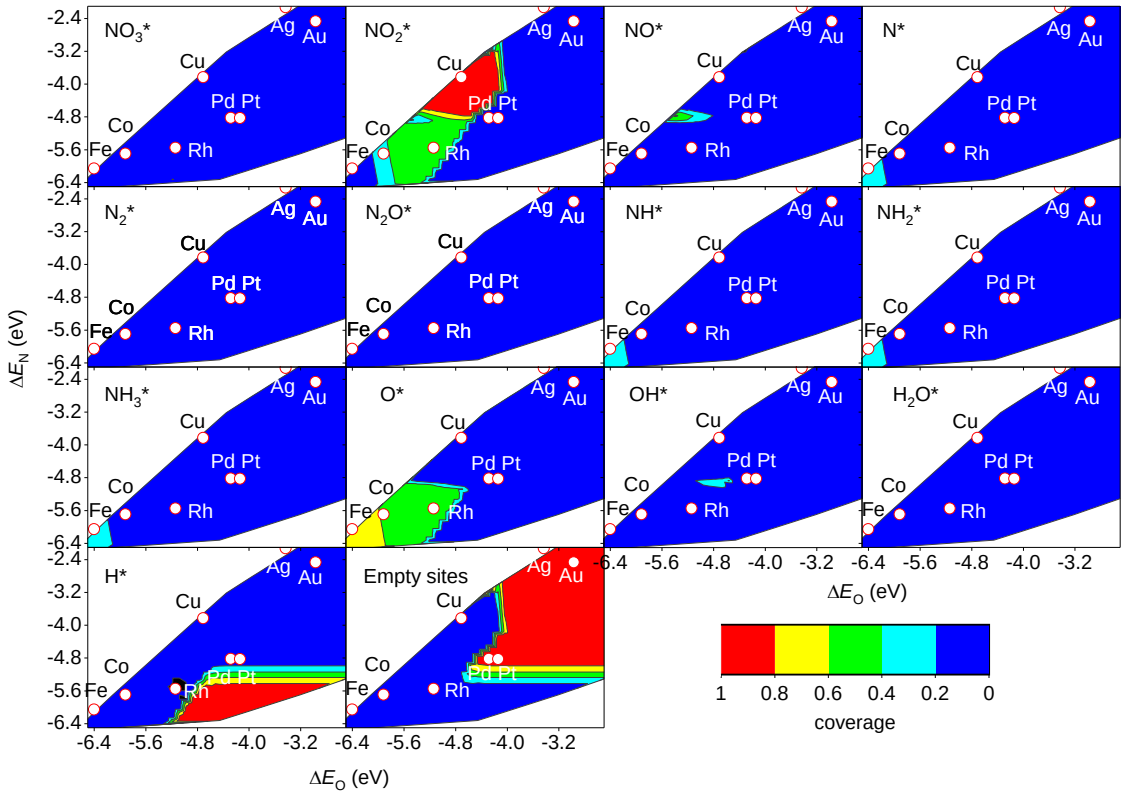

Figure B.11. The variation of coverage as a function of N and O adsorption energies for NO_3^- reduction by microkinetic simulations at 300 K and 0.2 V vs RHE.

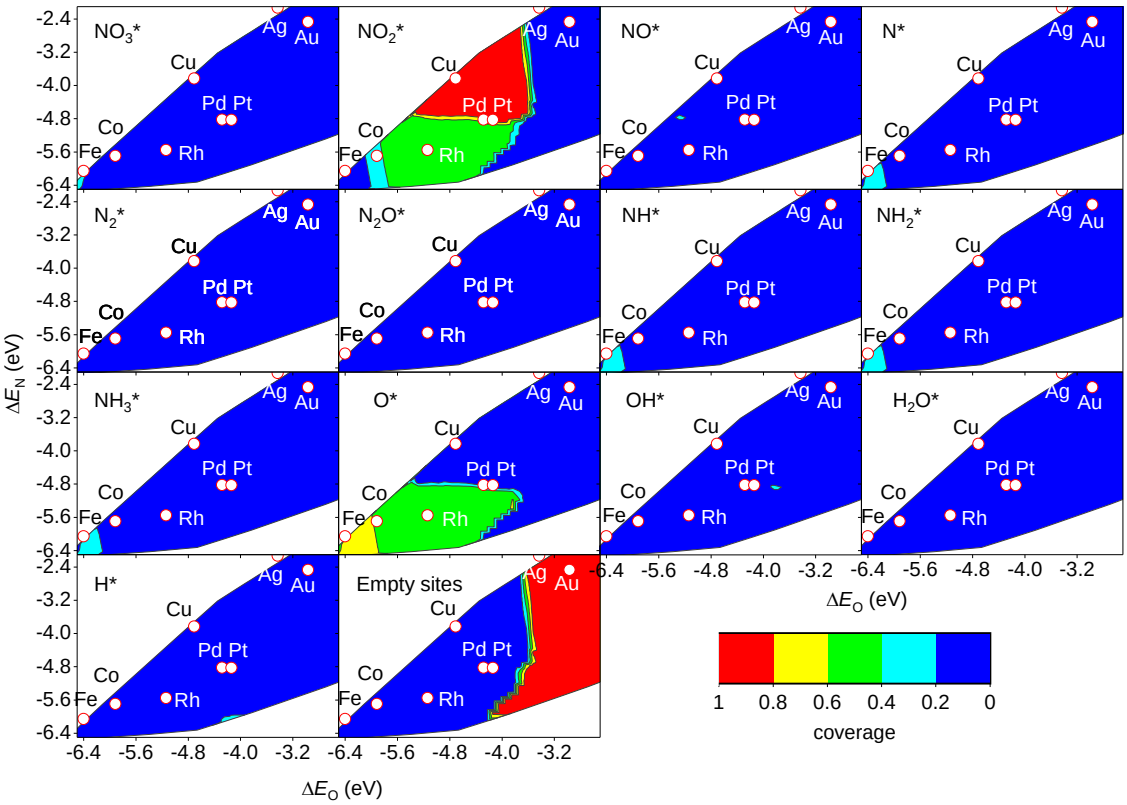

Figure B.12. The variation of coverage as a function of N and O adsorption energies for NO_3^- reduction by microkinetic simulations at 300 K and 0.4 V vs RHE.

Volcano Plot and Selectivity Map at 0.1 V vs RHE

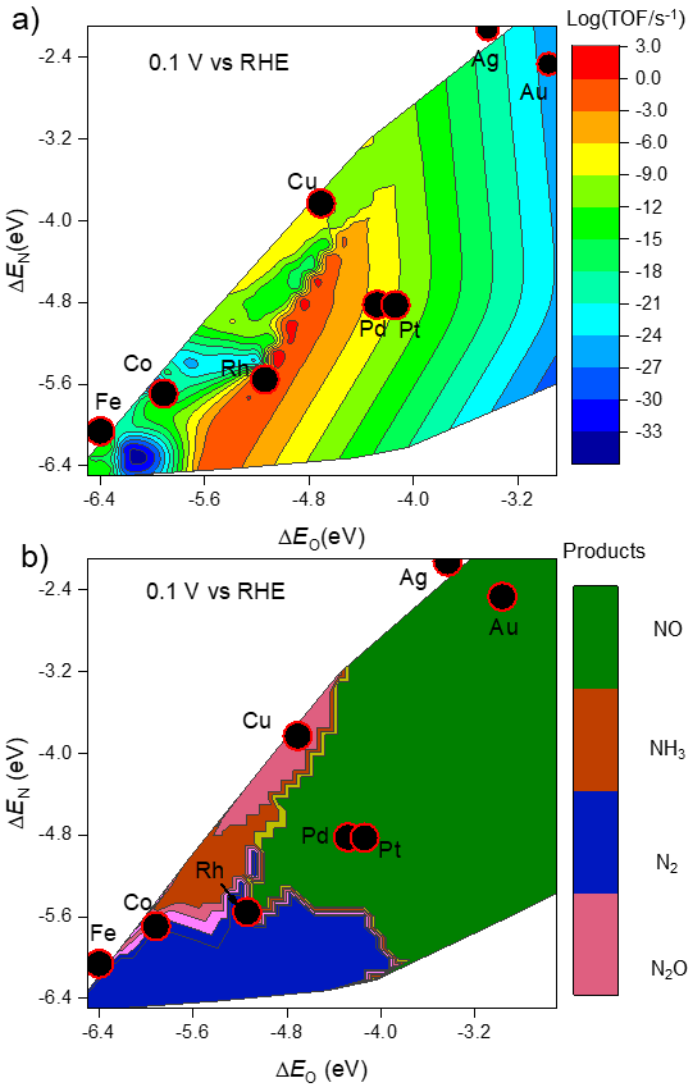

Figure B.13. Theoretical **a**) volcano plot and **b)** selectivity map as a function of atomic oxygen (ΔE_O) and nitrogen (ΔE_N) adsorption energies for NO_3RR on metals based on microkinetic simulations at 0.1 V vs RHE. In the selectivity map, the dominant product made in each region is colored.

Adsorption Configurations on Bimetallic Alloys

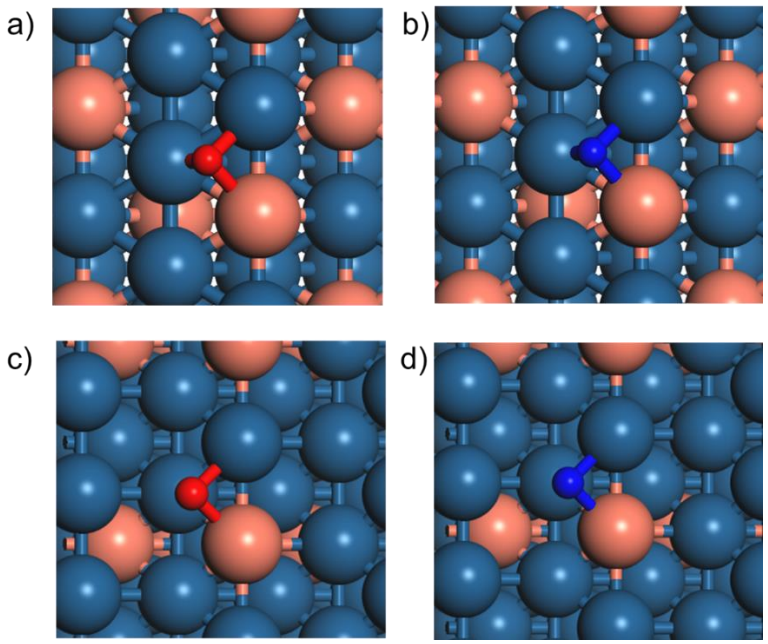

Figure B.14. Adsorption configurations for atomic nitrogen and oxygen on bimetallic stepped surfaces. a) and b) show nitrogen and oxygen adsorption on the same FCC $Pt_3M(211)$ and $Rh_3M(211)$ surfaces, respectively; c) and d) show nitrogen and oxygen adsorption on the BCC $Fe_3M(310)$ surface. Color legend: N = blue; O = red.

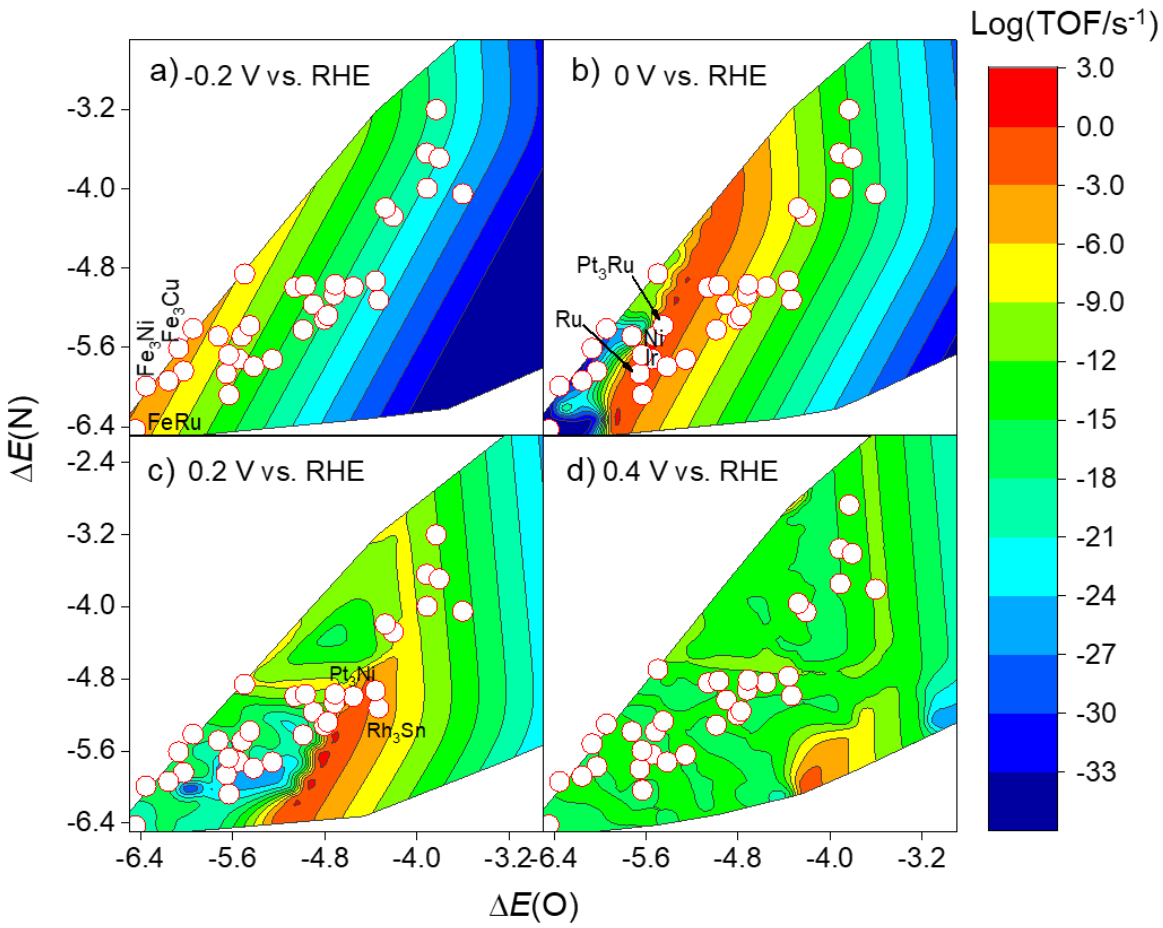

Figure B.15. Theoretical volcano plots of bimetallic alloys for NO_3RR at: a) −0.2 V, b) 0 V, c) 0.2 V, and d) 0.4 V vs RHE. Reaction conditions are T = 300 K with a H^+/NO_3^- molar ratio of 1:1. The solid white circles show the activity of Pt_3M, Pd_3M, Fe_3M, and Rh_3M (M = Ag, Co, Cu, Ni, Pt, Rh, Ru and Sn) alloys and Ru, Ir, Ni, and Zn metals predicted using adsorbate and BEP linear scaling relations. Only select bimetallics are labeled for clarity.

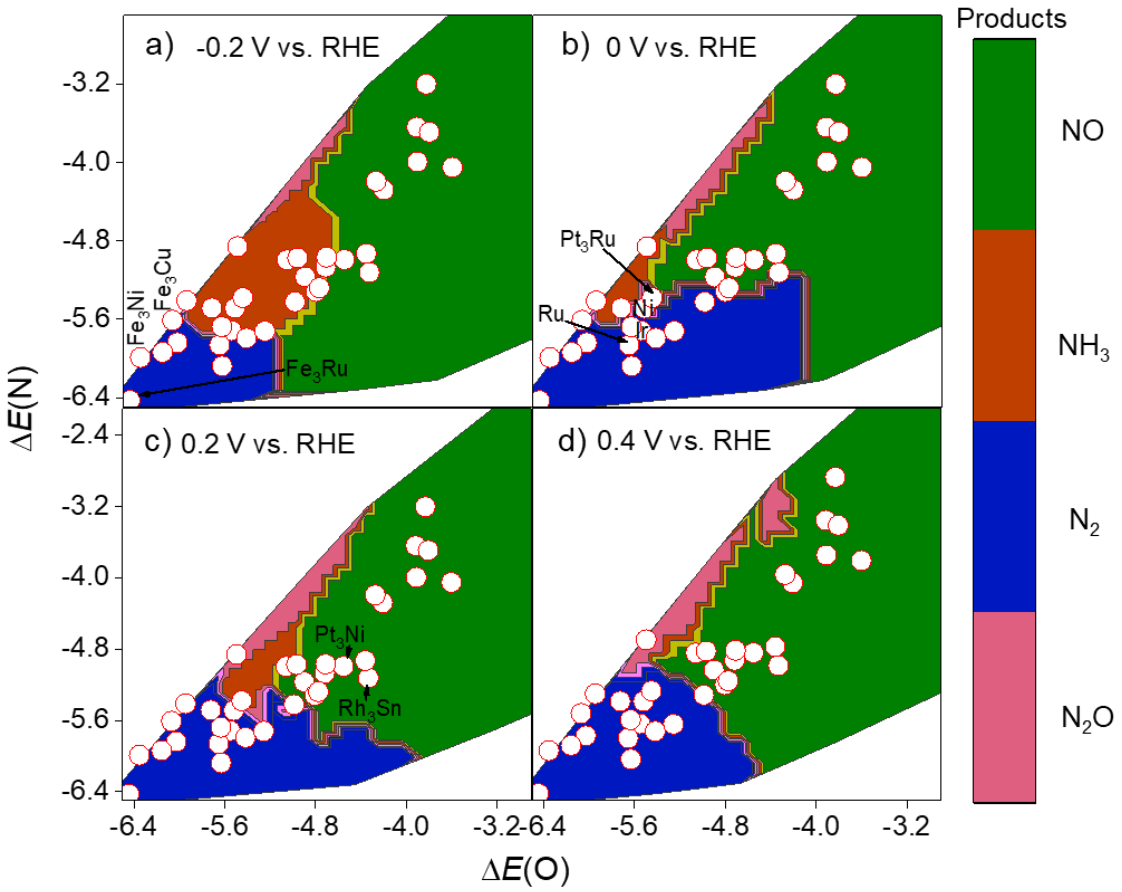

Figure B.16. Selectivity maps of bimetallic alloys for NO_3RR at: a) −0.2, b) 0.0, c) 0.2, and d) 0.4 V vs RHE. Reaction conditions are T = 300 K with a H^+/NO_3^- molar ratio of 1:1. The solid white circles show the location of the Pt_3M, Pd_3M, Fe_3M, and Rh_3M (M = Ag, Co, Cu, Ni, Pt, Rh, Ru and Sn) alloys and Ru, Ir, Ni, and Zn metals on the selectivity map. The dominant product made in each adsorption energy region is colored green (NO), brown (NH_3), blue (N_2), or pink (N_2O).

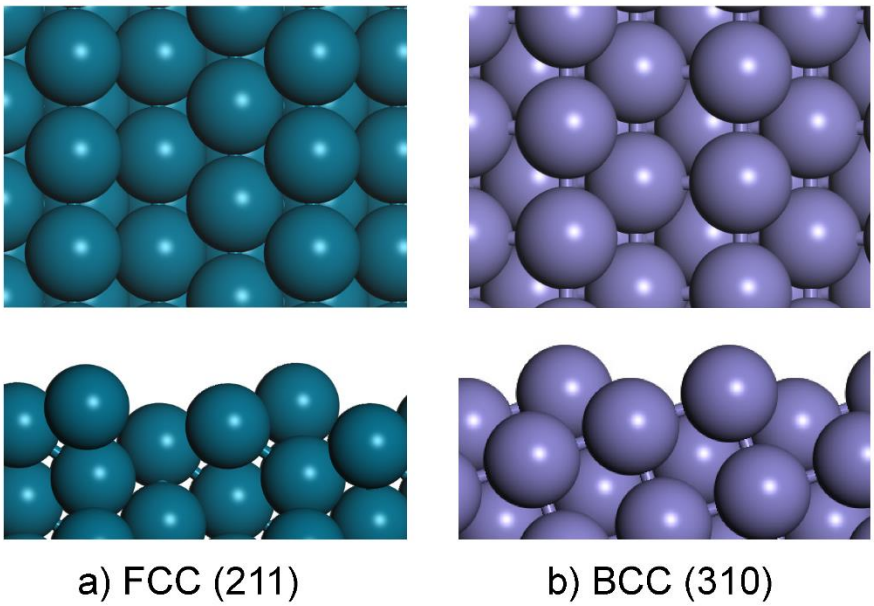

Figure B.17. Structures of the FCC(211) and BCC(310) surfaces for the eight transition metals studied via DFT modeling.

Density Functional Theory Modeling Methodology for Chapter 4

Geometry Relaxation and Transition State Search

DFT calculations were performed using the Vienna Ab Initio Simulation Package[18–21] with the BEEF-vdW functional.[22] BEEF-vdW exhibits similar or superior performance compared to functionals such as PBE, RPBE, and optPBE-vdW.[23] BEEF-vdW includes a van der Waals correction and yields its own error estimates of electronic energies. All calculations were spin-polarized and used the projector-augmented wave method,[24,25] a plane-wave kinetic energy cutoff of 400 eV, and Gaussian smearing of 0.05 eV. Geometry optimizations used differences of less than 0.02 eV $Å^{-1}$ for ionic steps and 10^{-4} eV for electronic steps as stopping criteria. Geometry optimization was done for bulk crystals to calculate lattice constants using a Γ-centered Monkhorst-Pack *k*-point grid (16×16×16 for metals, 4×4×4 for Rh_xS_y structures).[26] For metal surfaces, a 6×6×1 *k*-point grid was used, and slabs were built using a 3×4×4 supercell of the (211) facet. The bottom layer of atoms was fixed, and all other layers could relax, with 13 Å of vacuum space. The adsorption energies of NO_3^-, Cl^-, and H^+ were computed for the (211) stepped surfaces of Au, Ag, Cu, Pd, Pt, and Rh. Adsorption energies were calculated using coverages of 1/12 ML (for H^+ and Cl^-) or 1/6 ML (for NO_3^-). We choose (211) as a model site that is reported to be active for NO_3RR.[27–29] The choice of the (211) is also validated by our previous computational work, which reproduced experimental NO_3RR activity trends on transition metals using a microkinetic model built on step surface data.[27] For the (211) facet used, we extensively sampled possible adsorption sites on both the edge and terrace portions of this facet. The adsorption site selected was that with the most negative binding energy, which was the edge site on the (211) facet.

For models of pristine and S-defected Rh_xS_y surfaces (i.e., with sulfur vacancies), adsorption energies were calculated using a 3×3×1 *k*-point grid, with other DFT settings kept the

same as used for metal surfaces. To simulate similarly low coverages of adsorbates, each Rh_xS_y slab was repeated in the *x* and/or *y* directions to create a larger supercell such that the entire slab contained no more than 80 slab atoms. Enough layers were maintained in each supercell such that the slab thickness was approximately 8–10 Å. During geometry optimization, the bottom half of each Rh_xS_y slab was constrained and all other atoms could relax, with 38 Å of vacuum space. Electronic energies of isolated H_2, N_2, Cl_2, HCl, HNO_2, HNO_3, NO_3, and NO_2 species in the gas phase were calculated using the same DFT settings as used for pure metals, but with a plane-wave energy cutoff of 500 eV, Gaussian smearing of 0.2 eV, and a 1×1×1 *k*-point grid. To minimize interference of periodic images and excess symmetry, each gas-phase adsorbate was placed slightly off-center in a 15.00×15.11×15.21 Å cell.

Nitrate adsorption free energies in the aqueous phase were calculated at standard conditions (298.15 K, 1 M) via a thermodynamic cycle. Aqueous-phase solvation effects on surface energies, chloride and hydrogen adsorption, and transition state energies were not included

Nitrate dissociation activation energies on Rh and Rh_xS_y phases were identified using the climbing-image nudged elastic band method (NEB) method[30] (for the direct reduction mechanism) or the improved dimer method[31,32] (for the H-assisted reduction mechanism). Activation energy calculations on Rh and Rh_xS_y surfaces used the same DFT settings as used for geometry relaxations on pure metal and Rh_xS_y surfaces, with spring forces of 5 eV $Å^{-1}$ and with a climbing image used throughout the relaxation. The dimer method used a dimer length of 0.01 Å and step sizes ranging from 0.0018 Å to 0.0075 Å. The initial dimer images were estimated using an interpolated image slightly earlier than the transition state image predicted by NEB and atomic displacements tangent to the NEB curve at the transition state reaction coordinate, respectively. Initial trial dimer directions were estimated by inspection, by randomly displacing atoms in the adsorbate, and by

calculating eigenvectors from vibrational analysis of the initial dimer images. As with NEB and geometry relaxations, dimer optimization used an electronic tolerance of 10^{-4} eV and a maximum ionic force tolerance of 0.02 eV $Å^{-1}$.

Surface Facet and Termination Choice for Model Rh_xS_y Systems

Rh_xS_y is a mixture of Rh_3S_4, Rh_2S_3 and $Rh_{17}S_{15}$ phases. The bulk phase stability of Rh_xS_y has been determined using electrochemical measurements,[33] which concluded that Rh_2S_3 is the enthalpically most stable bulk phase by about 2 kJ mol^{-1}, followed by Rh_3S_4 and then $Rh_{17}S_{15}$, although experiments and theory disagree about this ordering.[34] Prior DFT modeling predicted stable surface terminations of low-index Rh_xS_y facets (i.e., Rh_2S_3(001), Rh_3S_4(100), and $Rh_{17}S_{15}$(100)) in the gas phase.[35] Based on this study, we chose to model adsorption and reactions on the termination of the lowest surface energy for each of these facets in the gas phase. For Rh_xS_y there are many possible locations along the facet's normal vector to cut the surface that will lead to different surface terminations. The Pymatgen software package[36,37] was used to search for symmetrically distinct surface terminations of these facets in a more exhaustive way than the prior study.[35] Symmetric terminations were enumerated from the Rh_2S_3(001), Rh_3S_4(100), and $Rh_{17}S_{15}$(100) facets using a per-atom surface energy metric. With a tolerance of 0.1 Å between successive cleave planes, 26 symmetrically unique terminations (five for Rh_2S_3(100), nine for Rh_3S_4(100), and 12 for $Rh_{17}S_{15}$(100)) were found. The most stable surface terminations are reported. Ultimately, our identified low-energy surface terminations agree with the previous study of Rh_xS_y.[35] We emphasize these are vacuum-phase model systems and that there may be surface reconstruction under acidic conditions and in the presence of an applied potential.[38] Nevertheless, we show that these model surfaces qualitatively rationalize our experimental observations.

To model Rh_xS_y surfaces with S vacancies, a single S atom was removed from each of the three pristine surface terminations that we identified as most stable. For each of these pristine surface terminations, the symmetrically distinct surface S atoms were located. A single S atom was removed at a time and the resulting energy of the defected surface calculated. The position of the S vacancy resulting in the lowest surface electronic energy was chosen as the vacancy position for that termination and was used when modeling adsorption of species. To limit complexity and computational expense, we limited our study to vacancies of only a single S atom in the supercell.

Calculating Adsorption Free Energies of Nitrate, Hydrogen, and Chloride

The Gibbs energy of nitrate adsorption at 0 V vs. SHE ($\Delta G_{\mathrm{NO_3}}(E = 0\ \mathrm{V\ vs.\ SHE})$) was computed using a thermodynamic cycle to include solvation and temperature effects, while avoiding the explicit DFT calculation of a nitrate anion in the aqueous phase.[27,28] For this correction, all tabulated values correspond to standard conditions (298.15 K, 1 bar). We use the generalized computational hydrogen electrode model (CHE)[39] to compute the potential-dependent adsorption free energy of nitrate, $\Delta G_{\mathrm{NO_3}}$. The adsorption of nitrate to a catalyst surface is:

$$\mathrm{NO_{3\ (aq)}^{-}} + * \rightleftharpoons \mathrm{NO_3^*} + \mathrm{e^-} \tag{B.32}$$

Figure S6 illustrates the thermodynamic cycle used to obtain $\Delta G_{\mathrm{NO_3}}$, which breaks the adsorption process into three steps:

The formation of liquid HNO_3 from its aqueous ion constituents, denoted as $\Delta G_{\mathrm{assoc}}(\mathrm{HNO_3})$.

The vaporization of liquid HNO_3 to form gaseous HNO_3, denoted as $\Delta G_{\mathrm{vap}}(\mathrm{HNO_3})$.

The dissociative adsorption of gaseous HNO_3 to surface-adsorbed $\mathrm{NO_3^*}$ and ½ H_2 on a bare metal surface (in vacuum), denoted as $\Delta G_{\text{diss-ads}}(\mathrm{NO_3^*})$. At 0 V vs. SHE and pH = 0, ½ H_2 is equilibrated with aqueous $\mathrm{H^+ + e^-}$.

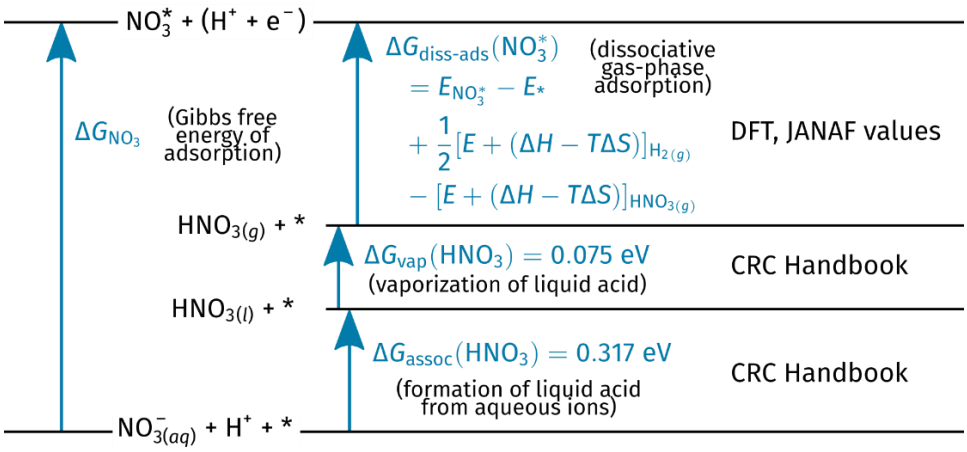

Figure B.18. Thermodynamic cycle used for calculation of Gibbs energy of nitrate adsorption at 0 V vs. SHE. Adapted from Calle-Vallejo and coworkers.[28] Values were retrieved from the CRC handbook[40] and the JANAF Thermochemical Tables.[41] The Gibbs energies of formation needed to calculate $\Delta G_{assoc}(HNO_3)$ and $\Delta G_{vap}(HNO_3)$ are given in **Table B.12.**

Table B.12. Gibbs energies of formation used to calculate $\Delta G_{assoc}(HNO_3)$ and $\Delta G_{vap}(HNO_3)$. Values taken from the CRC handbook.[40] Tabulated at 298.15 K and 1 bar.

Quantity	kJ mol^{-1}	eV
$\Delta G_f(H^+_{(aq)})$	0.0	0.000
$\Delta G_f(NO^-_{3(aq)})$	−111.3	−1.153
$\Delta G_f(HNO_{3(l)})$	−80.7	−0.836
$\Delta G_f(HNO_{3(g)})$	−73.5	−0.762

The energy of forming $HNO_{3(l)}$ from its aqueous ions is:

$$\Delta G_{assoc}(HNO_3) = \Delta G_f(HNO_{3(l)}) - \Delta G_f(NO^-_{3(aq)}) - \Delta G_f(H^+_{(aq)}) = -0.836\text{ eV} - (-1.153\text{ eV}) - 0\text{ eV} = \boxed{0.317\text{ eV}}. \quad \text{(B.33)}$$

The energy required to vaporize $HNO_{3(l)}$ to $HNO_{3(g)}$ is:

$$\Delta G_{vap}(HNO_3) = \Delta G_f(HNO_{3(g)}) - \Delta G_f(HNO_{3(l)}) = -0.762\text{ eV} - (-0.836\text{ eV}) = \boxed{0.075\text{ eV}}. \quad \text{(B.34)}$$

The term $\Delta G_{diss\text{-}ads}(NO_3^*)$ is defined as:

$$\Delta G_{diss\text{-}ads}(NO_3^*) = E_{NO_3^*} + \frac{1}{2}\left(E_{H_2} + \Delta H_{H_2} - T\Delta S_{H_2}\right)_{(g)} - E_* - \left(E_{HNO_3} + \Delta H_{HNO_3} - T\Delta S_{HNO_3}\right)_{(g)} \quad \text{(B.35)}$$

where E_i denotes a DFT-computed electronic energy and ΔH_i and ΔS_i represents enthalpic and entropic ideal-gas corrections, respectively, required to convert the electronic energies of the gaseous species *i* to standard conditions. Ultimately, the Gibbs energy of nitrate adsorption is:

$$\Delta G_{NO_3}(E = 0\,\text{V}) = \Delta G_{\text{diss-ads}}(NO_3^*) + \Delta G_{\text{vap}}(HNO_3) + \Delta G_{\text{assoc}}(HNO_3) \quad \text{(B.36)}$$

The Gibbs energy of nitrate adsorption as a function of applied potential *E* (vs. SHE) within the CHE framework is:[27]

$$\Delta G_{NO_3} = \Delta G_{NO_3}(E = 0\,\text{V}) - FE \quad \text{(B.37)}$$

Table B.13. Thermodynamic parameters used to correct gas-phase molecular DFT energies, taken from the JANAF thermodynamic tables.[41] All parameters are with respect to the reference state $T_{\text{ref}} = 298.15$ K and $P = 1$ bar.

Quantity	$H_{2(g)}$	$HNO_{3(g)}$	$Cl_{2(g)}$
T	298.15 K	298.15 K	298.15 K
$H(T)$	0.000 kJ/mol	0.000 kJ/mol	0.000 kJ/mol
$H(0\,\text{K})$	−8.467 kJ/mol	−11.780 kJ/mol	−9.181 kJ/mol
$S(T)$	130.680 J/mol-K	266.400 J/mol-K	223.079 J/mol-K
$S(0\,\text{K})$	0.000 J/mol-K	0.000 J/mol-K	0.000 J/mol-K
$\Delta H - T\Delta S$ (kJ/mol)	−30.495 kJ/mol	−67.647 kJ/mol	−57.330 kJ/mol
$\Delta H - T\Delta S$ (eV)	−0.316 eV	−0.701 eV	−0.594 eV

Dependence of Adsorption Gibbs Energies of Cl^- and H^+ on Applied Potential

The generalized CHE model was used to model the effect of applied potential on the adsorption free energies of Cl* and H*.[42] This model gives a thermodynamic approximation of the change in adsorption free energy that occurs in the aqueous phase at an applied potential compared to the gaseous phase with no applied potential. At standard conditions, H_2 molecules at the surface of the solution are in equilibrium with dissolved protons and electrons at the Fermi level of the metal electrode.[43]

$$\frac{1}{2}H_{2(g)} \rightleftharpoons H^+_{(aq)} + e^- \text{ [standard conditions]} \quad \text{(B.38)}$$

At equilibrium, the Gibbs energies of the species are related by a reaction quotient and a potential shift:

$$G_{\mathrm{H^+}} + G_{\mathrm{e^-}} = \frac{1}{2} G_{\mathrm{H_2}(g)} + RT \ln \left[\frac{a_{\mathrm{H^+}} a_{\mathrm{e^-}}}{\sqrt{a_{\mathrm{H_2}}}} \right] - nF\left(E - E^\circ(\mathrm{H_2})\right)$$
$$= \frac{1}{2} G_{\mathrm{H_2}(g)} - RT \ln 10\ (\mathrm{pH}) - nF(E - 0\ \mathrm{V\ vs.\ SHE}) \quad \text{(B.39)}$$

where G_{i} is the Gibbs energy of species i and a_i is the dimensionless thermodynamic activity. These activities are referenced to a concentration of 1 mol/L (for protons this implies pH = 0) and 1 bar (for gaseous species). E is the applied cell potential, $E^\circ(\mathrm{H_2}) = 0\ \mathrm{V\ vs.\ SHE}$ is the standard redox potential for the $\frac{1}{2}\mathrm{H}_{2(g)} \rightleftharpoons \mathrm{H}^+_{(aq)} + \mathrm{e}^-$ equilibrium, and n is the number of electrons transferred. Here, we have assumed activity coefficients of unity, and $n = +1$ for proton reduction.

The formalism for the CHE model is intuitively extended to other aqueous adsorbates formed from dissociation of a gaseous dimer.[43] For the adsorption of $\mathrm{Cl^-}$, the pertinent equilibrium reaction is:

$$\frac{1}{2}\mathrm{Cl}_{2(g)} + \mathrm{e}^- \rightleftharpoons \mathrm{Cl}^-_{(aq)}\ [\text{standard conditions}] \quad \text{(B.40)}$$

and the corresponding shift in Gibbs energy is given by:

$$G_{\mathrm{Cl^-}} - G_{\mathrm{e^-}} = \frac{1}{2} G_{\mathrm{Cl_2}(g)} + RT \ln \left[\frac{a_{\mathrm{Cl^-}}}{a_{\mathrm{e^-}}\sqrt{a_{\mathrm{Cl_2}}}} \right] - nF(E - E^\circ(\mathrm{Cl_2}))$$
$$= \frac{1}{2} G_{\mathrm{Cl_2}(g)} - RT \ln a_{\mathrm{Cl^-}} - nF(E - 1.36\ \mathrm{V}) \quad \text{(B.41)}$$

where we again assume activity coefficients of unity, but here $n = -1$ and we use the reduction potential of the chlorine redox couple, $E^\circ(\mathrm{Cl_2}) = 1.36\ \mathrm{V\ vs.\ SHE}$.

Using the CHE, the adsorption free energy of hydrogen (ΔG_{H}) as a function of potential to a site * at pH = 0 is:

$$\Delta G_{\mathrm{H}} = G_{\mathrm{H}*} - G_* - \frac{1}{2} G_{\mathrm{H_2}(g)} + FE = \Delta G_{\mathrm{H}}(E = 0\ \mathrm{V}) + FE \quad \text{(B.42)}$$

$$\Delta G_{\mathrm{H}} \approx [E_{\mathrm{H}*} + \Delta \mathrm{ZPE}_{\mathrm{H}*}] - E_* - \frac{1}{2} G_{\mathrm{H_2}(g)} + FE \quad \text{(B.43)}$$

where ΔZPE_{H*} is the zero-point energy correction for H adsorbed on the surface, and where we have assumed that the enthalpic and entropic contributions to the Gibbs energy of adsorbed H are small compared to those of gaseous H_2. Also, the Gibbs energy of the bare slab is assumed to have negligible difference from the bare slab's electronic energy ($G_* \approx E_*$). The adsorption energy of Cl^- at $[Cl^-] = 1\ \mathrm{mol/L}$ as a function of applied potential (ΔG_{Cl}) is modeled as:

$$\Delta G_{Cl} = G_{Cl^*} - G_* - \frac{1}{2} G_{Cl_{2(g)}} - F(E - E^\circ(Cl_2))$$
$$= E_{Cl^*} - E_* - \frac{1}{2} G_{Cl_{2(g)}} - F(E - 1.36\ \mathrm{V}) = \Delta G_{Cl}(E = 0\ \mathrm{V}) - FE \qquad \text{(B.44)}$$

where G_{Cl^*} is the Gibbs energy of adsorbed chloride. We neglect rotational and translational free energy contribution for adsorbed species and include zero-point corrections only for G_{H^*}, thus we assume that $G_{Cl^*} \approx E_{Cl^*}$. We did not treat solvation of metal surfaces or the Rh_xS_y surfaces with either explicit or implicit solvation methods. We note that the JANAF thermochemical data for gas-phase species is based on available experimental data (such as spectroscopic constants).[41]

Selection of Stable Rh_xS_y Surface Terminations

The structures of Rh_2S_3, Rh_3S_4, and $Rh_{17}S_{15}$ phases are such that different surface terminations of a given facet result in different stoichiometries of atoms exposed to the surface. This leads to different surface chemistry depending on which termination is used for further calculations (**Figure B.19**), unlike that of pure face-centered cubic (FCC) metals.

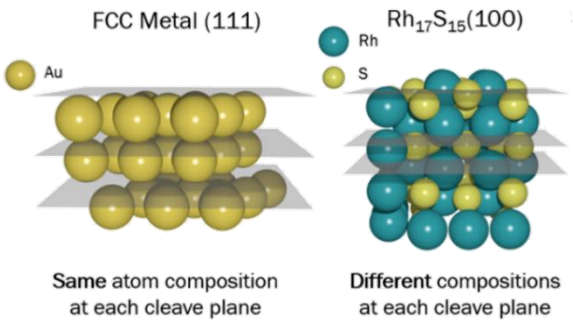

Figure B.19. Comparison of termination cuts for an FCC(111) surface and a $Rh_{17}S_{15}(100)$ surface.

The stable surface terminations were searched by computing atom-normalized surface energies of symmetric surfaces for Rh_2S_3(001), Rh_3S_4(100), and $Rh_{17}S_{15}$(100). The metric used for surface termination searching is an atom-normalized version of the normal surface energy metric for symmetric slabs:[44]

$$\frac{\gamma}{n_*} = \frac{1}{2A}\left(\frac{E_*}{n_*} - \frac{E_{\text{bulk}}}{n_{\text{bulk}}}\right) \tag{B.45}$$

where γ/n_* is the surface energy per surface atom, $2A$ is the combined geometric area of the top and bottom faces of the slab supercell, and E_*/n_* and $E_{\text{bulk}}/n_{\text{bulk}}$ are the DFT-predicted electronic energies per atom of the slab supercell and bulk primitive cell, respectively. Atom-normalized electronic energies were used for comparison because the bulk primitive has a fixed number of atoms, whereas the number of atoms in each generated termination may vary to keep the termination symmetric between the top and bottom surfaces. Thus, atom-normalized electronic energies yield a fairer comparison of which termination surface is lowest in energy relative to the bulk material. The $\frac{1}{2A}$ factor indicates calculation of a surface energy from a symmetric termination. Keeping both the top and bottom surfaces symmetric is a more accurate way to measure the cost of creating a surface from a bulk structure.[45]

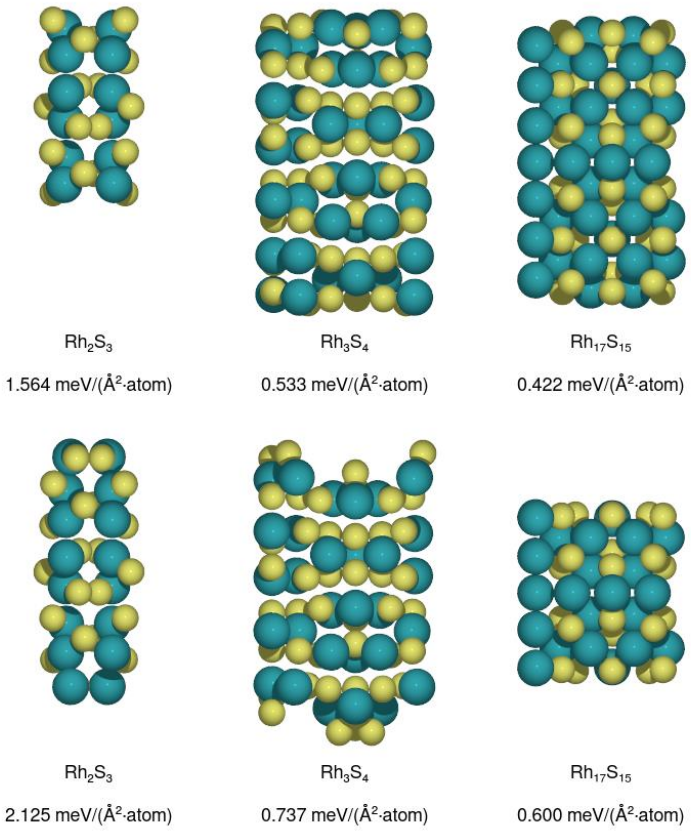

Figure B.20. Side views of the three Rh_xS_y facets (Rh_2S_3(001), Rh_3S_4(100), and $Rh_{17}S_{15}$(100)) studied. a) The most stable predicted surface terminations. b) The second most stable predicted surface terminations. The corresponding surface energies are given. Color legend: Teal = Rh; Yellow = S.

DFT-predicted Geometries

Table B.14 shows the lattice constants and cell angles of the sulfide and Pt bulk structures used to derive catalyst surfaces. Lattice constant calculation was done using a $10 \times 10 \times 10$ k point grid for Pt (FCC) and a $4 \times 4 \times 4$ k point grid for the sulfide crystals, in accordance with a $k_1 a \approx k_2 b \approx k_3 c \geq 24$ rule of thumb.

Table B.14. Lattice constants (Å) and cell angles (degrees) for each of the bulk structures used in the study.

Composition	a	b	c	α	β	γ
Rh_2S_3	6.085	6.242	8.617	90.000	90.000	90.000
Rh_3S_4	10.564	10.958	6.352	90.000	107.978	90.000
$Rh_{17}S_{15}$	10.085	10.085	10.085	90.000	90.000	90.000
Pt (FCC)	4.002	—	—	90.000	90.000	90.000

For both the transition metal and Rh sulfide surfaces, we extensively sampled the surface for possible adsorption sites. We used the AdsorbateSiteFinder module within the Pymatgen Python library to enumerate all possible single adsorption sites (for H^+ and Cl^- adsorbates) and all nearby pairs of single adsorption sites (for NO_3^-).

For the six transition metal catalysts consider (Au, Ag, Cu, Pd, Pt, and Rh), we used the FCC(211) step surface. We chose this surface based on our previous computational work, which showed that a microkinetic model for nitrate reduction built on data from FCC(211) step surfaces successfully reproduced key experimental trends.[27] This shows that the choice of the FCC(211) surface is a valid one for obtaining computational data that mirrors experimental results. Although previous literature has identified step surfaces as more active than terrace surfaces,[28,29] we extensively sampled adsorption energies on symmetrically district adsorption sites on this surface to ensure that we calculated binding energies at the most active site on the FCC(211) surface. These sites are shown in **Figure B.21**.

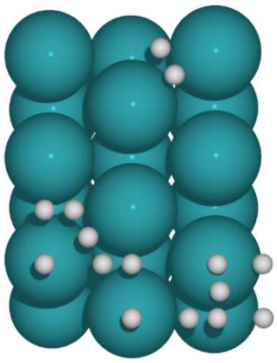

Figure B.21. Location of adsorption sites sampled on metal FCC(211) surfaces. Atom key: teal = metal, white = adsorption site.

Adsorption Energies and Predicted Binding Geometries

Figure B.22 shows the adsorption site geometries of the strongest predicted free energy for Cl^-, H^+, and NO_3^- on Rh_xS_y model surfaces. The predicted hydrogen adsorption energies for Rh_2S_3(001), Rh_3S_4(100), and $Rh_{17}S_{15}$(100) agree well with a prior study.[35] We show the adsorption sites geometries for the strongest predicted free energy for Cl^-, H^+, and NO_3^- on S-defected Rh_xS_y model surfaces in **Figure B.23**.

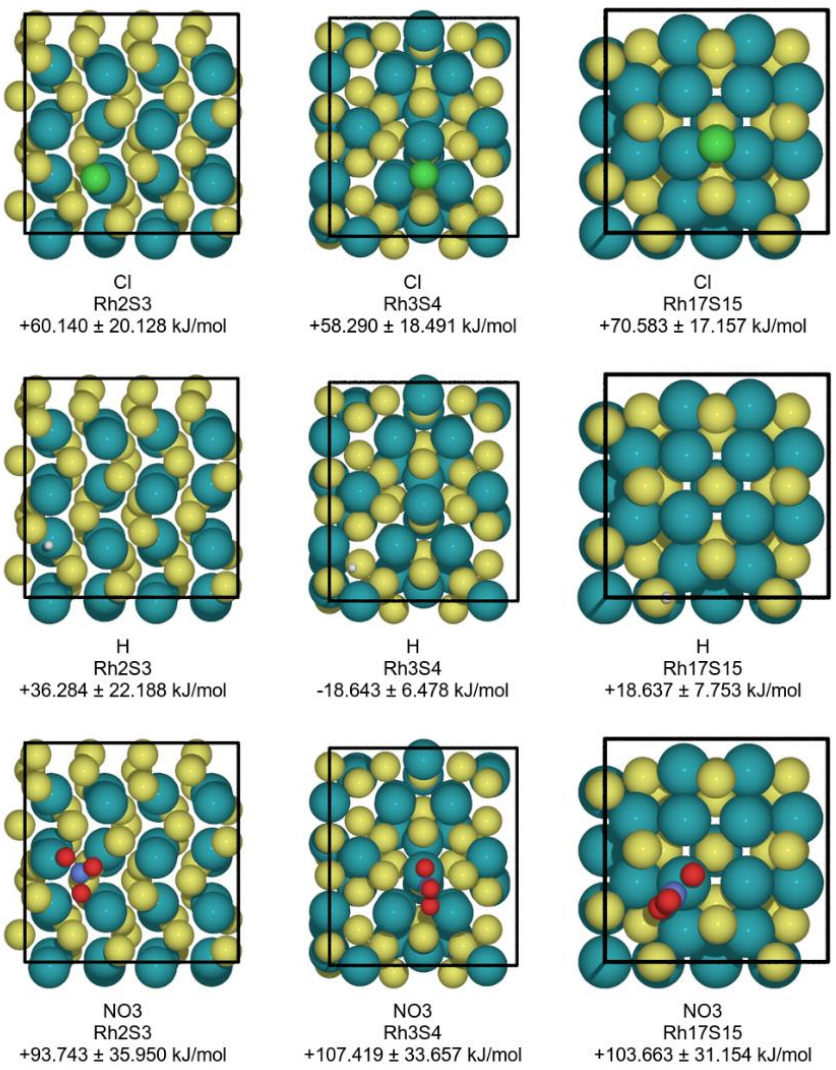

Figure B.22. Adsorption sites where Cl^-, H^+, and NO_3^- bind the strongest on pristine Rh_xS_y facets (Rh_2S_3(001), Rh_3S_4(100), and $Rh_{17}S_{15}$(100)). The caption underneath each image indicates the adsorbate, the bulk composition of the RhxSy slab, and the electronic binding energy with its BEEF-vdW uncertainty in kJ mol–1 calculated at 298.15 K and 0 V vs. SHE. Teal = Rh, yellow = S, green = Cl, white = H, red = O, indigo = N.

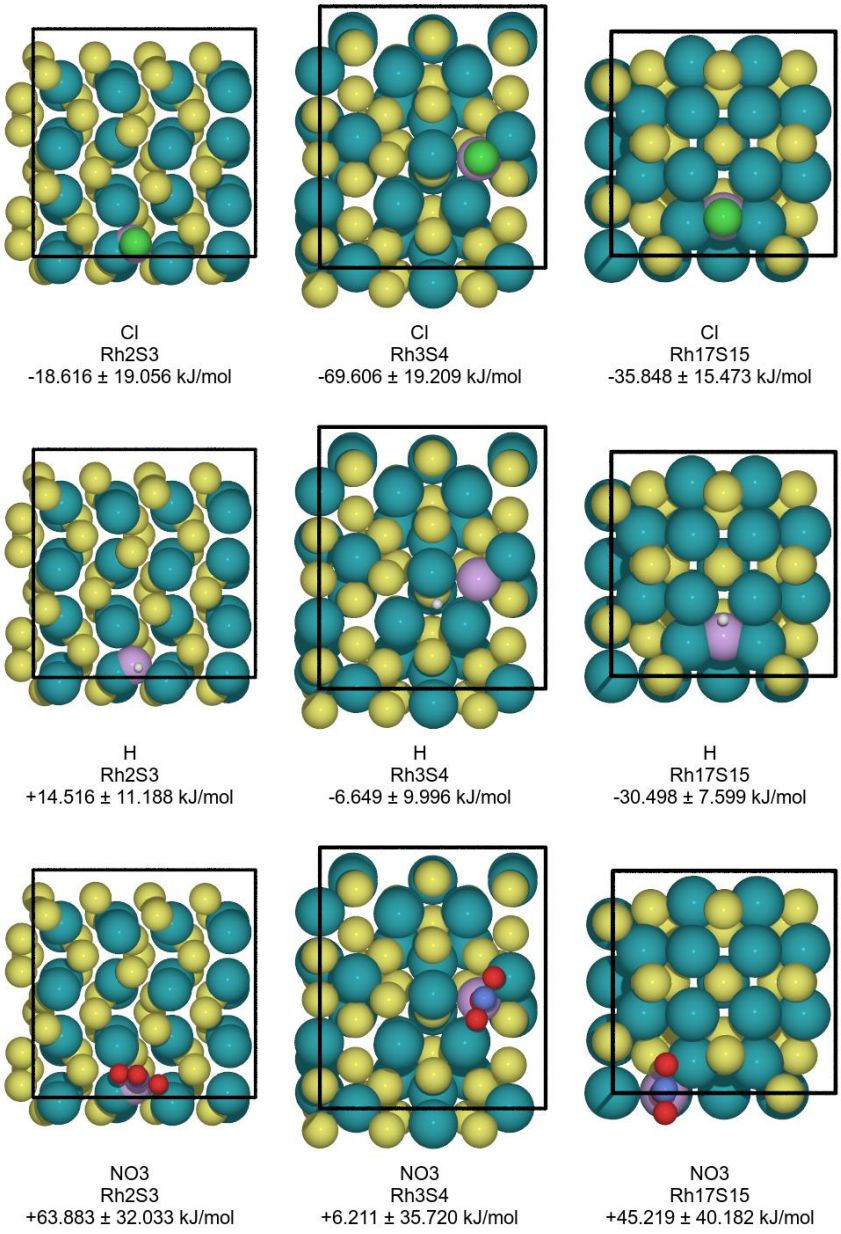

Figure B.23. Adsorption sites where Cl^-, H^+, and NO_3^- bind the strongest on S-defected Rh_xS_y facets (Rh_2S_3(001), Rh_3S_4(100), and $Rh_{17}S_{15}$(100)) . The caption underneath each image indicates the adsorbate, the bulk composition of the Rh_xS_y slab, and the electronic binding energy with its BEEF-vdW uncertainty in kJ mol^{-1} calculated at 298.15 K and 0 V vs. SHE and pH = 0. Teal = Rh, yellow = S, green = Cl, white = H, red = N, indigo = O, purple = S defect location.

Transition State Geometries

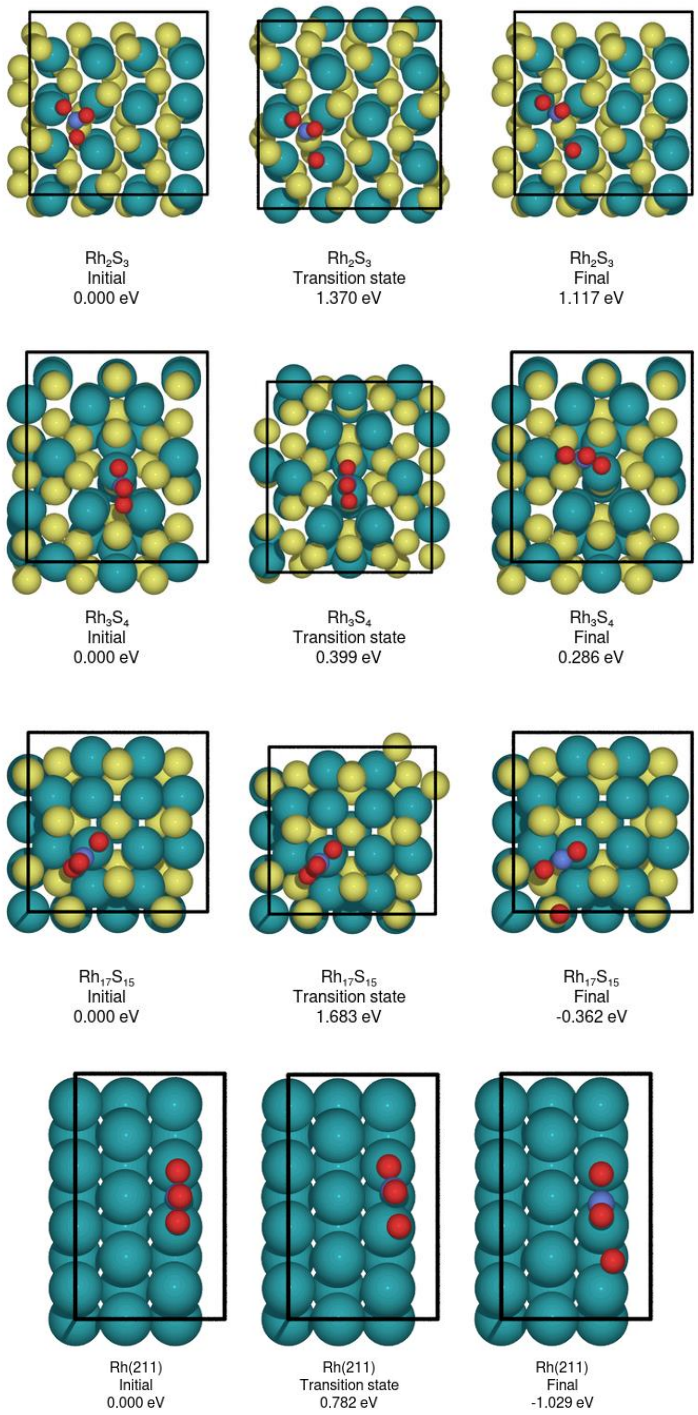

Figure B.24. Initial, transition state, and final geometries for direct nitrate reduction ($NO_3^* \rightarrow NO_2^* + O^*$) on Rh_2S_3(001), Rh_3S_4(100), $Rh_{17}S_{15}$(100) and Rh(211) surfaces. Energies are relative to the initial state for each surface.

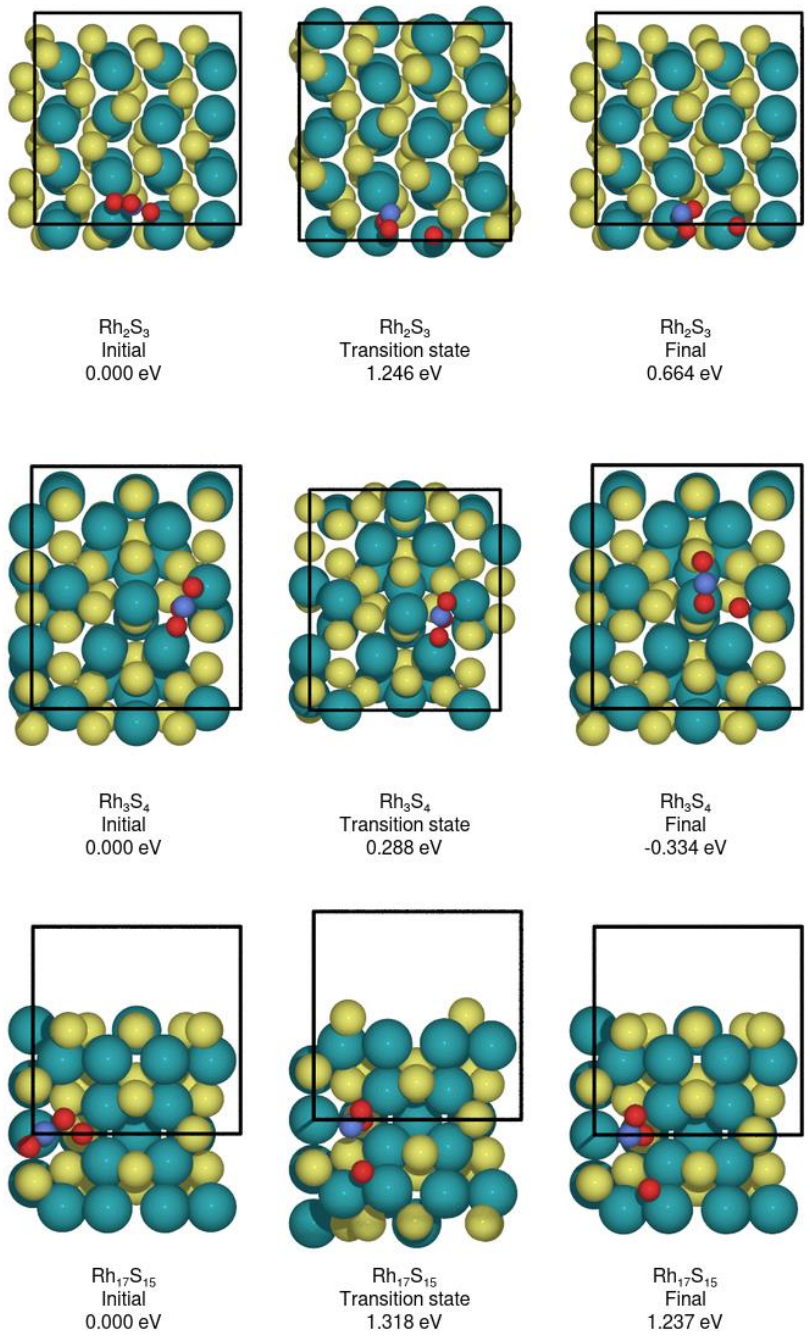

Figure B.25. Initial, transition state, and final geometries for direct nitrate reduction ($NO_3^* \rightarrow NO_2^* + O^*$) on S-defected Rh_2S_3(001), Rh_3S_4(100), $Rh_{17}S_{15}$(100) surfaces. Energies are relative to the initial state for each surface.

Rh_2S_3

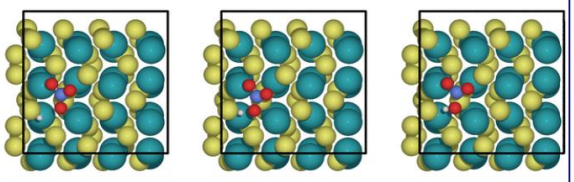

Rh_2S_3
Step 1
Initial
0.000 eV

Rh_2S_3
Step 1
Transition state
0.153 eV

Rh_2S_3
Step 1
Final
-0.316 eV

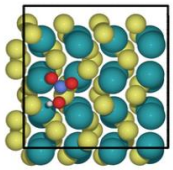

Rh_2S_3
Step 2
Initial
0.000 eV

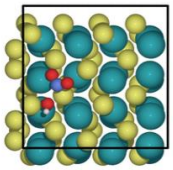

Rh_2S_3
Step 2
Transition state
1.222 eV

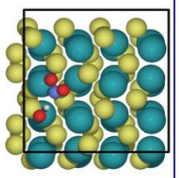

Rh_2S_3
Step 2
Final
-0.471 eV

Rh_3S_4

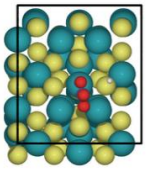

Rh_3S_4
Step 1
Initial
0.000 eV

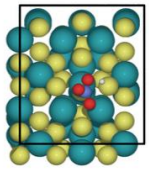

Rh_3S_4
Step 1
Transition state
0.730 eV

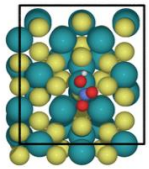

Rh_3S_4
Step 1
Final
-0.009 eV

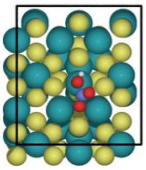

Rh_3S_4
Step 2
Initial
0.000 eV

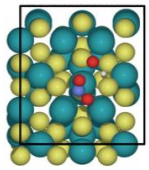

Rh_3S_4
Step 2
Transition state
2.390 eV

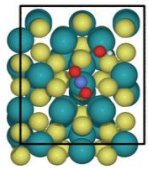

Rh_3S_4
Step 2
Final
-0.148 eV

$Rh_{17}S_{15}$

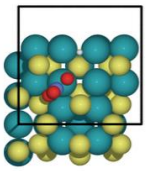

$Rh_{17}S_{15}$
Step 1
Initial
0.000 eV

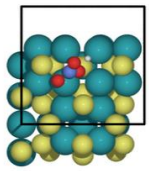

$Rh_{17}S_{15}$
Step 1
Transition state
0.857 eV

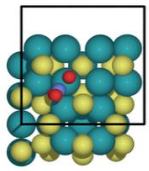

$Rh_{17}S_{15}$
Step 1
Final
-0.605 eV

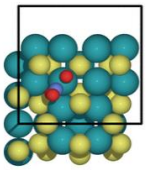

$Rh_{17}S_{15}$
Step 2
Initial
0.000 eV

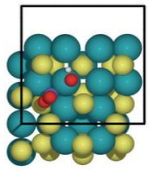

$Rh_{17}S_{15}$
Step 2
Transition state
0.583 eV

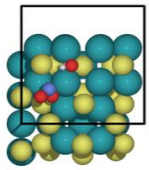

$Rh_{17}S_{15}$
Step 2
Final
-0.185 eV

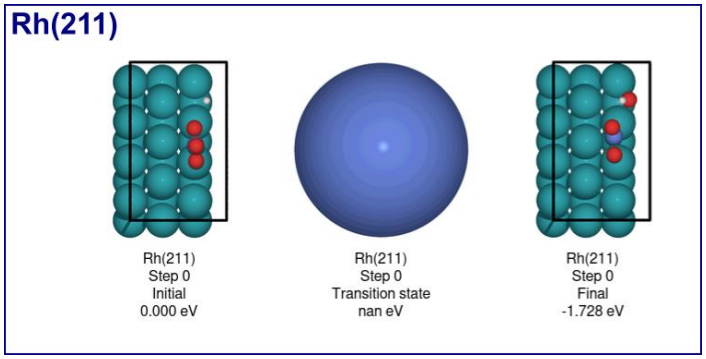

Figure B.26. Initial, transition state, and final geometries for H-assisted nitrate reduction ($NO_3^* + H^* \rightarrow HNO_3^* \rightarrow NO_2^* + HO^*$) on Rh_2S_3(001), Rh_3S_4(100), $Rh_{17}S_{15}$(100) and Rh(211) surfaces. Energies are relative to the initial state for each surface. A large blue sphere and a nan transition state energy indicate a transition state that could not be identified.

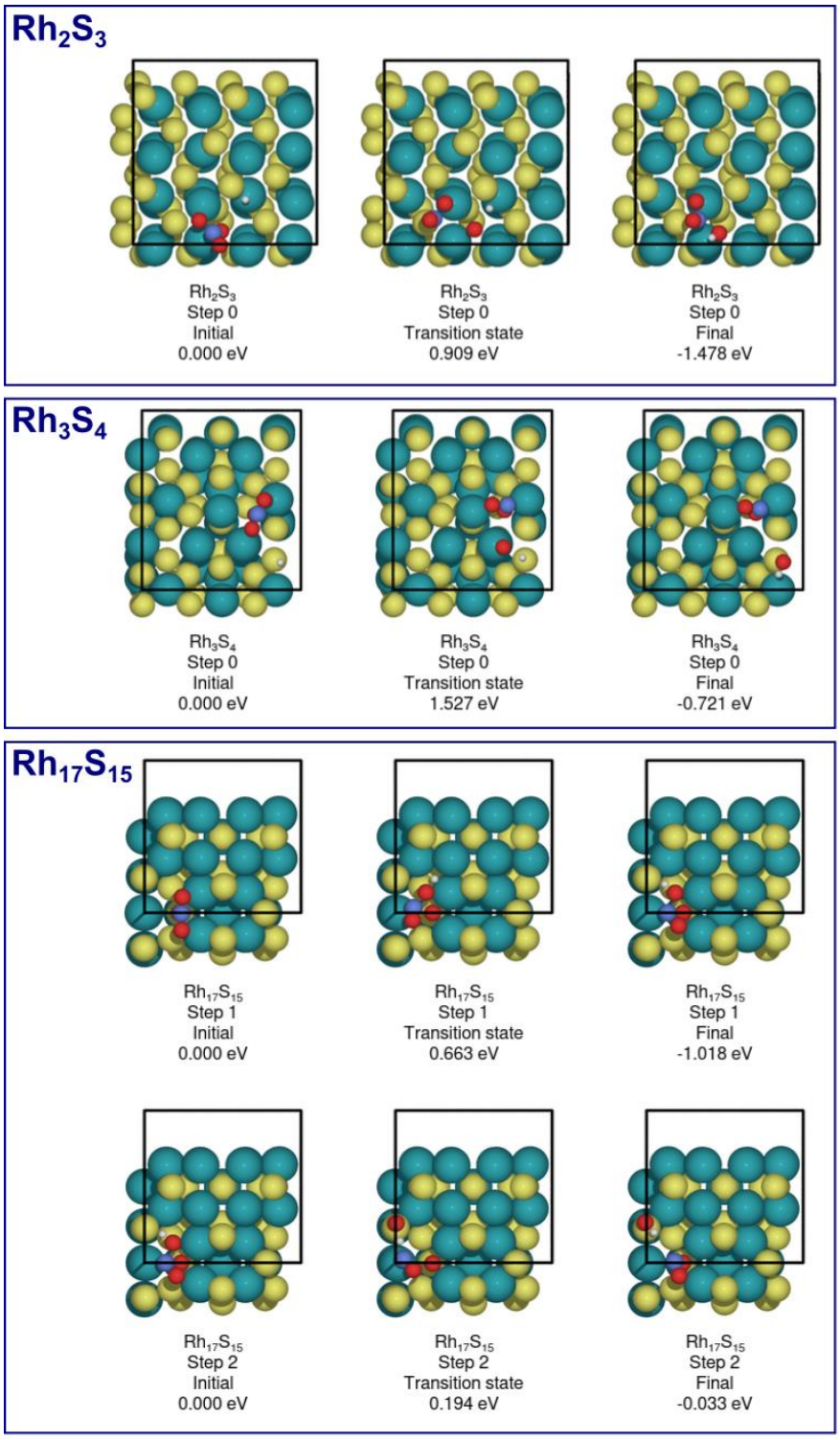

Figure B.27. Initial, transition state, and final geometries for H-assisted nitrate reduction ($NO_3^* + H^* \rightarrow HNO_3^* \rightarrow NO_2^* + HO^*$) on S-defected Rh_2S_3(001), Rh_3S_4(100), and $Rh_{17}S_{15}$(100) surfaces. Energies are relative to the initial state for each surface.

Coverage Model and Computational Cyclic Voltammograms

A Langmuir adsorption isotherm is used to analyze the competitive adsorption between hydrogen and chloride on Pt and Rh (**Chapter 4.3.2**) and to rationalize the change in H_{upd} charge in the experimental cyclic voltammograms (CVs) when chloride is added to the electrolyte (**Figure 4.2a–b**). To construct computational CVs, we use the predicted adsorption free energy (ΔG_i) of each species "i" and the applied potential (E) to calculate the coverage (θ_i) using adsorption equilibrium expressions. For the system with just hydrogen and chloride, the Langmuir isotherm considers two species which achieve an adsorption/desorption equilibrium while competing for active sites (indicated by *), as shown in **Equations B.46 and B.47** where $K_i(E)$ is the potential-dependent equilibrium constant for the adsorption/desorption reaction of the species indicated, F is Faraday's constant, ΔG_H and ΔG_{Cl} are as defined in **Equations B.42 and B.44**, R is the ideal gas constant, and T is the temperature. $[H^+]_0$ and $[Cl^-]_0$ are the concentrations of each species in the solution. The site balance includes the coverage of hydrogen and chloride and the remaining active sites.

$$K_H(E) = \exp\left(-\frac{\Delta G_H}{RT}\right) = \exp\left(-\frac{\Delta G_H(E = 0\ \mathrm{V}) + FE}{RT}\right) = \frac{\theta_H}{[H^+]_0 \theta_*} \tag{B.46}$$

$$K_{Cl}(E) = \exp\left(-\frac{\Delta G_{Cl}}{RT}\right) = \exp\left(-\frac{\Delta G_{Cl}(E = 0\ V) - FE}{RT}\right) = \frac{\theta_{Cl}}{[Cl^-]_0 \theta_*} \tag{B.47}$$

$$1 = \theta_* + \theta_H + \theta_{Cl} \tag{B.48}$$

The equilibrium constants, and thus adsorbate coverages, are each a function of the applied potential. The coverages can be expressed as a function of potential and concentration, as shown in **Equations B.49–B.51**.

$$\theta_{Cl} = \frac{K_{Cl}(E)[Cl^-]_0}{1 + K_H(E)[H^+]_0 + K_{Cl}(E)[Cl^-]_0} \tag{B.49}$$

$$\theta_{\mathrm{H}} = \frac{K_{\mathrm{H}}(E)[\mathrm{H}^+]_0}{1 + K_{\mathrm{H}}(E)[\mathrm{H}^+]_0 + K_{\mathrm{Cl}}(E)[\mathrm{Cl}^-]_0} \tag{B.50}$$

$$\theta_{*} = \frac{1}{1 + K_{\mathrm{H}}(E)[\mathrm{H}^+]_0 + K_{\mathrm{Cl}}(E)[\mathrm{Cl}^-]_0} \tag{B.51}$$

Once the coverage of each species is known as a function of applied potential, computational cyclic voltammograms were approximated by time differentiation of each coverage:

$$j_{\mathrm{theo,i}} = nF\frac{\mathrm{d}N_{\mathrm{i}}}{\mathrm{d}t} = ne\sigma\frac{\mathrm{d}\theta_{\mathrm{i}}}{\mathrm{d}E}\frac{\mathrm{d}E}{\mathrm{d}t} \tag{B.52}$$

where N_{i} is the number of sites with species "i" adsorbed, n is the number of electrons needed to adsorb/desorb from a single surface site (with positive sign when desorption reduces the adsorbed species and negative sign when desorption oxidizes it), e is the charge of an electron, σ is the areal dispersion of surface sites (1.5×10^{15} sites cm^{-2} geometric area), $\mathrm{d}\theta_{\mathrm{i}}/\mathrm{d}E$ is the derivative of the coverage, and $\mathrm{d}E/\mathrm{d}t$ is the CV scan rate. The derivatives may be approximated by finite differences. For example, the average current density for the desorption of a monolayer of H* over a potential window of 0.2 V at a scan rate of 100 mV s^{-1} would be:

$$j_{\mathrm{theo,\,H^*}} = ne\sigma\frac{\mathrm{d}\theta_{\mathrm{H}}}{\mathrm{d}E}\frac{\mathrm{d}E}{\mathrm{d}t} \approx ne\sigma\frac{\Delta\theta_{\mathrm{H}}}{\Delta E}\frac{\Delta E}{\Delta t} \tag{B.53}$$

$$= \frac{1\ \mathrm{e^-}}{1\ \mathrm{atom\ Pt}} \times \frac{1.602 \times 10^{-19}\ \mathrm{C}}{1\ \mathrm{e^-}} \times \frac{1.5 \times 10^{15}\ \mathrm{atoms\ Pt}}{1\ \mathrm{cm^2}} \times \frac{1}{0.2\ \mathrm{V}} \times \frac{0.1\ \mathrm{V}}{\mathrm{s}}$$

$$= 0.12\ \frac{\mathrm{mA}}{\mathrm{cm^2}}$$

Theoretical coverages for hydrogen and chloride between 0.05–0.4 V vs. RHE for Rh(211) and Pt(211) surfaces are shown in **Figure B.28**. The integrals of the coverages were used to create computational CVs for desorbing hydrogen and adsorbing chloride on these surfaces. Qualitatively comparing the experimental CVs on a Rh wire with adding chloride (**Figure 4.2a**) and the computational CVs on Rh(211) where we set [H$^+$] to 1 M then increase the chloride concentration,

the theoretical current for Rh(211) is close to zero at concentrations above 10^{-6} M Cl^-, whereas for the Rh wire the measured current is still significant even at 0.1 M Cl^-. The difference between the experimental and computational CVs may be because the saturation coverage of chloride experimentally is less than one monolayer and in experimental results we study polycrystalline surfaces and calculations are only on the (211) surfaces.[46] In the application of the adsorption isotherm, we have assumed that chloride can block all available sites in the computational model which would cause the current from hydrogen adsorption to be lower at even small chloride concentrations.

For the Pt CVs in **Figures 4.2b and B.28**, the relative charges between 0 to 0.4 V vs. RHE are due to chloride adsorbing on the surface as hydrogen is desorbing from the surface. In the computational Pt(211) CV, there is a shift in the peak in anodic current towards more negative potentials at higher chloride coverages. This shift in current is less obvious in the experimental CVs on the Pt RDE due to the two characteristic Pt H_{upd} peaks but the accumulation of charge across the potentials also indicates that the charge is transferred at more negative potentials on the Pt RDE with increasing chloride concentrations.

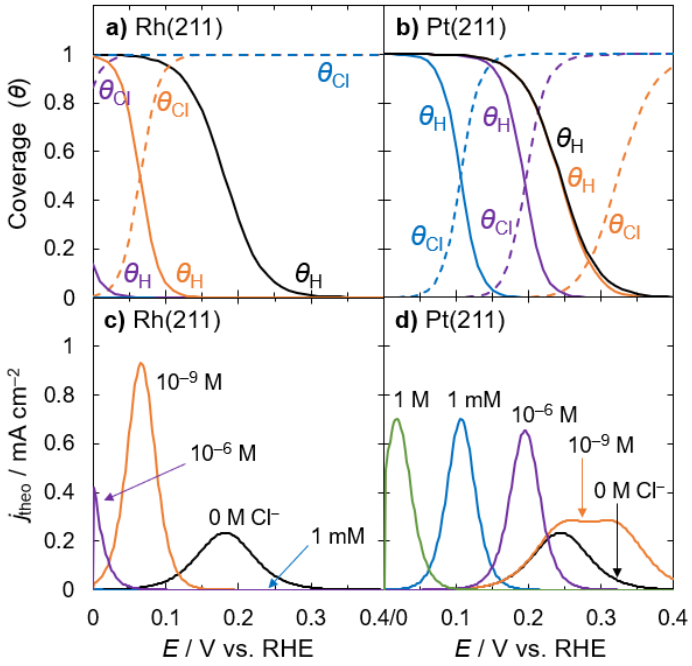

Figure B.28. Theoretical coverage plots generated using the Langmuir adsorption model for a) Rh(211) and b) Pt(211). These coverage plots are used to calculate the computational CVs for c) Rh(211) and d) Pt(211). Solid and dashed lines indicate the hydrogen and chloride coverages at each concentration, respectively.

The Langmuir adsorption model was expanded to include hydrogen, nitrate, and chloride species competing for the same active surface sites (**Equations 4.1-4.3**). We assume for simplicity that each molecule adsorbs only to one site, although NO_3 binds to two sites.[47] We fully describe the adsorption thermodynamics of all species in the system below.

$$K_{NO_3}(E) = \exp\left(-\frac{\Delta G_{NO_3}}{RT}\right) = \exp\left(-\frac{\Delta G_{NO_3}(E = 0\ V) - FE}{RT}\right) = \frac{\theta_{NO_3}}{[NO_3^-]_0 \theta_*} \tag{B.54}$$

$$1 = \theta_* + \theta_H + \theta_{Cl} + \theta_{NO_3} \tag{B.55}$$

The coverages as a function of potential and concentration from **Equations B49–B.51** are adjusted to include the contribution from nitrate in **Equations B.56–B.59**.

$$\theta_{Cl} = \frac{K_{Cl}(E)[Cl^-]_0}{1 + K_H(E)[H^+]_0 + K_{Cl}(E)[Cl^-]_0 + K_{NO_3}(E)[NO_3^-]_0} \tag{B.56}$$

$$\theta_H = \frac{K_H(E)[H^+]_0}{1 + K_H(E)[H^+]_0 + K_{Cl}(E)[Cl^-]_0 + K_{NO_3}(E)[NO_3^-]_0} \tag{B.57}$$

$$\theta_{\mathrm{NO_3}} = \frac{K_{\mathrm{NO_3}}(E)[\mathrm{NO_3}^-]_0}{1 + K_{\mathrm{H}}(E)[\mathrm{H}^+]_0 + K_{\mathrm{Cl}}(E)[\mathrm{Cl}^-]_0 + K_{\mathrm{NO_3}}(E)[\mathrm{NO_3^-}]_0} \tag{B.58}$$

$$\theta_{*} = \frac{1}{1 + K_{\mathrm{H}}(E)[\mathrm{H}^+]_0 + K_{\mathrm{Cl}}(E)[\mathrm{Cl}^-]_0 + K_{\mathrm{NO_3}}(E)[\mathrm{NO_3^-}]_0} \tag{B.59}$$

The coverages of hydrogen, nitrate, and chloride on Rh(211) and Pt(211) are shown in **Figure 4.3** for potentials between 0.05–0.4 V vs. RHE with 1 M H^+, 1 M NO_3^-, and 0, 10^{-10}, and 10^{-9} M Cl^-.

Simple Microkinetic Models for Nitrate Reduction on Pt/C and Rh/C

Four rate laws for nitrate reduction were considered to understand the effects of chloride on the reduction rate. The model approximating the rate determining step (RDS) as the dissociation of nitrate to nitrite via adsorbed hydrogen most closely matched our experimental observations and is written in **Chapter 4.2.6** and referred to here as model 1 (M1). Reactions from **Chapter 4.2.7** are rewritten below, where * represents an active site or adsorbed species. All four rate laws begin with the same adsorption steps.

$$H^+_{(aq)} + * + e^- \rightleftharpoons H^* \tag{4.1}$$

$$NO^-_{3\,(aq)} + * \rightleftharpoons NO^*_3 + e^- \tag{4.2}$$

$$Cl^-_{(aq)} + * \rightleftharpoons Cl^* + e^- \tag{4.3}$$

The equilibrium constants K_{H}, $K_{\mathrm{NO_3}}$, and K_{Cl} correspond to the reactions in **Equations 4.1-4.3** and are a function of potential. Following hydrogen, nitrate, and chloride adsorption, we modeled four rate laws. The rates predicted from the four models are presented in **Figure B.29** from 0 to 0.4 V vs. RHE for Rh(211) and 0 to 0.6 V vs. RHE for Pt(211). The rate from M1 is also in **Figure 4.3**.

Microkinetic Model 1 (M1)—H-assisted Nitrate Reduction.

The rate equation for M1 is given in **Equations 4.10 and 4.11** when **Equations 4.1–4.3** are considered in quasi-equilibrium, **Equation 4.9** is considered irreversible and rate determining, and the reactions in **Equations 4.6 and 4.7** are assumed to be infinitely fast. The rate constant k_9 is the rate constant for the forward reaction of **Equation 4.9**, θ_i is the coverage of species i, and $[NO_3^-]_0$, $[H^+]_0$, and $[Cl^-]_0$ are the concentrations of each species in the solution. M1 is the microkinetic model we use throughout the main text. We do not know the value of the rate constant k_9 so we plot the rate in **Equation 4.11** divided by k_9 in **Figure B.29**.

$$H^* + NO_3^* \rightleftarrows NO_2^* + HO^* \quad \text{RDS} \quad (4.9)$$

$$HO^* \rightarrow \text{products} \quad \text{infinitely fast} \quad (4.6)$$

$$NO_2^* \rightarrow \text{products} \quad \text{infinitely fast} \quad (4.7)$$

$$\text{rate}_{M1} = k_9 \theta_{NO_3} \theta_H \quad (4.10)$$

$$\text{rate}_{M1} = \frac{k_9 K_{NO_3} K_H [NO_3^-]_0 [H^+]_0}{\left(1 + K_H [H^+]_0 + K_{NO_3} [NO_3^-]_0 + K_{Cl} [Cl^-]_0\right)^2} \quad (4.11)$$

Alternatively, if we consider the reaction in **Equation B.60** as the RDS following quasi-equilibrated adsorption of nitrate and hydrogen, we attain a rate law identical to **Equations 4.10 and 4.11** except with k_{S31} as the rate constant instead of k_9. Due to the similar dependence on nitrate and hydrogen coverages, the rate law for the formation of adsorbed HNO_3 is only distinguished from the rate law for the formation of adsorbed NO_2 and HO by the rate constant of the RDS.

$$H^* + NO_3^* \rightleftarrows HNO_3^* + * \quad \text{RDS} \quad (B.60)$$

$$HNO_3^* \rightarrow \text{products} \quad \text{infinitely fast} \quad (B.61)$$

Microkinetic Model 2 (M2).

The second microkinetic model (M2) considers **Equations B.61 and B.62**. In M2, the reaction of adsorbed nitrate and a proton to form adsorbed nitric acid (**Equation B.61**) is assumed to be the RDS and irreversible. The rate equation for M2 is given in **Equation B.63**, where k_{S33} is the rate constant for the forward reaction of **Equation B.61**. We do not know the value of the rate constant k_{S33}, so when we model M2 from 0 to 0.6 V vs. RHE we normalize to k_{S33} at 0 V vs. RHE (e.g., at 0.2 V vs. RHE, the rate from **Equation B.63** is divided by the value of k_{S33} at 0 V vs. RHE). We approximate the voltage dependence of this rate constant using the Butler-Volmer equation with a symmetry coefficient of 0.5.

$$H^+_{(aq)} + NO^*_3 + e^- \rightleftarrows HNO^*_3 \qquad \text{RDS} \qquad \text{(B.62)}$$

$$HNO^*_3 \rightarrow \text{products} \qquad \text{infinitely fast} \qquad \text{(B.61)}$$

$$\text{rate}_{M2} = k_{S33}\theta_{NO_3}[H^+]_0 = \frac{k_{S33}K_{NO_3}[NO^-_3]_0[H^+]_0}{1 + K_H[H^+]_0 + K_{NO_3}[NO^-_3]_0 + K_{Cl}[Cl^-]_0} \qquad \text{(B.63)}$$

Microkinetic Model 3 (M3)—Direct Nitrate Reduction.

The third microkinetic model (M3) considered **Equations 4.4–4.7**. In M3, we consider nitrate dissociation to adsorbed nitrite and adsorbed O (**Equation 4.4**) as the RDS and the reduction of adsorbed oxygen and nitrite to other products (**Equations 4.5–4.7**) is infinitely fast. The rate equation for M3 is given in **Equation B.64**, where k_4 is the rate constant for the forward reaction in **Equation 4.4**. k_4 was previously calculated[27] on Pt(211) and Rh(211) as 0.2 and 3400 s^{-1}, respectively.

$$NO^*_3 + * \rightleftarrows NO^*_2 + O^* \qquad \text{RDS} \qquad (4.4)$$

$$O^* + H^* \rightleftarrows HO^* + * \qquad \text{infinitely fast} \qquad (4.5)$$

$$HO^* \rightarrow \text{products} \qquad \text{infinitely fast} \qquad (4.6)$$

$$NO^*_2 \rightarrow \text{products} \qquad \text{infinitely fast} \qquad (4.7)$$

$$\text{rate}_{M3} = k_4\theta_{NO_3}\theta_* = \frac{k_4K_{NO_3}[NO^-_3]_0}{\left(1 + K_H[H^+]_0 + K_{NO_3}[NO^-_3]_0 + K_{Cl}[Cl^-]_0\right)^2} \qquad \text{(B.64)}$$

Microkinetic Model 4 (M4).

The fourth microkinetic model (M4) considers **Equations 4.4–4.7** and the rate law was determined by assuming **Equations 4.4 and 4.5** are irreversible in the forward direction. In this model only, we included adsorbed oxygen in the active site balance. A pseudo-steady state assumption was made for the coverage of oxygen to solve for the rate equation. The rate equation for M4 is given in **Equation B.65**. k_4 and k_5 are the forward rate constants of the reactions in

Equations 4.4 and 4.5. Along with k_4, k_5 was previously calculated using DFT[27] on Pt(211) and Rh(211) as 14.5 and 23700 s^{-1}, respectively.

$$NO_3^* + * \rightarrow NO_2^* + O^* \qquad \text{irreversible} \qquad (4.4)$$

$$O^* + H^* \rightarrow HO^* + * \qquad \text{irreversible} \qquad (4.5)$$

$$HO^* \rightarrow \text{products} \qquad \text{infinitely fast} \qquad (4.6)$$

$$NO_2^* \rightarrow \text{products} \qquad \text{infinitely fast} \qquad (4.7)$$

$$\text{rate}_{M4} = k_4 \theta_{NO_3} \theta_* = \frac{k_4 K_{NO_3} [NO_3^-]_0}{\left[1 + K_H [H^+]_0 + K_{NO_3} [NO_3^-]_0 + K_{Cl} [Cl^-]_0 + \frac{k_4 K_{NO_3} [NO_3^-]_0}{k_5 K_H [H^+]_0}\right]^2} \qquad (B.65)$$

The nitrate reduction rates as a function of potential as predicted by the four rate laws are shown in **Figure B.29**, with M1 best matching the experimental trends observed on Pt/C in this work. For Pt(211) shown in **Figure B.29e–h**, M1 most closely captures what we observe experimentally, where nitrate reduction has a maximum in current between 0 and 0.4 V vs. RHE and when chloride is added, NO_3RR is inhibited. M2 inaccurately predicts that Pt would not have nitrate reduction above 0.1 V vs. RHE. M3 and M4 are very similar for their prediction of NO_3RR on Pt(211) (**Figure B.29g–h**) and both predict that NO_3RR will be greatest at potentials more positive than 0.4 V, which does not match what we experimentally observe on Pt (**Figure 4.1**). For all four models, Rh(211) (**Figure B.29a–d**) shows a maximum in predicted nitrate reduction rate near 0.1 V vs. RHE which is caused by the desorption of hydrogen allowing for an increase in nitrate coverage at this potential. The amount the rate is suppressed by chloride is dependent on the model, though all modeled rates are similarly affected by chloride.

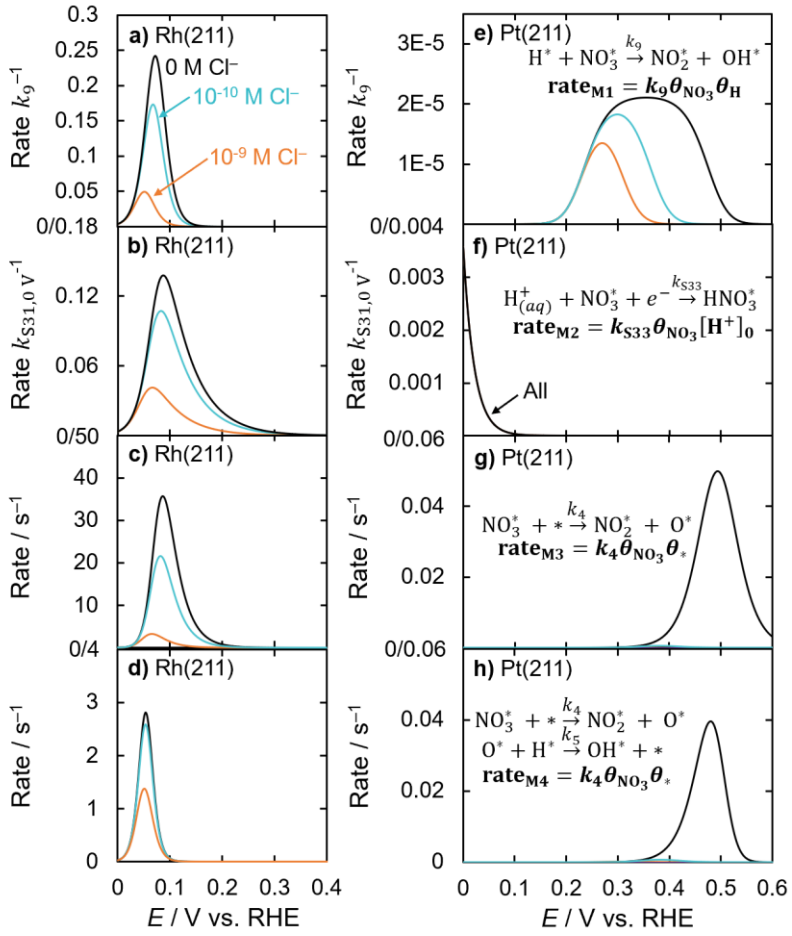

Figure B.29. Microkinetic models for nitrate reduction considering the adsorption of nitrate, hydrogen, and chloride with different rate determining steps on Rh(211) (a–d) and Pt(211) (e–f). In all models for both Rh(211) and Pt(211), the proton and nitrate concentration in solution is 1 M and only the concentration of chloride is increasing. The concentration of chloride is labeled in panels a) and e) as 0 M (black), 10–10 M (teal), and 10–9 M (orange). The data in panels (a) and (e) are shown in **Figure 4.3.**

H^+ and Cl^- Adsorption Energies on Transition Metals, Pristine Rh_xS_y, and S-defected Rh_xS_y Surfaces

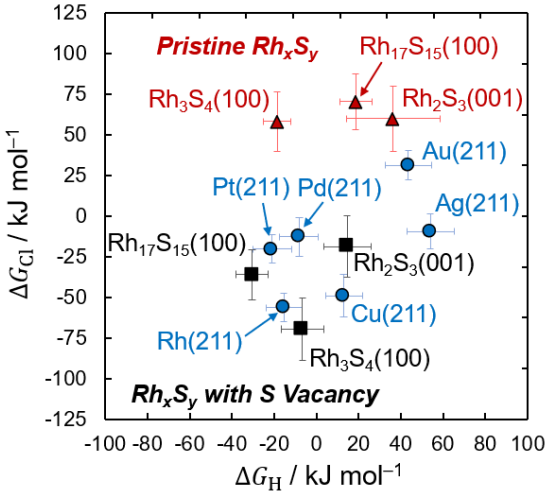

Figure B.30. Adsorption free energies at 0 V vs. SHE and 298.15 K for Cl^- and H^+ on pure metals (blue circles), pristine Rh_xS_y surfaces (red triangles), and sulfur-defected Rh_xS_y surfaces (black squares). Error bars are BEEF-vdW uncertainties.

Computed Kinetic and Thermodynamic Parameters for NO_3RR on Rh_xS_y

Table B.15. Computed kinetic and thermodynamic parameters for nitrate reduction on $Rh_3S_4(100)$, $Rh_{17}S_{15}(100)$, $Rh_2S_3(100)$, and Rh(211). Adsorption energies are from **Figure 4.4** and **Figure B.30**. Activation barriers are from **Figure 4.5**.

Surface	**Direct**			**H-assisted**			
	E_a / kJ mol^{-1}	k_4 / s^{-1}	ΔG_{NO_3} / kJ mol^{-1}	E_a / kJ mol^{-1}	k_9 / s^{-1}	ΔG_{NO_3} / kJ mol^{-1}	ΔG_H / kJ mol^{-1}
Rh(211)	75.46	5.91×10^{-2}	−1.44	—	—	−1.44	−15.39
Pristine $Rh_3S_4(100)$	38.52	1.77×10^{5}	107.42	70.47	4.44×10^{-1}	107.42	−18.64
Pristine $Rh_{17}S_{15}(100)$	162.38	3.44×10^{-17}	103.66	82.66	3.24×10^{-3}	103.66	18.64
Pristine $Rh_2S_3(100)$	132.19	6.75×10^{-12}	93.74	117.95	2.11×10^{-9}	93.74	36.28
S-defected $Rh_3S_4(100)$	27.78	1.35×10^{7}	6.21	147.37	1.47×10^{-14}	6.21	−6.65
S-defected $Rh_{17}S_{15}(100)$	127.15	5.15×10^{-11}	45.22	63.97	6.12×10^{0}	45.22	−30.50
S-defected $Rh_2S_3(100)$	120.19	8.54×10^{-10}	63.88	87.66	4.31×10^{-4}	63.88	14.52

Calculated TOFs with 10^{-9} M Chloride Poisoning

Figure B.31 shows computed TOF values assuming trace (10^{-9} M) chloride concentrations. It is the same methodology as **Figure 4.6**, but with chloride included in the model. The decrease in TOF when including chloride (by comparing **Figure 4.6** and **Figure B.31**) is generally largest for Rh_3S_4(100) and $Rh_{17}S_{15}$(100), which tend to bind chloride the strongest. Generally, pristine sulfide surfaces are not affected as they bind chloride very weakly. For S-defected sulfide surfaces, both Rh_3S_4(100) and $Rh_{17}S_{15}$(100) show sharp declines in activity. For S-defected Rh_2S_3(100), the TOF declines near $E = 0.4$ V vs. RHE rather than reaching a plateau as it did in the chloride-free case. Rh(211) also shows a lower TOF with chloride present, as expected. The computed TOF for Rh(211) in **Figure B.31a** is the same as that shown in **Figure B.29c** above, just on a log plot here.

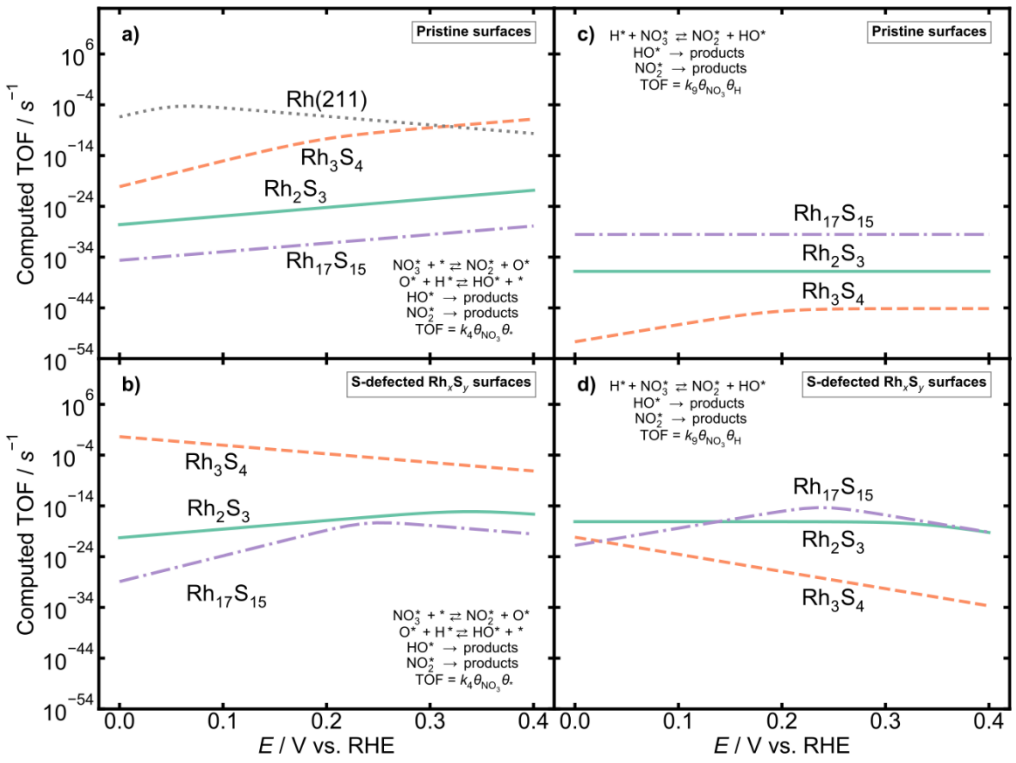

Figure B.31. Computed potential-dependent TOFs for pristine (a, c) and S-defected (b, d) surfaces, assuming a direct (a, b) or H-assisted (c, d) reaction mechanism. For all TOF calculations, we assume $[NO_3^-]_0 = 1$ M, $[H^+]_0 = 1$ M, and $[Cl^-]_0 = 10^{-9}$ M.

References

1. van Santen, R. A., Markvoort, A. J., Filot, I. A. W., Ghouri, M. M. & Hensen, E. J. M. Mechanism and microkinetics of the Fischer-Tropsch reaction. *Physical Chemistry Chemical Physics* **15**, 17038–17063 (2013).
2. Nitoń, P., Zywociński, A., Fiałkowski, M. & Hołyst, R. A 'nano-windmill' driven by a flux of water vapour: A comparison to the rotating ATPase. *Nanoscale* **5**, 9732–9738 (2013).
3. Filot, I. A. W., van Santen, R. A. & Hensen, E. J. M. The optimally performing Fischer-Tropsch catalyst. *Angewandte Chemie - International Edition* **53**, 12746–12750 (2014).
4. Filot, I. A. W. *et al.* First-Principles-Based Microkinetics Simulations of Synthesis Gas Conversion on a Stepped Rhodium Surface. *ACS Catal* **5**, 5453–5467 (2015).
5. https://www.mkmcxx.nl/ . (2018).
6. Campbell, C. T. Future Directions and Industrial Perspectives Micro- and macro-kinetics: Their relationship in heterogeneous catalysis. *Top Catal* **1**, 353–366 (1994).
7. Campbell, C. T. Finding the rate-determining step in a mechanism: Comparing DeDonder relations with the 'Degree of Rate Control'. *Journal of Catalysis* vol. 204 520–524 Preprint at https://doi.org/10.1006/jcat.2001.3396 (2001).
8. Stegelmann, C., Andreasen, A. & Campbell, C. T. Degree of rate control: How much the energies of intermediates and transition states control rates. *J Am Chem Soc* **131**, 8077–8082 (2009).
9. Calle-Vallejo, F., Huang, M., Henry, J. B., Koper, M. T. M. & Bandarenka, A. S. Theoretical design and experimental implementation of Ag/Au electrodes for the electrochemical reduction of nitrate. *Physical Chemistry Chemical Physics* **15**, 3196 (2013).
10. Lide, D. R. CRC Handbook of Chemistry and Physics. *eBook* 3485 (2003) doi:978-1466571143.
11. Chase Jr, M. *et al. Janaf Thermodynamic Tables*. (American Chemical Society/American Institute of Physics/National Bureau of Standards, 1985).
12. Nørskov, J. K. *et al.* Trends in the Exchange Current for Hydrogen Evolution. *J Electrochem Soc* **152**, J23 (2005).
13. Dima, G. E., de Vooys, A. C. A. & Koper, M. T. M. Electrocatalytic reduction of nitrate at low concentration on coinage and transition-metal electrodes in acid solutions. *Journal of Electroanalytical Chemistry* **554–555**, 15–23 (2003).
14. Lu, X., Xu, X., Wang, N. & Zhang, Q. Bonding of NO2 to the Au atom and Au(111) surface: A quantum chemical study. *Journal of Physical Chemistry A* **103**, 10969–10974 (1999).
15. Getman, R. B. & Schneider, W. F. DFT-based characterization of the multiple adsorption modes of nitrogen oxides on Pt(111). *Journal of Physical Chemistry C* **111**, 389–397 (2007).
16. Sebastiani, D. & Delle Site, L. Adsorption of water molecules on flat and stepped nickel surfaces from first principles. *J Chem Theory Comput* **1**, 78–82 (2005).
17. Kolb, M. J., Calle-Vallejo, F., Juurlink, L. B. F. & Koper, M. T. M. Density functional theory study of adsorption of H2O, H, O, and OH on stepped platinum surfaces. *Journal of Chemical Physics* **140**, (2014).

18. Kresse, G. & Furthmüller, J. Efficient Iterative Schemes for Ab Initio Total-Energy Calculations Using a Plane-Wave Basis Set. *Phys Rev B Condens Matter Mater Phys* **54**, 11169–11186 (1996).
19. Kresse, G. & Furthmüller, J. Efficiency of Ab-Initio Total Energy Calculations for Metals and Semiconductors Using a Plane-Wave Basis Set. *Comput Mater Sci* **6**, 15–50 (1996).
20. Kresse, G. & Hafner, J. Ab Initio Molecular-Dynamics Simulation of the Liquid-Metalamorphous- Semiconductor Transition in Germanium. *Phys Rev B* **49**, 14251–14269 (1994).
21. Kresse, G. & Hafner, J. *Ab Initio* Molecular Dynamics for Liquid Metals. *Phys Rev B* **47**, 558–561 (1993).
22. Wellendorff, J. *et al.* Density Functionals for Surface Science: Exchange-Correlation Model Development With Bayesian Error Estimation. *Phys Rev B* **85**, 235149 (2012).
23. Mallikarjun Sharada, S., Karlsson, R. K. B., Maimaiti, Y., Voss, J. & Bligaard, T. Adsorption on transition metal surfaces: Transferability and accuracy of DFT using the ADS41 dataset. *Phys Rev B* **100**, 035439 (2019).
24. Joubert, D. From Ultrasoft Pseudopotentials to the Projector Augmented-Wave Method. *Phys Rev B Condens Matter Mater Phys* **59**, 1758–1775 (1999).
25. Blöchl, P. E. Projector Augmented-Wave Method. *Phys Rev B* **50**, 17953–17979 (1994).
26. Wisesa, P., McGill, K. A. & Mueller, T. Efficient generation of generalized Monkhorst-Pack grids through the use of informatics. *Phys Rev B* **93**, 155109 (2016).
27. Liu, J.-X., Richards, D., Singh, N. & Goldsmith, B. R. Activity and Selectivity Trends in Electrocatalytic Nitrate Reduction on Transition Metals. *ACS Catal* **9**, 7052–7064 (2019).
28. Calle-Vallejo, F., Huang, M., Henry, J. B., Koper, M. T. M. & Bandarenka, A. S. Theoretical Design and Experimental Implementation of Ag/Au Electrodes for the Electrochemical Reduction of Nitrate. *Physical Chemistry Chemical Physics* **15**, 3196 (2013).
29. Taguchi, S. & Feliu, J. M. Electrochemical Reduction of Nitrate on Pt(S)[n(1 1 1) × (1 1 1)] Electrodes in Perchloric Acid Solution. *Electrochim Acta* **52**, 6023–6033 (2007).
30. Henkelman, G., Uberuaga, B. P. & Jónsson, H. A Climbing Image Nudged Elastic Band Method for Finding Saddle Points and Minimum Energy Paths. *J Chem Phys* **113**, 9901–9904 (2000).
31. Henkelman, G. & Jónsson, H. A dimer method for finding saddle points on high dimensional potential surfaces using only first derivatives. *J Chem Phys* **111**, 7010–7022 (1999).
32. Heyden, A., Bell, A. T. & Keil, F. J. Efficient methods for finding transition states in chemical reactions: Comparison of improved dimer method and partitioned rational function optimization method. *J Chem Phys* **123**, 224101 (2005).
33. Jacob, K. T. & Gupta, P. Gibbs Free Energy of Formation of Rhodium Sulfides. *J Chem Thermodyn* **70**, 39–45 (2014).
34. Diéguez, O. & Marzari, N. First-Principles Characterization of the Structure and Electronic Structure of A-S and Rh-S Chalcogenides. *Phys Rev B* **80**, 214115 (2009).
35. Singh, N. *et al.* Investigation of the Active Sites of Rhodium Sulfide for Hydrogen Evolution/Oxidation Using Carbon Monoxide as a Probe. *Langmuir* **30**, 5662–5668 (2014).
36. Ong, S. P. *et al.* Python Materials Genomics (Pymatgen): A Robust, Open-Source Python Library for Materials Analysis. *Comput Mater Sci* **68**, 314–319 (2013).

37. Montoya, J. H. & Persson, K. A. A high-throughput framework for determining adsorption energies on solid surfaces. *NPJ Comput Mater* **3**, 14 (2017).
38. Wei, L., Liu, D. J., Rosales, B. A., Evans, J. W. & Vela, J. Mild and Selective Hydrogenation of Nitrate to Ammonia in the Absence of Noble Metals. *ACS Catal* **10**, 3618–3628 (2020).
39. Nørskov, J. K. *et al.* Origin of the Overpotential for Oxygen Reduction at a Fuel-Cell Cathode. *J Phys Chem B* **108**, 17886–17892 (2004).
40. Rumble, J. R., Lide, D. R. & Bruno, T. J. *CRC Handbook of Chemistry and Physics: A Ready-Reference Book of Chemical and Physical Data*. (2019).
41. NIST. NIST-JANAF Thermochemical Tables. *NIST Standard Reference Database 13* (1985).
42. Akhade, S. A., Bernstein, N. J., Esopi, M. R., Regula, M. J. & Janik, M. J. A Simple Method to Approximate Electrode Potential-Dependent Activation Energies Using Density Functional Theory. *Catal Today* **288**, 63–73 (2017).
43. Gossenberger, F., Roman, T. & Groß, A. Hydrogen and Halide Co-Adsorption on Pt(111) in an Electrochemical Environment: A Computational Perspective. *Electrochim Acta* **216**, 152–159 (2016).
44. Sun, W. & Ceder, G. Efficient Creation and Convergence of Surface Slabs. *Surf Sci* **617**, 53–59 (2013).
45. Tran, R. *et al.* Surface Energies of Elemental Crystals. *Sci Data* **3**, 160080 (2016).
46. Li, N. & Lipkowski, J. Chronocoulometric Studies of Chloride Adsorption at the Pt(111) Electrode Surface. *Journal of Electroanalytical Chemistry* **491**, 95–102 (2000).
47. Nakata, K. *et al.* Surface-Enhanced Infrared Absorption Spectroscopic Studies of Adsorbed Nitrate, Nitric Oxide, and Related Compounds 2: Nitrate Ion Adsorption at a Platinum Electrode. *Langmuir* **24**, 4352–4357 (2008).